Kuiper Belt to Capture

The coupled orbital-interior evolution of Triton

Q.B. van Woerkom

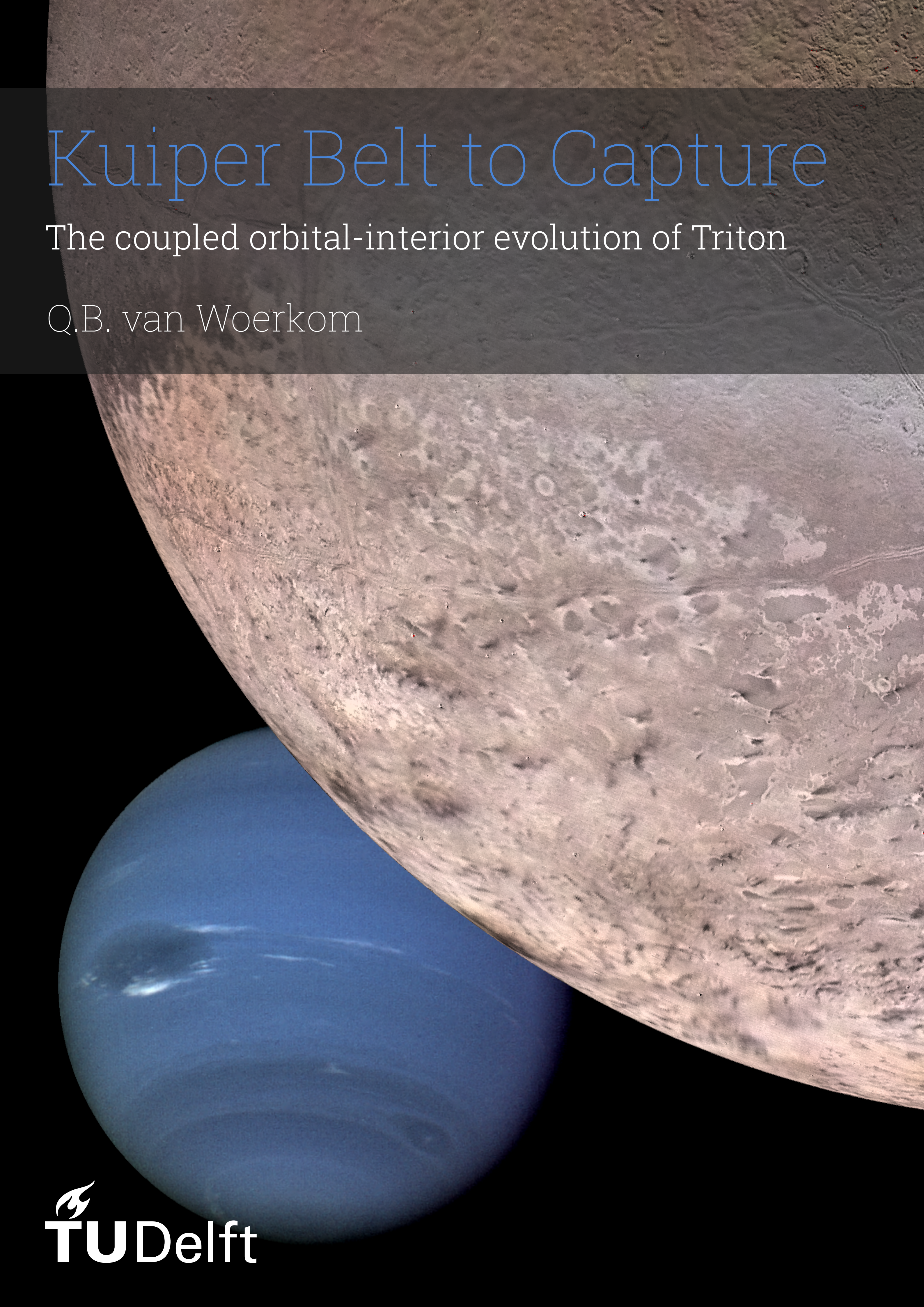

TU Delft

Kuiper Belt to Capture

The coupled orbital-interior evolution of Triton

by

Q.B. van Woerkom

to obtain the degree of Master of Science
at the Delft University of Technology
to be defended publicly on Friday May 9, 2025 at 10.45.

Student number:	4663861
Date:	Friday 25th April, 2025
Thesis supervisors:	Dr Bart Root & Dr Marc Rovira-Navarro

Cover: NASA-PIA00340, NASA/JPL/USGS

TU Delft

Preface

In front of you lay the product of the past seven months' worth of work, though in truth this thesis is part of a much larger effort, which I have not undertaken alone. To start with, I owe a great deal to the enthusiastic Planetary Exploration group at TU Delft, who showed me the beauty of planetary sciences and convinced me to pursue the field further, leading first to the pursuit of a second degree in Astronomy in Leiden, and finally to this work.

In particular, I owe a great deal of gratitude to my supervisors, Bart and Marc: thank you for affording me the luxury of having a weekly discussion on my favourite moon with two experts in their respective fields, and for being engaged, involved and endlessly positive in our collaboration. Bart: thank you for the endless enthusiasm, planetary interior-knowledge, rigour, and patience you have brought to this project, for enduring all the times when Marc and I derailed our meetings to discuss tides and dynamics, and thank you for the humour and positivity you bring to your work. I am looking forward to hearing more on Mars and Ceres from you in the coming years! And Marc: when I approached you two years ago, I could not have imagined all the places and experiences our collaboration would bring. Thank you for your unwavering support, bottomless optimism and continued encouragement throughout the past two theses; for affording me the freedom to explore my interests in depth where appropriate, and for gently telling me when we've gone far enough where necessary. I'm looking forward to spending the coming four years working on the next thesis with you, expanding our horizon beyond "Tito"!

Of course, my gratitude does not end there: over the past years and throughout this work, there have been many who've helped and supported me. My friends from Dronten, who've been by my side all this way; my fellow students at Aerospace Engineering, my committee mates at the VSV "Leonardo da Vinci" and those by my side in room 6.19; my rowing teammates (though we've given up rowing a while ago now...) of CoolBest. Thank you for being here with me all this time, and hopefully for long to come!

Finally, I would like to extend my thanks to those dearest to me: thank you, *pa en ma*, for supporting me in my choices even where those would not align with yours. Even though you may not have any background in astronomy or planetary sciences, I'm confident I'll manage to explain my work to you at some point! Aïcha, thank you for being my safe haven, and for enduring the late nights I've spent on this project. And finally, thank you to my brother, Quinten, for keeping me grounded, and for letting me see all the perspectives I could not.

To each of you: this is just as much your work as it is mine. Let us keep elevating one another.

Quirijn B. van Woerkom
Delft, April 2025

Summary

Neptune's lone large moon Triton is a unique object in the Solar System: its highly inclined, retrograde orbit, its composition and its status as Neptune's sole large moon betray a history and formation unlike that of the other large Solar System moons. Rather than having formed around Neptune, Triton is thought to have formed as one part of a binary pair of Kuiper belt-objects, whose disruption in an encounter with Neptune led to Triton being captured on a highly-eccentric orbit around the planet. The resulting process of tidally-driven circularisation to its present-day circular orbit will have released an amount of energy sufficient to melt Triton in its entirety several times over. Whether any such catastrophic consequences actually came to pass, however, and whether they may leave their mark into the present, depends strongly on when and where this energy is dissipated, factors for which previous authors have unfortunately found conflicting results. Such previous efforts attempting to model this process have relied on untested assumptions or a variety of simplified dynamical models, both of which were shown to lead to inconsistent predictions in previous work.

In an attempt to reconcile these past results, we therefore self-consistently couple a high-fidelity dynamical model developed in previous work to novel interior-evolution and deformation models of Triton. In doing so, we relax several assumptions applied in previous work, accounting for the non-synchronicity of Triton's rotation to its orbit, the frequency-dependence of Triton's deformation, higher-order terms in the Darwin-Kaula expansion, and the possibility of subsolidus convection in Triton's silicate interior. We then study the evolution of Triton with and without tides, and assess the sensitivity of Triton's evolution to variations in uncertain or unconstrained interior and initial parameters.

We find that not all assumptions applied in previous work are justified or even useful: premature truncation of the Darwin-Kaula expansion leads to a significant underestimation of tidal heating, whereas uncoupled dynamical-interior or fixed-interior models will significantly overestimate dissipation, and so none of these are useful in describing (even in a qualitative sense) the high-eccentricity regime of Triton's evolution. We find that Triton spends the majority of its tidal evolution stuck in higher-order spin-orbit resonances, being in an equilibrium but not synchronous rotational state (as was assumed in previous studies) until its eccentricity falls to ~ 0.2. However, this fact as well as the frequency-dependence of the tidal response play a limited role in Triton's evolution as we also find that Triton's tidal response does not vary by more than an order of magnitude over the range of frequencies excited at any given time, and so we find that the constant phase-lag model of MacDonald (1964), alone out of all simplified dynamical models, gives a qualitatively (though not quantitatively) correct description of its evolution.

In agreement with earlier results found using this constant phase-lag model, we find that Triton dissipates the vast majority of its orbital energy in its icy shell rather than in its silicate mantle: consequently, its shell recedes to thicknesses of 10 km or less over Gyr-timescales or longer, but circularisation leaves little if any mark in the mantle, nor in the shell after tidal dissipation ceases. Additionally, we find that these conclusions are not sensitive to choices in interior or initial parameters, though the timescale of circularisation varies between $\sim 1-4$ Gyr as a strong function of the reference viscosity of the icy shell. Moreover, Triton almost certainly reached the temperatures required to set on the development of an iron core, but not because of capture (as envisioned by early work on the moon): core formation is potentially promoted but never initiated by tidal dissipation.

Contents

List of Figures

List of Tables

Nomenclature

Abbreviations

CAI	Calcium-aluminium rich inclusions, the formation of which is commonly used to date the formation of the Solar System.
CI	Ivuna-type carbonaceous chondrite
CM	Mighei-type carbonaceous chondrite
CPL	Constant phase lag
CTL	Constant time lag
CV	Vigarano-type carbonaceous chondrite
GIA	Glacial isostatic adjustment
KBO	Kuiper belt object
LL	Low iron, low metal ordinary chondrite

Symbols

$\bar{k}_l(\omega)$	Complex Love number of degree l
β	Reduced mass $\frac{M_T M_N}{M_N+M_T}$
ΔT	Temperature difference across the convective mantle region
δ_{ij}	Kronecker delta
$\dot{\theta}$	Sidereal rotation rate
$\dot{E}$	Dissipated energy
$\epsilon_l(\omega)$	Phase lag
η	Viscosity
γ	Temperature contrast across the convective region
Λ_l	Thin-shell spring constant
$\mathcal{M}$	Mean anomaly
μ	Complex rigidity
μ_e	Elastic rigidity
μ_{mantle}	Effective (complex) rigidity of the mantle
Ω	Longitude of the ascending node
ω	Tidal or rotational frequency
$\phi_c(\omega)$	Frequency-dependent partitioning of total dissipated power between the mantle and shell.
ρ	Density
τ_i	Half-life of a radioisotope i
$\tilde{C}$	Moment of inertia
ϖ	Argument of pericentre
a	Semi-major axis of an elliptical orbit

C	Specific heat
$C = \frac{\tilde{C}}{MR^2}$	Moment of inertia factor
C_i	Elemental abundance of species i for CI-chondrite
c_i	Present abundance for a radioisotope i as fraction of all isotopes of the species
C_k	Constant of proportionality for the conductivity of ice
D_{conv}	Thickness of the convective mantle region
D_{shell}	Ice shell thickness
e	Orbital eccentricity
F_b	Basal heat flux
$F_{lmp}(i)$	Inclination functions
g	Gravitational acceleration
$G_{lpq}(e)$	Eccentricity functions
H_i	Specific radiogenic heating rate for a radioisotope i
H_{rg}	Volumetric radiogenic heating rate
i	Obliquity of an object with respect to the mutual orbit; for the primary, equivalent to the usual orbital inclination.
$k_l(\omega)$	Dynamical Love number
l	Spherical harmonic degree
l_a	Activation parameter of the Arrhenius viscosity-law.
L_s	Latent heat of the shell
M	Mass
N	Subscript denoting "of Neptune"
n	Mean motion
P	Pressure
q_{cond}	Flux conducted away from the boundary between the conductive and convective mantle regions
q_{conv}	Heat flux out of the convective mantle region
R	Radius (as property of a body, layer or boundary): if without subscript, referring to the radius of Triton
r	Radius (as radial coordinate)
R_N	Neptune's radius
R_{oc}	Radial position of the ocean melting front
T	Temperature, or subscript denoting "of Triton"
T_{int}	Interior temperature of the well-mixed convective region
T_{top}	Temperature at the top of the convective part of the mantle
T_{eq}	Equilibrium temperature
top	Subscript relating to the top of the well-mixed convective mantle region

1 Introduction

Studying the orbital and interior evolution of an outlier moon like Triton requires a firm understanding of the details going into such evolution models: Triton's history pushes the boundaries on matters such as the eccentricities and interior conditions that previously used models (for other icy moons) can handle, with eccentricities far in excess of those found for other Solar System moons, and incredible amounts of tidal dissipation to accompany those eccentricities. This challenges a large number of assumptions implicitly or explicitly made in those models, which therefore need deeper scrutiny than in most applications. Beyond modelling efforts, reaching Neptune's orbit is expensive, and so in-situ studying of Triton is limited to fly-by efforts such as the 1989 visit of *Voyager 2* (e.g. Smith et al., 1989) or the proposed *Trident* mission (Prockter et al., 2019), unless flagship-mission budgets are dedicated to the effort (e.g. the *Odyssey* concept: Rymer et al., 2021). Then why, despite all this added difficulty, is the study of Triton worthwhile?

1.1. The astrobiological potential of icy moons like Triton

Before moving into a description of and discussion on Triton, its history and the current scientific understanding of the Neptunian moon, it is important that we motivate our study. At face value, one can consider the knowledge of Triton *in se* worthwhile; more broadly, one could see the value in a bettered understanding of captured moons, or more broadly yet, of icy moons. In the context of present scientific literature one can, however, find a reason that is compelling beyond simply the descriptive or phenomenological: astrobiology.

Early astrobiological considerations were limited to the other two terrestrial planets inhabiting our Solar System, Venus and Mars. As the name terrestrial already suggests, being derived from the Latin word *terrestris*, meaning "Earth-like" or "Earthly", Mars and Venus provide the closest analogues to the Earth in the Solar System, being of roughly comparable size, mass, as well as bulk composition and density; possessing solid surfaces, thin atmospheres (compared to their radius), and geological features (e.g. Lissauer & De Pater 2019). Especially Mars, whose thin atmosphere could be penetrated visually by naked-eye observers using optical telescopes, captured the imagination of scientists in the 19th and first half of the 20th century: perhaps wishfully observing what they wanted to see, they had thought to observe irrigation canals and vegetation on Mars. Their dreams of an intelligent civilisation of Mars were cut short by results sent back by *Mariner 4* in 1963, thanks to which (and the many other probes that have visited the planet since then) we now know Mars to be a far more inhospitable world than they had imagined (for a review on the history of these purported signs of life on Mars and their eventual dispelling, see e.g. Zahnle 2001). Later that decade, combined analysis of data obtained by the US *Mariner 5* and the Soviet *Venera 4* probes precluded the presence of habitable conditions on Venus' surface, too (Sagan, 1969). While it is likely that both Venus and Mars possessed substantial reservoirs of (surface) liquid water in their past (the only ecological requirement for life they otherwise lack; e.g. McKay & Davis 2014, Tab. 10.1), with Mars' being retained probably for a geologically relevant amount of time roughly coincident with the origin of life on Earth, these are now gone (McKay & Davis, 2014).

With that, the door seems to have closed for Earth-like life on these planets. If it ever arose during such putative early habitable times, life on Mars or Venus would have almost surely been exterminated in the transition to present-day conditions, though subsurface conditions may speculatively be such that life could have survived there on Mars (McKay & Davis, 2014). Where one door closes, another opens: and so it was when in the 1970s, it was hypothesised that icy satellites may possess subsurface oceans of liquid water (Lewis, 1971). A more in-depth analysis by Cassen et al. (1979) later that decade, in anticipation of the *Voyager* visits, posited that such a subsurface ocean could have been maintained on Europa if the Laplace resonance is primordial; later, on the basis of these *Voyager*-observations, Squyres et al. (1983) argued for the existence of just such a subsurface ocean of liquid water on Europa, which they show in a companion paper could enable Earth-like conditions (Reynolds et al., 1983). Later, this led Reynolds et al. (1987) to formulate the concept of a "tidally-heated habitable zone", where oceans on the surface of a moon are kept liquid by tidal heating, rather than solar flux as they are on Earth. Such excessive tidal heating of a moon by its host to habitable temperatures (or beyond) has received extensive treatment in literature, and it has been shown that significant heating (though not necessarily to habitable temperatures) is not implausibly a general feature of planetary systems (e.g. Williams et al. 1997; Limbach & Turner 2013; Forgan & Kipping 2013; Dobos & Turner 2015; Forgan & Dobos 2016; Rovira-Navarro et al. 2021; Dobos et al. 2022). It seems that rather than Earth-like planets, icy moons bearing subsurface oceans may provide environments analogous to those which currently harbour and may even have originated life on Earth in the form of hydrothermal vents (McKay & Davis, 2014).

Later, magnetometer observations from the *Galileo* mission at Jupiter would provide additional evidence for a salt-bearing subsurface ocean on Europa: what was perhaps more surprising in light of this prior fixation on tides is that these same measurements also showed that the tidally inactive Callisto might well possess a similar subsurface ocean (Khurana et al., 1998; Kivelson et al., 2000; Zimmer et al., 2000). Not much later, Kivelson et al. (2002) provided similar evidence that Ganymede plausibly also contains a liquid water ocean under its icy surface. At least among the icy Galilean moons, the count of possible subsurface oceans was now three for three, even without significant tidal heating on Callisto. *Cassini* data later provided evidence for a subsurface ocean on Titan (Baland et al., 2011; Bills & Nimmo, 2011; Iess et al., 2012), though its density is still disputed (Goossens et al., 2024); Enceladus was shown to emit plumes fed by a reservoir of hot liquid water (Porco et al., 2006; Hansen et al., 2011) in contact with rock (Hsu et al., 2015), direct evidence of an presently-active environment analogous to hydrothermal systems on Earth. The case seemed stronger and stronger for the presence of subsurface liquid-water oceans on most medium-to-large icy moons or indeed any sufficiently large icy object. Indeed, Hussmann et al. (2006) showed that presently-persisting subsurface oceans are a distinct physical possibility if not inevitability for Europa, Triton, Pluto and Eris, and that they are possible on Rhea, Titania, Oberon, Sedna and Orcus given plausible ammonia abundances. Recent evidence shows that the Uranian moon Miranda likely possesses a subsurface ocean at present (Strom et al., 2024), bringing the number of planets observationally constrained to host moons with subsurface oceans up to three: Jupiter, Saturn and Uranus. Though no observational constraints definitely confirming the existence of a subsurface ocean on Triton exist, modelling studies consistently show that it almost certainly possesses an ocean at present by radiogenic heating alone (Nimmo & Spencer, 2015; Hammond & Collins, 2024), though it will otherwise certainly have possessed an ocean in the past (see Sec. 2.4.2).

In our Solar System alone, then, habitable conditions on icy moons already vastly outnumber habitable planets, both in the past (counting Venus and Mars) and at present (with only the Earth remaining), accounting for the ecological requirements for life as formulated by McKay & Davis (2014). Further study of icy moons as potential abodes for life may therefore allow us to potentially include or rule out a class of habitable objects that could vastly outnumber Earth-like planets (by any criterion for Earth-like). But what justifies the study of Triton in particular, if there are numerous icy moons for which more detailed observations are available?

1.2. Triton: unique among the icy moons

Triton, uniquely among all mid-size and large Solar System moons, orbits retrograde i.e. opposite to the direction of spin of its host. This fact alone does not make it particularly interesting, however: what does, is the origin of this retrograde orbit. Comparison to other similarly-sized objects in the Solar System shows that Triton is compositionally (1) inconsistent with formation around a giant planet and (2) far more like the dwarf planets found in our Solar System than any of the moons (see Sec. 2.1.2 for a more detailed treatment). Consequently, Triton is thought to have formed originally in the Kuiper belt, to be captured into orbit around Neptune at some later time. This capture would inject it onto a retrograde orbit, a sense of orbit which cannot be attained by natural satellites that form in a circumplanetary disc around their host (unless they are consequently disturbed by an external object). We will defer a more detailed discussion of the observational qualities that lead us to posit (the specifics of) this circumsolar origin of Triton to Ch. 2.1; a complete account of the current consensus as to Triton's evolutionary history (insofar as one exists) is given in Ch. 2.4. We will, however, briefly discuss why this extraneptunian origin makes Triton a unique target of study among the icy moons.

While a large number of other icy moons and even some dwarf planets are known to possess or have possessed an ocean in the past, the presence of such an ocean alone does not necessarily constitute a perfect analogue to the early Earth. As we have discussed in Sec. 1.1, the major reasons for looking to icy moons rather than Mars and Venus are the fact that (some of) the icy moons still possess the conditions in which life could exist at present, while Venus and Mars likely no longer do. The reasons for looking to these terrestrial planets in the first place is the fact that they did (plausibly) at one time possess conditions similar to those under which life arose on the early Earth (see Secs. 6.2 and 6.3.2 in McKay & Davis 2014): icy moons do not, generally speaking, satisfy this criterion. Early conditions on icy moons only mirror those in the deep oceans on the Hadean and Archean Earth, when microbial life first originated (>3.4 Gyr ago at the very least, and possibly >3.8 Gyr ago; McKay & Davis 2014). Shallow-ocean and surface conditions would be markedly different, under the influence of a secondary atmosphere and bombarded by ultraviolet radiation from a young Sun. Instead, oceans on icy moons are shielded by an ice shell, and their oceans are not in contact with any atmosphere in as direct a fashion as the oceans on the early Earth.

For Triton, however, such conditions insulating the deep oceans from the world above may not have lasted: upon capture, its ice shell will have started to recede as tidal heating intensified. Sufficient excess orbital energy (compared to its present-day orbit) would have been available to melt the entire ice shell several times over (McKinnon & Kirk, 2014): hence, if this process proceeded sufficiently rapidly, Triton's ice shell may well have molten entirely. Equilibrium calculations in previous work show that Triton's ice shell will, at the very least, have receded to be on the order of $\sim 10 - 1000$ m thick (Van Woerkom, 2024). Taking into account the figures of (Lunine & Nolan, 1992), at such dissipation rates, Triton will have raised an optically thick atmosphere that might serve to insulate the moon, possibly raising the surface temperature sufficiently that the ocean may come in direct contact with the atmosphere. What can be concluded is that on Triton, uniquely, the prospect exists not just of it presently possessing the conditions under which life could persist (as is the case for a plethora of icy moons): it also at one point may have possessed conditions similar to those under which life arose on the early Earth. Determining whether such conditions were actually ever present requires the evaluation of more detailed thermal-interior models taking into account the intricacies of high-eccentricity orbital evolution.

1.3. Applications to exoplanetary science

Beyond the astrobiological case for Triton, there are other reasons that make the moon a compelling target of study. A particular point of embarrassment in the exoplanet community has been the failure of astronomers to confidently identify moons orbiting the thousands of planets orbiting stars other than our Sun that have been discovered in the past three decades. Though several candidates have been put forward (e.g. Cabrera et al. 2014; Teachey et al. 2018; Teachey & Kipping 2018; Teachey et al. 2020; Fox & Wiegert 2021; Kipping et al. 2022), these have all been disputed (e.g. Kipping et al. 2015; Kreidberg et al. 2019; Heller et al. 2019; Kipping 2020; Tokadjian & Piro 2022; Moraes et al. 2023; Heller & Hippke 2024), and no conclusive, direct detection of any such moon has been made as of yet.

At first glance, this puts us in an uncomfortable position: while our Solar System harbours a large number of moons, none have been observed elsewhere. At face value, this would imply an apparent contradiction: this contradiction is quickly accounted for when considering what it takes (beyond those capabilities already present now that we can observe exoplanets) to observe exomoons. Indeed, evidence for exomoons has already been found at secondary and population levels (Kenworthy & Mamajek, 2015; Hippke, 2015; Teachey et al., 2018; Oza et al., 2019; Saillenfest et al., 2023): it is only a direct detection that is as of yet missing. That is to say: while we know that exomoons exist, they are simply evading our detection by being too small, too faint, or by not being massive enough to affect (the light of) their host star in the same way that planets do. Consequently, we do not, at present, have access to the masses, radii, or spectra of exomoons like we do for exoplanets.

Nonetheless, moon formation science has been informed by the plethora of moons in our Solar System. For giant planets (which are easiest to observe in extrasolar systems and therefore most plentiful in observations), moons are thought to form by co-accretion in a circumplanetary disc around the forming planet (e.g. Canup & Ward 2002; Barr 2016): in the study of this scenario, a key result has been the fact that moons cannot grow more massive than about $\sim 10^{-4}$ times the mass of their host (Canup & Ward, 2006), with the total mass in all moons of a planet not exceeding $\sim 10^{-3}$ host masses, a fact which is consistent with all Solar System moons thought to have formed in this way, as well as observations of circumplanetary discs (Benisty et al., 2021). This mass-scaling result has been studied extensively and reproduced for (analogues to) the Galilean satellites (e.g. Miguel & Ida 2016; Moraes et al. 2018; Cilibrasi et al. 2018), though it has also been shown to hold for the ice giants and their (primordial) moons (e.g. Szulágyi et al. 2018; Rufu & Canup 2022). This thus provides a natural explanation for the absence of direct exomoon detections: they are simply, in general, not large or massive enough for modern instrumentation to observe them.

However, this fact only holds for moons that formed by co-accretion: a similar result predicts that planets with moons formed by giant impacts are similarly unlikely to be large compared to their hosts for super-Earths $> 1.6\ R_\oplus$(Nakajima et al., 2022). Out of all moon formation scenarios (co-accretion, giant impacts and capture; Barr 2016), only capture remains as a viable pathway by which moons may arise that are sufficiently large to observe at present. Consequently, those exomoons which are massive and/or large enough to be observed by modern instrumentation are likely to be captured outliers (see e.g. Sec. 2.4 in Barr 2016): even as instrumentation advances to the point where Solar System-like moons may be detected (as is likely to happen when the ELT sees first light; e.g. van Woerkom & Kleisioti 2024), the study of exomoons is likely to be dominated by excessively large, massive or hot moons, just as the study of exoplanets was initially dominated by hot Jupiters. Triton, the only large captured moon in our Solar System, is therefore almost certain to provide the closest analogue to the first exomoons we detect. The study of Triton is therefore likely to generate insights that are useful for the study of exomoons once their detection is commonplace.

1.4. Conclusions

It is thus clear why the study of Triton is useful if not important: it presents clear, unique prospects in terms of habitability and exoplanetary science not found anywhere else in the Solar System. This motivates us to analyse the coupled interior-orbital evolution of Triton, which is a large part of what makes it such a unique object.

The structure of this work is as follows: before moving on to our model and its results, we will give an overview of the scientific background surrounding the study of Triton and objects like it in Ch. 2: this motivates us to formulate a number of open questions on Triton and captured moons like it to answer. We then describe the methodology of our study in Ch. 3. Before evaluating the coupled evolution of Triton's orbit and interior, we develop a "control scenario" and assess the unperturbed, interior evolution of a tideless Triton in Ch. 4; we then study the coupled orbital-interior evolution for a Triton that *is* perturbed by the dynamical process of circularisation from a highly-eccentric post-capture orbit in Ch. 5, and assess the robustness of those results to variation in our assumptions in Ch. 6. We discuss the consequences of these results, as well as several shortcomings we wish to remedy in ongoing work (as well as their impact on our results) in Ch. 7. Finally, we are poised to answer the questions we set out to answer: we conclude by giving these answers in Ch. 8.

2 Scientific background

Having established why we wish to study Triton in Ch. 1, we move on to a description of the scientific background in which our research is situated; readers already familiar with this scientific background may prefer to continue on to the methodology presented in Ch. 3. The "boundary conditions" constraining our work in the form of observations available for Triton are given in Sec. 2.1. Afterwards, we will move on to a brief description of the modelling efforts necessary to study the history of Triton in Sec. 2.2 as well as an overview of previous modelling studies on the moon in Sec. 2.3, to be followed by a summary of the present-day understanding the scientific community has of Triton's past in Sec. 2.4. Finally, gaps can be identified in this understanding by putting all of these together: we posit a set of open questions in Sec. 2.5.

2.1. Observations of Triton

Unfortunately, the ice giants' relative distance from the inner Solar System, as well as the absence of the abundance of large moons such as that found around the gas giants mean that the ice giants have not been an attractive object of study for dedicated scientific missions. Consequently, few high-quality observations are available for Triton: we give a brief overview of those that do exist in Sec. 2.1.1; what observational constraints can and have been derived from these observations will be summarised in Sec. 2.1.2.

2.1.1. An observational history of Triton

The observational history of Triton, of course, begins with the discovery of its planetary host, Neptune, in 1846: within a month, William Lassell identified a moon in orbit around the new planet (McKinnon & Kirk, 2014). Unlike the multiple satellites known to orbit the other giant planets at that time, no additional satellites would be identified around Neptune for more than a century (Buratti & Thomas, 2014). Though this may have already been a first indication that the Neptunian satellite system was unique, Triton was additionally found to orbit in a retrograde fashion in 1854 by John Russell Hind (Hind, 1854): this made it unique among the planetary satellites known at the time (Buratti & Thomas, 2014), and to date it remains the only large satellite to do so, though a true appreciation of the uniqueness and implications of this fact would of course have to wait until a theory of satellite formation was formulated.

In the century and a half that followed, all additional information on Triton that was known was a result of ground-based observations. With the benefit of hindsight, we know that this information was unfortunately rarely reliable: (mostly brightness-based) radius estimates did not yield usefully constraining values[1] (e.g. Cruikshank et al. 1979), and the corresponding mass estimates reported in common reference texts of the period were therefore unreliable (e.g. Allen 1973); astrometry-based estimates pre-dating digital photography were also not particularly accurate and in mutual tension (Nicholson et al., 1931; Alden, 1940). The values used for Triton's mass until the arrival of *Voyager 2* were consequently off by an order of magnitude (e.g. McCord 1966; Message 1972; Lewis 1973; Allen 1973), and its density was not meaningfully constrained until that time either.

With the arrival of *Voyager 2* at Neptune, this finally changed: Tyler et al. (1989) and Smith et al. (1989) reported the first measurements of Triton's mass and radius, respectively, reconcilable with the accepted modern values, and the derived density showed a world far more similar to Pluto than the other Solar System moons, suggestive of a different past than is usual for large satellites. The first resolved images of Triton also showed, surprisingly, a world that was geologically active very recently (e.g. Smith et al. 1989; Soderblom et al. 1990; Strom et al. 1990; also, see Fig. 2.1), and littered by a morphological unit termed "cantaloupe terrain" by Smith et al. (1989), that was unlike anything seen elsewhere (the top-left feature seen in Fig. 2.1).

While this would be the only time close-up, high-resolution imagery of Triton was taken, this would not be the end of observations of Triton: the unique presence of an atmosphere and apparent seasonal variations so far from the inner Solar System has spurred observational and modelling studies of Triton, and in particular its surface climate, up until the present (e.g. Elliot et al. 1998; Grundy et al. 2010; Holler et al. 2016; Merlin et al. 2018; Bertrand et al. 2022). High-resolution imagery of Triton is not a possibility from the ground, and so detailed geological surveys of the moon as well as studies of localised terrain rely on the *Voyager 2* data still; as observational constraints for the present-day interior and tidal state of Triton mostly rely on such geological data, we will for the most part rely on *Voyager 2* observations and the results derived from these data in this work.

[1] An exception is the diameter estimate given by Bonneau & Foy (1986), though with the *Voyager 2*-data coming in three years later this came too late to make a difference.

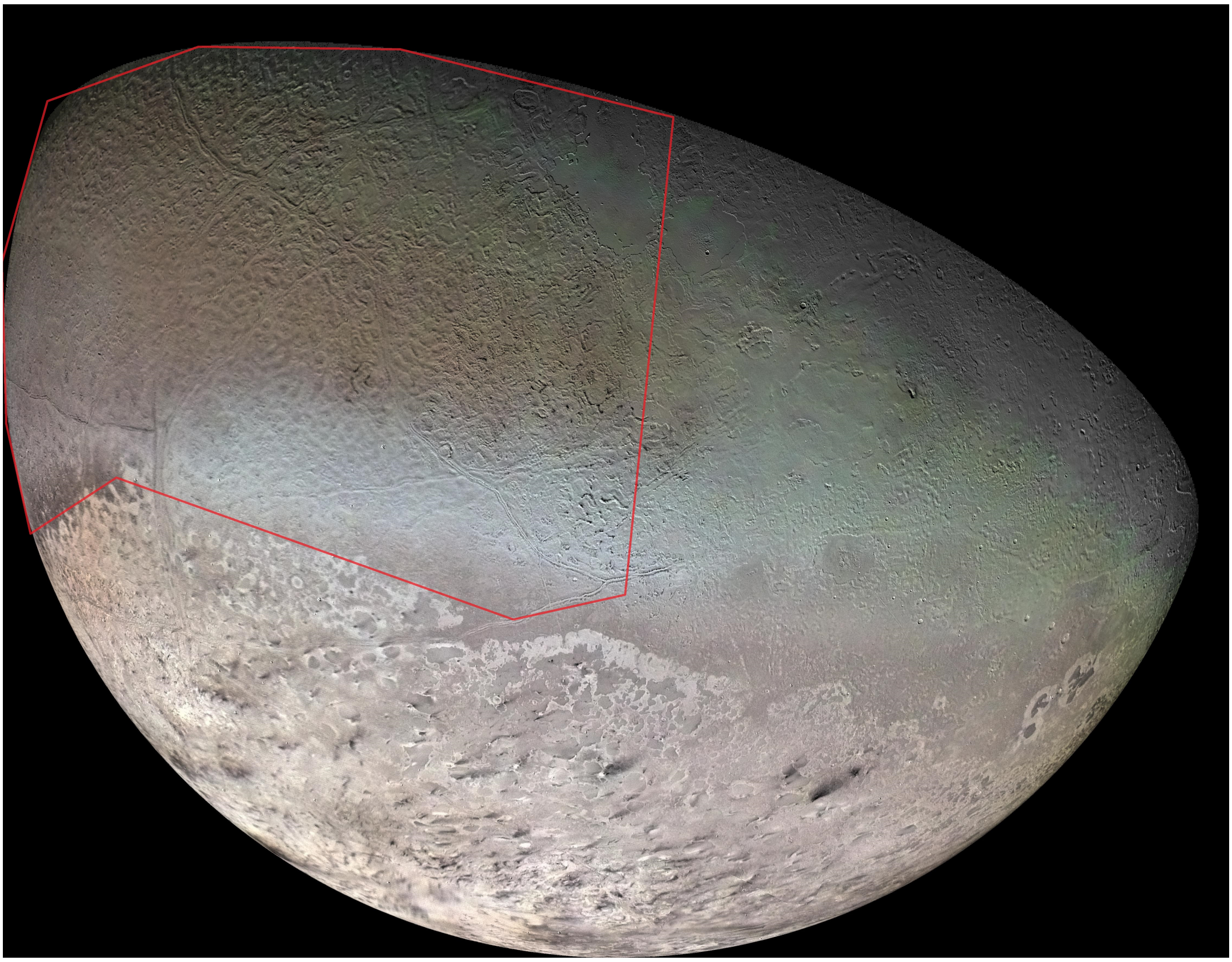

Figure 2.1: A global colour photomosaic of Triton's southern hemisphere synthesised from high-resolution images of the moon taken by *Voyager 2* through its orange, violet and ultraviolet filters, displayed as red, green and blue in this image. The visible terrain covers the largest part of the Tritonian surface for which high-resolution imaging is available. Triton is shown from the Neptune-facing side, such that the eastern hemisphere is its leading one. Triton's cantaloupe terrain (the visible part of which is demarcated by a red line) is clearly visible over the equatorial part of the western hemisphere, extending out until the polar cap. Image adapted from NASA/JPL/USGS, PIA00317.

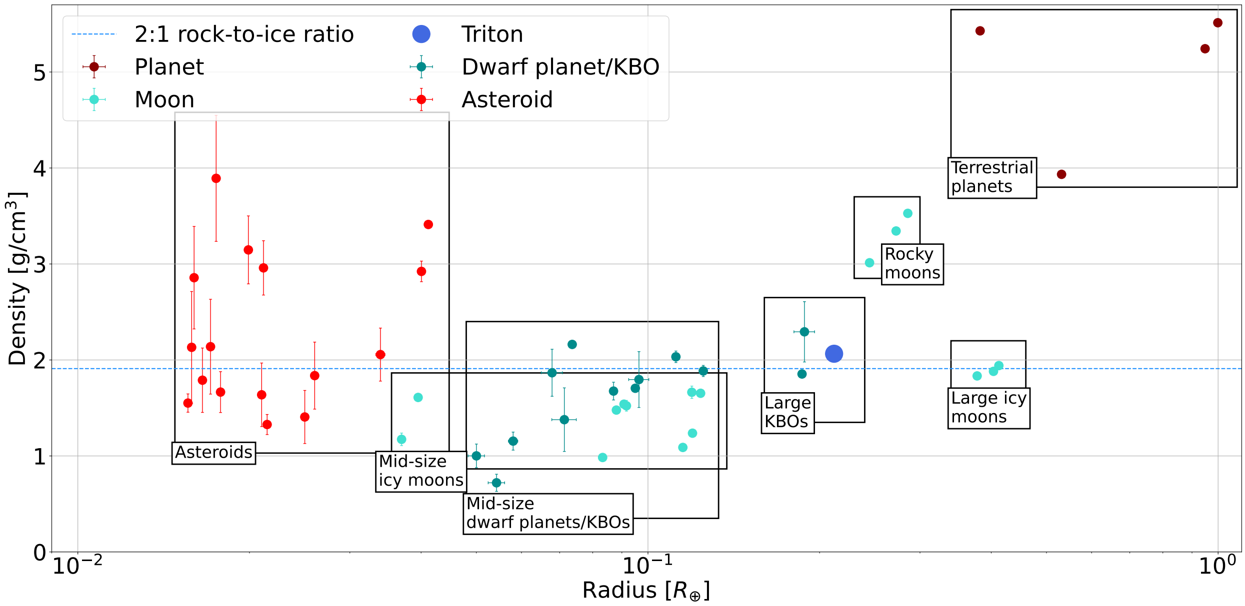

Figure 2.2: The (volume- or area-equivalent) radius and density of all Solar System objects > 100 km in radius whose mass and dimensions have been measured such that their density is determined to within 30%[2]. The blue dashed line indicates the 2:1 rock-to-ice ratio boundary for a rock density of 3.5 g/cm^3 (as would be appropriate for the high-pressure environment deep in the larger moons). Populations of objects with analogous formation histories have been marked accordingly, from which it is clear that Triton is more analogous to Pluto and Eris than any of the other moons.

2.1.2. Observational constraints for Triton

Consequently, let us describe the major observational constraints that *do* exist for Triton. Here, we will discuss high-level quantities such as its bulk and orbital quantities, followed by a treatment of the geological inferences concerning Triton's interior-tidal state that have been made from the available data.

Bulk and orbital properties

Known bulk and orbital properties for Triton are summarised in Tab. 2.1: detailed estimates for the full present-day orbital elements and precession rates for the Neptunian satellites were determined by Jacobson (2009), but will not be necessary for this work. In general, with the exception of the variable surface temperature, these parameters rely on *Voyager 2*-data: the temporal variability of Triton's surface frost temperature was established through a set of stellar occultation measurements in combination with the *Voyager 2*-data (Elliot et al., 1998), though over the timespan 2010-2013 the surface temperature was again commensurate with the *Voyager 2*-value (Merlin et al., 2018). Unfortunately, the *Voyager* data are not sufficiently accurate to constrain the moment of inertia (e.g. Thomas 2000) or gravity field of Triton, limiting the number of useful observational constraints on the interior.

An interesting issue arises when comparing Triton's density to other large objects beyond the asteroid belt: as evidenced by Fig. 2.2 its density is, more than any of the moons, like that of Kuiper belt objects (KBOs) (Hussmann et al., 2006). Triton's density corresponds to a rock-to-ice ratio significantly greater than 2:1, which is anomalously dense even for the large icy moons Ganymede, Titan and Callisto; the only large Solar System giant planet moons of a greater density are the rocky moons Io and Europa. While the exact mechanism by which such a rocky composition arose for these two moons is still not conclusively known (and an answer will likely have to wait until the arrival of deuterium measurements by JUICE and Europa Clipper; e.g. Bierson & Nimmo 2020; Mousis et al. 2023), a density gradient like that observed for the Galilean moons is certainly not expected for moons forming in-situ around the ice giants. Simulations instead predict that Neptune should have formed with a Uranus-like system of smaller icy moons (Szulágyi et al., 2018); then why is that not what we observe today?

Indeed, there is more that troubles the idea of Triton forming in-situ: moon formation in a circumplanetary disc (e.g. Canup & Ward 2002, 2006; Barr 2016) precludes moons from forming on a retrograde and highly inclined

[2]Masses, radii and accompanying uncertainties taken from NASA JPL Solar System Dynamics Planetary Physical Parameters (`https://ssd.jpl.nasa.gov/planets/phys_par.html`) and Planetary Satellite Physical Parameters (`https://ssd.jpl.nasa.gov/sats/phys_par/`) on 4 November 2024, with the exception of Vesta (Russell et al., 2012) and the other asteroids (Vernazza et al., 2021), Haumea (Ragozzine & Brown, 2009; Ortiz et al., 2017), Gonggong (Kiss et al., 2019), Quaoar (Morgado et al., 2023), Orcus (Brown & Butler, 2023), Salacia (Brown & Butler, 2017; Grundy et al., 2019b), Varda (Souami et al., 2020), 2002 UX$_{25}$ (Brown, 2013; Fornasier et al., 2013), 2007 UK$_{126}$ (Benedetti-Rossi et al., 2016; Grundy et al., 2019a) and Vanth (Brown & Butler, 2023).

Table 2.1: Bulk and orbital parameters for Triton given by McKinnon & Kirk (2014), with the exception of the radius, which is given by Thomas (2000), and the mass, which is derived from the gravitational parameter given by Jacobson (2009) with the 2022 CODATA value for *G* (Tiesinga et al., 2024). The thicknesses of the various interior layers are for a reference model given by McKinnon & Kirk (2014); insufficient observational constraints are available to establish (bounds on) the true present-day interior layering without additional modelling, which is part of the aims of this work.

Quantity	Value	Unit(s)	Remarks
Radius	1353.4 ± 0.9	km	From Thomas (2000)
Mass	$(2.1394 \pm 0.0052) \cdot 10^{22}$	kg	From Jacobson (2009)
Bulk density	2.0603 ± 0.0055	g/cm^3	From mass and radius
Surface temperature	~ 40	K	Apparently season-dependent
Hydrosphere thickness	~ 400	km	Reference model
Silicate mantle thickness	~ 350	km	Reference model
Metallic core thickness	~ 600	km	Reference model
Semi-major axis	354.8	Mm	14.33 Neptune radii
Orbital period	5.877	d	-
Eccentricity	<0.0016	-	Consistent with zero eccentricity
Inclination	156.8	°	-

orbit like Triton's. This fact is precisely what drove Lyttleton (1936) to hypothesise a common circum-Neptunian origin for Pluto and Triton when Pluto was discovered on an orbit crossing that of Neptune; Lyttleton (1936) proposed that Pluto and Triton formed as a pair of direct-orbiting satellites of Neptune, and that some dynamical event ejected Pluto, and left Triton on a highly eccentric, retrograde and inclined orbit. McCord (1966) showed that Triton could have circularised from such an orbit to its present-day one within the lifetime of the Solar System, but also proved that it could equally well have done so from a parabolic orbit, implying capture from heliocentric orbit instead. Slowly, however, Lyttleton's hypothesis proved inconsistent with increasingly accurate observations of Pluto and the discovery of Charon orbiting it, and so capture of Triton rather than ejection of Pluto was to explain Triton's orbit (e.g. McCord 1966; Pollack et al. 1979; Farinella et al. 1980). Finally, McKinnon (1984) showed that reversal of Triton's orbit was not a dynamical possibility allowed by the masses of Triton and Pluto, and so capture remained as the sole viable option; indeed, the density prediction made by McKinnon & Mueller (1989) was borne out by the observations of *Voyager 2* (Smith et al., 1989), and the common origin of Triton and Pluto was further strengthened by their similar densities. This common origin, it turned out, was not a circum-Neptunian formation, as Lyttleton (1936) envisioned: instead, it lay in the Kuiper belt.

Perhaps more intriguing than the similarities between Triton and Pluto are their differences. Based on its bulk density, Mandt et al. (2023) argue that the relative abundances of several species on Triton and Pluto does indeed point to a common origin for both, consistent with accretion from building blocks analogous to comets and chondrites in the young Kuiper belt. An interesting corollary of the results presented by Mandt et al. (2023), however, is that the deficiency of methane observed on Triton when compared to Pluto as well as the presence of carbon dioxide on Triton (being absent on Pluto) can both be explained by a longer-lasting presence of aqeuous processes converting methane to carbon dioxide and ammonia to molecular nitrogen: Mandt et al. (2023) propose this to be the result of hydrothermal processes caused by sustained tidal heating in Triton, as discussed by Shock & McKinnon (1993) and Stevenson & Gandhi (1990) shortly after publication of the *Voyager 2*-results. An interesting note not touched upon by Mandt et al. (2023) is the fact that, as discussed by Lunine & Nolan (1992), such modification of Triton's volatile inventory is also possible by the existence of a dense atmosphere on the body, possibly raised by severe tidal heating following capture. Whatever the case, comparative planetology between Triton and Pluto suggests either intense or lasting consequences (or both) of tidal interaction between Triton and Neptune might be the root cause of chemical differences observed between Triton and Pluto.

Geological inferences

Chemical abundances and orbital constraints are not the only indicators that Triton must have been geologically active over an extended period, however: *Voyager 2* mapped roughly 40% of Triton's surface at sufficiently high resolution that geological interpretation thereof was possible (Smith et al., 1989)[3]. Crater counts suggests that the surface is uniquely young, with the only known comparable surfaces at the time being that of Io and Europa (Smith et al., 1989), though more recent work has shown Enceladus (Spencer & Nimmo, 2013) and possibly Mimas (Ferguson et al., 2024) to be of similar youth as well. Various estimates for Triton's surface age have been made, with bounds varying from $0.1 - 0.3$ Gyr (Stern & McKinnon, 2000) to $6 - 50$ Myr (Schenk & Zahnle, 2007) or $10 - 100$ Myr (McKinnon et al., 2024). Interestingly, Schenk & Zahnle (2007) and McKinnon et al. (2024) find

[3]This therefore warrants the disclaimer that over half of Triton's surface remains, unfortunately, unknown to us at any significant resolution. This covers most of the northern hemisphere of the moon.

that the impactor distribution reflected by Triton's craters appears to correspond to a planetocentric population of origin: such a planetocentric population of origin would push all three of these surface age estimates to the lower end, indicating unprecedented, intense geological activity even at present. It is not clear what the source of such a planetocentric impactor population could be, however, and McKinnon et al. (2024) propose two plausible explanations: debris from irregular satellite breakup (though the Neptunian irregular population is not well-characterised enough to draw this conclusion; however, for a dynamical consideration, see Marchi et al. 2004), or distal secondaries belonging to some large unaccounted-for impact somewhere on Triton[4].

In addition to these low crater-counting ages (noting that even the higher-end estimates of $0.1 - 0.3$ Gyr corresponding to heliocentric impactors qualify as geologically recent), Smith et al. (1989) identified plume-like features on *Voyager 2*-imagery of Triton. While Soderblom et al. (1990) proposed that these were the result of a greenhouse-like effect in Triton's surface nitrogen-ice layer, and Ingersoll & Tryka (1990) proposed that these were atmospheric phenomena, Brown et al. (1990) added geothermal heat as a possible auxiliary mechanism. Unfortunately, it appears that different scenarios for Triton's plumes cannot be distinguished without another mission to the Neptunian system (Hofgartner et al., 2022).

That being said, the claim of present-day geological activity does not only rest on crater counting ages of craters whose origin is uncertain or plumes produced by an ambiguous mechanism: there are clear indications of endogenic activity in the *Voyager 2*-data in the form of geologically recent cryovolcanism or tectonic activity (e.g. Croft 1990; Schenk 1992; Croft 1993; Ruiz 2003; Martin-Herrero et al. 2018; Sulcanese et al. 2023; for an extensive discussion, see Sec. 2.2 of Van Woerkom 2024). Perhaps most intriguing of these indications is the dimpled "cantaloupe terrain" littering large parts of equatorial Triton (the top-left feature on Fig. 2.1): this terrain is not observed on any of the other icy bodies in the Solar System. Schenk & Jackson (1993) propose that this terrain is analogous to the diapirs found in the Great Kavir on Earth, in which case the terrain would be the result of some density inversion of the ice shell possibly deposited by cryovolcanism. While this is not the only hypothesis that has been levied to explain this terrain, it is usually considered the leading explanation (McKinnon & Kirk, 2014); notably, however, all other explanations are also endogenic in nature (Boyce, 1993; Hammond et al., 2018), and so this terrain can be considered a clear and unambiguous indicator that geological activity is still ongoing on Triton. Unfortunately, even if we were to understand the root cause of the cantaloupe terrain, its localised nature would mean that a detailed volatile transport model as well as more detailed chemical-compositional data would be required to derive any interior constraints from the presence of the cantaloupe terrain.

2.1.3. Conclusions

While few observations are thus available for Triton, we can conclude two things from those that do exist: (1) Triton is a unique object in the Solar System, and (2) Triton is presently (and likely has always been) a geologically active world. Though little detailed data on the body exists compared to other well-studied worlds such as the Jovian and Saturnian satellites, for example, *Voyager 2* has provided sufficient observational data that a thermal-orbital model can at least be reasonably constrained in terms of the present-day orbital and thermal state, as well as in terms of initial conditions (i.e. as a captured KBO). What remains, then, is of course to formulate how such models can be constructed: this is the subject of Sec. 2.2.

2.2. Orbital-interior modelling of a lone moon

With the appropriate observational background in place, we can move on to a discussion of modelling techniques to be used for Triton. As the Neptune-Triton system is gravitationally dominated by those two bodies, with Nereid (the next most massive moon of Neptune following Triton) being three orders of magnitude less massive (Barr, 2016), it will suffice to treat only the gravitational (and thus tidal) effects imposed on Triton by Neptune, as well as the mutual dynamical evolution of the two. This sets it apart from multi-moon systems like the Jovian one, where mean-motion resonances also play a significant role in the dynamical (and thus tidal and consequently interior) evolution.

As shown in Fig. 2.3, we can generally identify three modules to thermal-orbital models in the single-moon case: one describing the thermal state and evolution of its interior (e.g. temperature, pressure, density and chemical-compositional profiles), one describing the dynamics and orbital evolution of the two bodies, and one describing how the two model components interact (e.g. producing the tidal deformation from the interior profiles, or determining the orbital energy dissipated in each layer). Correspondingly, we will discuss these three components, and how they have been presented in literature: Sec. 2.2.1 describes the process of thermal-interior modelling of planetary bodies. Sec. 2.2.2 discusses the process of dynamical modelling of tidally perturbed natural satellites, and Sec. 2.2.3 discusses how these are coupled to produce a simultaneously and consistently evolving model of the dynamics and interior.

[4] McKinnon et al. (2024) propose it may hide in the aforementioned unmapped northern hemisphere of Triton.

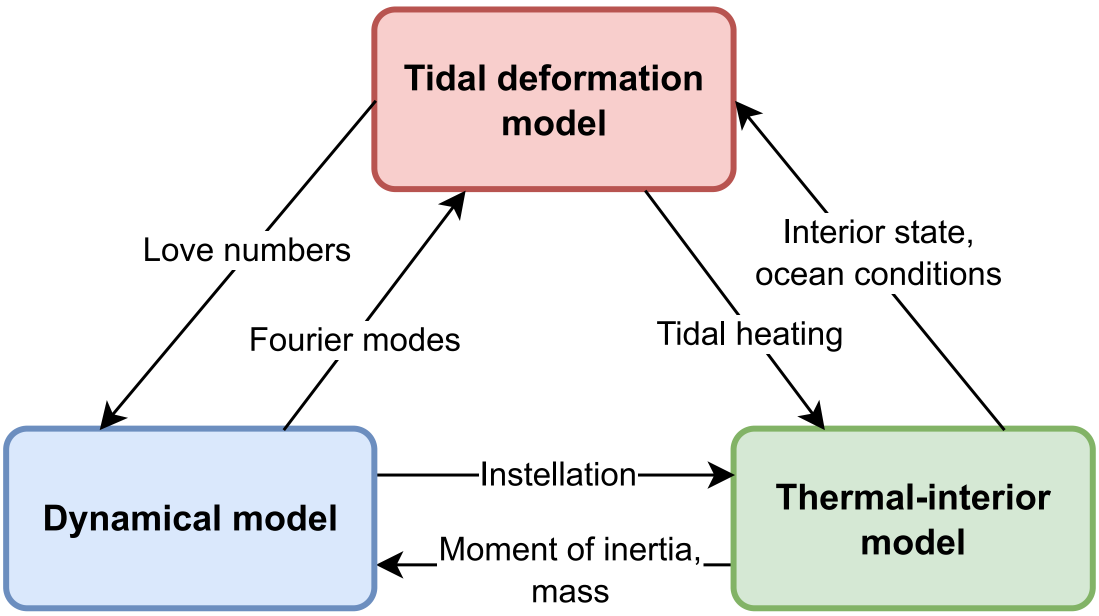

Figure 2.3: General model components that can be identified for the thermal-orbital evolution model of a tidally perturbed natural satellite (like Triton), with examples of interactions between the model components on the edges.

2.2.1. Thermal-interior modelling: describing the interior state and evolution of a planetary body

The geological activity described in Sec. 2.1.2 must be driven by some interior engine producing sufficient heat (flows): more interesting yet, perhaps, is the fact that Triton's twin world, Pluto, does not display the same kind of cantaloupe terrain (though some geological activity is certainly still present; Moore & McKinnon 2021). Explaining these differences, then, warrants modelling of the interior and thermal state of Triton. We will briefly discuss the manner in which such a state is usually described, as well as what energy sources contribute to thermal evolution and how the evolution of this thermal state due to these heat sources is expressed.

Interior profiles

To describe the evolution of Triton through time, it is important to specify what it is that we wish to see the evolution of exactly. This does not just concern the quantities that we should like to know to answer scientific questions explicitly (e.g. whether, at some interior depth, the hydrosphere of Triton is liquid or solid, signalling the presence of an ocean), but also those necessary to describe the full state of the body as well as its evolution (for a useful introductory text, though aimed at the Earth, see Van Zelst et al. 2022).

Fundamentally, describing the interior state of a body starts with the equation of state, which describes the density of a given material (and oftentimes other properties, such as phase) as a function of its pressure and temperature. Depending on the material one is working with, different equations of state are required: fortunately, such equations of state are nowadays compiled into automated software packages such as *Perple_X* (Connolly, 1990) and *BurnMan* (Cottaar et al., 2014) for commonly encountered (rocky) minerals, and *SeaFreeze* (Journaux et al., 2020) for (water-)icy materials. If the location-wise composition, temperature, pressure and density for a planetary body are self-consistently determined at some time and throughout the body, this then fully fixes the problem. In the case of a smaller body like Triton, variations in temperature and pressure throughout the shell and mantle are relatively mild compared to those found in larger bodies like the Earth, and constraints are scarce. Hence, it is commonplace to assume a homogeneous density for each of the layers of the body (e.g. Smith et al., 1989; Ross & Schubert, 1990; McKinnon & Kirk, 2014; Hammond & Collins, 2024): we will take a similar approach, and account for any resulting error by varying the mantle density (which is most uncertain), as discussed in further detail in Sec. 3.5.1.

While the problem of interior evolution is fundamentally a complicated three-dimensional fluid dynamics problem involving a plethora of variables to be tracked (see e.g. Van Zelst et al. 2022, Sec. 2.3 for a discussion), the scarcity of data available for Triton (in particular regarding its interior state) does not warrant such a complicated model. That is not to say that three-dimensional or flow effects are of no influence: lateral variations are well-known to be of importance on icy moons (e.g. Tobie et al. 2005; Roberts & Nimmo 2008a; Beuthe 2018;

Rovira-Navarro et al. 2020, 2023), and convection-driven surface yielding is presumed by some authors to be the ultimate process by which Triton's present-day geologically-active surface is generated (Nimmo & Spencer, 2015). However, tracking three-dimensional geophysical variations is highly computationally expensive, and with the goal being a 4.5 Gyr-long history of Triton this is neither feasible nor useful (given the lack of constraints available even for present-day Triton); we therefore decide that a one-dimensional (radial) approach will suffice, and we will indeed see in Sec. 2.3.1 that existing work on Triton has largely been restricted to one-dimensional modelling, which amounts to the assumption of spherical symmetry.

Under this assumption of spherical symmetry, the problem of characterising the state of a planetary body simplifies down to finding a self-consistent set of functions $P(r)$, $T(r)$, $\rho(r)$ for the pressure, temperature and density as a function of radius r; for a body in hydrostatic equilibrium, which is applicable for Triton (McKinnon & Kirk, 2014), this amounts to integration downward of the equation of hydrostatic equilibrium (Lissauer & De Pater, 2019) once the temperature profile is known (the temperature profile and its computation will be discussed in Sec. 2.2.1):

$$\frac{\mathrm{d}P}{\mathrm{d}r} = -g(r)\rho(r) \tag{2.1}$$

where $g(r)$ is the local value of the gravitational acceleration at radius r. For smaller (icy) bodies like Triton, it is not unusual to assume little-to-no dependence of material phase and density on pressure and temperature, with the exception of the phase transition between liquid water and water-ice, which results in the assumption of constant density throughout a layer (e.g. Hussmann & Spohn 2004; Hussmann et al. 2006; Bagheri et al. 2022a). This assumption cuts on two sides: it yields faster computation of interior pressure profiles through an analytical solution of Eq. 2.1, but also allows for the use of analytical models with which the tidal quality function can be evaluated (see Sec. 2.2.3). The flip-side is that more complicated behaviour, such as the representation of high-pressure ice phases such as those present underneath Ganymede's ocean (Bland et al., 2009) or of phase transitions such as those that might occur in Triton's deep interior (Cioria & Mitri, 2022) must be accounted for manually, if they are accounted for at all. Well-known codes that describe the pressure- and temperature-dependent behaviour of ices and minerals are the aforementioned SeaFreeze (Journaux et al., 2020) for ices, and *Perple_X* (Connolly, 1990) and *BurnMan* (Cottaar et al., 2014) for rocky materials.

For Triton, the only direct constraints available for the interior pressure, density and composition profiles are those given by its mass and radius (see Tab. 2.1). Normally, an additional constraint can be given by the moment of inertia of a body, if it has been determined or constrained (see e.g. Fortes 2012 for the case of Titan): in this case, however, we must resort to evaluation of a spectrum of possible interior profiles to see which are compatible with observations and plausible histories. Consequently, details like the presence of an iron core or the existence of an ocean can therefore not uniquely be constrained from observational data. Assuming an undifferentiated silicate mantle with a density of $\sim$ 3500 kg/m^3 and a hydrosphere with a density of $\sim$ 1000 kg/m^3 throughout, Nimmo & Spencer (2015) do derive a mantle radius of $\sim$ 1030 km and a maximum ice shell thickness of $\sim$ 327 km using a two-layer constant-density model. This is in good agreement with the conservative results derived by Hussmann et al. (2006) and therefore likely constitutes a good order-of-magnitude estimate, but it already disagrees with the model provided by McKinnon & Kirk (2014), for example, who propose a thicker hydrosphere, which would be appropriate if high-pressure ice phases form (as shown in Fig. 2.4), given their increased density compared to ice-I and liquid water. The presence of such high-pressure ice phases atop the mantle is highly dependent on a multitude of factors: while the formation of high-pressure ice phases other than ice-II or ice-III is not possible at the pressures obtained at the bottom of plausible thicknesses of Triton's hydrosphere ($\lesssim$350 MPa), regardless of the presence of liquidus-suppressing contaminants, ice-II and ice-III may form if the ice shell or ocean (if one forms) is held at a sufficiently low temperature (Choukroun & Grasset, 2010). Such a configuration would require ocean conditions far from thermodynamic equilibrium, which we therefore do not deem plausible in the absence of any mechanism driving them, and so we will not account for the possibility of ice-II/III at the bottom of Triton's ocean in any scenario.

A more plausible manner of constraining the present (and past) interior structure than by direct observation is the use of thermal evolution models (e.g. Gaeman et al. 2012; Nimmo & Spencer 2015; Hammond & Collins 2024), which can constrain the range of plausible interior structures that could have resulted from plausible initial conditions. Doing so, however, requires a thermal evolution model that can describe the evolution of these interior profiles over time: construction of such a model, however, also requires that the relevant energy sources be considered.

Energy sources and sinks

A variety of heat sources and sinks contribute to the thermal evolution of a body; for the natural satellites observed in our Solar System, insolation, radiogenic heat, accretional heat, differentiation heating, impactor heating, various forms of tidally-forced heating (e.g. spin-down heating but also eccentricity and obliquity

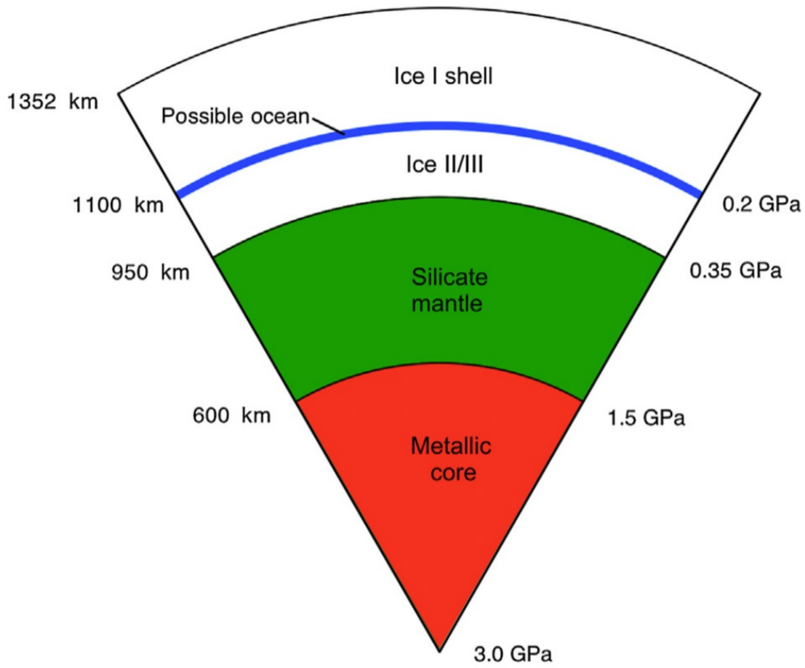

Figure 2.4: Plausible present-day interior structure produced by McKinnon & Kirk (2014) on the basis of the assumption of a hydrostatic, fully differentiated Triton that satisfies mass- and radius-constraints.

tides) and phase transitions can be energy sources of varying degrees of importance depending on the body in question (see Hussmann et al. 2010 for a review).

For Triton in particular, the primordial sources of heat (accretional, spin-down and differentiation heating) are fully overpowered by the potential energy released during its capture (Hussmann et al., 2010; Van Woerkom, 2024), and so whatever effect they may have is mostly overshadowed by the uncertainties that exist on Triton's initial capture orbit; a remark that must be made here is that this is not necessarily the case for spin-down happening *during* Triton's capture, which may have produced episodic bursts of significantly increased tidal dissipation (Van Woerkom, 2024). Radiogenic heat is certainly still present, though the degree to which it is important depends on the size and composition of Triton's core: it does seem, however, that radiogenic heating is sufficient to maintain a Tritonian subsurface ocean into the present (Nimmo & Spencer, 2015), and so inclusion in a thermal model is certainly justified. Insolation, while important for surface processes (and significantly greater in magnitude than interior processes at present; Brown et al. 1991), does not contribute significantly to interior processes (Hussmann et al., 2010): reflected and thermal heat from Neptune are two orders of magnitude lower still (Brown & Kirk, 1994), and so are certainly not of influence. Tidal heating was certainly dominant during capture, but even at present obliquity tides are expected to be responsible for Triton's youthful surface (Nimmo & Spencer, 2015). Finally, phase changes (in a broad sense) are also of importance: the natural example is the phase change between the ocean and the ice shell, but the core may also reach temperatures that allow formation of silicate melt (McKinnon, 1988; Hammond & Collins, 2024), and the presence of a liquid ocean overlaying a rocky core may trigger serpentinisation (Cioria & Mitri, 2022), the latter of course provided that Triton's silicate interior was not already hydrated.

Thermal evolution

A thermal evolution model, then, takes the aforementioned interior profiles, evaluates all relevant heat sources, and describes how this heat is transported through (and, eventually, out of) the planetary body. The equation of conservation of energy then dictates in this manner how the temperature profile of the body evolves with time (Van Zelst et al., 2022, Sec. 2.1.3).

Heat transport in a planetary body can happen by conduction (diffusion of heat upward or downward through the body) or convection (movement of heat with moving material), and either corresponds to different simplifications or parametrisations of the energy-conservation equation. Whichever is dominant depends on a variety of quantities, and will vary throughout the body: in practice, icy bodies will develop a so-called stagnant lid in their hydrosphere, where a conductive layer of ice overlays a convective layer (Deschamps & Vilella, 2021). As convection is difficult to incorporate physically, one-dimensional models usually account for it by a parametrised convection model (e.g. Hussmann & Spohn 2004; Nimmo & Spencer 2015; Hammond & Collins 2024), with recent work mostly using the scaling laws developed by Deschamps & Vilella (2021).

Conductive heat transport can be modelled through the conductive version of the energy-conservation equation (e.g. Spohn & Schubert 2003; Gaeman et al. 2012; Bagheri et al. 2022a), and also applies in the core so long as it is rigid; the structure of Triton's core is, unfortunately, as of yet unknown (McKinnon & Kirk, 2014; Cioria & Mitri, 2022), though Hammond & Collins (2024) did find moderate evidence for melt formation in the core in some scenarios, even though their models do not account for the associated heat flux. Interestingly, such tidally induced melt upwelling has already been proposed to occur on Europa, and would be responsible for changes in ocean chemistry (Běhounková et al., 2021). Heat transport between the core and ice shell through the ocean is conventionally taken to happen instantaneously through an inviscid, adiabatic ocean (e.g. Gaeman et al. 2012; Bagheri et al. 2022a).

Fixing the thermal profile for this thermal evolution does, however, require that the temperature or heat flux be (assumed to be) known at the appropriate boundary conditions. The temperature at the ice shell-ocean interface is given by the liquidus (i.e. melting) temperature of the ocean; if the ice shell is in contact with the rocky interior, continuity of the temperature profile throughout the interior provides the appropriate condition. For cold outer Solar System-bodies like Pluto and Triton, the surface temperature is often set equal to the present-day surface temperature (e.g. Gaeman et al. 2012; Bagheri et al. 2022a). This boundary condition at the surface is not the only allowable solution, however: in modelling of stellar atmospheres, the effective (i.e. brightness) temperature of a star is often used to constrain the surface heat flux (LeBlanc, 2010), and the thermal heat-flux at least for terrestrial-like surface materials corresponds roughly to the blackbody flux at their surface temperatures (Hu et al., 2012). One could therefore conceive a temperature boundary condition such that the blackbody temperature (or a graybody approximation, with some value for the emissivity derived from observations or theory) corresponds precisely to the outgoing flux: observability studies for tidally heated exomoons, for example, have seemed to embrace this approach by assuming thermal equilibrium (e.g. Rovira-Navarro et al. 2021; Kleisioti et al. 2023). Better yet, though rarely applied for interior models of Solar System satellites, is to couple the interior model to an atmospheric model, fixing their boundary conditions to one another. We will refrain from discussing a treatment along the latter lines until it is clear whether Triton did indeed experience the surface fluxes necessary to raise an atmosphere (e.g. Lunine & Nolan 1992).

2.2.2. Dynamical modelling of tidally perturbed natural satellites

For Triton, Sec. 2.2.1 tells us that aside from more usual heat sources like radiogenic heating, eccentricity tides will have played a major role in its early post-capture evolution, which possibly drove its interior into a more-evolved, differentiated and dehydrated state, whereas at present obliquity tides are more important and still drive geological activity unlike anywhere else. Evaluating when and how this transition took place and modelling how Triton ended on its present-day orbit that allows obliquity tides in the first place thus requires that its dynamics be modelled. This work builds on previous work that already implemented these dynamics (Van Woerkom, 2024), so we will only briefly summarise the literature on the equations of motion governing tidal evolution. We will then follow on this with an overview of the techniques employed in past work to model high-eccentricity orbital evolution.

Evaluating the equations of motion

The motion of a celestial body in a two-body system perturbed by some arbitrary potential is, in general, governed by the Lagrange planetary equations (Boué & Efroimsky, 2019). Studies simulating the evolution of such bodies use a variety of approaches, depending on their aims and assumptions: for the integration of spacecraft orbits or for estimation of ephemerides, the usual practice is to numerically integrate these or equivalent equations directly (e.g. Fayolle et al. 2022, 2023; Hu et al. 2023; some studies do still resort to a formalism like ours, however, e.g. Kruzynska et al. 2013), which is possible for such relatively short-term simulations. Doing so over astronomical timescales, however, is impractical, and such analysis requires additional consideration: fortunately, analyses such as that with which we are concerned do not care much for predictions of the exact position of Triton or Neptune at any point in time. Rather, we would like to know how their mutual orbit evolves over the long term, and how the associated tidal evolution progresses over astronomical timescales.

To solve precisely this problem (though he was concerned with the motion of the Earth and the Moon), Kaula (1964) repurposed his Kaula (1961) formalism for spacecraft orbits into one applicable to tidally evolving bodies by cleverly disposing of all short-period oscillatory terms in an averaged version of the Lagrange planetary equations (e.g. Murray & Dermott, 1999), such that only the secular (long-term) evolution remained. As Darwin (1879, 1880) had previously derived a partial sum of the series expansion that Kaula found, the resulting formalism has been termed the Darwin-Kaula expansion (or sometimes simply Kaula's expansion). While it is most often used to describe tidal evolution, the Darwin-Kaula formalism is equipped to handle any potential perturbation that can be described as a decomposition in spherical harmonics, and so it has also been used to describe, for example, the dynamical evolution of oblate or triaxial bodies (e.g. Luna et al. 2020). Recently, Boué & Efroimsky (2019) re-derived Kaula's expressions in a modern form, and corrected some irregularities in Kaula's work.

Unfortunately, the Darwin-Kaula expansion (see Sec. 3.1 for an overview of the terms relevant for our work, or App. D for the "proper" Darwin-Kaula expansion) contains two nested infinite sums that must be truncated, as well as the so-called Hansen coefficients or eccentricity functions[5], the evaluation of which even for only marginally excited eccentricities is described in a rich literature going back centuries (e.g. Hansen 1855; Tisserand 1889; Von Zeipel 1912; Izsak et al. 1964; Cherniack 1972; Hughes 1981; Proulx & McClain 1988; Wnuk 1997; Wu & Zhang 2024), and in practice often requires the evaluation of another infinite sum or the use of convoluted recurrence relations. Additionally, the evaluation of these equations relies on knowledge of the so-called tidal quality function (the evaluation of which is discussed in Sec. 2.2.3) that describes the deformation of a body under a tidal potential, accurate computation of which is expensive and requires a detailed internal model of the body in question (see Sec. 2.2.3). As a result of this, early (and unfortunately, at times also recent) literature on tidal evolution turned to toy models for this tidal quality function that have some desirable properties, at the cost of physicality.

While the manner in which these toy models are implemented varies[6], one will normally find that the simplifications made using these models can be traced back to one of the following assumptions: (1) the tidal bulge lags the planet-moon line by some constant angular displacement, independent of forcing frequency, or (2) the tidal bulge lags the planet-moon line by some constant time lag, also independent of forcing frequency. For obvious reasons, the first model is oftentimes referred to as the constant phase lag (CPL) model[7], whereas the second is often termed the constant time lag (CTL) model. These assumptions feature in the derivation of such expressions, but do not always feature clearly in the resulting expression, such that authors will sometimes use the expressions derived using these assumptions while explicitly using expressions for the tidal Love number that violate them.

Clear objections against these models have been raised by Efroimsky & Makarov (2013) and Makarov & Efroimsky (2013) for the CPL and CTL models, respectively, and so one should be wary to trust the results of either in more than a qualitative manner, though they do remain in use by some authors. Notably, oft-cited studies using the CPL model are those by MacDonald (1964) and Goldreich et al. (1966), and it is also treated in the standard reference text by Murray & Dermott (1999); Goldreich et al. (1966) also treated the CTL model, as did Hut (1981), Mignard (1979, 1980) and Néron De Surgy & Laskar (1997). One should therefore be wary when these studies are invoked to support use of a particular set of tidal-evolution equations for bodies with a significant solid layer. For gaseous bodies without any significant (visco)elastic layer, such as gas giants or stars, the assumptions underpinning the CTL model are apparently more justified, and so Renaud & Henning (2018) find that it holds up well when applied to such bodies.

Dynamical modelling of highly eccentric objects

A particular reason for which the CTL model is often called upon is the fact that it allows one to rewrite the Darwin-Kaula expansion as a finite sum of finite polynomials in eccentricity (see e.g. Wisdom 2008; Correia & Valente 2022). It is therefore uniquely attractive when working with bodies on highly eccentric orbits, which would otherwise require inclusion of laboriously many terms in Kaula's expansion: this is why, for example, Correia (2009) turned to the CTL formalism to model early Triton.

Unfortunately, it has been shown that approximations (ab)used in prior literature lead to severe under- or misestimation of the tidal evolution of celestial bodies: when truncating powers of the eccentricity in the Darwin-Kaula expansion prematurely, Renaud et al. (2021) find that tidal effects are severely underestimated (and can even be assigned the wrong sign), whereas Van Woerkom (2024) found that use of the CTL model for icy satellites at Triton-like forcing frequencies is not justified, and that using CTL to simulate highly-eccentric objects will fail to reproduce the progression through spin-orbit resonances that more advanced tidal models predict. In analogous systems of low-mass (rocky) exoplanets orbiting M-type stars, Walterová & Běhounková (2020) also find that such resonances are a common feature, even when including realistic features such as a layered interior including a layer of fluid melt. Hence, dynamical models of objects on highly eccentric orbits should include a full, well-supported evaluation of the Darwin-Kaula expansion up to a sufficient number of terms: there are no shortcuts. A code to perform this evaluation of the Darwin-Kaula expansion was the product of the work by Van Woerkom (2024), and will form the foundation upon which our full thermal-orbital model is built.

2.2.3. Coupled thermal-orbital modelling

With high-fidelity dynamical models using simplified thermal-interior models for Triton predicting ~Myr timescales for its circularisation (e.g. Van Woerkom, 2024), and high-fidelity interior models using simplified

[5]The term eccentricity polynomials, though not strictly correct, can also be found in literature.

[6]One will often find their implementation combined with a given truncation level on the powers of the eccentricity found in the equations of motion, presented as a "ready-to-use" set of equations that can be integrated upon inserting some value for the tidal Love number.

[7]The term MacDonald torque, after the work by MacDonald (1964), as well as the term constant-Q model, after the tidal quality factor $Q = 1/\left|\sin \epsilon_{ph}\right|$ that is often used to parametrise the phase lag ϵ_{ph} (e.g. Efroimsky & Makarov 2013), are also used with some regularity.

dynamical models predicting ~Gyr timescales (e.g. Hammond & Collins, 2024), we must make efforts to reconcile these numbers. It seems plausible that the reality lay somewhere in the middle, and finding out where would thus require the best of both worlds: that is, we need to couple a high-fidelity dynamical model to a high-fidelity thermal-interior model. We will briefly review what this entails, followed by a brief discussion on the methods available when restricting ourselves to spherically symmetric bodies. Finally, we will review some commonly used simplifications to speed up computations derived using the propagator-matrix method.

Coupling dynamical and thermal-interior models

In essence, coupling thermal-interior and dynamical models requires solely that the effect one has on the other be acknowledged: energy dissipated from Triton's orbit must be reflected in its thermal evolution, for example, and conversely the dynamical effects of a thermally evolving Triton (e.g. substantial melting or freezing in the hydrosphere) must be accounted for, too. In general this then comes down to the evaluation of two effects: (1) the relevant dynamical properties that appear in the Lagrange planetary equations, where dictated by the interior, must be evaluated as the interior changes, and (2) the thermal-interior effects due to dynamics must be evaluated as the dynamics evolve.

Accounting for the first effect will come down to evaluation of the so-called tidal Love numbers that appear in the Darwin-Kaula expansion, as well as the moment of inertia, both as a function of a changing interior. While the moment of inertia can be calculated straightforwardly once the density structure of the body is known, evaluation of the tidal Love number is more involved (see Secs. 2.2.3-2.2.3). A quick clarifying note that must be made here regards the different terminology applied to refer to the as-of-yet ambiguously mentioned tidal Love number in literature (a review of this terminology and its origin is given by Bagheri et al. 2022b, Secs. 4.1-4.3: we only give a brief introductory overview here): reflecting the shift to the (complex) Fourier domain that is made when considering time-dependent tides, the term multiplying the inducing potential to yield the additional tidal potential is often termed the complex Love number $\bar{k}_l(\omega)$, in analogy to the real Love number that appears for static tides. When expressing this complex number in polar form, its magnitude is endowed the name of "dynamical Love number", $k_l(\omega)$, while the negative of its argument is called the phase lag $\epsilon_l(\omega)$, such that $\bar{k}_l(\omega) = k_l(\omega)e^{-i\epsilon_l(\omega)}$. In each of these terms, the subscript l refers to the spherical harmonic degree l, which dictates the form of the frequency-dependence of these terms. This frequency-dependence is itself denoted using the frequency ω, and is added to remind us that, contrary to the case of static tides, these quantities are frequency-dependent in the time-varying case. In the study of tidally-driven dynamical evolution, a quantity that arises with particular regularity is the negative imaginary part of the complex Love number. For this quantity, one will therefore sometimes encounter several (equivalent) forms of notation and appellation (e.g. Boué & Efroimsky 2019; Bagheri et al. 2022b):

$$-\operatorname{Im}(\bar{k}_l(\omega)) = k_l(\omega)\sin\epsilon_l(\omega) = \frac{k_l(\omega)}{Q_l(\omega)} = K_l(\omega) \tag{2.2}$$

where $Q_l(\omega) = |\sin\epsilon_l(\omega)|^{-1}$ is the tidal quality factor, and $K_l(\omega)$ is the tidal quality function of degree l: Fig. 2.5 illustrates what the typical frequency-dependence of the tidal quality function looks like. In this work, we will generally prefer to speak of the tidal quality function $K_l(\omega)$ in mathematical contexts, reflecting the variation with degree and frequency, though we will also at times refer to "evaluation of the (tidal) Love number(s)" when discussing the process of determination of any of these quantities, acknowledging that this terminology is somewhat outdated in the present paradigm of frequency-dependent tidal deformation. Though we will prefer to keep the discussion general where applicable (and so include the subscript l and the frequency-dependence ω explicitly), it should also be noted that the $l = 2$-term is often dominant and previous work often assumed frequency-independence, and so other authors will at time limit themselves to that case, dropping the subscript and functional notation to write k and Q as constants.

The second effect will entail the evaluation of the tidal dissipation throughout the body as a function of changing orbital elements. One additional trouble this coupling introduces is the timescales involved: while the slowly-varying orbital elements like eccentricity and semi-major axis normally vary on timescales of $\sim 100-1000$ Myr, rotational evolution can proceed at ~kyr timescales or faster (e.g. Van Woerkom 2024), and thermal-interior evolution can be expected to fall somewhere in between. In the particular case of Triton, this is further exacerbated by the wildly varying range of timescales on which even individual processes take place, with initial evolution following Triton's capture likely taking place on ~kyr timescales or shorter for most if not all processes. This timescale problem drove Walterová & Běhounková (2020), for example, to divide propagation of different processes into a short and long integration loop; Hammond & Collins (2024) solve this problem by updating the Love number only when sufficient change in interior conditions (in their case, in ice shell-base viscosity) has taken place.

Even resolving this, propagating this evolution over Gyr-timescales requires that the tidal deformation and internal conditions of Triton be evaluated too often to resort to high-resolution, complicated methods like those

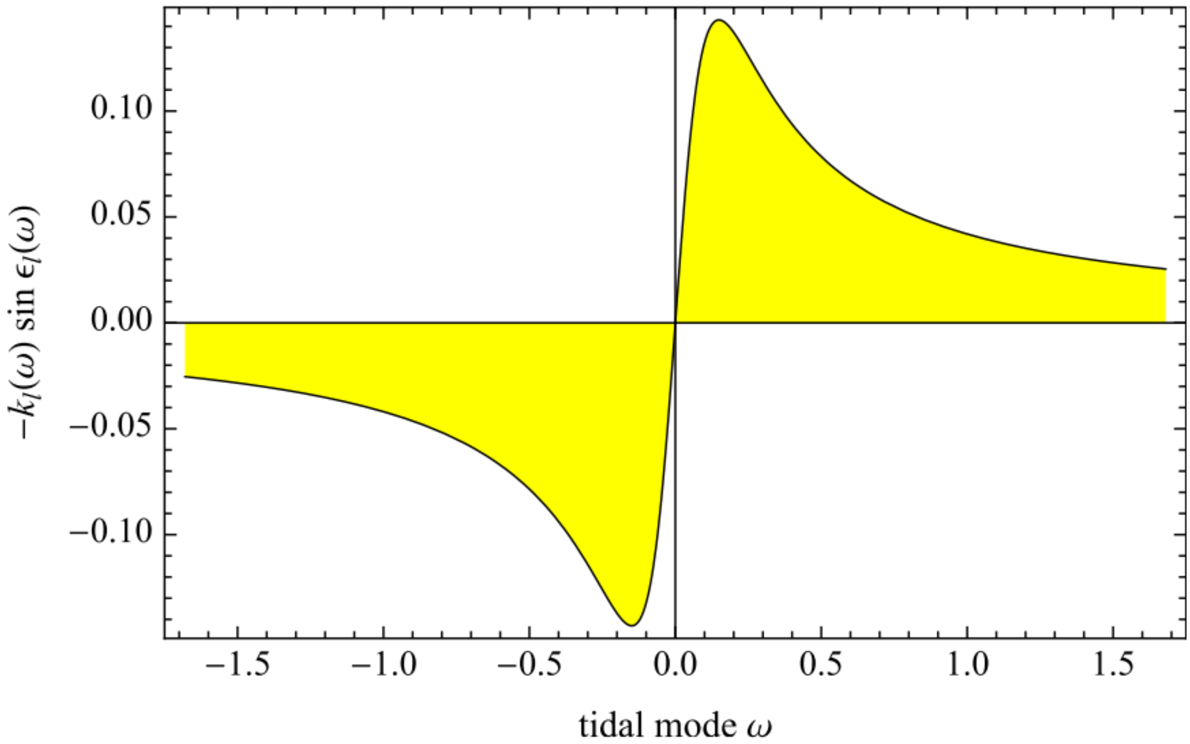

Figure 2.5: Typical shape for the tidal quality function (though the values do not correspond to any real body), from Noyelles et al. (2014).

conventionally used to model shorter-scale matters like giant impacts (e.g. Wada et al. 2006) or glacial isostatic adjustment (GIA; e.g. Huang et al. 2023); besides, our limited knowledge on Triton does not justify the use of such complex models. Hence, we will have to rely on simpler, faster-to-evaluate methods, requiring suitable assumptions.

Deformation of (near-)spherically symmetric bodies

On this topic, we can fortunately draw from a large body of prior work. The evaluation of the deformation of (near-)spherically symmetric bodies is not a novel issue: the matter of deformation and relaxation of the solid Earth, in fact, forms its own entire field of study. In the (modern) context of this subfield of geosciences (though the foundations of this field go back to the work of Augustus Love in the late 19th century), Peltier (1974), Wu & Peltier (1982) and Sabadini et al. (1982) first developed general analytical expressions for the deformation and induced potential suffered by an incompressible, layered Earth. In this case, one tracks the stresses, displacements and potentials (usually framed in terms of a set of six "radial functions": see Sabadini et al. 2016, Sec. 1.4) through a spheroidal layered body using a set of six first-order differential equations governing them (the viscoelastic-gravitational equations: e.g. Takeuchi & Saito 1972, Eq. 82).

Though a general implementation hereof was developed by Wahr et al. (2009), various simplifications and extensions are possible: under certain assumptions on the materials in question, the propagator matrix-method allows for particularly efficient analytical computations (see e.g. Sabadini et al. 2016, Ch. 2 for the incompressible case). Jara-Orué & Vermeersen (2011) (see also Sabadini et al. 2016, Ch. 9) developed an extension to this theory using normal mode theory, which allows this incompressible propagator matrix-approach to extend to icy satellites possessing subsurface oceans experiencing arbitrary types of forcing (tidal and non-tidal).

Other authors have pursued different directions: Beuthe (2015a,b, 2016) has developed an impressive bibliography on the basis of treating the icy shell of icy satellites as deformed membranes, which allows him to derive a variety of expressions even foraying into the domain of laterally-varying shells, so as to describe Enceladus' south polar anomaly (Beuthe, 2018, 2019). For the purposes of this work, an important contribution in this area is the derivation of a relation between the so-called "fluid-crust" Love number, without an icy shell, and the Love number including the icy shell (Beuthe, 2015a): this allows one to relate the Love numbers of Earth-like bodies (with surface oceans) to those for equivalent icy satellites (with subsurface oceans), as per Eq. E.4 in the work of Beuthe (2019), which leads directly to useful expressions for the tidal dissipation respectively in the core and in the shell of such a body. A (non-exhaustive) summary of the methods available for tidal response-computations is given in Tab. 2.2.

Table 2.2: Methods to compute the tidal response of inhomogeneous spherically symmetric bodies. References are as follows: W+06 (Wada et al., 2006), H+23 (Huang et al., 2023), JV11 (Jara-Orué & Vermeersen, 2011), S+16 (Sabadini et al., 2016), B15+ (Beuthe, 2015b,a, 2016, 2018, 2019).

Method	Examples	Applications	Remarks
Finite element	W+06, H+23	Giant impact, GIA	Slow
Normal mode theory	JV11	GIA, arbitrary forcing of homogeneously layered bodies	Complicated for ocean worlds
Viscoelastic propagator matrix	S+16	Tidal forcing of homogeneously layered bodies	Restriction of normal mode theory
Membrane theory	B15+	Thin-shell worlds	Requires thin ice shell

Analytical estimates for the tidal quality function

Under suitable assumptions, simple analytical estimates can even be established for the tidal Love number directly. Such assumptions start with the particularly simple case of a fully homogeneous interior: in that case, a simple relation follows for both the complex Love number and tidal quality function as a function of the (frequency-dependent) complex compliance of the material making up the body (e.g. Bagheri et al. 2022b, Eqs. 56-58). The propagator matrix formalism allows for construction of an analytical expression for the complex Love number and tidal quality function of any layered incompressible solid body (Sabadini et al., 2016), though such expressions become somewhat unwieldy for anything more complicated than a two-layer body; this formalism can be extended to include fluid layers, though this requires additional assumptions and a slightly altered approach (e.g. Beuthe 2015b, App. F; Jara-Orué & Vermeersen 2011 or Sabadini et al. 2016, Ch. 9). The previously discussed CPL and CTL models, when viewed through this lens, amount to assuming that (1) the magnitude of the tidal quality function is constant with frequency or that (2) all excited tidal Fourier modes lay on the (near-)linear part of the graph of the tidal quality function (see Fig. 2.5). The objections of Efroimsky & Makarov (2013) and Makarov & Efroimsky (2013) can then be augmented by the fact that the first assumption does not approximate any realistic tidal quality function, and that the second will only hold for a very limited range of (low) eccentricities before tidal modes in the non-linear part of Fig. 2.5 are excited.

Beyond these expressions, the approach of Beuthe (2015a,b) also allows establishing of equivalent "membrane" versions of bodies without an ice shell for which the tidal Love number is already known, which reasonably approximates icy satellites with thin ice shells. In particular, this allows the extension of analytical Love number formulae available of bodies comprising a core/mantle and surface ocean to the icy-satellite domain: as a multitude of such expressions were derived to approximate the behaviour of the Earth in the early 20th century, this method is tremendously powerful. Beuthe (2015b) uses this approach to derive analytical expressions describing icy satellites comprised of a homogeneous, incompressible mantle, a subsurface ocean and an icy shell, that is applicable to icy satellites with shell thicknesses $\lesssim$ 10% of their total extent: these might therefore be applicable for Triton whenever it possesses a substantial surface ocean, though the extent of Triton's hydrosphere is unfortunately sufficiently large that these expressions may not be applicable if the hydrosphere is largely solid. We will see, however, that Triton's shell is very thin during the epoch of strong eccentricity tides, such that the use of these expressions is warranted.

2.3. Existing orbital-interior models of Triton

Having described the process of orbital-interior modelling of a single-moon system like the Neptune-Triton system in Sec. 2.2, we will now introduce all such models that have been applied to Triton. Here, we will once again distinguish between the interior models that have been used to describe Triton (Sec. 2.3.1), the dynamical models that have been applied to the moon (Sec. 2.3.2), and finally the coupling of those two model components (Sec. 2.3.3). The context provided by a proper understanding of each of these will allow us to finally move on to a description of our present understanding of Triton's history in Sec. 2.4.

2.3.1. Thermal-interior evolution models of Triton

With the data from *Voyager 2* coming in, sufficient data was finally available to start modelling the thermal-interior conditions on Triton, though a lot of features of later models are still missing at that time: Brown & Kirk (1994)[8], for example, modelled radiogenic heating and insolation, but did not include tidal heating as this was at the time not thought to be a major contributor to Triton's heat budget[9] (e.g. Brown et al. 1991). A first thermal-evolution model was given by Ross & Schubert (1990), though their innovation lay mostly in coupling a thermal and

[8]Though the ultimate goal of their model was the evaluation of volatile transport, not strictly modelling of the interior state of Triton.

[9]The idea of obliquity tides on Triton had been proposed already by Jankowski et al. (1989), but the obliquity of $\sim 100°$ they envisioned was not compatible with *Voyager 2*-observations that came in later that year, and so it seems the idea was promptly dismissed.

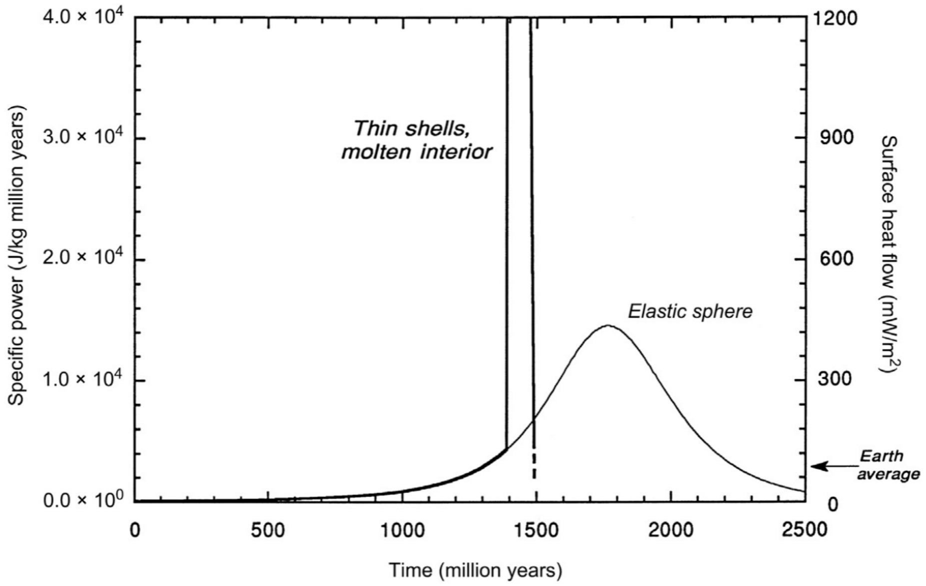

Figure 2.6: Example heat flow over time for a tidally circularising Triton assuming the tidal response of an elastic sphere, and of a body that starts as an elastic sphere and then transitions to a body comprising two thin shells with molten interiors of ice and rock, illustrating runaway melt (though in reality the thin-shell graph would depart from the elastic sphere-graph much earlier). Reprinted from McKinnon & Kirk (2014), who adapted it from McKinnon et al. (1995).

orbital model (see Sec. 2.2.3) rather than in their thermal model, which they admit to be limited even for the time. Later modelling would significantly expand on this, however, and so we will give a brief overview of the models that have been used to describe Triton's hydrosphere, mantle and composition.

Triton's hydrosphere

More sophisticated thermal-interior modelling of Triton would have to wait until the work of Gaeman et al. (2012), who applied methods previously used to model Enceladus by Roberts & Nimmo (2008b) to Triton. While this included an evaluation of the thermal state of the hydrosphere, they did not model the silicate core (rather assuming that all radiogenic heat was transported out of the core efficiently into the overlaying ocean) or any high-pressure ice phases, nor did they include convection. Though it appears no interior-evolution study has as of yet accounted for high-pressure ice phases[10], this latter objection regarding convection was remedied in the model used by Nimmo & Spencer (2015)[11], who then used their model to show that convection set on by obliquity tides could be responsible for the yielding of the ice shell observed on Triton's surface.

Hammond & Collins (2024), finally, incorporated the thermal evolution of the full length of Triton's interior (i.e. including the silicate core, too). They found levels of present-day obliquity tidal heating consistent with those obtained by Nimmo & Spencer (2015), though they do in contrast find that ice shell convection ceases shortly (< 100 Myr) after capture, and blame over-pressurisation of a freezing ocean rather than convection for the yielding observed on the Tritonian surface.

Out of all three "complete" thermal-interior models (Gaeman et al. 2012; Nimmo & Spencer 2015; Hammond & Collins 2024), Nimmo & Spencer (2015) and Hammond & Collins (2024) find that an ocean will likely have persisted into the present, whereas only Gaeman et al. (2012) suggest it need not have: as noted by Nimmo & Spencer (2015), this is likely a result of their underestimation of the radiogenic heating experienced by Triton, and so it seems very likely that Triton maintains an ocean even today, especially when additionally heated by obliquity tides and with a liquidus temperature suppressed by the presence of ammonia.

Triton's silicate mantle

Beyond this modelling of the hydrosphere, not much is known with any degree approaching certainty about Triton's interior structure, mostly due to the lack of additional observational constraints. While it is widely accepted that Triton suffered ice-silicate differentiation, if not already preceding capture then at least during capture (Smith et al., 1989; McKinnon & Benner, 1990; McKinnon & Kirk, 2014), its deep interior might additionally well have reached sufficient temperatures to start differentiating silicates and iron during capture: McKinnon & Kirk (2014) base their proposed interior structure on this assumption.

[10] And neither do we, as we find that plausible hydrosphere thicknesses do not provide the required thickness except in thermodynamically unstable scenarios: see the discussion in Sec. 2.2.1.

[11] Nimmo & Spencer (2015) additionally take note of an error in the volume Gaeman et al. (2012) used to compute radiogenic heat.

Comparison with the twin world Pluto cannot save us here: Pluto does not appear to have ever reached sufficient temperatures to set on iron-silicate differentiation (see e.g. Bagheri et al. 2022a), but of course also did not undergo the vigorous tidal heating that Triton must have. Even the putative Charon-forming impact could not, on the basis of momentum constraints, have been sufficiently catastrophic to match the energy imparted upon Triton by its capture and circularisation (McKinnon et al., 1995). On this basis though, one might still posit that Pluto can at least provide a reasonable analogue for pre-capture Triton, which would suggest that Triton possibly suffered or was in the process of ice-silicate differentiation even before capture (cf. Stern 2014; Stern et al. 2018): in particular, this comparison suggests that a plausible hot end-member state for pre-capture Triton is a nearly fully liquid hydrosphere atop a silicate mantle, though the state of this mantle (in terms of differentiation) is uncertain. On the basis of the pressures reached in Triton's interior, a porous core like that of Ceres can certainly be excluded both in the past and present, however (Zolotov, 2009; Malamud & Prialnik, 2015), as Triton is well beyond the transition regime where such porosity is plausible (Grundy et al., 2019a).

Going back to models of Triton, McKinnon (1988) proposes, arguing on the basis of the order of magnitude of the energy dissipated during capture and circularisation, that Triton's core and hydrosphere both melted, leaving only thin solid shells on top of either; this picture is further supported by simulations of McKinnon (1992) and McKinnon et al. (1995). Hammond & Collins (2024) do not observe this melting, but do note that this is possibly a consequence of their use of Maxwell rheology, which underestimates silicate tidal dissipation compared to the higher-fidelity Andrade model (e.g. Bierson 2024). Using a reduced effective silicate viscosity to mimic the values found by the Andrade model in their Maxwell implementation, Hammond & Collins (2024) find that the core can reach the temperatures prerequisite to set on melting. In that case, if core differentiation behaves as a runaway process like alluded to by McKinnon et al. (1995) (differentiation releases ~ 50 K worth of heat: Hammond & Collins 2024), Triton should have once possessed a liquid iron core; McKinnon & Benner (1990) do indeed find such a substantial liquid core in all their models, but without a detailed description of those models it is not possible to ascertain whether their models suffer from any assumptions that have been superseded by modern understanding (and it is not clear, for example, why their model does not suffer the same rheological shortcomings that Hammond and Collins encounter).

All in all, it thus seems possible if not probable that Triton, uniquely for a body of its size, also underwent some degree of silicate-iron differentiation through the formation of a liquid layer in its silicate core. Whether this core consequently solidified or the liquid layer endures into the present appears to be an unresolved matter, though. Assuming that such a liquid core at least once existed, Triton should presently indeed have a fully differentiated four-layer structure as proposed by McKinnon & Kirk (2014), with an iron core.

Mineralogy and proto-Triton's composition

Attaining the types of temperatures required to cause iron-silicate differentiation has interesting implications for the deep interior of Triton: in analogy to the process of antigorite dehydration in the oceanic mantle on Earth, dehydration could start occurring at the temperatures (> 800 K) attained in Triton's interior (Perrillat et al., 2005). A similar process is expected to have dehydrated at least the interior part of Titan's core (Tobie et al., 2014), for example, though the process is only partially complete and possibly still ongoing there if part of Titan's ^{40}K is leached into its ocean (Castillo-Rogez & Lunine, 2010); on Ganymede, the assertion of a partially dehydrated silicate mantle atop an iron-sulfur core is additionally supported by constraints arising from observational data (Sohl et al., 2002; Scott et al., 2002). In contrast, modelling of the Sputnik Planitia-forming impact on Pluto shows that its core must be significantly hydrated (Denton et al., 2021). In terms of mineralogy, Triton therefore appears to punch above its weight-class among the Solar System satellites as a result of its heliocentric origin: depending on the intensity of its post-capture tidal heating, Triton's deep interior will be somewhere on the continuum from a fully hydrated, undifferentiated Pluto-like core to a differentiated, dehydrated silicate mantle overlaying an iron core like Ganymede's, with intermediate states somewhat analogous to Titan.

This variety of possibilities is what led Cioria & Mitri (2022) to consider three possible (analogue) precursor materials for proto-Triton: an Orgueil-like (used as reference), Murchison-like and Allende-like composition. These materials reflect three varying degrees of primordial dehydration histories (for an extensive discussion, see Cioria & Mitri 2022, Sec. 3), reflecting a dehydration event at moderate temperatures (Orgueil and Murchison), or in a higher-temperature primordial environment (Allende). As Triton is, based on elemental abundances, hypothesised to have formed in the Kuiper belt, or perhaps as part of a now-extinct population of Kuiper belt objects between Uranus and Neptune (McKinnon et al., 1995), only an Orgueil-like composition is strictly compatible with this history, as Mighei-type (CM) and Vigarano-type (CV) chondrites (the classes to which the Murchison- and Allende-meteorites belong, respectively) are thought to form strictly interior to Jupiter, whereas Inuva-type (CI) chondrites (such as the Orgueil-meteorite) are thought to originate from ≥ 15 AU (Desch et al., 2018): the use of a Murchison-like and Allende-like composition by Cioria & Mitri (2022) is then intended strictly to simulate iron enrichment and varying degrees of water alteration, reflective of a lower degree of iron-silicate differentiation in the Tritonian interior.

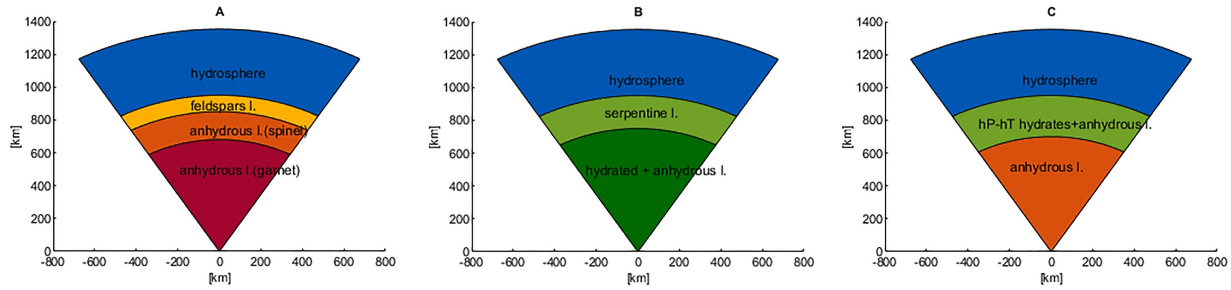

Figure 2.7: Plausible models for the present-day silicate interior of Triton assuming no iron-silicate differentiation took place, adapted from Cioria & Mitri (2022): (A) a fully dehydrated interior, (B) a fully hydrated interior and (C) a partially hydrated interior.

Going along with the analysis of Desch et al. (2018), it is likely that proto-Triton was composed of a CI-like material. Even if partial differentiation occurred (as we have previously discussed to be likely), it is likely that this behaves as a runaway process (McKinnon & Leith, 1995), such that the formation of a partially differentiated deep core with iron-enriched (but not fully differentiated) silicate as modelled using CV- and CM-type material by Cioria & Mitri (2022) is unlikely: either Triton did not differentiate at all, and the silicate core is fully described by a CI-like material, or Triton's silicate core differentiated into a silicate layer atop an iron core. In the latter case, modelling the silicate layer by a CI-like material is still appropriate, though perhaps at a reduced iron content (cf. Néri et al. 2020). The major uncertainty is then how (de)hydrated Triton's deep interior is, as hydrous mineral assemblages will display lower densities, especially at lower temperatures and pressures, than their anhydrous cousins (cf. Tabs. 2-5 in Cioria & Mitri 2022): this is reflected in the three models proposed by Cioria & Mitri (2022), as shown in Fig. 2.7. While they proposed that these can be differentiated by measurements of Triton's gravity field coefficient C_{22}, no such measurements are available at present: thermal modelling may provide a way out, by constraining the regions of Triton's interior that could have reached the temperatures necessary for dehydration. Doing so, however, requires that Triton's dynamical evolution be modelled in tandem, as the presence of such temperatures is likely to have been driven by tidal evolution.

2.3.2. Dynamical evolution models of Triton

Even though the aim of this work will not be to construct a fully new dynamical model of Triton, it is instructive to give a brief overview of and comparison between existing dynamical models of the moon. The first such model exploring Triton's evolutionary history in a scenario commensurate with our present understanding of its formation is perhaps that by McCord (1966); his use of the formalism of MacDonald (1964), however, and the lack of constraints available on the tidal properties of Neptune and Triton at the time mean that his model can only give a qualitative history of Triton. An interesting feature that is already present here is the fact that McCord (1966) records little change in Triton's inclination, nor in Neptune's obliquity or spin rate.

More such models in literature, naturally, arose when the captured nature of Triton became apparent; while McKinnon (1984) uses astrodynamical arguments to show that Triton cannot have had its orbit reversed by an ejected Pluto, because of his lack of exploration of the dynamics of capture an argument can be made that the honour of the first true dynamical model of the past evolution of Triton's orbit in the new capture paradigm belongs to Chyba et al. (1989)[12]. Rather than propagate the full set of equations of motion, Chyba et al. (1989) assume that the z-component of Triton's orbital angular momentum is conserved, and compute the variation of the coupled semi-major axis with either the eccentricity or inclination (assuming that the other quantity remains fixed). This approach works remarkably well for Triton's future evolution (cf. Van Woerkom 2024), but fails altogether for its past evolution. In expectation of the *Voyager 2*-data coming in later that year, Goldreich et al. (1989) also examined Triton's evolution: though they did not expand the Darwin-Kaula expansion in full (which is understandable given the computational limitations of the time), they did examine both the low- and high-eccentricity regimes using asymptotic approximations, showing that Kozai-Lidov oscillations induced by solar gravitational influences will affect the evolution of Triton's inclination at orbital distances greater than $\sim 100R_N$, but also showing probabilistically that Neptune's regular satellite system was almost certainly disrupted (if not cannibalised) by circularising Triton.

Perhaps more interesting models came after *Voyager 2* had accurately constrained Triton's orbital and physical properties. Ross & Schubert (1990) used the same asymptotic expressions as Goldreich et al. (1989), but now coupled them to a simple thermal model and excluded solar influences (though noting that their results are hardly affected for identical parameters). Their most interesting result, then, was primarily the fact that

[12]Though it must be noted that earlier work by the same team (Jankowski et al., 1989) predates this by a couple of months; at that time, they only considered the present rotational state, not the full orbital evolution of Triton, however.

coupling a thermal model to a dynamical model yielded qualitatively very different behaviour, demonstrating the importance of a coupling between thermal and orbital models in the case of Triton. The next examination of Triton's dynamical evolution would have to wait another two decades[13], for the research of Correia (2009), who, apparently unphased by the warning of Ross & Schubert (1990), applied a fixed-interior CTL model to Triton's evolution. For the first time, Correia (2009) included the rotational state of Triton in its dynamical evolution. Nogueira et al. (2011) consequently used a modified version of this model to couple capture- and circularisation-simulations of Triton, showing that early capture through binary-exchange (Agnor & Hamilton, 2006) followed by circularisation through tides alone is capable of producing Triton on its current orbit.

Later, Van Woerkom (2024) examined the dynamics of Triton under the assumption of a homogeneous Maxwell body, showing that Triton will have progressed through a cascade of spin-orbit resonances as it circularised over a period of $\sim$ 10 Myrs, unless its viscosity is sufficiently lowered by the influx of tidal heat. We will see shortly (Sec. 2.3.3), however, that this result is at odds with the results of previous coupled interior-orbital models, including the more recent work of Hammond & Collins (2024). Coupling a thermal to an orbital model is thus seemingly necessary to capture the full complexity of Triton's evolution. We will therefore give a brief overview of the presently existing body of literature on Triton's coupled interior-orbital evolution.

2.3.3. The present state of coupled thermal-orbital models of Triton

Given the relative expense of coupled thermal-orbital modelling, both in terms of theory and in terms of computational intensity, as well as the lack of observational constraints available for Triton, it is no surprise that little such work has been done on Neptune's moon. Even then, as the preferred model for Triton's capture was, until the work of Agnor & Hamilton (2006), capture by gas drag (see Secs. 2.4.2, 2.4.5), most models before that time assumed that Triton was largely circularised by gas drag, not tides, during which process Triton's interior would be heated far less than during capture by tidal dissipation. Thermal-orbital modelling was, consequently, less of a concern.

Nonetheless, some attempts were made under the assumption of capture by gas drag followed by circularisation from high eccentricities through tides after dissipation of whatever nebula was presumed to have captured Triton: among these, we find the work of Ross & Schubert (1990), who parametrise the viscosity of Triton's icy shell (and consequently, its degree-2 tidal Love number) as a function of its temperature, and find that a process of runaway melt and circularisation seems likely, though they did not account for the tidal consequences of a thinning shell as an ocean forms and thickens[14]. McKinnon (1988); McKinnon & Benner (1990); McKinnon (1992) did account for this thinning of the ice shell, and find correspondingly that Triton's tidal dissipation is slowed, such that it can remain hot for $> 100 - 500$ Myr. They never published their work on the topic in full detail, however, such that we can not be sure of the workings of their model. McKinnon et al. (1995), like Ross & Schubert (1990), assume that runaway melt and differentiation occurs after a period of $\sim$ 1.5 Gyrs (when, in their model, sufficient orbital energy is drained to do so), though they do not substantiate this claim with any explicit computations on the value of the tidal quality factor Q_2: they simply assumed that it must have dropped severely as Triton melted and became less rigid, and modelled the process to happen instantaneously accordingly (see Fig. 2.6).

This conclusion of runaway melt is disputed by Hammond & Collins (2024), who explicitly include the computation of the tidal quality factor in their thermal-orbital coupling. They find that no such runaway melt occurs, but rather that the process can be maintained over ~Gyr timescales because the thinned shell does not dissipate as much heat: the tidal quality factor Q_2 increases with a thinning shell in their model (see Fig. 2.8), precluding runaway melt, as opposed to the decrease predicted by previous work: their conclusion is consistent with the formulae of Beuthe (2015a,b), whose analytical work shows that a body with an infinitely rigid mantle covered by an ice shell-less liquid layer will not dissipate any energy through tidal heating in the static limit of the viscoelastic-gravitational equations (see Beuthe 2015b, Sec. 2.3 for a discussion on the applicability of this limit). Nonetheless, in the models of Hammond & Collins (2024) sufficient heat is dissipated altogether in the remainder of the ice shell that Triton can remain warm and active over the timespan of its circularisation. Unfortunately, the dynamical equations they use (assuming a CPL Triton; see Sec. 2.2.2) were shown by Van Woerkom (2024) to be inappropriate for the high eccentricities early Triton encountered, such that this conclusion cannot be drawn with certainty. Similar high-eccentricity modelling was recently undertaken by Bagheri et al. (2022a) for the Pluto-Charon system, where tidal dissipations can damp similarly extreme eccentricities on a timescale of only $\sim$ 100 kyr, even incorporating the damping effect of a thinning ice shell: this aligns with the conclusions of Renaud et al. (2021), who find that versions of the Kaula-Darwin expansion that are truncated to include only first-order effects, such as the equations used by Hammond & Collins (2024), tend to significantly underestimate tidal heating at high eccentricities ($e \gtrsim 0.1$). Though the Pluto-Charon system is

[13]During this time, any attention given to Triton's dynamics would concern its dynamics of capture: we will discuss these models in Sec. 2.4.2

[14]The commonplace existence of such subsurface oceans in icy moons was not widely accepted in literature at the time: see Sec. 1.1.

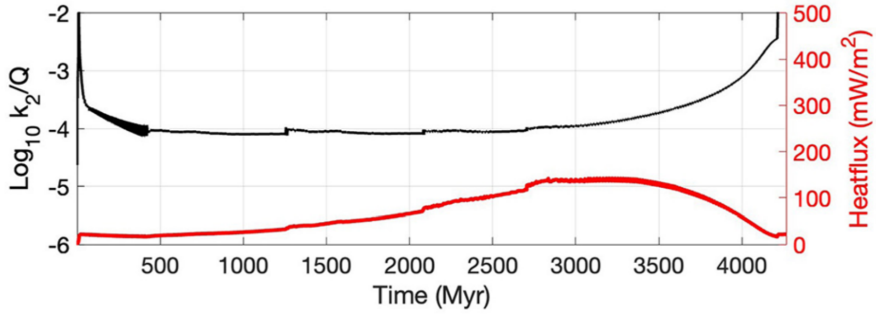

Figure 2.8: Heat flux and tidal quality function as function of time for a tidally circularising Triton not experiencing runaway melt, reprinted from Hammond & Collins (2024). Thinning of the ice shell precludes runaway melt as shown in Fig. 2.6, extending Triton's tidal evolution to $\gtrsim$ 3 Gyrs. The jumps visible in the graph are artefacts of the integration process used by Hammond & Collins (2024), not real phenomena.

Table 2.3: The circularisation timescale for Triton and whether runaway melting of the ice shell occurs for a selection of (thermal-)orbital models of Triton. References are as follows; RS90 (Ross & Schubert, 1990), MB88+ (McKinnon, 1988; McKinnon & Benner, 1990; McKinnon, 1992), M+95 (McKinnon et al., 1995), C09 (Correia, 2009), HC24 (Hammond & Collins, 2024), VW24 (Van Woerkom, 2024). Studies using the CPL- and/or CTL-derived equations of motion (EoM) are marked as such (see Sec. 2.2.2).

Work	Circ. timescale	Runaway?	Remarks
RS90	~ 1 Gyr	Yes	CPL EoM
MB88+	~ 0.1 – 0.5 Gyr	No	No publications beyond conference abstracts
M+95	~ 0.5 – 1.5 Gyr	Yes	CPL EoM
C09	~ 0.5 Gyr	N/A	Fixed Io-like interior, CTL EoM
HC24	~ 3.5 Gyr	No	Self-consistent interior-orbital evolution, CPL EoM
VW24	~ 10 Myr	N/A	Fixed Maxwell interior; simulates rotational state; includes higher tidal frequencies

not exactly analogous to the Neptune-Triton system, this does show that this damping effect is not necessarily inevitable when including thinning of the ice shell.

While the occurrence of thermal runaway like predicted by Ross & Schubert (1990) and McKinnon et al. (1995) can thus not be excluded with any certainty as of yet, it seems that a self-damping effect is more likely as the shell thins. The apparent stabilisation of the tidal quality function in model of Hammond & Collins (2024) makes it plausible that Triton will simply melt to the point that its tidal quality function is sufficiently low to reach a thermal equilibrium state of the ice shell, which would suggest that Triton's orbital energy is gradually dissipated over a long period of time, somewhere in between the > 3.5 Gyr they predict and the ~ 10 Myr predicted for a fixed interior by Van Woerkom (2024), rather than in a single runaway thermal event. As of yet, there is no consensus between these models, however: a summary of a selection of (thermal-)orbital models of Triton and their predictions on the circularisation timescale and the occurrence of runaway melt are given in Tab. 2.3. The coupling between the thermal and orbital models, as illustrated by Hammond & Collins (2024), will be instrumental in determining the true duration of this warm phase in Triton's history among these given estimates.

With this understanding of the thermal-orbital models that underpin the our current understanding of Triton's thermal-orbital history, we are now equipped to discuss the present understanding of Triton's history. As we have hitherto only alluded to this history broadly and loosely where necessary in the context of the models used to describe it, the object of Sec. 2.4 is to give a summary of the present status of our knowledge of Triton's past.

2.4. The present understanding of Triton's thermal-orbital history

Though we have established that previous models of Triton's evolution contain some known imperfections, we can now at the very least start compiling an overview of the present canonical understanding of Triton's history: the gaps or uncertainties we establish here can then inform the formulation of our research questions in Ch. 2.5. As the preceding chapter has discussed Triton's history only loosely and in the context of the models used to study it, in what follows we will briefly summarise the current understanding of Triton's formation (Sec. 2.4.1), its consequent capture by Neptune (Sec. 2.4.2), the circularisation phase that follows (Sec. 2.4.3) and finally its circularised evolution into the present day (Sec. 2.4.4). Finally, we will discuss some alternative histories that have been proposed for Triton, and why we think these may or may not hold merit, in Sec. 2.4.5.

2.4.1. Formation

As already briefly discussed in Sec. 2.1.2, what little knowledge we have of Triton is not consistent with it having formed around Neptune. With its retrograde orbit, relatively large mass (compared to Neptune) and particularly high density (McKinnon & Kirk, 2014), it seems unavoidable that Triton experienced some ancient cataclysm that sets it apart from other large satellites. The retrograde orbit of Triton had long been an enigma, and had already spurred Lyttleton (1936) to theorise on the anomalous conditions which could have brought Triton onto its present-day orbit from an initial formation around Neptune; McKinnon (1984) showed, however, that reversal of the sense of Triton's orbit by any presently-attested to Solar System object is dynamically forbidden (see Sec. 2.4.5 for alternative scenarios, however). Models predict that moons forming around ice giants are unlikely to be as massive as Triton (Canup & Ward, 2006; Szulágyi et al., 2018) and its density is far greater than other medium-sized icy moons and even Titan (Hussmann et al., 2006), when they should be comparable if the formation mechanisms and conditions of these objects were similar. The type of conditions thought to have caused the enhanced densities of the inner Galilean satellites (e.g. Bierson & Nimmo 2020; Mousis et al. 2023) are not applicable to early Neptune, and so can also not be responsible.

The true smoking gun is found in the presence of N_2 and particularly CO on Triton (McKinnon et al., 1995), which would have been reprocessed into NH_3 and CH_4 in the circumplanetary nebula of young giant planets (Prinn & Fegley, 1981). Instead, Triton's volatile budget is far more similar to that which is theorised of the solar nebula, or that which is observed in comets (McKinnon et al., 1995). The conclusion is then that, unlike the other satellites of the giant planets, Triton did not form in a circumplanetary nebula: rather, it formed in a heliocentric orbit, and was consequently captured (see Sec. 2.4.2).

Triton thus accreted in a solar orbit, as we will see shortly (Sec. 2.4.2) likely as part of a binary KBO, which are hypothesised to form through the streaming instability (Morbidelli & Nesvorný, 2020). Plausible formation locations therefore constrain proto-Triton to have been made of a CI chondrite-like material (Desch et al., 2018), which is additionally consistent with Triton's density and bulk composition (e.g. Cioria & Mitri 2022). Accretional energy and short-lived isotopes can have heated proto-Triton substantially (McKinnon et al., 1995; Hussmann et al., 2010); additionally, formation of binaries through the streaming instability can lead to high eccentricities (Nesvorný et al., 2010) which might have led to tidal action (and the accompanying heating) between proto-Triton and its binary companion, but analogy with the Pluto-Charon system as explored by Bagheri et al. (2022a) makes it plausible that Triton is relatively unaffected by this, particularly at the time of its capture (tidal heating would only dominate radiogenic heating for $\lesssim$ 1 kyr after formation). McKinnon et al. (1995) assume that proto-Triton would not have grown much hotter than $\sim$ 100 K on the basis of the relatively rapid pace at which a small body like Triton could have lost this heat, which should have led to an undifferentiated Triton at the time of capture. Analogy with Pluto (which is smaller than Triton), however, tells us that it is very unlikely that Triton was not in the process of ice-silicate differentiation, whatever the source of heating, even before capture (Stern et al., 2018; Bierson et al., 2020) (as discussed in Sec. 2.3.1). There is, however, no evidence that Pluto was sufficiently hot to start iron-silicate differentiation and form an iron core (Nimmo & McKinnon, 2021), though this need not be evidence of the absence of such a core. Evidence pointing toward the absence of such is a core is given by the fact that the substantially larger Titan (which should therefore have accreted hotter) is likely not to possess a substantial iron core, though its presence is not necessarily excluded by observations (Fortes, 2012). Its accretional circumstances are certain to have been significantly different from those forming proto-Triton, however.

While pre-capture proto-Triton is thus almost certain to have been sufficiently hot that ice had already differentiated from silicate, it cannot be said with any certainty whether its deep interior was also ever molten or not. We can therefore delineate two plausible extrema for proto-Triton's state immediately preceding capture: if Triton formed cold and was captured late, it will have been frozen solid but differentiated at least into an icy mantle atop a silicate interior. If, instead, it formed hot and was captured early, its icy shell will necessarily have been largely (if not entirely) molten, and its silicate interior may well also have been.

2.4.2. Capture

Some time after formation, Triton suffered an encounter with Neptune which saw it captured into orbit around the planet: when exactly this happened is not at present constrained, though an early capture ($\sim$ 4.5 Gyr ago) is generally accepted or assumed as the most plausible scenario (e.g. Correia 2009; Nogueira et al. 2011; McKinnon & Kirk 2014; Hammond & Collins 2024), as the number of Triton-sized objects in the Kuiper belt was orders of magnitude greater in the early Solar System (Vokrouhlickỳ et al., 2008; Nesvorný & Vokrouhlický, 2016). After McKinnon (1984) showed that Triton almost certainly did not form around Neptune, two main methods of capture were put forward: (1) capture by gas drag in a circumplanetary disc (e.g. McKinnon & Leith 1995), or (2) capture by collision with a primordial regular satellite of Neptune (e.g. Goldreich et al. 1989). McCord (1966) had also suggested a purely tidal capture of Triton was possible, but this requires significant fine-tuning of the conditions of capture that make it implausible.

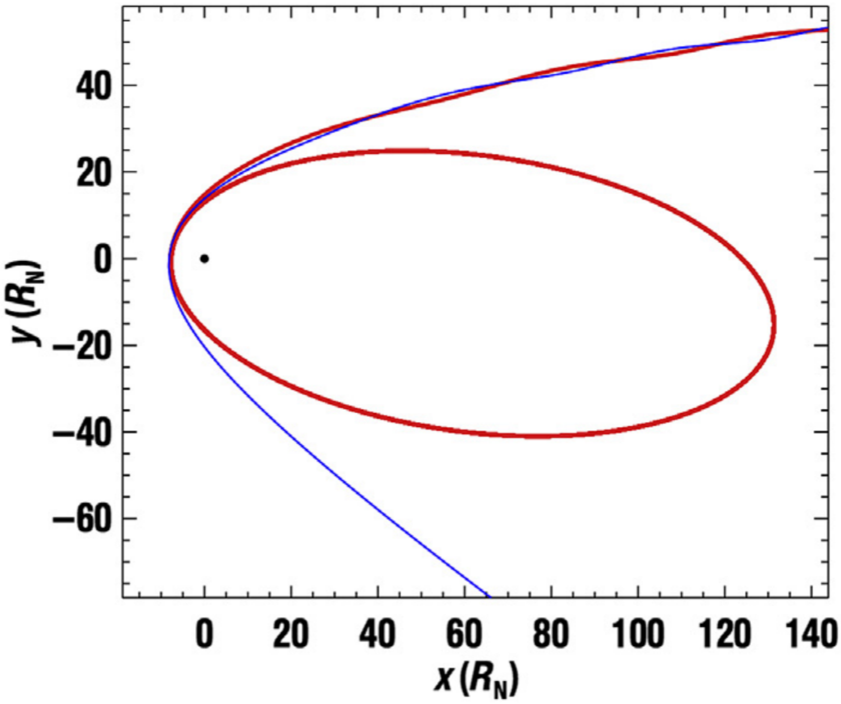

Figure 2.9: Example simulation of binary-exchange capture such as that which likely captured proto-Triton: one part of the binary-KBO pair (red) is captured around Neptune, while the other continues on a heliocentric orbit (blue). Reprinted from McKinnon & Kirk (2014), who adapted it from Agnor & Hamilton (2006).

Capture by gas drag and by collision were eventually understood to also be highly unlikely events, however, and as the Kuiper belt was eventually found to harbour a large number of binary objects, Agnor & Hamilton (2006) showed that exchange reactions with such objects, where a three-body interaction ejects one binary partner, leaving its sibling bound to a planet (e.g. Fig. 2.9), are much more likely to have originated Triton. This is especially likely in the early Solar System, as KBOs form largely if not entirely as pairs of multiples (Fraser et al., 2017): the fact that the dynamically hot[15] population of KBOs contains fewer binaries can be explained by dissociation of binaries by encounters with Neptune (see e.g. Morbidelli & Nesvorný 2020, Sec. 2.2), strengthening the idea that a large number of such objects experienced encounters with (proto-)Neptune in the past. Under such a mechanism, the probability of capture is greatest for binary systems with equal partners (Nogueira et al., 2011), in which case Triton will almost certainly obtain eccentricities $e \gtrsim 0.9$ (Vokrouhlickỳ et al., 2008). Even if Triton's binary partner was not of equal mass, Triton's capture will have set it on an orbit with $e \gtrsim 0.9$ in $\sim 90\%$ of cases; additionally, it is likely that Triton ends up on a retrograde and inclined orbit, like the one we find it on today (Nogueira et al., 2011). Such a scenario is therefore both plausible and commensurate with Triton's existence, its present-day orbit and its KBO-like appearance.

Once Triton is captured, Nogueira et al. (2011) find that Neptune's primordial satellite system should quickly have been swept from their initial orbits, either colliding with Neptune or being ejected from the system altogether within a couple ~ 10 kyr. Similar work by Rufu & Canup (2017) and Ćuk & Gladman (2005) found that Triton should have disrupted any pre-existing Neptunian satellite system interior to its orbit within a timespan of $\lesssim 1$ Myr and ~ 1 kyr, respectively. While they use this fact to propose non-tidal circularisation methods for Triton (collision and debris disc drag, respectively) such that Nereid could potentially be preserved on its present-day orbit throughout Triton's eventual circularisation, Nogueira et al. (2011) and Hammond & Collins (2024) propose a simpler explanation: Nereid could simply have been captured by Neptune onto its present-day orbit after Triton had already migrated sufficiently far inward (through tides) so as not to disrupt it. Such slow migration of Neptune (over timescales $\gtrsim 10$ Myr) is consistent with the observed inclination structure of the Kuiper belt (Nesvorný, 2015), and continued close Neptune-KBO encounters (during which Nereid might be captured) are required to explain the prevalence of KBOs on non-resonant orbits (Nesvorný & Vokrouhlický, 2016). While the premise of the argument by Ćuk & Gladman (2005) and Rufu & Canup (2017) is then essentially correct (Triton *would* have disrupted proto-Nereid on its present orbit), their conclusion does not follow: a Nereid-like object could instead have been captured later, and have migrated to its present-day orbit even under the influence of Triton.

[15] In this context, "hot" refers to their inclined orbits (e.g. Nesvorný 2015), not a thermal state.

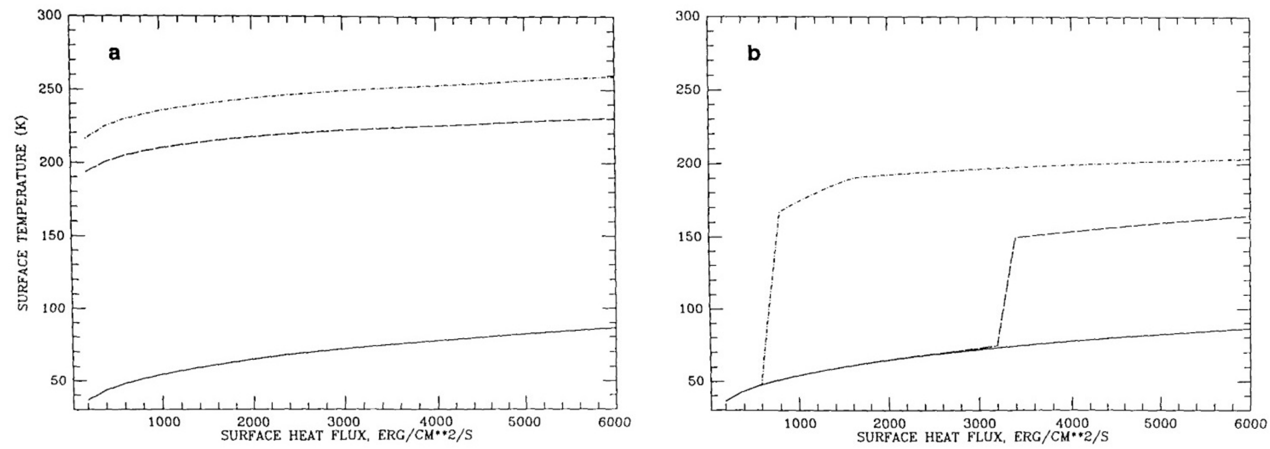

Figure 2.10: Surface temperature as a function of surface heat flux for various atmospheric compositions of a primordial atmosphere on early Triton with (a) 300 bar and 30 bar of CO and CH_4, respectively, available by outgassing and (b) 30 bar and 3 bar of CO and CH_4. The solid, dashed and dash-dot lines correspond to a constant hydrogen mixing ratio of 0.001%, 0.01% and 0.1%, respectively. Adapted from McKinnon et al. (1995), who (re)produced these results using the radiative methods described in Lunine & Nolan (1992). Note that these simulations incorporate solely atmospheric opacities due to collisions between CH_4, N_2, CO and H_2; at the high end of the considered temperature ranges, CO_2 and NH_3 would mobilise and provide significant additional infrared opacity.

After the proto-Neptunian satellites are disrupted or ejected, Triton will thus find itself by far the most massive object in orbit around Neptune (as it still is today; e.g. Barr 2016), on a highly eccentric, inclined and retrograde orbit, potentially heated by non-disruptive collision with one of Neptune's proto-satellites. Exactly what orbit Triton will be on is difficult to constrain without exact knowledge of the proto-Neptunian satellite system, which we will likely never have. Instead, this is where the contribution of this work will lay: we will have to constrain plausible scenarios from its present-day orbit, by accounting for Triton's initial circularisation (Sec. 2.4.3) and consequent evolution onto its present-day orbit (Sec. 2.4.4).

2.4.3. Circularisation

Satellites of non-negligible size (compared to their semi-major axis) on eccentric orbits are gravitationally perturbed by their host: consequently, their orbits shrink and their eccentricity is damped. Such orbital circularisation is certain to have occurred for Triton, as its present-day eccentricity is almost entirely negligible (e.g. Jacobson 2009; McKinnon & Kirk 2014) to a degree that cannot be explained by capture: in the simulations of Nogueira et al. (2011), only a negligible fraction of captured Tritons start at eccentricities $\lesssim 0.5$, and a negligible eccentricity requires sufficient fine-tuning so as to be, for all intents and purposes, impossible.

It is this epoch of circularisation that truly sets Triton apart from the other (large) satellites in the Solar System: during circularisation, Triton dissipates the majority of its orbital energy (evolution under the influence of the tides it raises in Neptune can plausibly only move Triton's orbit inward by $\lesssim 2R_N$ over $\sim$ 4.5 Gyr; see Van Woerkom 2024 or Sec. 2.4.4). Though McCord (1966) was seemingly the first person to consider a tidal capture origin for Triton, the first person to have realised the spectacular consequences of such an event seems to have been McKinnon (1984), as McCord (1966) seems to have misjudged the degree of heating this would impose upon the body. On the basis of a back-of-the-envelope calculation, McKinnon (1984) proposed that reasonable values for the tidal quality factor of Triton would result in full melting of the icy mantle of the moon over this evolutionary phase, unlike anything seen elsewhere in the Solar System.

Of course, the true degree of tidal heating depends on the timescales over which Triton is moved onto a circular orbit, as well as the interior model that is used for Triton. Existing estimates in literature, as we have extensively discussed in Sec. 2.3.3, vary substantially, and estimates for the circularisation timescale range from $\sim$ 10 Myr to $\sim$ 3.5 Gyr, though estimates including some degree of temperature-dependent tidal response tend to lean toward timescales of $\gtrsim$ 0.5 Gyr at the very least, even when including runaway melt (e.g. Ross & Schubert 1990; McKinnon et al. 1995; Hammond & Collins 2024). Even at such timescales, tidal heating seems to be a partially self-stabilising phenomenon in the models of Hammond & Collins (2024), giving rise to the existence of a substantial ocean over the duration of circularisation with ice shell thicknesses receding to $\lesssim$ 10 km.

Several phenomena might plausibly set Triton apart from other satellites over this period, even if no geological evidence thereof remains at present due to the moon's vigorous resurfacing. It is possible that other evidence of this epoch does remain, however: the existence of a warm subsurface ocean in contact with a silicate interior implies that hydrothermal processes are a very real possibility (e.g. Shock & McKinnon 1993). In the simulations of Hammond & Collins (2024), while appreciable (and well in excess of the surface heat outflow on the present-day continental Earth crust), the surface heat flow is not sufficient to raise a thick atmosphere like that suggested by Lunine & Nolan (1992) (unless Triton possessed a substantial primordial atmosphere of molecular hydrogen, or an excessive reservoir of CO and CH_4: see Fig. 2.10): the dynamical equations they use are likely to underestimate tidal heating significantly, however (Renaud et al., 2021), and so it does not seem unlikely that at least initially tidal heating may have been sufficiently severe that an atmosphere was raised. Even if the self-damping effect due to thinning of the ice shell described by Hammond & Collins (2024) is sufficient to counteract this, transitions between spin-orbit resonances can potentially excite heat fluxes sufficient to raise an atmosphere (Van Woerkom, 2024). Once an atmosphere is raised, it can be maintained even once tidal heating ceases (Lunine & Nolan, 1992). The resulting atmosphere will then serve as a thermal blanket, possibly further lengthening Triton's circularisation: additionally, a sufficiently thick atmosphere will suffer atmospheric escape, which Barr & Schwamb (2016) used to explain Triton's comparatively high density even for a KBO. We can thus identify two plausible avenues by which Triton's volatile inventory will have been altered throughout the process of circularisation: hydrothermal processing, and atmospheric escape. Indeed, surface volatiles on Triton, when compared to Pluto, appear to have been modified by some such process (Mandt et al., 2023). This might be an avenue by which the duration of Triton's circularisation can thus be established independently from orbital modelling in the future.

2.4.4. Evolution into the present

After this epoch of circularisation, whatever its duration, Triton is deposited onto an orbit close to its present-day one, though possibly slightly further out depending on the time of capture and duration of circularisation (see e.g. Van Woerkom 2024, Sec. 6.1): though eccentricity tides no longer dissipate orbital energy in Triton itself, its retrograde orbit with respect to Neptune's spin will raise a tidal bulge that slightly lags the moon in its orbit, leading it to be dragged toward its host slowly. Though Triton's ocean will start to thin, radiogenic heating keeps it from freezing over entirely (Nimmo & Spencer, 2015), and the ice shell will not thicken much beyond ~ 60 km (Hammond & Collins, 2024). If Triton ever possessed a substantial atmosphere, it will possibly outlast eccentricity tides by a couple ~ 100 Myrs (Lunine & Nolan, 1992), but then collapse and leave only its present thin atmosphere.

This does not mark the end for Triton's activity, however: indeed, geological activity continues into the present, as we have previously discussed in Sec. 2.1.2. Nimmo & Spencer (2015) blame this on tidal heating in Triton's ocean, driven by its obliquity: this obliquity is non-zero as Cassini states[16] generally have a non-zero obliquity for non-equatorial inclinations like that of Triton. Nimmo & Spencer (2015) posit that this tidal heating drives sufficiently intense convection that Triton's surface will start to yield. While this requires that Triton's ocean occupy a relatively narrow temperature range, they argue that convective yielding is a self-stabilising process through the NH_3-concentration in the ocean, such that Triton is driven towards this state. Hammond & Collins (2024), however, generally observe that convection ceases $\lesssim 50$ Myr after capture, though they do not include NH_3 in the ocean in the bulk of their simulations: regardless, their ocean temperatures and obliquity tidal heating fluxes would have resulted in convective yielding at the present according to the criteria of Nimmo & Spencer (2015), so the incongruency seems to be a difference in the parametrisation of convection used in either work. Absent convective yielding as a mechanism by which Triton's recent geological activity can be explained, Hammond & Collins (2024) explain its youthful surface either by the presence of a thick layer of fast-flowing ices, remnant of a now-collapsed thick atmosphere, or by over-pressurisation of Triton's ocean due to rapid thickening of the ice shell, which cracks the shell and enables cryovolcanic resurfacing on a global scale.

Whatever the case, all elements are apparently in place such that Triton's present-day orbit and appearance can be explained self-consistently, starting from its formation. Yet, some uncertainties remain: before formulating these uncertainties in Ch. 2.5, we will briefly comment on some alternative evolutionary histories that have been proposed for Triton.

2.4.5. Alternative evolutionary histories

Though a consistent pathway for Triton to end up on its present orbit with its present features is thus available, it is premature to exclude other histories entirely. Indeed, such thinking has led to incorrect assumptions on Triton's evolution in the past: before Agnor & Hamilton (2006) described the binary exchange process that we have now adopted as the most plausible progenitor process, the dominant theories for Triton's capture were capture by disc drag and collision (see Sec. 2.4.2), for example. We will therefore briefly examine other evolutionary histories that have been proposed for Triton (besides those already discussed and discounted previously), and discuss why we reject them in this work.

One possible scenario that has been raised multiple times in literature starts with the hypothesis put forward by Lyttleton (1936), that Triton and Pluto originated as direct satellites of Neptune, disrupted by some dynamical

[16]Cassini states are the stable equilibrium rotational states that a satellite can occupy (e.g. Jankowski et al. 1989).

event. Apparently pre-empting the conclusion of McKinnon (1984) that such a scenario is impossible without intervention of some third extra-Neptunian interloper, Harrington & Van Flandern (1979) proposed that this might have been the result of an encounter with a $\sim 3M_\oplus$-planet, rejecting the capture hypothesis on the basis of a supposed upper limit on Neptune's tidal quality factor of 10^3 derived by McCord (1966). Farinella et al. (1980) (who had previously discussed the capture hypothesis for Triton; Farinella et al. 1979) point out, however, that their rejection of the capture hypothesis rests on a misunderstanding of the work of McCord (1966): it was not the tidal quality factor of Neptune that he constrained to be less than 10^3, but Triton's, a far more reasonable constraint. There was no need to reject the capture hypothesis, and consequently, no need to invoke some unattested additional planet to have come and reversed Triton's initially prograde orbit.

Nonetheless, the introduction of the five-planet Nice model[17] saw the idea of orbit reversal by an encounter with a now-gone planet reintroduced (Li & Christou, 2020), as well as the idea of Triton having formed in orbit around this other planet before being captured by Neptune in a similar encounter (Li et al., 2020). These scenarios suffer several issues, however, in which we will echo the critique Farinella et al. (1980) levied against Harrington & Van Flandern (1979): (1) they require the existence of and an encounter with some unobserved body, and (2) Neptune's orbital eccentricity is not suggestive of any past close encounters with sufficiently massive objects. With our present body of knowledge, we can add to this the fact that the compositions of Triton and Pluto are not compatible with formation in a circumplanetary disc (see Secs. 2.1.2, 2.4.1), and that a theory explaining the formation of KBOs and Neptune-resonant objects like the Plutinos is now well-developed (e.g. Morbidelli & Nesvorný 2020), meaning that Pluto's existence and orbit need no further explaining.

More recent work by Gomes & Morbidelli (2024) explored the idea of formation of retrograde Triton from an initially prograde orbit by two finely tuned successive collisions of Neptune with planetary embryos, in efforts to explain the retention of Nereid on its present orbit (see Sec. 2.4.2 for a discussion hereof in the context of the capture scenario): here, too, we can cite Triton's KBO-like composition as a counter-argument, but we additionally note that Gomes & Morbidelli (2024) do not provide a mechanism by which this would retain Neptune's inner regular satellites, or at the very least produce a prograde debris disc from which they may eventually re-accrete.

Discounting the idea of circumplanetary formation, then, we point our attention at the capture hypothesis again: as alluded to previously, even the timeline of the capture hypothesis is not a certainty. Previous work has explored the idea of capture by drag due to a disc of debris, rather than binary exchange (e.g. Ćuk & Gladman 2005). While this idea is natural, as Triton's disruption of any proto-satellite system of Neptune would plausibly have resulted in the presence of such a disc, Rufu & Canup (2017) showed that the re-accretion timescale of Neptune's inner satellites is simply too fast for this to effectively capture Triton.

Rufu & Canup (2017) instead propose rapid (near-)circularisation and shrinking of Triton's orbit by collision with one of Neptune's proto-satellites, so as to preserve Nereid. As discussed in Sec. 2.4.2, this is not a necessary feature of Triton's capture. While we can take the results of Rufu & Canup (2017) to indicate that non-disruptive collisions between Triton and one or more primordial satellites of Neptune may plausibly have occurred, this need not indicate, therefore, that these necessarily happened, so as to put it onto an orbit interior to Nereid's. Even if it did, high-eccentricity tidal evolution must still follow to place Triton onto its present orbit, and the history discussed previously does not change. Capture by collision alone (without binary exchange) is severely less likely to happen than capture through binary exchange (McKinnon & Kirk 2014; of course, this does not exclude binary exchange *followed by* collision with a primordial satellite), and so while strictly speaking possible, it is unlikely that this happened, especially as such a collision would be more likely to disrupt Triton than capture it.

2.5. Open questions in Triton's thermal-orbital history

We have now discussed the scientific background in which we wish to investigate Triton: the major scientific impetus for investigating the behaviour of captured icy moons like Triton (Ch. 1) and the observational history of and constraints on the moon (Sec. 2.1). We have additionally discussed thermal (Sec. 2.2.1) and dynamical (Sec. 2.2.2) modelling of planetary bodies, how these are coupled (Sec. 2.2.3) and in each case what such models already exist for Triton (Sec. 2.3). Finally, we have detailed the present understanding of Triton's evolutionary history (Sec. 2.4). With this, we are now equipped to formulate the gaps in our scientific understanding of Triton we wish to fill. To start off with, we formulate an overarching question:

> **What are the thermal-interior and dynamical consequences of the process of capture and high-eccentricity tidal circularisation on an icy moon like Triton?**

[17] The five-planet Nice model is a variant of the Nice model of the migration of the giant planets, where an additional ice giant formed in the Solar System, but was ejected or deposited on a long-period, presently unobserved orbit during planetary migration (e.g. Nesvorný 2011; Roig & Nesvorný 2015).

In this phrasing, we would like to emphasise the role of Triton as the subject of a case study: though we have argued in Sec. 2.4.5 why we think the presented history of Triton is most plausible, it is likely that we can never truly be certain of the process of capture and the manner in which it proceeded. In discussing and simulating Triton's evolution, however, we may surely be able to establish some generalities about or expectations on the process of capture of Triton-like bodies in exoplanetary systems.

To establish a satisfactory answer to this first question, we formulate a set of subsidiary questions (which we divide into sub-questions in turn where appropriate). These are as follows:

1. **What are the consequences of different modelling approaches to Triton's orbital-interior evolution?**
   (a) **Are simplified expressions acceptable for computation of its high-eccentricity evolution?**
   (b) **What forcing frequency ranges shape the tidal evolution of circularising Triton?**
2. **How did capture affect Triton's thermal-interior state?**
   (a) **Did capture set on the development of a core?**
   (b) **Could early Triton have possessed a substantial atmosphere?**
   (c) **How far did Triton's primordial ocean extend?**
3. **What does the process of Triton's capture look like?**
   (a) **Will partially-molten Triton undergo spin-orbit resonances?**
   (b) **Would capture of exo-Tritons be observable in exoplanetary systems?**
4. **Do any constraints on Triton's capture and history remain into the present?**
   (a) **Could geological or geochemical evidence of Triton's capture remain?**
   (b) **Does the evolution of Triton affect its current ocean thickness?**

Questions 1 and 2 will dictate the factors that need to go into our models, and how complex these will need to be: nonetheless, some of the answers that arise there are already scientifically interesting. More interesting, however, are the answers to questions 3 and 4: answering question 3 will give us fundamental insights into the history of Triton and the process of capture of dwarf planets, while question 4 will allow us to prescribe requirements for any future mission headed toward the moon.

3 Methods

To describe the structure of our model by which we set out to answer the open questions posed in Ch. 2, we will recall the three model components identified in Fig. 2.3. Our model, and consequently the description thereof, is setup in accordance with this outline: we have implemented a dynamical model and a thermal-interior model, and coupled them by the use of a deformation model. We will describe the expressions we use to propagate Triton's dynamical evolution in Sec. 3.1, and follow those up with a description of our interior-evolution model in Sec. 3.2. We will describe the expressions used to compute the tidal response of Triton (which couple the interior to the dynamical evolution) in Sec. 3.3.

Of course, mathematical expressions do not solve themselves, and so we express the design of our integration and propagation algorithm in Sec. 3.4. Finally, we motivate and describe the setup of our numerical experiments in Sec. 3.5.

3.1. Dynamical evolution: Darwin-Kaula theory

Our dynamical evolution of Triton consists of two components; the expressions we use for the general dynamical evolution of Triton's orbital elements over astronomical timescales are given in Sec. 3.1.1. As the rotational rate evolves over much shorter timescales, we compute its evolution under the assumption of rotational equilibrium once it has reached an equilibrium state: this process is described in Sec. 3.1.2.

3.1.1. The Lagrange planetary equations for a tidally perturbed body

Though the development of the dynamical part of our model so as to allow it to handle the high eccentricities found for early Triton was the subject of previous work (Van Woerkom, 2024), we repeat the expressions governing the dynamical evolution of the Neptune-Triton system averaged over the fast angles[1] here for convenience (see Van Woerkom, 2024, and references therein):

$$\left\langle \frac{\mathrm{d}a}{\mathrm{d}t} \right\rangle = 2na\left(\frac{M_N}{M_T}\left\langle \frac{\partial U_T}{\partial \mathcal{M}} \right\rangle + \frac{M_T}{M_N}\left\langle \frac{\partial U_N}{\partial \mathcal{M}} \right\rangle \right) \tag{3.1}$$

$$\begin{aligned}\left\langle \frac{\mathrm{d}e}{\mathrm{d}t} \right\rangle = n\frac{\sqrt{1-e^2}}{e}\Bigg[&\sqrt{1-e^2}\left(\frac{M_N}{M_T}\left\langle \frac{\partial U_T}{\partial \mathcal{M}} \right\rangle + \frac{M_T}{M_N}\left\langle \frac{\partial U_N}{\partial \mathcal{M}} \right\rangle \right) \\ &- \left(\frac{M_T}{M_N}\left\langle \frac{\partial U_N}{\partial \varpi_N} \right\rangle + \frac{M_N}{M_T}\left\langle \frac{\partial U_T}{\partial \varpi_T} \right\rangle \right) \Bigg]\end{aligned} \tag{3.2}$$

$$\begin{aligned}\sin i_j \left\langle \frac{\mathrm{d}i_j}{\mathrm{d}t} \right\rangle = \frac{M_k}{M_j}\Bigg[&\frac{\mathcal{G}M_jM_k}{a\tilde{C}_j\dot{\theta}_j}\left(\left\langle \frac{\partial U_j}{\partial \varpi_j} \right\rangle - \cos i_j \left\langle \frac{\partial U_j}{\partial \Omega_j} \right\rangle \right) \\ &- \frac{n}{\sqrt{1-e^2}}\left(\left\langle \frac{\partial U_j}{\partial \Omega_j} \right\rangle - \cos i_j \left\langle \frac{\partial U_j}{\partial \varpi_j} \right\rangle \right) \Bigg]\end{aligned} \tag{3.3}$$

$$\left\langle \frac{\mathrm{d}\dot{\theta}_j}{\mathrm{d}t} \right\rangle = -\frac{\mathcal{G}M_k^2}{a\tilde{C}_j}\left\langle \frac{\partial U_j}{\partial \Omega_j} \right\rangle \tag{3.4}$$

where a is the semi-major axis of the mutual orbit, e is its eccentricity, i is the obliquity of an object with respect to the mutual orbit[2], $\dot{\theta}$ is the sidereal rotation rate of an object, n is the mean motion of the orbit, $\tilde{C}$ is the moment of inertia of a body, M is the mass of a body, $\mathcal{M}$ is the mean anomaly of a body, ϖ is the argument of pericentre (with the subscript denoting from which body's equator it is measured), Ω is the longitude of the ascending node (with the subscript again denoting the reference body), and $\mathcal{G}$ is the gravitational constant. The subscripts j and k denote a body and its tidal partner, respectively, as in Renaud et al. (2021), and we will use the subscripts T and N to denote Triton and Neptune in this context. The notation $\langle\cdot\rangle$ denotes an averaging over the

[1] By "fast angles" we mean the mean motion, argument of pericentre, and longitude of the ascending node; these quantities evolve over much shorter timescales than the semi-major axis, eccentricity and inclination of the orbit. Over astronomical timescales, it is therefore chiefly the evolution of the latter quantities that is important, especially as their variation is consequently responsible for the (variation of) tidal energy dissipated in a body. While the rotational rate of a body varies on equally short timescales, its evolution between various resonances is interesting to investigate, and its behaviour is not quasi-periodic like the other fast angles; hence, we track it as well.

[2] In this definition, which is admittedly non-standard in astrodynamics, we follow the terminology used by Kaula (1964) and Boué & Efroimsky (2019). Confusingly, the inclination i_N then refers to the obliquity of Neptune with respect to the mutual Triton-Neptune orbit, which is equal to the conventional orbital inclination, while i_T refers to the obliquity of Triton with respect to the orbit, which we will assume to be negligible.

fast angles, which amounts to a disposing of the terms periodic in the mean anomaly, argument of pericentre and longitude of the ascending node in the Darwin-Kaula expansion for the tidal potential. These expressions, often referred to as the Lagrange planetary equations, give the evolution of the Keplerian elements of a body on an orbit perturbed by the tidal potentials U_T and U_N; here, U_j is the tidal potential of a body j, made positive and dimensionless according to the convention used by Luna et al. (2020):

$$U_j = -\frac{a}{\mathcal{G}M_k}\tilde{U}_j \tag{3.5}$$

where $\tilde{U}_j$ is the usual additional tidal potential (e.g. Eq. 134 in Boué & Efroimsky, 2019). Note that Eqs. 3.1-3.4 implicitly assume that we neglect whatever triaxiality Neptune and Triton have (cf. Luna et al., 2020). To circumvent numerical instabilities that arise in this context, we employ the following substitutions in our numerical implementation of Eqs. 3.1-3.4:

$$x_j = \cos i_j \tag{3.6}$$

$$\xi = \sqrt{1-e^2} \tag{3.7}$$

though we will prefer to discuss matters in terms of the more familiar variables e and i_j.

The derivatives of the potentials U_j as well as the orbital energy dissipated in a body, $\dot{E}$, are given by the following Fourier expansion developed by Darwin (1879, 1880) and Kaula (1961, 1964), which we will refer to as the *Darwin-Kaula expansion*[3] (Renaud et al., 2021):

$$\begin{bmatrix} \partial U_j/\partial\mathcal{M} \\ \partial U_j/\partial\varpi_j \\ \partial U_j/\partial\Omega_j \\ \dot{E}_j \end{bmatrix} = -\sum_{l\geq 2}\left(\frac{R_j}{a}\right)^{2l+1}\sum_{m=0}^{l}\frac{(l-m)!}{(l+m)!}(2-\delta_{0m})\sum_{p=0}^{l}F^2_{lmp}(i_j)$$
$$\times \sum_{q=-\infty}^{\infty} G^2_{lpq}(e)K_{l,j}(\omega_{j,lmpq})\begin{bmatrix} l-2p+q \\ l-2p \\ m \\ -\omega_{j,lmpq}n^2a^2\beta M_k/M_j \end{bmatrix} \tag{3.8}$$

where we have dropped the time-averaged notation for convenience. In this expression, δ_{ij} is the Kronecker delta, $F_{lmp}(i)$ and $G_{lpq}(e)$ are respectively the inclination and eccentricity functions, which we define as in Kaula (1961), and $\beta = \frac{M_T M_N}{M_N+M_T}$ is the reduced mass. Both the computation of $F_{lmp}(i)$ and $G_{lpq}(e)$ and the determination of the values of the index q to include in a truncated version of this expression as a function of e are elaborated upon in Van Woerkom (2024), and will not be discussed here; it is important to note, though, that it is precisely those quantities in which the difficulties of high-eccentricity evolution arise. Consequently, we generate an interpolant for the eccentricity functions up to $e \approx 0.97$ using the tools of Van Woerkom (2024), which corresponds to roughly the median eccentricity found for a post-capture Triton by Nogueira et al. (2011): while this means our analysis is limited only to those eccentricities, we find no reason by which to expect that the results we find change at higher eccentricities.

Finally, the Fourier modes ω_{lmpq} at which the tidal quality function $K_l(\omega)$ is evaluated are approximated[4] as:

$$\omega_{lmpq} = (l-2p+q)n - m\dot{\theta}. \tag{3.9}$$

The use in Eq. 3.8 is in decomposing the tidal evolution of a body through Eqs. 3.1-3.4 into components attributable to the tidal response evaluated at a number of discrete frequencies (given by Eq. 3.9), $K_{l,T}(\omega_{T,lmpq})$. We will therefore often refer to this effect as the Darwin-Kaula expansion "sampling" the tidal quality function.

We will make the following simplifying assumptions:

- We neglect the tidal deformation of Neptune, i.e. we set $U_N = 0$.
- We assume that the obliquity $i_T = 0$, which effectively means that we neglect any triaxiality of Triton and that we assume its spin is damped to its equilibrium position: we justify this assumption in Sec. 3.1.2.
- We neglect the contribution of spherical harmonic degrees greater than $l = 2$, as higher degrees do not affect the dynamical evolution of Triton much (Van Woerkom, 2024).

[3]Formally, the Darwin-Kaula expansion refers solely to a particular expression for the time-averaged perturbed tidal potential, which we give explicitly in App. D. In passing use, we find it more convenient to refer to these products derived from the Darwin-Kaula expansion as such as well.

[4]See Boué & Efroimsky (2019) for the full expression, and Van Woerkom (2024, Sec. 3.2) for a discussion of the consequences of this approximation.

- We neglect tidal heating (and friction) in the ocean. At early times this is justified, but obliquity tides are thought to be important following Triton's circularisation (e.g. Nimmo & Spencer, 2015).

The first of these means that we will from now on drop the subscript T in the tidal quality function $K_{l,T}$, denoting the tidal quality function of Triton by K_l and the associated tidal mode by ω_{lmpq}. The first and second amount to a simplification to the equations of motion (Eqs. 3.1-3.4), such that the dynamics are now fully described by:

$$\left\langle \frac{\mathrm{d}a}{\mathrm{d}t} \right\rangle = 2na\frac{M_N}{M_T}\left\langle \frac{\partial U_T}{\partial \mathcal{M}} \right\rangle \tag{3.10}$$

$$\left\langle \frac{\mathrm{d}e}{\mathrm{d}t} \right\rangle = n\frac{\sqrt{1-e^2}}{e}\frac{M_N}{M_T}\left[\sqrt{1-e^2}\left\langle \frac{\partial U_T}{\partial \mathcal{M}} \right\rangle - \left\langle \frac{\partial U_T}{\partial \varpi_T} \right\rangle\right] \tag{3.11}$$

$$\left\langle \frac{\mathrm{d}\dot{\theta}_T}{\mathrm{d}t} \right\rangle = -\frac{\mathcal{G}M_N^2}{a\tilde{C}_T}\left\langle \frac{\partial U_T}{\partial \Omega_T} \right\rangle \tag{3.12}$$

Finally, in our implementation, we wish to avoid a costly numerical integration of the rapidly-varying rotational rate (whose timescale of variation is far shorter than that of the other values), which would prohibit the adaptive step-size integrator we use from lengthening its timestep to useful lengths. Hence, we adopt an approach similar to Walterová & Běhounková (2020): we evolve Triton's initial spin rate by direct propagation using Eq. 3.4 until it reaches an equilibrium state, and assume that Triton is thereafter continuously in a state of rotational equilibrium, and take its rotational rate to always be equal to its equilibrium value instead. As the equilibrium state can (and often does) occur at a rotational acceleration that is small but non-negligible, we will take the rotational state to be in equilibrium whenever:

$$\left|\frac{\mathrm{d}(\dot{\theta}/n)}{\mathrm{d}t}\right| \leq 0.01/\mathrm{kyr} \tag{3.13}$$

Previous work found that Triton takes only ~Myrs to reach an equilibrium rotational state at most (Van Woerkom, 2024), and afterwards stabilises on ~kyr timescales, justifying this assumption. Efficiently computing the value of the equilibrium rotational rate at each timestep requires particular consideration, however.

3.1.2. Computing the equilibrium rotation rate

As stated previously, the rotational rate varies on timescales much faster than the other quantities we would like to track. To avoid having to explicitly compute through numerical integration the evolution of the rotational rate, we will rather assume the rotational rate to always take its equilibrium value after it first reaches equilibrium.

To achieve this in an efficient manner, we (re)introduce several simplifying assumptions. As we assume no triaxiality for Triton implicitly in using Eqs. 3.1-3.4, the stable equilibrium state of the obliquity of Triton is $i_T = 0$, and even for moderate values of Triton's triaxiality its true stable rotation state yields $i_T \sim 0$ (Correia, 2009, and references therein); hence, we assume that Triton has an obliquity $i_T = 0$ at all times. The $l = 2$-contribution to Triton's rotational evolution is by far most influential, and the error introduced by neglecting of higher-degree terms mostly serves to move spin-orbit transitions back- or forward in time by kyrs or less (Van Woerkom, 2024), and so we neglect terms corresponding to $l > 2$ (not just in the rotational rate, but in all dynamics). To $\mathcal{O}(i^2)$ the only non-zero squares of the inclination functions $F_{lmp}(i)$ for $l = 2$ are those corresponding to $(lmp) = (201), (220)$ (Gooding & Wagner, 2008; Luna et al., 2020), and the factor of m in the expression for $\frac{\partial U_j}{\partial \Omega_j}$ in Eq. 3.8 eliminates all terms belonging to $(lmp) = (201)$. Consequently, only the value $F_{220}^2(i)$ remains, for which we take its value at $i_T = 0$ ($F_{220}^2(0) = 9$). The rotational acceleration of Triton can then be written in a particularly simple form (cf. Luna et al., 2020, Eq. 55a):

$$\left\langle \frac{\mathrm{d}\dot{\theta}_T}{\mathrm{d}t} \right\rangle = \frac{3}{2}\frac{\mathcal{G}M_N^2}{aC_TM_TR_T^2}\left(\frac{R_T}{a}\right)^5 \sum_{q=-\infty}^{+\infty} G_{20q}^2(e)K_{2,T}((2+q)n - 2\dot{\theta}_T) \tag{3.14}$$

where $C = \frac{\tilde{C}}{MR^2}$ is the moment of inertia-factor of a body. Finding the (time-averaged) equilibrium rotation rate in a given state then requires solving Eq. 3.14 for $\left\langle \frac{\mathrm{d}\dot{\theta}_T}{\mathrm{d}t} \right\rangle = 0$. It is possible that multiple solutions exist: in that case, the "true" equilibrium rotation rate is the one accessible from its last calculated rotation rate, which generally tends to simply be the fastest stable equilibrium rotation rate[5]. We avoid explicitly having to make this

[5]The initial rotation rate for Triton, unknown but best estimated by the rotation rates of binary KBOs, will likely have been significantly in excess of its initial mean motion (Perna et al., 2009; Thirouin et al., 2014); consequently, it is most plausible that Triton "cascaded" through spin-orbit resonances starting from the fastest stable one, and dropping down to the next-fastest available one as the top one becomes unstable.

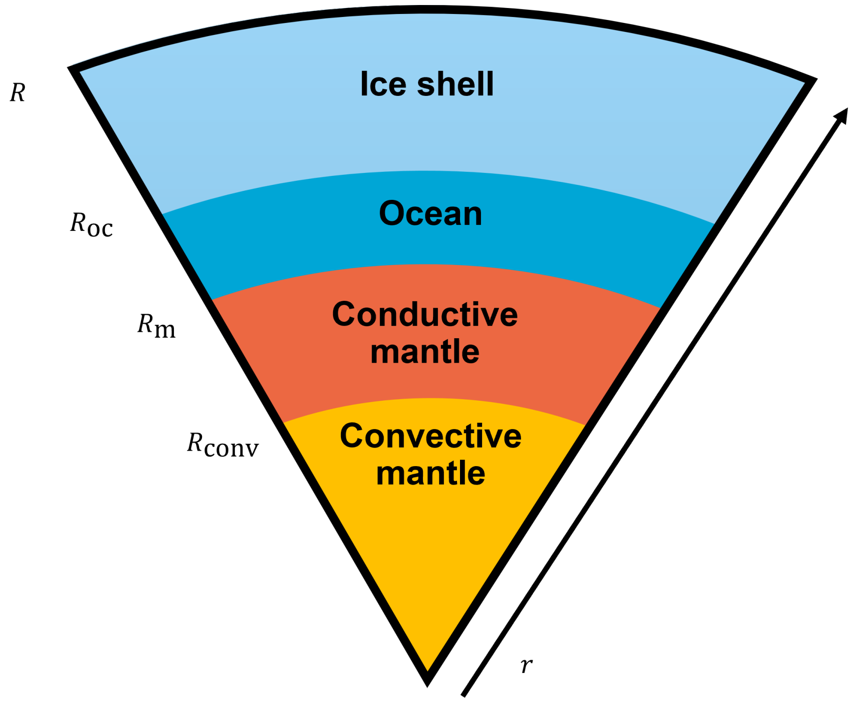

Figure 3.1: Terminology and definitions of the conventions we use for the naming of layers and the transitions between them.

assumption by, at each timestep, starting Triton on its previous rotation rate, and propagating Eq. 3.14 forward keeping all values but $\dot{\theta}_T$ constant (see e.g. Walterová & Běhounková 2020 for a similar approach). The stable value of $\dot{\theta}_T$ in which it settles provides the equilibrium rotation rate in the given state; the time it took for $\dot{\theta}_T$ to reach this state provides a natural a posteriori-verification of the rotational equilibrium assumption.

3.2. Describing the interior structure and evolution of Triton

With the dynamical evolution out of the way, let us move on to our description of the interior structure and evolution of Triton. As several different terms are in use throughout literature, we introduce the terminology we will use to describe the ice, water and silicate layers on Triton in Fig. 3.1. We will first introduce the conductive heat equation in Sec. 3.2.1 as well as the corresponding radiogenic heating term in Sec. 3.2.2, and we then describe how we apply the conductive heat equation to the shell and the conductive part of the mantle in Secs. 3.2.3 and 3.2.4, respectively. We finally describe our mantle convection model in Sec. 3.2.5.

3.2.1. The conductive heat equation

Thermal evolution in the conductive part of the mantle and in the shell is described through the time-dependent heat equation in spherical coordinates (assuming spherical symmetry; Carslaw & Jaeger 1959):

$$\rho C \frac{\partial T}{\partial t} = \frac{1}{r^2} \frac{\partial}{\partial r} \left(r^2 k(t, r, T) \frac{\partial T}{\partial r} \right) + f(t, r, \mathbf{x}) \tag{3.15}$$

where r is the radial coordinate, t time, k the thermal conductivity (though we will assume it to be an explicit function of temperature T only, and an implicit function of r by changing k between layers, our implementation allows use of time- and location-dependent conductivities), ρ is the density of the layer, C is the specific heat of the layer, and $f(t, r, \mathbf{x})$ is a source term encompassing radiogenic and tidal heating, but also possibly other matters such as energy necessary for or released by phase changes if so desired. The notation $\mathbf{x}$ simply expresses that f can depend on the full state (i.e. also the orbital parameters), not just the interior values described by the heat equation: whereas we assume homogeneous dissipation in the mantle, our code is designed to work for arbitrary dissipation profiles. We use the radiogenic heating rates for CI chondrite of Hussmann et al. (2010), and will evaluate the sensitivity of our analysis to this particular choice in Sec. 4.2.1. The possibility of heating by short-lived isotopes such as ^{26}Al is accounted for by varying the initial temperature profile, though we note that KBOs are generally believed to have formed late (Bierson & Nimmo, 2019; Morbidelli & Nesvorný, 2020), therefore not suffering heating by short-lived isotopes.

To avoid having to estimate the numerical derivative of a numerical derivative, we expand the partial derivative

Table 3.1: Half-lifes τ_i, isotopic abundances c_i, CI-chondrite elemental abundances C_i and specific radiogenic heating rates H_i for the four long-lived radioisotopes ^{238}U, ^{235}U, ^{232}Th and ^{40}K. Adapted from Tabs. 3 and 4 of Hussmann et al. (2010).

i	Isotope	τ_i [Gyr]	c_i [-]	C_i $\left[10^{-9}\right]$	H_i [μW kg^{-1}]
1	^{238}U	4.468	0.992745	8	94.8
2	^{235}U	0.7038	0.0072	8	569
3	^{232}Th	14.05	1.0	29	26.9
4	^{40}K	1.277	0.000117	0.550	29.2

in r:

$$\rho C \frac{\partial T}{\partial t} = k(t,r,T)\frac{\partial^2 T}{\partial r^2} + \left[\frac{2k(t,r,T)}{r} + \frac{\partial k}{\partial r} + \frac{\partial k}{\partial T}\frac{\partial T}{\partial r}\right]\frac{\partial T}{\partial r} + f(t,r,\mathbf{x}) \tag{3.16}$$

and implement the numerical version using this expression; by limiting ourselves to profiles of k expressible analytically in terms of r and T, there is no need to numerically approximate the partial derivatives $\frac{\partial k}{\partial r}$ and $\frac{\partial k}{\partial T}$. In the mantle, we discretise Eq. 3.16 using a grid of values along the radius of Triton, and estimate the derivatives $\frac{\partial T}{\partial r}$ and $\frac{\partial^2 T}{\partial r^2}$ using a 6th-order finite difference scheme described in App. A.1; in the shell, we find that an equilibrium profile suffices for the purposes of this work. We will briefly discuss the implementation of both of these components of the interior model in Secs. 3.2.3 and 3.2.4: first, we will give a brief overview of our radiogenic heating model in Sec. 3.2.2.

3.2.2. Radiogenic heating

The source term f in Eq. 3.16 comprises two components that we account for: radiogenic heating and tidal dissipation. The latter also requires that we construct a deformation model for Triton, and so we introduce that model component in more detail in 3.3. We do not account for radiogenic species leaching into the ocean, and therefore assume all radiogenic heating happens in the silicate mantle. We compute the volumetric[6] radiogenic heating rate H_{rg} as a function of time accounting for the abundances of the long-lived isotopes ^{238}U, ^{235}U, ^{232}Th and ^{40}K appropriate for CI-chondrite (Hussmann et al., 2010, and references therein):

$$H_{\mathrm{rg}}(t) = \rho \sum_{i=1}^{4} c_i C_i H_i \exp\left(-\frac{\ln 2}{\tau_i}(t - t_{\mathrm{pr}})\right) \tag{3.17}$$

where c_i is the present abundance for a radioisotope as fraction of all isotopes of the species, C_i is the elemental abundance of a species i for CI-chondrite, H_i is the specific radiogenic heating rate for a radioisotope i and τ_i is the corresponding half-life; the values of each of these for the four radioisotopes we account for are given in Tab. 3.1. t_{pr} is the present time since CAI (calcium-aluminium rich inclusions, the formation of which is commonly used to date the formation of the Solar System, and which forms the datum for our time coordinate), for which we use a value of t_{pr} = 4.5687 Gyr following Piralla et al. (2023).

3.2.3. Thermal evolution of the shell

We assume that the shell is always conductive, though the validity of this assumption depends on the shell thicknesses and thermal structures encountered by Triton's shell (cf. Sec. 3.2.5). Correspondingly, no consensus exists in literature on the (continued) presence of shell convection or not: Hammond & Collins (2024) find that shell convection only happens initially, but quickly ceases once the shell thins sufficiently; however, Nimmo & Spencer (2015) propose that convection is still happening at present as a result of obliquity tides. We assess the applicability of this assumption in further detail in Sec. 7.2.3, and leave the proper treatment of ice shell convection for future work. In Sec. C.2.2 we show that Triton's shell is well-described by an equilibrium conductive profile, and so we will derive the equation describing the equilibrium conductive shell profile for a shell with temperature-dependent conductivity[7]: to fix this profile, we need two boundary conditions, however. These are given by two conditions: (1) the transfer of heat between a conductive shell and a well-mixed ocean, and (2) surface radiation according to a grey-body radiation law. We will treat the equations describing each of these in order before moving on to the equilibrium conductive profile.

Boundary conditions for a grey-body radiating conductive shell in contact with an ocean

We assume, conservatively, that an ocean forms whenever the temperature at the shell-mantle interface exceeds 273 K, neglecting solidus-suppressing impurities or the pressure-dependence of the melting point. The net

[6] As Eq. 3.16 is written in terms of a volumetric energy balance.

[7] To do so, we also derive boundary conditions for the time-dependent, discretised thermal evolution of the shell. These are given in Sec. A.3 for completeness.

effects of such impurities (commonly modelled using ammonia) will be to suppress the melting point of water, and also to increase the pressure at which high-pressure ices form (Leliwa-Kopystyński et al., 2002; Choukroun & Grasset, 2007, 2010); see e.g. Bagheri et al. 2022a for the possible planetological consequences of such impurities. At increasing pressures the melting temperature of water generally lowers, such that neglecting this effect is also conservative (Choukroun & Grasset, 2007, 2010).

Rather than explicitly modelling the thermal and chemical evolution of and heat transport through the ocean, we will assume that the ocean is well-mixed, and that the pressure difference is sufficiently little that the adiabatic temperature gradient between top and bottom is negligible. Consequently, the ocean is kept uniformly at its melting temperature of 273 K, and so this provides (Dirichlet) boundary conditions for the temperature at the top of the mantle and the bottom of the shell:

$$T(R_m) = T(R_{\mathrm{oc}}) = T_{\mathrm{melt}} \tag{3.18}$$

As high-pressure ices only form at pressures in excess of $\sim$ 600 MPa for an ocean at this temperature (while Triton realistically does not achieve pressures beyond $\sim$ 400 MPa in its hydrosphere), we also do not consider the possibility of high-pressure ice forming at the base of the ocean. For a well-mixed ocean directly atop the mantle, the heat conducted out of the mantle is then immediately transferred to the shell, and we assume that whatever energy cannot be conducted away by the ice shell goes into melting the base of the ice shell (or, conversely, into freezing it, if the flux conducted away exceeds that expelled by the mantle). Hence, the movement of the ocean melting front R_{oc} is given by:

$$\rho_s L_s \frac{\mathrm{d}R_{\mathrm{oc}}}{\mathrm{d}t} = k_s \frac{\partial T(R_{\mathrm{oc}}^+)}{\partial r} - \left(\frac{R_m}{R_{\mathrm{oc}}}\right)^2 k_m \frac{\partial T(R_m^-)}{\partial r} + F_b \tag{3.19}$$

where the notation $f(x^+)$ and $f(x^-)$ denotes a limit from above respectively below, L_s is the latent heat required to melt the shell, and F_b is the basal heat flux, a term through which we will incorporate the tidal dissipation in the shell. The inclusion of this latter term in this way amounts to assuming that all tidal dissipation happens at the very base of the shell: as a result of the strong temperature-dependence of the viscosity of ice (see Sec. 3.3.1), we expect that the imaginary component of the complex rigidity is largest at the bottom of the ice shell, which translates to a concentration of tidal dissipation heating at the base (Tobie et al., 2005, Eqs. 33, 35), justifying this assumption. The temperature gradient in the mantle is determined using a 6th-order finite difference scheme described in Sec. A.1.

The boundary condition at the surface is given by balancing the conductive flux out of the shell with a conductivity $k_s(T) = C_k/T$ W/m/K (with the temperature in K and $C_k = 566.8$ W/m) appropriate for ice (Slack, 1980; Andersson & Suga, 1994; Deschamps, 2021) with grey-body radiation and the incoming solar flux:

$$-\frac{C_k}{T(R)} \frac{\mathrm{d}T(R)}{\mathrm{d}r} = \varepsilon \sigma_{SB} \left(T^4(R) - T_{\mathrm{eq}}^4\right) \tag{3.20}$$

where we will use a value of $T_{\mathrm{eq}} = 31.6$ K appropriate for a Triton with a Bond albedo of 0.85 (e.g. Brown et al. 1991; McKinnon & Kirk 2014, though see Nelson et al. (1990) for a dissenting opinion), though the dependence on the exact value is only weak, and an emissivity of $\varepsilon = 0.6$. The latter is only the preferred value, with plausible values ranging from 0.5-1 per Brown et al. (1991); while this is not likely to drive significant temperature change in the computed temperature profile because of the order-5 behaviour of the term in T, the associated energy conducted out of the shell is (to first order) linear in ε. In practice, such a change will lead to a more efficient expelling of energy at the same shell thickness, resulting in a thicker equilibrium conductive shell; as thicker shells dissipate more tidal energy, this will lead to shorter circularisation timescales. As an evaluation of the consequences of this behaviour would benefit from a more complete radiative transfer model of Triton's tenuous atmosphere (e.g. like that of Nolan & Lunine, 1988; Lunine & Nolan, 1992), we leave an investigation of the consequences thereof to future work.

The equilibrium conductive shell profile

The time-dependent conduction code we developed for the mantle has trouble operating efficiently for the thin shells, and introduces discretisation artefacts unless using an excessive number of gridpoints. This is undesirable, as the shell viscosity and therefore tidal response of Triton are highly sensitive to these artefacts, as temperature gradients at the bottom of the shell are steep. While we aim to resolve this using a non-uniform grid in future work, we find that thin shells are well-approximated by an equilibrium thermal profile after only a relatively short amount of time, especially once they grow thin (we validate this claim in Sec. C.2.2); hence, we assume that Triton's shell is well-described by an equilibrium profile for the purposes of this work.

We derive an expression for the equilibrium profile as a function of ocean radius, as the movement of the ocean melting front through Eq. 3.19 is what is responsible for the eventual settling of the shell into a thickness corresponding to the equilibrium flux. This expression can be cast into the following form, which can be derived by application of the boundary conditions given by Eqs. 3.18 and 3.20 to the source-less steady-state version of Eq. 3.15:

$$T(r) = T_{\text{surf}} \exp\left[\frac{C_1}{C_k}\left(\frac{1}{r} - \frac{1}{R}\right)\right] \tag{3.21}$$

$$C_1 = \varepsilon\sigma_{SB}R^2\left(T_{\text{surf}}^4 - T_{\text{eq}}^4\right) \tag{3.22}$$

$$T_{\text{surf}} = T_{\text{eq}}\left[\frac{W_0\left(K\left(\frac{T_{\text{melt}}}{T_{\text{eq}}}\right)^4 \exp(K)\right)}{K}\right]^{1/4} \tag{3.23}$$

$$K = \frac{4\varepsilon\sigma_{SB}RT_{\text{eq}}^4}{C_k}\left(\frac{R}{R_{\text{oc}}} - 1\right). \tag{3.24}$$

Here, $W_0(x)$ is the principal branch of the Lambert W-function, defined as the positive real solution y to $ye^y = x$; we use the implementation provided by *SciPy*'s *special* module (Virtanen et al., 2020) to compute its value. Eqs. 3.21-3.24 uniquely fix the conductive shell profile at any ocean radius in terms of known quantities. There is not (in general) an equilibrium conductive shell profile that will satisfy both the constraints of temperature continuity and energy conservation both at the shell-mantle interface and the surface, and so we terminate our simulations whenever the ocean freezes over. In our sensitivity analysis, we sometimes find that this hinders our ability to compare between scenarios, in which case we additionally perform runs assuming a fixed ocean thickness to evaluate the sensitivity of mantle evolution over the full timespan: in future work we aim to remedy this issue by using the time-dependent (i.e. non-equilibrium) heat equation for this regime.

3.2.4. Thermal evolution of the conductive mantle

As is the case for the shell, the conductive mantle is fixed to the melting temperature of the ocean at the ocean-mantle interface. The boundary condition at the bottom of the conductive part of the mantle depends on the presence of a convective layer: if the bottom part of the mantle is convective, this boundary condition is given by T_{top}, the temperature at the top of the convective part of the mantle (see Sec. 3.2.5). If the mantle is fully conductive, conservation of energy dictates that no heat is conducted through the centre of Triton, and so the bottom temperature is instead fixed to satisfy $\frac{\partial T(0^+)}{\partial r} = 0$, computed using a 6th-order finite difference approximation.

3.2.5. Mantle convection

Once temperature contrasts in the mantle rise sufficiently, one can expect mantle convection to occur. As mantle convection increases the efficiency with which heat can be expelled from the mantle compared to the conductive case, this is an important effect to consider, potentially having a major effect on the temperatures reached in the mantle, as well as the thicknesses obtained for the ice shell. Here, we will briefly outline the mantle convection model we use, as well as the method by which we evaluate whether convection is likely to have initiated.

Thermal evolution by parametrised mantle convection

If convection occurs, we will describe the convective part of the mantle using a parametrised convection model. Absent plate tectonics, as is the case on Earth, the majority of bodies in the Solar System appear to be undergoing stagnant lid convection (e.g. Reese et al., 1999; Stevenson, 2003; O'Neill et al., 2007; Breuer et al., 2022). We will follow the approach of Hussmann & Spohn (2004), who base their analysis on the work of Davaille & Jaupart (1993), Solomatov (1995), and Grasset & Parmentier (1998).

In the approach of Hussmann & Spohn (2004), stagnant lid convection is modelled using two coupled ordinary differential equations, describing parametrically the evolution of two new state variables: the temperature T_{int} and thickness D_{conv}, respectively, of a well-mixed convective layer overlaid by a conductive layer; T_{int} is assumed constant through the convective layer. The evolution of the conductive layer is largely identical to our approach in Sec. 3.2.1, though the boundary condition of no heat-flow through the centre of the body that applies in the fully conductive case is now replaced by fixing the lower boundary temperature of the conductive region to the temperature at the top of the convective region, T_{top}. This temperature is fixed uniquely by the assumption that the temperature contrast across the convective region is some constant value γ, and we neglect the thermal boundary layer transitioning from T_{int} to T_{top}: to compute the viscosity as a function of temperature, we use an Arrhenius law (Eq. 3.30; see Sec. 3.3.1). A reasonable but somewhat arbitrary value is $\gamma = 10$, as used e.g. by Solomatov (1995); Grasset & Parmentier (1998); Spohn & Schubert (2003); Hussmann & Spohn (2004); Multhaup & Spohn (2007), and so that is the value we will resort to. The heat flux q_{conv} out of the convective interior is computed using a Rayleigh-Nusselt number relationship (Hussmann & Spohn, 2004):

$$q_{\mathrm{conv}} = k_m \frac{\Delta T}{D_{\mathrm{conv}}} a Ra^{\beta} \tag{3.25}$$

where ΔT is the temperature difference across the convective region, Ra is the Rayleigh number, and $a = 0.13$ and $\beta = 0.3$ are numerical constants such that the critical Rayleigh number is $Ra_{\mathrm{crit}} = 10^3$. The Rayleigh number is computed as

$$Ra = \frac{\alpha \rho_m^2 C_m g \Delta T D_{\mathrm{conv}}^3}{k_m \eta(T_{\mathrm{int}})}, \tag{3.26}$$

where α is the thermal expansion coefficient of silicate. Given the inherent uncertainty in assuming a critical Rayleigh number, we will prefer in general to use a value of $\frac{\alpha \rho_m^2 C_m g}{k_m} \approx 1.1 \cdot 10^5$ Pa s K m^{-3} appropriate for $\alpha = 5 \cdot 10^{-5}$ K^{-1} and $g = 0.5$ m s^{-2} over re-computing the coefficient in this expression for every evaluation.

The two equations of motion for the temperature and thickness of the convective region then result from conservation of energy (cf. Hussmann & Spohn, 2004):

$$\rho_m C_m (T_{\mathrm{int}} - T_{\mathrm{top}}) \frac{\mathrm{d}D_{\mathrm{conv}}}{\mathrm{d}t} = q_{\mathrm{conv}} - q_{\mathrm{cond}} \tag{3.27}$$

$$\frac{4}{3}\pi D_{\mathrm{conv}}^3 \rho_m C_m \frac{\mathrm{d}T_{\mathrm{int}}}{\mathrm{d}t} = \dot{E}_{\mathrm{int}} - 4\pi D_{\mathrm{conv}}^2 q_{\mathrm{conv}} \tag{3.28}$$

where q_{cond} is the flux conducted away from the boundary between the conductive and convective mantle regions (computed using a finite difference scheme applied to the conductive mantle grid), and $\dot{E}_{\mathrm{int}}$ is the total (radiogenic and tidal) heat produced in the convective region.

Transitioning from conduction to convection

Bodies of Triton's size are not commonly assumed to have a convective mantle, at least initially: we will see (Sec. 4.2.3) that this assumption is justified for all plausible initial conditions, while later conditions are such that mantle convection might reasonably be expected. We must therefore not just account for evolution of a convective mantle as shown in the preceding section, but also for the transition from a fully conductive mantle to one with a convective layer.

As we follow, in general outline, the mantle convection model used by Hussmann & Spohn (2004), we will follow the approach of Multhaup & Spohn (2007) in modelling the onset of convection. Multhaup & Spohn (2007) adapted a convection model used by Spohn & Schubert (2003), which is in broad strokes comparable to that used by Hussmann & Spohn (2004), to account for this transition in the mid-sized icy moons of Saturn. To assess whether the mantle is possibly convective, we take the minimum viscosity in the conductive mantle η_{min} (in our case, always found at the centre, where the maximum temperature T_{max} is found) and compute the temperature corresponding to a γ-fold viscosity increase using Eq. 3.30 (as before, $\gamma = 10$ is a reasonable value) to find the temperature T_{top} at the top of the potentially convective layer. We compute the mantle radius R_{top} at which this temperature is found (if any) by interpolation of the discretised temperature grid, and compute the Rayleigh number Ra with Eq. 3.26 assuming a convective layer through that part of the mantle, with a well-mixed interior temperature equal to T_{max}, and the appropriate viscosity. If the corresponding Ra exceeds the critical value Ra_{crit}, we conclude that convection starts and re-initialise the integrator using the convective equations of motion for interior evolution, with $T_{\mathrm{int}} = T_{\mathrm{max}}$ and $D_{\mathrm{conv}} = R_{\mathrm{top}}$. The assumption $T_{\mathrm{int}} = T_{\mathrm{max}}$ overestimates slightly the post-convection onset temperature profile in the convective region, but doing so prevents us from having to iteratively determine (at each timestep) the temperature of the convective interior that is consistent *both* with convection starting and with the precise amount of thermal energy present in the newly-convecting layer. As the temperature profile deep in Triton is close to homogeneous in preliminary runs, we expect that the difference is of negligible influence compared to other uncertainties inherent to the parametrised convection model (e.g. in assumed values of the critical Rayleigh number).

3.3. Tidal deformation and dissipation

So far, we have described separately the orbital (Sec. 3.1) and interior (Sec. 3.2) evolution of Triton. Our goal is, of course, to unify the two: to do so, we need to compute the tidal potential generated by a tidally deformed Triton, parametrised by the tidal quality function, $K_l(\omega)$ (see Sec. 2.2.3), and correspondingly the energy dissipated in the shell and mantle. Before describing the formalism we use to compute the tidal quality function in Sec. 3.3.2, we will first introduce the expressions through which we model the rheology of Triton in Sec. 3.3.1.

3.3.1. Rheology

The tidal quality function $K_l(\omega)$ depends on the (layered) structure of Triton as well as its mechanical properties, and the interaction between these components. Computing it therefore requires that we formulate a constitutive law relating stress to strain, which depends on the rheology of the body. Hence, to evaluate the tidal quality function $K_l(\omega)$, we need to know the value of the complex[8] rigidity $\mu(\omega)$ throughout Triton's mantle and shell. To do so, we use the Maxwell rheological model, which may be applied both to the ice and silicate layers (Bagheri et al., 2022b). We do note that more advanced rheological models (at the cost of a greater number of degrees of freedom which must be constrained empirically) have been shown to give a better description of tidal heating in rocky bodies (Bierson & Nimmo, 2016; Renaud & Henning, 2018; Bierson, 2024). Renaud & Henning (2018) find that the Maxwell model underestimates tidal heating by a factor ~ 10 for a warm, Io-like body, making it a conservative but still reasonable choice: we will see in Ch. 6 that other choices affect our results to a far greater extent still. For the shell, more advanced models have also been shown to be preferable (e.g. Castillo-Rogez et al., 2011). We will assess the possible consequences of the use of more detailed rheological models in Sec. 7.3.1.

In the Maxwell model of viscoelastic behaviour, the complex rigidity depends on the elastic rigidity μ_e and viscosity η through the following expression (e.g. Beuthe, 2018):

$$\mu(\omega) = \frac{\mu_e}{1 - i\frac{\mu_e}{\omega\eta}} \tag{3.29}$$

where both μ_e and η are real quantities. The elastic rigidity is a material constant: we will use a rigidity of 50 GPa for silicate and a rigidity of 3.3 GPa for ice (Hussmann & Spohn, 2004, and references therein). To describe the variation of viscosity with temperature, we use an Arrhenius law like that used by Hussmann & Spohn (2004):

$$\eta(T) = \eta_0 \exp\left[l(T_{\text{ref}}/T - 1)\right] \tag{3.30}$$

where $l_a = 27$ (not to be confused with the spherical harmonic degree) is a dimensionless parameter parametrising the activation energy for the material in question. η_0 is the reference viscosity at the temperature T_{ref}. Following Hussmann & Spohn (2004), we will use a value of $\eta_0 = 5 \cdot 10^{13}$ Pa s at $T_{\text{melt}} = 273$ K for ice; in keeping with Hammond & Collins (2024) we will use a value of $\eta_0 = 10^{19}$ Pa s at $T_{\text{sol}} = 1500$ K for the mantle. We will evaluate the effects of changing these values from their nominal values in Ch. 6, and discuss a realistic range over which they may vary in Sec. 3.5.

In practice, we will also bound the allowed viscosities above: while the tidal quality function (see Sec. 3.3.2) is generally sampled only near the orbital rate or at higher frequencies, near-resonant (spin-orbit) frequencies will sample it very close to zero. As the locations of the peak frequencies of the tidal quality function are controlled by the viscosity, extremely high viscosities as might be encountered at low temperatures will move the peak behaviour of the tidal quality function to extremely low frequencies, which introduces apparent (i.e. unphysical) discontinuities close to spin-orbit resonances. This introduces undesirable behaviour in combination with our adaptive step-size integrator, such that we bound the viscosities at 10^{26} Pa s (corresponding to a temperature of ~ 941 K) for the mantle, and at 10^{20} Pa s (corresponding to a temperature of ~ 175 K, similar to the elastic-viscoelastic boundary for ice at 160 K used by Hussmann et al. (2002) and Ellsworth & Schubert (1983)). This does not affect the behaviour of the tidal quality function at tidal frequencies (see Sec. C.3.2), but resolves the (unphysical) discontinuities otherwise encountered for spin-orbit resonances: note that these are different from the true discrete behaviour (i.e. in the spin rate) that arises in the decay between spin-orbit resonances, which remains.

The rigidity profile of the shell is incorporated into the computation of the tidal quality function (see Eq. 3.33) by the terms μ_0, μ_1, and μ_2 (which enter into the computation through expressions given in App. B.1), computed using

$$\mu_p(\omega) = D_{\text{shell}}^{-p-1} \int_{R-D_{\text{shell}}}^{R} \mu(\omega, r)(r-R)^p \, \mathrm{d}r \tag{3.31}$$

where D_{shell} is the thickness of the shell. Beuthe (2019) assumes a uniform rigidity profile for Enceladus, but we do not find this to be a realistic assumption given the temperature differences we expect for Triton's mantle. Hence, we use a similar expression to Eq. 3.31, the use of which as an "effective rigidity" is motivated by the form of the viscoelastic-gravitational equations from which the expressions of Beuthe (2019) arise (see Beuthe (2015b, Sec. 3.3) for a discussion), to compute the effective rigidity of the mantle μ_{mantle}, which also enters into the computation of the tidal quality function through the terms given in App. B.1:

$$\mu_{\text{mantle}} = \frac{1}{R_m} \int_0^{R_m} \mu(\omega, r) \, \mathrm{d}r \tag{3.32}$$

[8]Complex numbers arise in this context because the Fourier decomposition in Eq. 3.8 fundamentally derives from a Fourier transform.

which we compute analogously to Eq. 3.31. In either case, the complex rigidity is computed as a function of radius using Eq. 3.29; the viscosity as a function of radius, in turn, is computed using Eq. 3.30, where the temperature as a function of radius is determined by the temperature profile at each timestep. To compute the integrals for μ_0, μ_1, μ_2, and μ_{core}, we use the *SciPy* function *interpolate.PchipInterpolator* to compute the integrand, and we evaluate the integral using the function *integrate.quad* (Virtanen et al., 2020).

3.3.2. Tidal quality function and the partitioning of dissipated energy

For icy satellites possessing subsurface oceans covered by thin shells, Beuthe (2015a,b, 2016, 2018, 2019) has worked out a formalism that gives analytical Love numbers at relatively little computational cost compared to the classical propagator matrix or other methods. Thin shell theory can generally be applied to shells thinner than 5 – 10% of the body's radius (Beuthe, 2018), but Beuthe (2018, 2019) shows that the error in the thin-shell approach is of order $\lesssim$ 10% when the shell thickness d reaches $d/R \sim 0.2$ in the case of Enceladus. For Triton, the hydrosphere stretches far enough that $d/R \lesssim 0.2$, and so given the uncertainties in all other parameters going into our analysis, we deem the thin-shell approach to be acceptable. The main advantage to this approach lay in allowing us to evaluate the role of feedback effects between tidal heating and tidal response in an efficient manner, while the behaviour of this relation is still captured at least qualitatively by the thin-shell approximation. Future work will evaluate the consequences of relaxing the thin-shell assumption.

As the computation of the tidal quality function involves the computation of a large number of intermediate terms, we will only give the most important and meaningful expressions here. The reader is referred to App. B.1 for further details of this computation. The tidal quality function is given by the negative imaginary part of the gravitational tidal Love number $\bar{k}_l$, which can in turn be computed from the radial tidal Love number $\bar{h}_l$ and the thin-shell spring constant Λ_l (Beuthe, 2019, and references therein);

$$K_l(\omega) = -\operatorname{Im}(\bar{k}_l(\omega)) \tag{3.33}$$

$$\bar{k}_l(\omega) = (1+\Lambda_l)\bar{h}_l(\omega) - 1 \tag{3.34}$$

$$\bar{h}_l(\omega) = \frac{\bar{h}_l^\circ}{1 + (1 + \xi_l \bar{h}_l^\circ)\Lambda_l}. \tag{3.35}$$

Here, $\xi_l = \frac{3}{2l+1}\frac{\rho_s}{\rho_b}$, with ρ_s and ρ_b being the shell and bulk density, respectively, and $\bar{h}_l^\circ$ being the fluid-crust radial Love number i.e. the radial Love number corresponding to an identical body but with a fluid rather than solid shell; analytical expressions for Λ_l and $\bar{h}_l^\circ$ exist, and are given in App. B.1. For our purposes, it suffices to know that they depend on the characteristic dimensions of the body (i.e. the mantle, ocean and total radii), the bulk and shell density, the total mass, the Poisson ratio ν (which we set to a value of $\nu = 1/3$ appropriate for ice, though see Beuthe (2018) for a discussion on the validity of using a homogeneous value for ν), and the rigidity profiles through the shell and mantle. Each of these terms can be computed algebraically as a function of frequency using straightforward relations given in App. B.1, with the exception of the rigidity profiles, the computation of which we have described in Sec. 3.3.1.

Here, we note that the form of the tidal quality function only depends on the spherical harmonic degree l (for which we will always take only $l = 2$); the dependency on the indices mpq of Eq. 3.8 enters only through the particular frequencies ω_{lmpq} at which the Darwin-Kaula expansion samples K_l. Hence, we find it conceptually more useful to treat the evolution of the tidal quality function $K_l(\omega)$, which is a function only of spherical harmonic degree and the interior structure of the body, separately from the frequencies ω_{lmpq} at which it is evaluated. Indeed, as the Darwin-Kaula expansion evaluates the tidal quality function at an excessively large number of points for high eccentricities, we will use this fact to our advantage and pre-compute an interpolant for the tidal quality function.

Besides the expressions for the tidal quality function, the formalism of Beuthe (2019) also readily provides the partitioning of the total dissipated power between mantle and shell. As the tidal quality function, this also only depends on the spherical harmonic degree l, with all other dependencies on the indices mpq of the Darwin-Kaula expansion "hidden away" in the argument ω_{lmpq}, where again we will forego the indices $lmpq$ outside contexts explicitly concerning the Darwin-Kaula expansion (Beuthe, 2019):

$$\varphi_c(\omega) = \left|\frac{\bar{k}_l(\omega) + 1}{\bar{h}_l^\circ(\omega)}\right|^2 \frac{\operatorname{Im}(\bar{h}_l^\circ(\omega))}{\operatorname{Im}(\bar{k}_l(\omega))} \tag{3.36}$$

which, we see, is computed with ease from the terms already computed in the determination of the tidal quality function K_l. The total power dissipated in the mantle then follows from the total power dissipated throughout Triton by multiplication of each of the terms in the sum for the dissipated energy (Eq. 3.8) by the value of φ_c

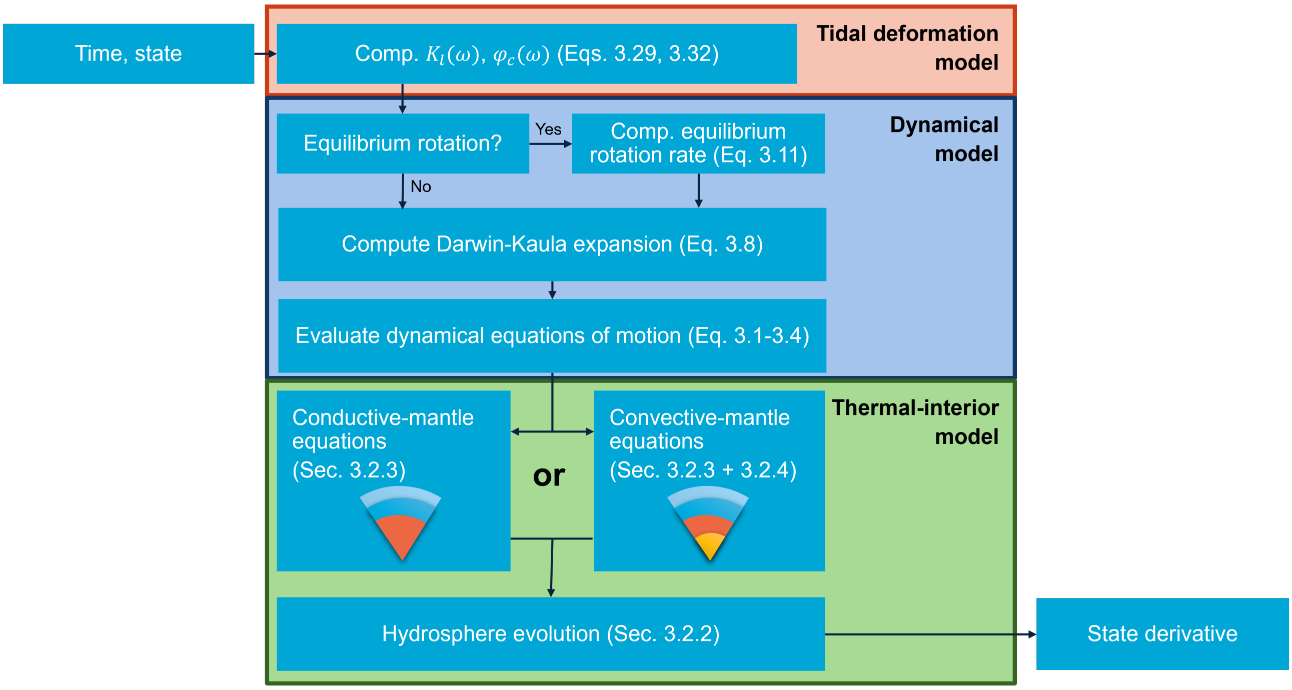

Figure 3.2: Schematic overview of the evaluation of the equations of motion as used by the integrator.

evaluated at the appropriate tidal mode i.e. $\varphi_c(\omega_{lmpq})$:

$$\dot{E}_{\text{mantle},lmpq} = \varphi_c(\omega_{lmpq})\dot{E}_{lmpq}(\omega_{lmpq}) \tag{3.37}$$

$$\dot{E}_{\text{mantle}} = \sum_{l\geq 2}\sum_{m=0}^{l}\sum_{p=0}^{l}\sum_{q=-\infty}^{\infty} \dot{E}_{\text{mantle},lmpq} \tag{3.38}$$

$$= n^2 a^2 \beta \frac{M_N}{M_T} \sum_{l\geq 2}\left(\frac{R}{a}\right)^{2l+1} \sum_{m=0}^{l} \frac{(l-m)!}{(l+m)!}(2-\delta_{0m}) \sum_{p=0}^{l} F^2_{lmp}(i_T) \sum_{q=-\infty}^{\infty} G^2_{lpq}(e) K_l(\omega_{lmpq})\omega_{lmpq}\varphi_c(\omega_{lmpq}) \tag{3.39}$$

such that the total power dissipated in the shell is given by

$$\dot{E}_{\text{shell}} = \dot{E}_{\text{tot}} - \dot{E}_{\text{mantle}} \tag{3.40}$$

where $\dot{E}_{\text{tot}}$ is the total dissipation predicted by Eq. 3.8. As the viscosity in the shell is largest at its base, we assume all tidal heat is dissipated there (see Eq. 3.19); in the mantle, we do not account for the variation of viscosity (and correspondingly, rigidity) with radius (e.g. Tobie et al., 2005), and assume instead that $\dot{E}_{\text{mantle}}$ is spread uniformly throughout. We will assess the validity of this assumption in future work.

3.4. Algorithm design

We implement the model described in Secs. 3.1-3.3 in Python 3.11.7; the code is available on request from the author, though future work will aim to release the code for public use under the name *DelfTide*. To discretise the heat equation (Sec. 3.2.1), we implement a 6-th order scheme by which to numerically approximate the first and second derivative with respect to radius, with a dynamic grid to account for the variation of the conductive part of the mantle with a moving boundary between the convective and conductive parts of the mantle: the implementation of the finite difference schemes and the dynamic grid is documented in App. A. The procedure followed to compute the equations of motion as a function of time and state is illustrated schematically in Fig. 3.2.

We propagate the equations of motion using a custom implementation of the Dormand-Prince 5(4) (DOPRI5) numerical integration scheme, based on the description of Hairer et al. (2008) and tested against *SciPy*'s *integrate.solve_ivp* implementation of the same integration routine as well as a set of analytical test functions. During propagation, the integrator may encounter termination events, divided into those which require us to switch to re-initialise the integrator with a different set of equations of motion or initial conditions, such as the switch from to the convective-mantle scenario, and those at which we terminate integration altogether, such as the end of the integration interval being reached (for which we will generally use an end time of 5 Gyr), or the ocean freezing over. The former type of termination event we call “local” termination events; the latter we call

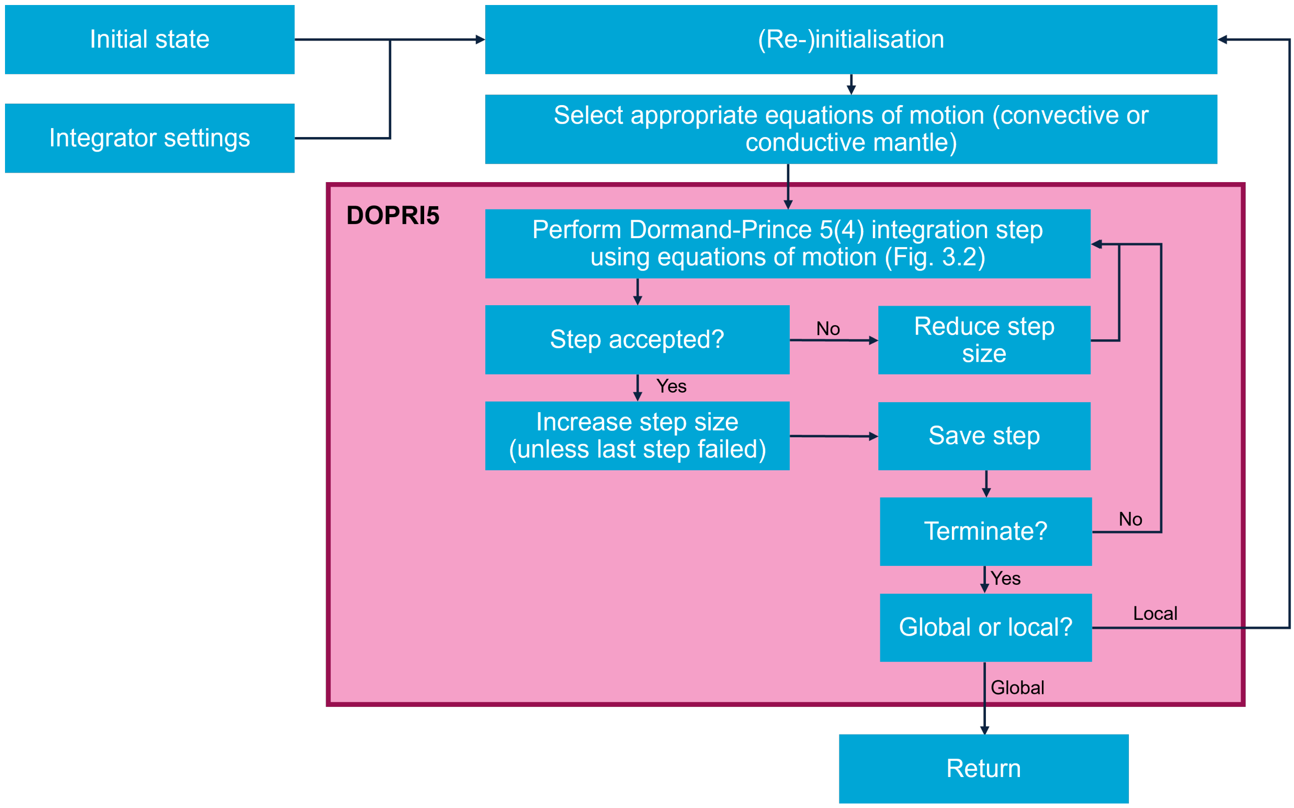

Figure 3.3: Schematic illustration of the integrator.

"global" termination events. A schematic description of the functioning of the integrator is given in Fig. 3.3. Validation and verification of the code is presented in App. C for the sake of brevity.

3.5. Experiment structure and design

We have now introduced the three components to our model (Secs. 3.1-3.3), the algorithm in which we have implemented them (Sec. 3.4). Before this puts us in a place where we can answer the questions laid out in Ch. 2, however, we must conduct experiments using this model. To do this, however, we must assume values for a handful of parameters; while those describing present-day Triton have already been given in Tab. 2.1, we must assume some additional values to be able to describe the coupled thermal and orbital evolution of Triton. Some of these we will keep constant throughout this work: these are given in Tab. 3.2.

However, for Triton, no measurements are available from which its interior structure can be constrained beyond its mass and radius. Additionally, especially given its enigmatic origin, the composition of its mantle and correspondingly neither the radiogenic species present in Triton nor its (effective) viscosity or density can be constrained (tightly) a priori. To accommodate this uncertainty, we will designate a plausible range of values for such parameters, and perform trial runs with a number of trial values in this range. This will allow us to assess the sensitivity of our results to the uncertainty in these parameters. We give the nominal and trial values for each of these parameters in Tab. 3.3, and will give a brief explanation for the range and values chosen for each.

3.5.1. Plausible estimates for the mantle density and radius of Triton

Even if Triton retained all its accretional heat (Hussmann et al., 2010, Tab. 7), this is only enough to raise its temperature uniformly by ~ 700 K at most (assuming a specific heat of $\sim 10^3$ J/kg/K appropriate for silicate). Hence, Triton will not have started iron-silicate differentiation spontaneously. By contrast, ice-rock differentiation *can* be assumed to have happened (e.g. by analogy with smaller Pluto; Stern 2014; Stern et al. 2018). We will therefore assume that Triton initially has a silicate mantle comprised of CI-chondrite material (see Sec. 2.3.1), which is thought to be appropriate for Solar System objects that formed exterior to Jupiter (e.g. Desch et al., 2018). As the precise density (profile) of such material is dependent on hydration state, interior temperatures and other factors for which no constraints are present in the case of Triton (see e.g. Cioria & Mitri 2022), we will prefer to parametrise matters in terms of the density of the mantle, and perform a sensitivity analysis in Secs. 4.2.2 and 6.2.1. Based on the analysis of Cioria & Mitri (2022), plausible densities for Triton's mantle assuming a CI-chondrite composition range from 2800 kg/m^3 for a cold, hydrated mantle to 3400 kg/m^3 for a cold but dehydrated mantle. 3100 kg/m^3, also used e.g. for Pluto by Bagheri et al. (2022a), therefore seems like

Table 3.2: Thermal and interior properties kept constant throughout this work. References are as follows; B+22: Bagheri et al. (2022a); HS04: Hussmann & Spohn (2004); D21: Deschamps (2021); CG07: Choukroun & Grasset (2007).

Parameter	Value	Units	After	Remarks
		Mantle		
k_m	2.4	W/m/K	B+22	
C_m	1100	J/kg/K	B+22	
μ_e	50	GPa	HS04	
l_a	27	-	HS04	
T_{sol}	1500	K	HS04	
		Shell		
k_s	$566.8/T$	W/m/K	D21	T in K
C_s	$7.037T + 185$	J/kg/K	B+22	T in K
μ_e	3.3	GPa	HS04	
l_a	27	-	HS04	
T_{melt}	273	K	CG07	
T_{eq}	31.6	K	-	
ρ_s	920	kg/m^3	B+22	Also for ocean

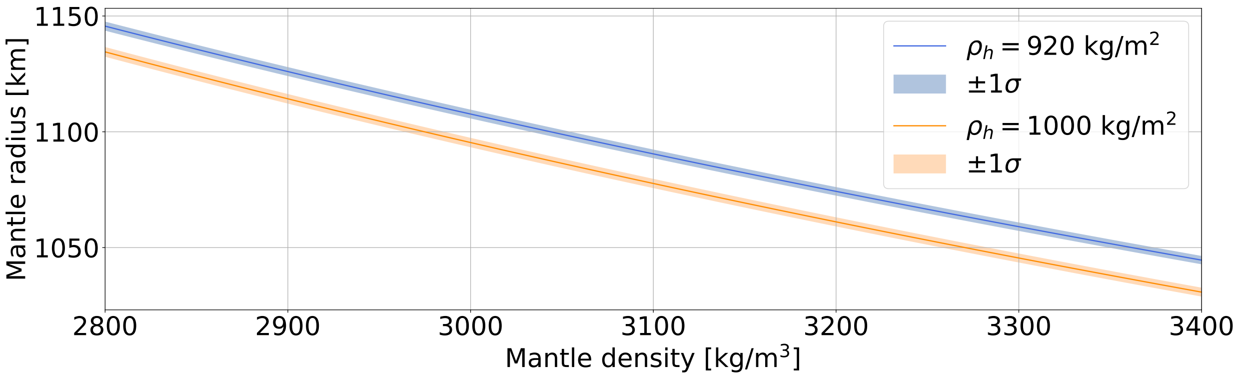

Figure 3.4: Mantle radius as function of mantle density, computed through the mass-radius constraints of Jacobson (2009) and Thomas (2000), respectively. $\pm 1\sigma$ uncertainties are computed by propagating the uncertainties on the mass and radius of Triton. Our reference mantle density is 3100 kg/m^3, leading to a reference mantle radius of 1091 km.

a plausible middle ground, and we take it as nominal value.

As we compute the mantle radius to satisfy the mass- and radius constraints available for Triton (Tab. 3.2), we wish to explicitly highlight the consequences of this dependency (though our code accounts for this self-consistently). To satisfy the mass- and radius-constraints, a mantle radius R_m at a given mantle density ρ_m must satisfy:

$$R_m = \left(\frac{\frac{3M_T}{4\pi} - R_T^3 \rho_h}{\rho_m - \rho_h} \right)^{1/3} \tag{3.41}$$

where ρ_h is the average density of the hydrosphere. We assume a relatively low value of $\rho_h = 920$ kg/m^3 (as used e.g. for Pluto's shell by Bagheri et al. 2022a), though we will also show the results for a higher value of $\rho_h = 1000$ kg/m^3 for comparison. Fig. 3.4 shows the resulting variation of mantle radius as function of assumed mantle density; we see that the consequences of the assumed value of the hydrosphere density do not have nearly the same effect that changing the mantle density over a plausible range of values does. Hence, we will vary only the mantle density, evaluating the two end-member densities 2800 and 3400 kg/m^3, and a nominal scenario of 3100 kg/m^3.

3.5.2. Estimates for the radiogenic heating rate

The radiogenic heating rate is a relatively strong function of composition, and so its value hinges on our assumption of a CI-chondritic composition (see Sec. 3.2.2 and Tab. 3.1). Part of this uncertainty is due to the total mass of rocky material (i.e. bearing radioactive species) in Triton; this uncertainty is consistently accounted for by our variation of the mantle density in agreement with Eq. 3.17, and therefore does not need to be accounted for here. A second component to the uncertainty on the radiogenic heating rate is found in the composition of the material itself, which translates to an increase or decrease in *specific* radiogenic heating rate. This uncertainty, in turn, is made up of two components: (1) uncertainties in composition data, as our computation of the radiogenic heating rate (Eq. 3.17) is, through the isotopic abundances c_i, based on elemental composition data from Lodders & Fegley (1998), who do not provide uncertainties on their data, and (2) systematic uncertainties in the elemental abundances C_i: for example, radiogenic material can, during periods of hydrothermal alteration, leach into the ocean (see e.g. Castillo-Rogez & Lunine, 2010, for Titan), where radiogenic heat is more efficiently lost, such that we would potentially (depending on the degree of depletion in the interior) drastically overestimate the radiogenic heating rate because of systematic overestimation of the terms C_i in Eq. 3.17. Similarly, CI-chondrite, having the lowest radiogenic heating rate of all meteoritic classes, has a radiogenic heating rate about 1.7 times lower than that of LL chondrites (which have the highest specific radiogenic heating rate Hussmann et al., 2010). If Triton's mantle turns out to originate from a precursor material other than CI-chondrite, we can therefore potentially drastically *under*estimate the radiogenic heating rate.

We expect that the effect of the uncertainties in composition data (i.e. the first uncertainty component, through the isotopic abundances c_i) for CI-chondrite will not exceed a multiplicative factor of about $0.9 - 1.1$; systematic uncertainties, such as the aforementioned leaching or a Tritonian mantle that turns out to be composed of one of the more radiogenically active meteoritic classes, however, might alter this number up to a factor of ~ 2 (through the elemental abundances C_i). Hence, we will vary the radiogenic heating rate by a broader range of multiplicative factors from the nominal value (that of Hussmann et al. 2010) to reflect these possibilities. A variation of ±10% will allow us to examine the effects of nominal uncertainties, while more drastic variations of ±50% and +100% will allow us to assess the consequences of systematic issues in the radiogenic heating rate.

The effects of radiogenic heating by short-lived isotopes and the associated uncertainties are accounted for by varying the initial temperature profile, though we note that KBOs are thought to have formed some ~ 4 Myr after CAI based on evidence for a lack of heating by short-lived radioisotopes in smaller KBOs (Bierson & Nimmo, 2019; Bierson et al., 2020). In that scenario, no heating by short-lived isotopes will have taken place.

3.5.3. Variation of initial interior conditions

We generally initialise Triton with a uniform temperature profile in the mantle, and an equilibrium shell profile appropriate for the initial ocean radius: rather than explicitly considering various accretion models, we will vary the initial temperature Triton starts with. Our results are not sensitive to the initial ocean radius, as it rapidly adapts to the mantle heat outflow, and so we will in general set the ocean thickness to start at 200 km (and we will momentarily see that the presence of such an ocean at formation is justified).

The initial temperature is more delicate: while as much as $\sim 600 - 700$ K worth of potential energy was released during accretion and ice-rock differentiation of Triton (Hussmann et al., 2010), whether Triton was able to retain all of this energy is heavily dependent on the timescale over which its accretion occurred. Though no true consensus is as of yet reached, KBOs are generally believed to initially form through the streaming instability, with their later growing to larger sizes fed by pebble accretion (Morbidelli & Nesvorný, 2020); initial formation by the streaming instability tends to form binary objects (Nesvorný et al., 2010), a requirement for capture of Triton by the mechanism of Agnor & Hamilton (2006). As the streaming instability operates on timescales of ~kyr (Nesvorný et al., 2010), the formation timescale of Triton will have been sufficiently short that it may well have retained a large amount of accretional heat: extensional features on Pluto and Charon suggest that both formed hot, with an ocean already present initially (Bierson et al., 2020). It is therefore plausible that Triton retained a significant fraction of its accretional heat, raising its interior temperature to well above the equilibrium temperature of ~ 32 K in the surrounding nebula. As ice and rock differentiated in Triton, we take a plausible lower bound for the initial mantle temperature to be ~ 200 K, congruent with similar values assumed e.g. by Bierson et al. (2020) for Pluto, or by Hammond & Collins (2024) for Triton.

The process of accretion will in general, counter-intuitively[9], lead to a temperature-inverted profile (e.g. Ellsworth & Schubert, 1983); the process of differentiation of ice from rock should re-homogenise the body, however, and so we will assume a homogeneous temperature in the mantle initially. To evaluate the consequences of more or less efficient post-accretion heat retention, we therefore test initial mantle temperatures of 200, 300, 450, and 600 K, representing a lower-bound, a nominal, and two hot-start scenarios, respectively.

3.5.4. Changing the reference viscosity of the shell and mantle

Generally speaking, the viscosity values and structure of the mantle and shell of icy satellites are poorly constrained, and with the viscosity normally measured in orders of magnitude, so are its uncertainties. Even for the Earth's mantle, only the average viscosity is relatively well-constrained to about $3 \cdot 10^{21}$ Pa s: see e.g. Karato (2010) for a review. We will thus not pretend that we can know the viscosity structure of Triton any better than

[9] That is, different from the temperature profiles one is used to from studying bodies that have undergone evolution since accretion.

Table 3.3: Overview of the nominal values, plausible variation of those values around the nominal value, and the trial values used in our sensitivity analysis. H+10: Hussmann et al. (2010).

Parameter	Nominal value	Plausible range	Trial values	Units	Remarks
Mantle density	3100	2800-3400	2800, 3400	kg/m^3	
Radiogenic heating rate multiplier	1	0.9-1.1	0.5; 0.9; 1.1; 1.5; 2	-	Compared to H+10
Initial mantle temperature	300	200-600	200, 450, 600	K	
Mantle ref. viscosity	10^{19}	$10^{17} - 10^{21}$	$10^{17}, 10^{18}, 10^{20}, 10^{21}$	Pa s	
Shell ref. viscosity	$5 \cdot 10^{13}$	$10^{12} - 10^{16}$	$5 \cdot 10^{11}, 5 \cdot 10^{12}, 5 \cdot 10^{14}, 5 \cdot 10^{15}$	Pa s	

we do the Earth's. However, the viscosity values we use impact both the convection model (with lower mantle viscosities convecting much more readily; see Sec. 3.2.5) and the deformation model (as low-viscosity bodies are much more prone to tidal deformation than high-viscosity ones; see Sec. 3.3). Though unconstrained, the reference viscosities are therefore important parameters.

Consequently, we will take a reference value of the viscosity of $\eta_0 = 10^{19}$ Pa s for the mantle (e.g. Hammond & Collins, 2024), and $\eta_0 = 5 \cdot 10^{13}$ (e.g. Hussmann et al., 2010), and vary both values by several orders of magnitude. For the mantle, we evaluate out to values of $\sim 10^{21}$ Pa s, though we find little difference when increasing the viscosity (as we will see, the mantle is hardly affected by dissipation, so the only factor affected is mantle convection), and as low as necessary to reproduce the predictions of Andrade rheology using a Maxwell model (10^{17} Pa s: see e.g. Hammond & Collins, 2024, Sec. A.6). For the ice shell, we cover the range of ice shell viscosities of order $\sim 10^{14} - 10^{16}$ found by Hammond & Collins (2024), who compute the viscosity from a cumulative flow law by accounting for the appropriate deformation mechanisms, as well as the slightly lower viscosities of order $\sim 10^{13}$ used in older literature (e.g. Hussmann & Spohn, 2004). Here we note that the geological analysis by Schenk et al. (2021) seems to favour a comparatively low viscosity for Triton's shell.

3.5.5. Initial dynamical state

In initial runs, we find that the end-state of Triton is only very weakly affected by the initial dynamical state of the moon, and so we do not vary its initial dynamical state. We will, however, note that the initial dynamical state of Triton is only very poorly constrained: capture simulations by Nogueira et al. (2011) show that Triton very likely did not get captured on an orbit with an eccentricity lower than ~ 0.9, with their median eccentricity upon capture being as high as 0.97. Hence, we will initialise Triton with an eccentricity of 0.97 and a semi-major axis of $\sim 242R_N$ that satisfies conservation of its orbital angular momentum; this latter constraint guarantees that Triton will end up on its present-day orbit, as the dynamical-evolution expressions that we use can be shown to, in general, satisfy conservation of Triton's orbital angular momentum[10]. This is no longer true when accounting for tides on Neptune, but previous work showed that those only act significantly once Triton has already migrated inwards to close to its present-day orbit, and even then only over long timescales (Van Woerkom, 2024).

As for Triton's initial rotational state, we choose an arbitrary value of 24 h, in alignment with Correia (2009): this is relatively slow for a (binary) KBO (e.g. Perna et al., 2009; Thirouin et al., 2014), but we find that its value does not matter much, with Triton rapidly (within ~Myrs) reaching an equilibrium rotation state.

3.5.6. Experiment structure

With the components of our model ready and the relevant parameter (ranges) selected (summarised in Tabs 3.2 and 3.3). To be able to draw robust conclusions from these experiments, we structure them as follows: in Ch. 4, we will first perform a set of experiments without our dynamics module, assuming that Triton experiences no tidal interaction. We additionally perform a sensitivity analysis on these results (using the values given in Sec. 3.5), allowing us to assess how robust these results are given the uncertainties on Triton's interior. This gives us a base scenario against which we can compare and quantify in a more meaningful way what the effect is of capture (which allows us to answer our second research question). We then move on to a study of the coupled interior-orbital evolution of Triton in Ch. 5: here, we also perform a comparison against a set of simplified tidal models, which gives us the results necessary to answer our first research question, as well as a first, tentative answer to questions 3 and 4. To be able to answer those with more confidence, however, we finally perform a sensitivity analysis on the coupled orbital-interior evolution of Triton in Ch. 6.

[10]Strictly speaking, it is the total (i.e. orbital and rotational) angular momentum of Triton that is conserved by our expressions, though the contribution of the rotational rate is negligible.

4 Isolated evolution of Triton's interior

Before moving on to an evaluation of the coupled interior and dynamical evolution of Triton, we consider the isolated, tideless interior evolution of a Triton-like body. This serves two purposes: to start with, the interior evolution of a dwarf planet like proto-Triton is interesting in its own right. Secondly, we will see in Ch. 5 that the thermal evolution of Triton's mantle is largely impervious to tidal influences. Hence, we will present the tideless interior evolution of Triton in the nominal scenario in Sec. 4.1. An evaluation of the sensitivity of Triton's isolated interior evolution to the various assumptions we have made therefore largely transfers to the tidally heated scenario, and so we present just such a sensitivity analysis in Sec. 4.2.

4.1. Nominal results

We will first briefly show the results for the nominal scenario, with an initial temperature of 300 K, a mantle density of 3100 kg/m^3 and the nominal radiogenic heating rate for CI-chondrite from Hussmann et al. (2010): we will provide the nominal evolution of the temperature profile through Triton in Sec. 4.1.1, followed by an overview of the relevant heat-flows in Sec. 4.1.2. Finally, we give results on the occurrence of a convective region in the mantle, as well as the conditions in that region, in Sec. 4.1.3.

4.1.1. Time-evolution of the thermal profile

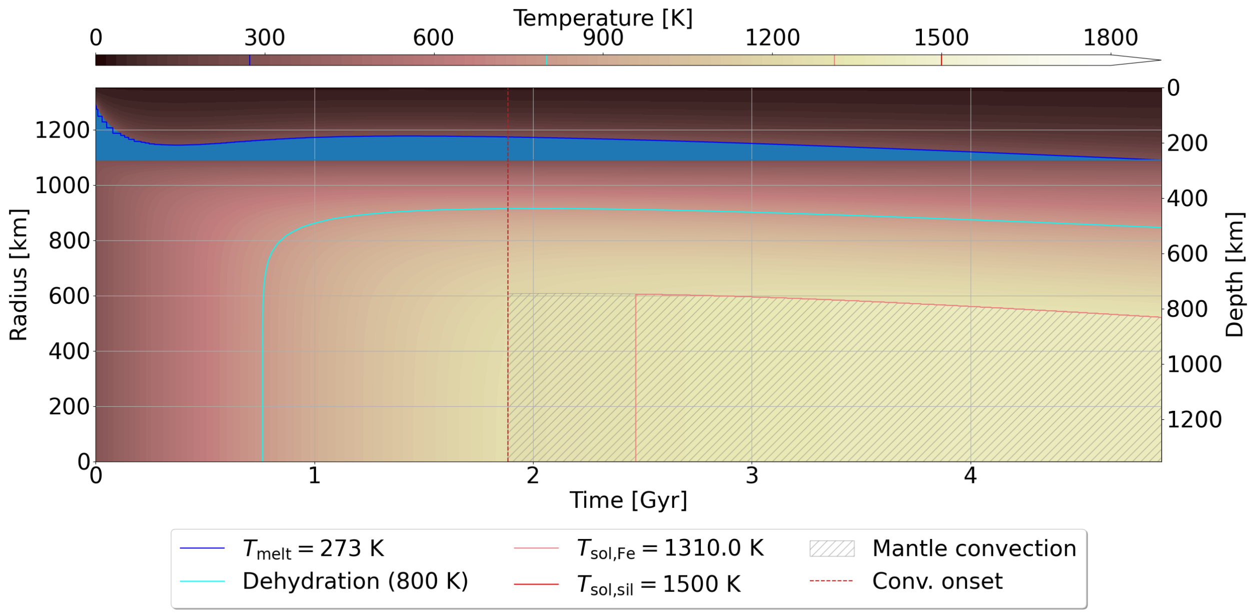

Figure 4.1: Evolution of the thermal profile throughout Triton through time in the nominal case, neglecting tides. The stair-step pattern at the ocean-ice interface is a plotting artefact, and the true evolution of the ocean thickness is continuous and smooth (see Fig. 4.2). Also indicated are the convective region, the melting temperature of pure water, as well as approximate values for the temperature of dehydration onset in silicate (Perrillat et al., 2005), the solidus temperature of silicates (Hammond & Collins, 2024) and the 20% melt-fraction temperature of iron (Taylor, 1992; Neumann et al., 2012).

We show the evolution of the nominal thermal profile over time for an isolated (i.e. tideless) Triton in Fig. 4.1. In the profile, we indicate several important temperatures, being the melting temperature of pure water ice, the temperature at which we expect dehydration to start occurring (~ 800 K: Perrillat et al., 2005), and an estimate for the 20% melt-fraction temperature of iron (Taylor, 1992; Neumann et al., 2012), as well as, though not reached in this run, the solidus temperature of silicates used by Hammond & Collins (2024); the 20% melt-fraction temperature of iron is one at which we conservatively expect runaway core formation (i.e. iron-rock differentiation) by percolation through an interconnected melt network to start (Ghanbarzadeh et al., 2017; Berg et al., 2017, 2018). We note two important points: (1) the mantle reaches the temperatures required to start large-scale dehydration after ~ 0.8 Gyr, and (2) mantle convection starts after ~ 2 Gyr; we will give the results pertaining to the conditions in the convective mantle region in more detail in Sec. 4.1.3.

Fig. 4.1 shows a stair-step pattern in the evolution of the shell: this is an artefact of our plotting routine, and so

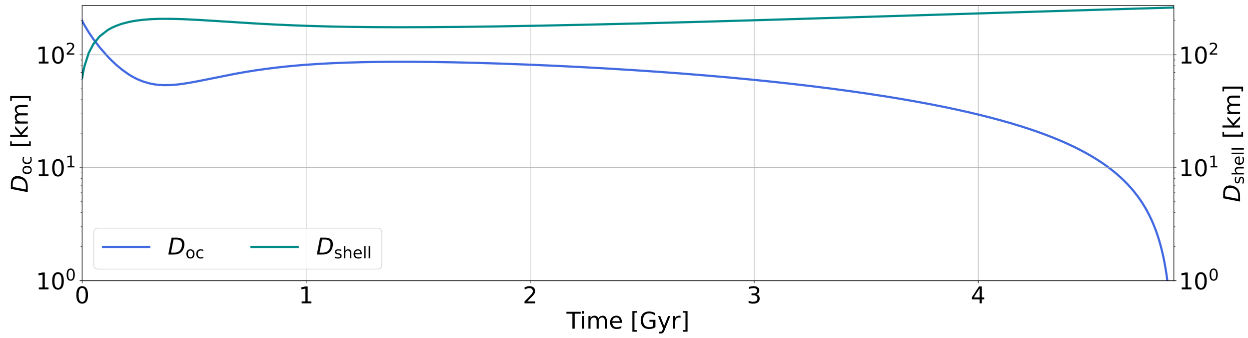

Figure 4.2: Evolution of the ocean and shell thickness over time for the isolated nominal interior.

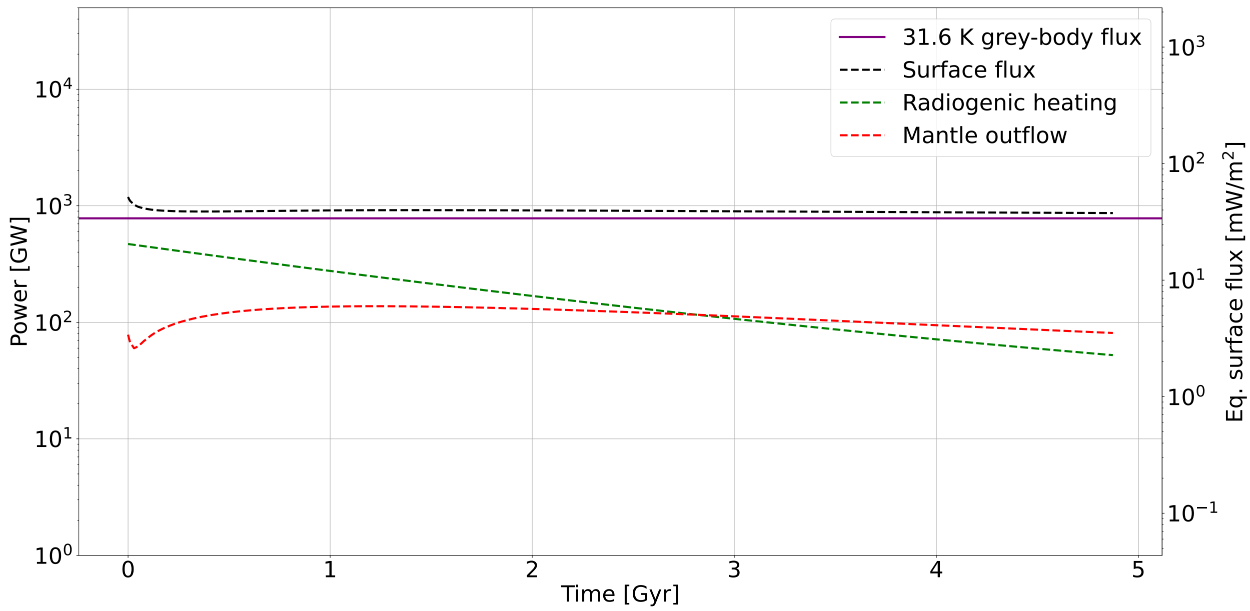

Figure 4.3: Relevant heat flows over time for the nominal, tideless interior evolution of Triton. Shown are the total power and the equivalent surface flux i.e. the power normalised to the surface area of Triton (and so the mantle outflow is *not* scaled to the mantle area, and should therefore be scaled by $(R_m/R)^2$ to yield the true mantle heat flux). For comparison, the surface heat flux expected for a body of Triton's size and emissivity emitting grey-body radiation at the equilibrium temperature at Neptune are shown.

we separately show the evolution of the ocean and shell thickness in Fig. 4.2. The ocean is thickest ($\sim$ 85 km) after 1.5 Gyr, and starts freezing over afterward. Note that the ocean freezes over at $\sim$ 4.9 Gyr, after which we stop our simulation. Not accounting for tides, we therefore expect that Triton should at present retain a thin ocean of $\sim$ 10 km thick, in the process of freezing over for the past $\sim$ 3 Gyr.

Fig. 4.4, finally, shows the temporal evolution of the surface temperature T_{surf} as well as the core (i.e. highest) temperature T_{core}; once mantle convection initiates, we show instead the evolution of the temperature in the well-mixed interior of the convective region T_{int} and the temperature at the top of the convective region T_{top} (we provide more detail regarding the results on convection in Sec. 4.1.3). The solidus of silicate as well as the 20% melt-fraction temperature of iron are also shown: in this scenario, the convective region reaches temperatures thought to be sufficient to start differentiating iron from rock after $\sim$ 2.5 Gyr. As we do not model core formation, we do not expect that the evolution of the deep interior after this time is fully accurate. Yet, as core formation is expected to release $\sim$ 50 K worth of thermal energy (Hammond & Collins, 2024), it is plausible that the temperature of the mantle will not exceed the silicate solidus based on these results.

4.1.2. Heat flows

Fig. 4.3 shows the nominal heat flows through a tideless Triton, as well as the grey-body emission that might be expected of a body of Triton's size and emissivity in equilibrium for the solar flux at Neptune. Two important results follow; (1) for a tideless Triton, the emitted radiation is always dominated by the re-emitted solar flux (as also evident from the surface temperature in Fig. 4.4), and (2) the heat flow out of the mantle is never in equilibrium with the produced radiogenic heat due to thermal inertia of the mantle. We observe that the mantle

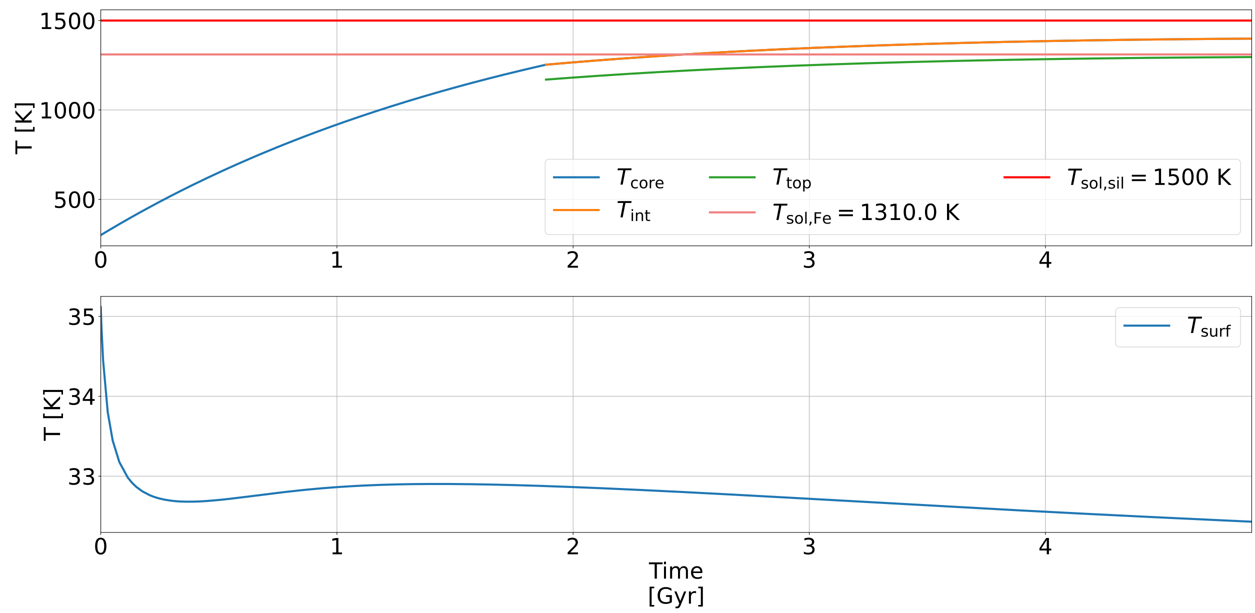

Figure 4.4: The time-dependent evolution of key mantle temperatures (top) and the surface temperature (bottom) for a nominal, tideless Triton.

is heating up for the first ~ 3 Gyr, and starts to cool down afterward.

4.1.3. Mantle convection

Of particular interest is the convective mantle region, as convection has hitherto not been considered for Triton's mantle. Hence, we show the evolution of the Rayleigh number and the thickness of the convective region over time in Fig. 4.5. Here, it is clear that, though the thickness of the convective region falls, the temperature of the convective region (see Fig. 4.4) increases sufficiently (and the viscosity consequently decreases sufficiently) to counteract this, and the Rayleigh number quickly increases after convection sets on, stabilising only after 5 Gyr. Consequently, convection would remain active well into the present. Though we do not account for this, melt formation in the convective region once its temperatures exceed the iron solidus (see Fig. 4.4 and the corresponding text in Sec. 4.1.1) is likely to significantly reduce the viscosity, further strengthening the convective motions in the mantle.

4.1.4. Summarising the nominal results

In the nominal scenario, we thus observe the following (roughly qualitative) results for a tide-less Triton:

- A large part of Triton's mantle reaches temperatures necessary for dehydration after ~ 1 Gyr.
- Mantle convection starts after ~ 2 Gyr.
- Triton's ocean has been freezing over for the past ~ 3 Gyr.
- Triton's mantle never reaches equilibrium with the radiogenic heat produced within.
- Triton's convective region reaches the temperatures required to start differentiating iron from silicate after ~ 2.5 Gyr.

As noted in Ch. 3, though, we have made assumptions on several parameters for which a reasonable value is not fully fixed by observation. Consequently, before moving on to the coupled thermal-orbital evolution, we will evaluate how sensitive the results for an isolated interior are to choices of the radiogenic heating rate, mantle composition and initial temperature.

4.2. Sensitivity to mantle conditions

To check whether these nominal results are sensitive to our assumed parameters, we have also run simulations with varied parameters. Here, we will show how varying the radiogenic heating rate (Sec. 4.2.1), mantle composition (Sec. 4.2.2) and initial temperature (Sec. 4.2.3) over the reasonable values selected in Sec. 3.5 affects the evolution of a tideless Triton.

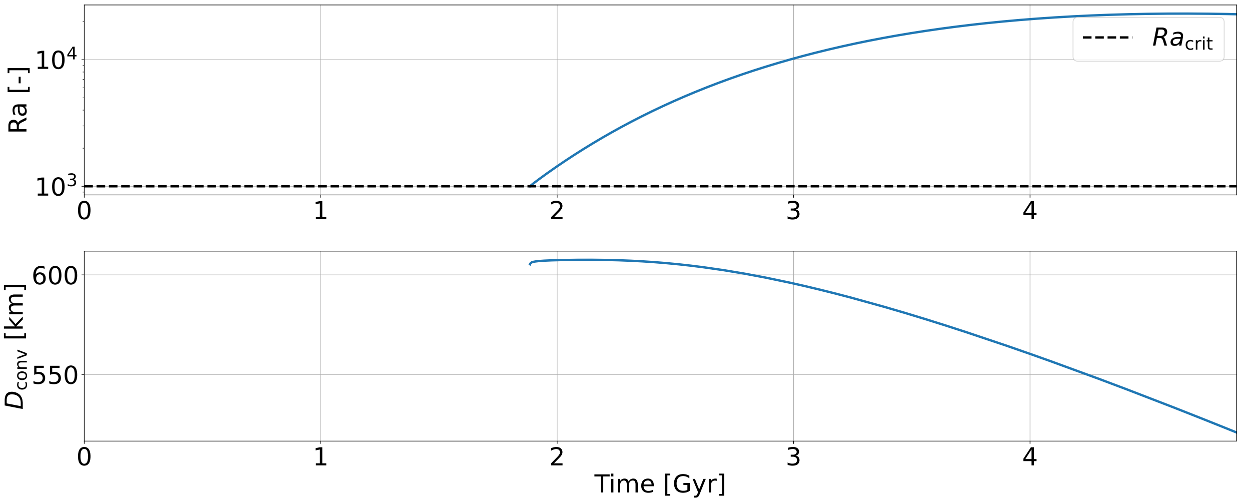

Figure 4.5: Rayleigh number (top) and thickness (bottom) of the convective mantle region over time for the nominal scenario. The dashed line indicates the critical Rayleigh number Ra_{crit}, for which we use a static value of 1000.

4.2.1. Radiogenic heating rate

We have varied the radiogenic heating rates over the range discussed in Sec. 3.5: the resulting evolution of the maximum mantle temperature, ocean thickness, relative heat outflow, as well as the onset of mantle convection, are illustrated in Fig. 4.6. The maximum attained temperature appears relatively stiff to the radiogenic heating rate: increasing the radiogenic heating rate two-fold, in excess even of the 1.7× increase predicted for LL-chondrite by Hussmann et al. (2010), only results in a ~ 250 K (20%) increase in the maximum attained temperature. Varying it by a more modest (and reasonable) ±10% yields a change of only ~ 30 K. More interesting, perhaps, is the difference in the time of convection onset, which appears to be more sensitive to the assumed radiogenic heating rate. Nonetheless, only the lowest assumed radiogenic heating rate never sees convection occurring altogether. A more general statement can be made about dehydration: in all cases, Triton's mantle reaches the temperatures necessary to start dehydration.

For the ocean thickness, the inverse holds: while its value is reasonably sensitive to the assumed radiogenic heating rate, its timeline is less affected. Only the 0.5× radiogenic heating-Triton shows a significant divergence, freezing over within 500 Myr. In all other cases, the ocean thickness for the first ~ 1 − 1.5 Gyr or so, and then proceeds to freeze over for the next 3 Gyr. With the exception of the 0.9× scenario, the ocean is at present thinning, but not (yet) frozen over. This behaviour can largely be attributed to the response of the mantle outflow to a change in radiogenic heating rate, shown in the bottom panel of Fig. 4.6: the radiogenic heating rate largely appears to serve to scale the mantle heat outflow nearly proportionally; the mantle heat outflow in turn controls the shell thickness. As we do not include several factors (e.g. solidus-depressing impurities, obliquity tides) that serve to promote the present-day presence of an ocean, we expect that all scenarios will possess an ocean at present once these factors are accounted for.

4.2.2. Mantle composition

To assess the effects of our assumed mantle composition (or rather, the parameters chosen to hide our ignorance thereon), we also vary the mantle density and mantle viscosity. The results of this variation are shown in Fig. 4.7: in interpreting these relations, we recall that the mantle radius is computed self-consistently as a function of the assumed mantle density, so as to satisfy the mass- and radius-constraints available for Triton. Two effects are clear: (1) the (maximum) temperature and onset of convection depend only very weakly on the assumed mantle density, and (2) the difference in ocean thickness is explained entirely by the change in hydrosphere thickness. The mantle flux for a low-density Triton eventually overtaking the outflow for the higher densities seems counter-intuitive, but can be blamed on the higher rock-to-ice (mass) ratio that follows from a lower density (at the same total mass), which in turn results in a higher radiogenic heating rate. This effect is, however, counteracted by the smaller hydrosphere freezing over much quicker. The primary effect of a changing mantle density therefore is found in the resulting change in mantle radius; the only qualitative result that this therefore affects is whether the ocean freezes over or not.

The picture for the mantle reference viscosity is quite different: Fig. 4.8 shows the maximum attained mantle temperature over time for mantle viscosities ranging over five orders of magnitude; ocean thickness and mantle outflow were also compared, but do not differ significantly between scenarios. For these variations of viscosity,

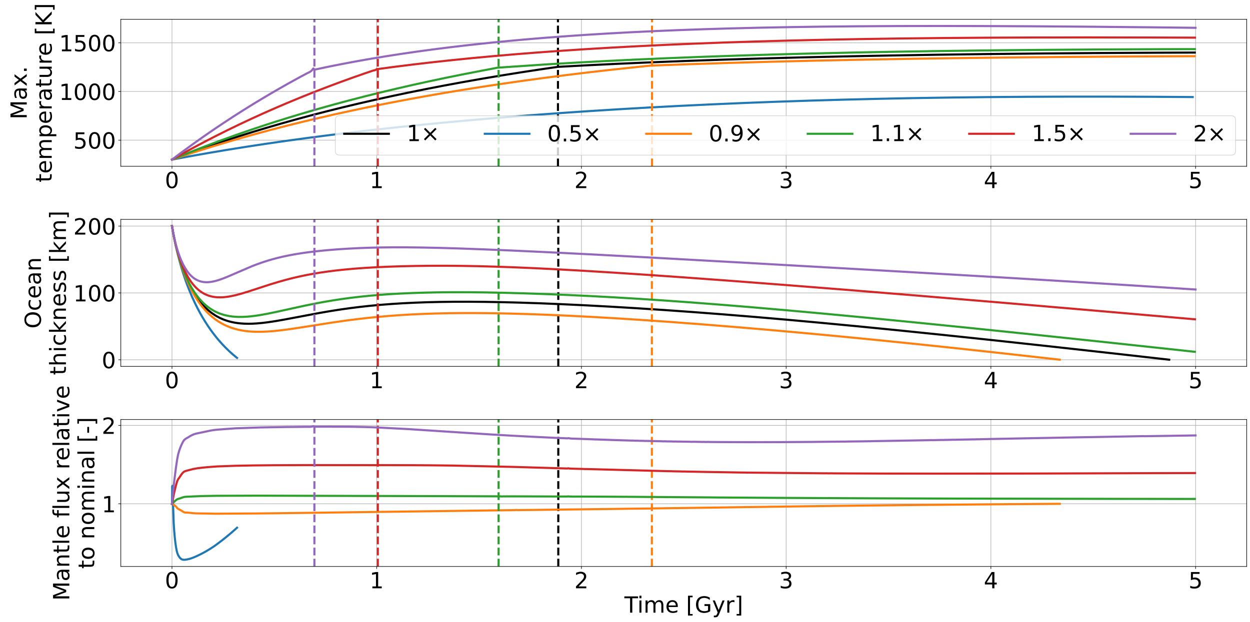

Figure 4.6: Sensitivity of the maximum attained mantle temperature (top), ocean thickness (middle), and mantle heat outflow (relative to the nominal case; bottom) to a multiplicative change in the radiogenic heating rate. Dashed vertical lines indicate the onset of convection in each case.

the time at which convection initiates is pulled forward or delayed by ~ 0.5 and ~ 1 Gyr, respectively. As convection is more efficient at transporting heat out of the mantle than pure conduction, lower viscosities (enabling convection at lower temperature contrasts) suppress the core temperature, while higher viscosities enable pure conduction to endure for longer, leading to higher core temperatures. The variation in attained temperatures at any time when convection has started is on the order of ~ 50 K per order of magnitude change in mantle viscosity, and so this would potentially (though barely) be sufficient to prevent the core from ever exceeding the core formation temperature of ~ 1300 K. As dehydration occurs significantly below the temperatures typically associated with convection, the occurrence thereof is not affected. In the context of Triton, an interesting side-note is the fact that lower mantle viscosities lead to increased mantle dissipation, which might offset this effect for tidally heated moons.

4.2.3. Initial temperature

Finally, we vary the temperature at which we initialise the Tritonian mantle. The resulting evolution of the maximum mantle temperature, ocean thickness and mantle flux are shown in Fig. 4.9. An important observation is the fact that convection stiffens the maximum attained temperature to the initial value. The naive idea that an increase in initial temperature translates to a roughly identical increase in mantle temperature at later times fails when convection has set on; whatever the initial temperature, the maximum mantle temperature after 3 Gyr remains in the region of 1300 – 1500 K. The chief difference between different initial temperatures is the time at which convection initiates.

As can be expected, the increase in available thermal energy associated with a higher initial temperature does translate to an increase in mantle heat outflow, though this difference largely disappears (though never entirely) after ~ 2 Gyr or so (which is expected, as the timescale of diffusion for a rocky body of Triton's size is ~ 3 Gyr). In the most extreme case, this translates to an ocean that is nearly frozen over at present, though a variation of initial temperature cannot alone be sufficient to prevent a present-day ocean. On a qualitative level, changes in radiogenic heating rate and temperature have the same consequences.

4.3. Conclusions

From this sensitivity analysis, we can conclude what the primary effects are of changes in assumed radiogenic heating rate, mantle composition and initial conditions:

- The primary effect of a change in the radiogenic heating rate is to scale the mantle heat outflow, even though the mantle is not in equilibrium. The consequent heating will change the timeline of thermal evolution, but only marginally affects the final temperatures reached. Present-day ocean thickness does vary significantly, from being frozen over at present for the very lowest heating rates, to 100 km thick in the highest-radiogenic heating scenario.

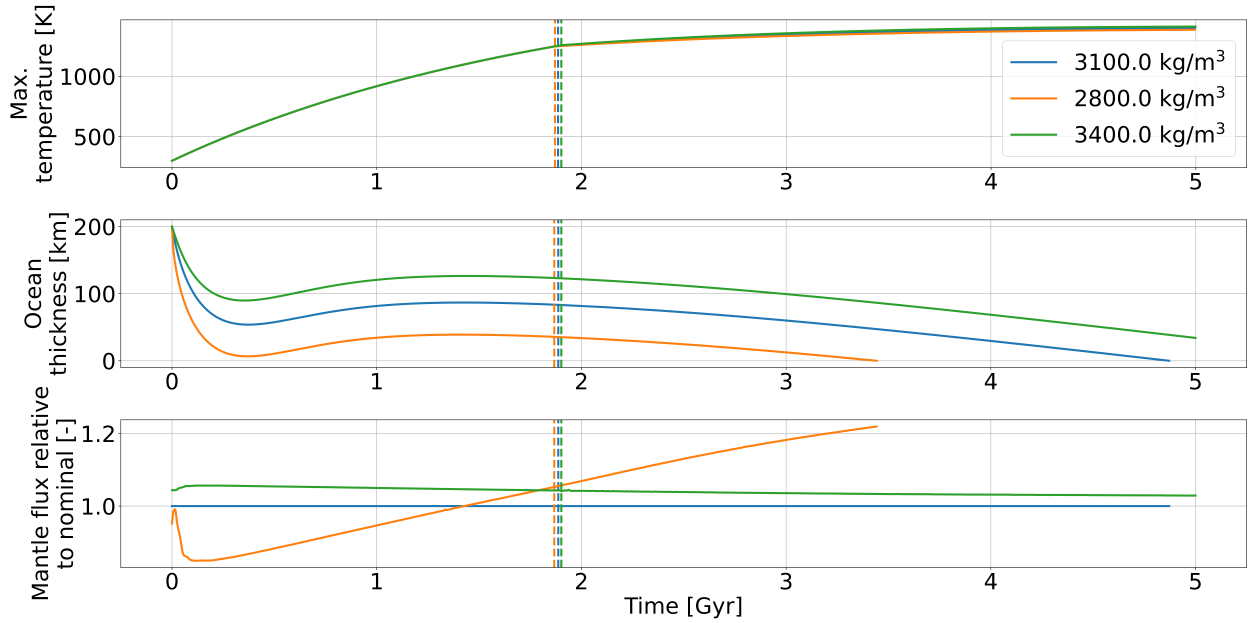

Figure 4.7: Sensitivity of the maximum attained mantle temperature (top), ocean thickness (middle), and mantle heat outflow (relative to the nominal case; bottom) to the assumed mantle density. Dashed vertical lines indicate the onset of convection in each case.

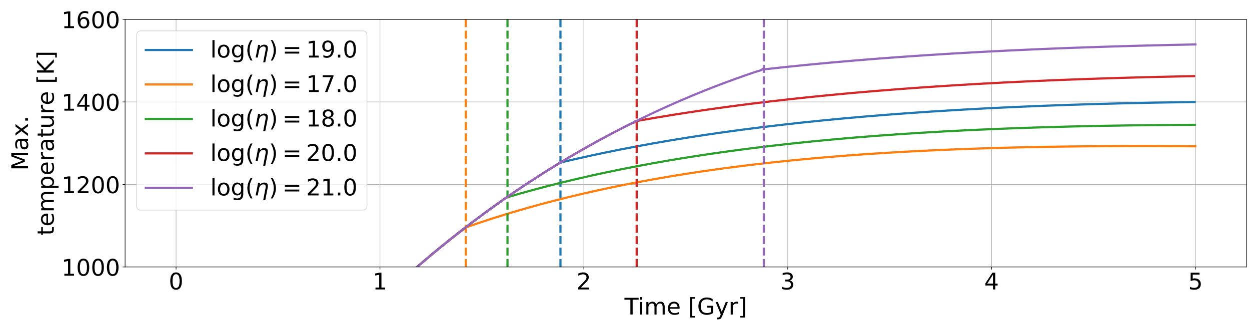

Figure 4.8: Sensitivity of the maximum attained mantle temperature over time as well as the onset of convection to the reference mantle viscosity. Dashed vertical lines indicate the onset of convection. Viscosity values are given in Pa s.

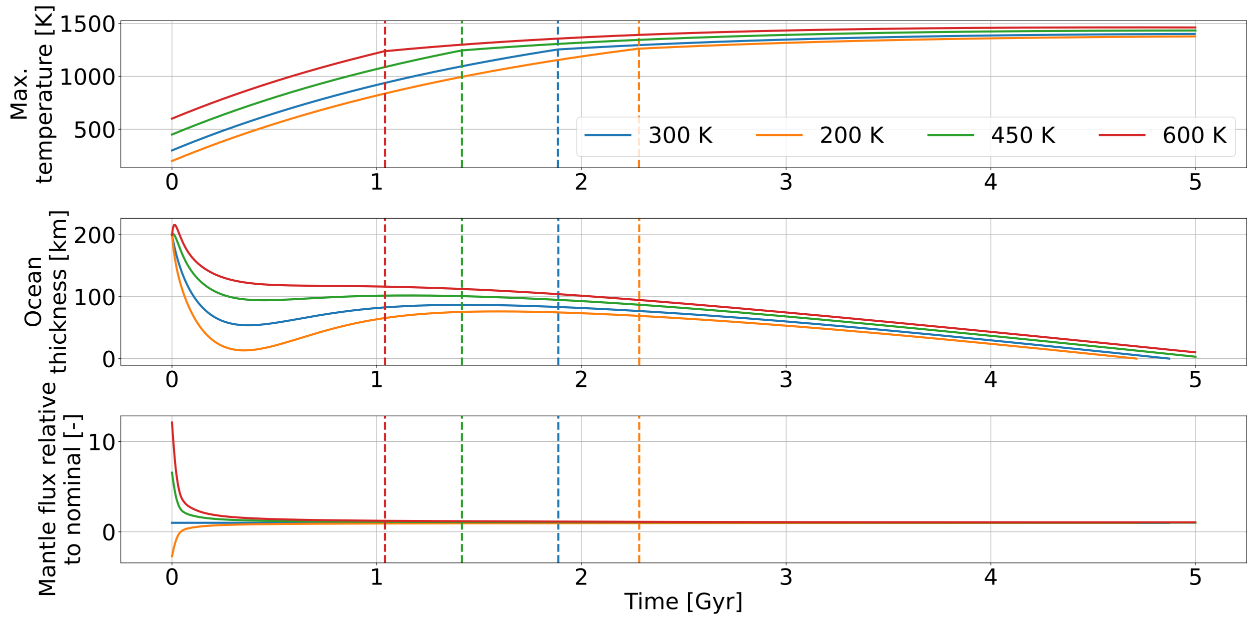

Figure 4.9: Sensitivity of the maximum attained mantle temperature (top), ocean thickness (middle), and mantle heat outflow (relative to the nominal case; bottom) to the assumed initial mantle temperature. Dashed vertical lines indicate the onset of convection in each case. The initially negative mantle outflow for an initial temperature of 200 K is an expected result for mantle temperatures below the ocean temperature, not an anomaly.

- Altering the initial temperature profile leads to a similar shift in the conductive regime, but does not affect the maximum temperatures attained over the convective regime much. Heuristically, changes in the initial temperature and radiogenic heating rate have similar effects.
- The effect of a change of mantle density is most significant in its secondary effects due to the mass-radius constraints: that is, in the associated change in mantle radius, rock-to-ice ratio and consequently in the radiogenic heating rate.
- Changes in mantle viscosity delay or expedite the onset of mantle convection by up to ~ 1 Gyr, leading to changes in the maximum mantle temperature on the order of ± 100 K.

With these results of the sensitivity analysis, we can thus apply some nuance to the nominal results of Sec. 4.1. With this in mind, we find the following for a Triton not subject to tides:

- Triton's mantle largely reaches the temperatures necessary for dehydration, regardless of our assumed values or initial conditions. For the most plausible scenarios, this happens between $\sim 0.5 - 1.5$ Gyr after CAI.
- Triton's mantle starts convecting, unless we significantly overestimate radiogenic heating. Most plausibly, this happens somewhere between $\sim 1.5 - 2.5$ Gyr after CAI.
- Triton's ocean has been freezing over for the past $\sim 3 - 3.5$ Gyr.
- Triton's mantle does not reach equilibrium with the radiogenic heat produced within, though the non-equilibrium mantle outflow does scale roughly proportional to radiogenic heat.
- Unless we significantly overestimate radiogenic heating, Triton's deep interior reaches temperatures at which we can expect rock-iron differentiation to occur. For plausible scenarios, this first happens after ~ 2 Gyr, though a particularly hot start or enhanced radiogenic heating might push this back to ~ 1.5 Gyr.

Additionally, one conclusion that can be drawn from the sensitivity analysis is interesting in its own right in the context of the coupled results that we will present in Ch. 5: the enhanced convection enabled by lower viscosities more efficiently cools the mantle, potentially offsetting the additional tidal heating a lower viscosity might enable.

5 Thermal-orbital evolution

With the tideless thermal evolution of Ch. 4, we now have a reference scenario against which to interpret the effects of combined thermal-orbital evolution. Hence, Sec. 5.1 presents the combined thermal-orbital evolution for our reference scenario. In Sec. 5.2, we present a comparison of this nominal model to a set of interior models coupled to simplified dynamical models. The results presented in Secs. 5.1 5.2 warrant a deeper dive into the evolution of Triton's tidal response, which is presented in Sec. 5.3. Finally, we conclude with an overview of the nominal results we derive on Triton's thermal-orbital evolution in Sec. 5.4.

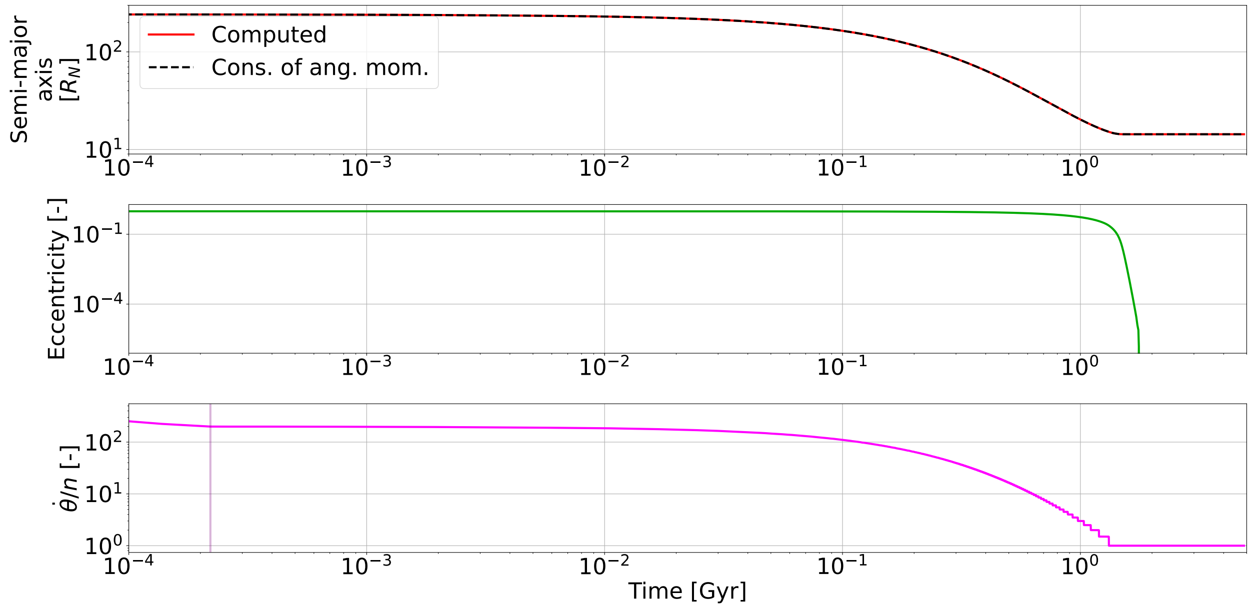

Figure 5.1: Evolution of the semimajor axis (top), eccentricity (middle), and rotational rate (in units of mean motions; bottom) over time for the nominal scenario. The dashed line indicates the evolution of the semi-major axis consistent with conservation of angular momentum according to the evolution of the eccentricity, which we can see is identical to that returned by the integrator. The vertical purple line in the evolution of the rotational rate indicates the time beyond which we assume equilibrium rotation. The stair-step behaviour of the rotational rate is real (i.e. not an integration artefact), and shows the decay of Triton through spin-orbit resonances, finally ending in the 1:1 resonance.

5.1. Nominal results

We will start by showing the nominal results: in Sec. 5.1.1, we will present the dynamical results of this simulation, and Sec. 5.1.2 will show the accompanying results on interior evolution. In Sec. 5.1.3, we return to dynamics to take a deeper look at the feedback between spin- and orbit in particular, as that part of the dynamics is best understood with the background of the interior evolution in mind.

5.1.1. Dynamical evolution

We will first provide the results for the dynamical evolution, as these provide the backdrop against which the interior must be compared to the isolated, tideless case of Ch. 4. Fig. 5.1 shows the evolution of the three orbital quantities that we propagated, being the semi-major axis, eccentricity and the rotational rate. The semi-major axis computed by conservation of angular momentum through the eccentricity (see Sec. C.1.2) is also shown, and corresponds to that returned by the integrator. The rates of change of the semi-major axis and eccentricity are also given in Fig. 5.2. We show the energy dissipated in Triton's shell and mantle in Fig. 5.3: we can check that the combined dynamical and interior evolution satisfy conservation of energy (Sec. C.1.2), as indicated by the dashed line. Note that we show dynamical quantities using a logarithmic time-scale, so as to highlight the early evolution: keep in mind that we will instead prefer to show the interior results using a linear scale.

In this scenario, Triton takes about ~ 1.7 Gyr to circularise. While this is in agreement with what Hammond & Collins (2024) find, they find different circularisation timescales dependent on the rheology assumed for ice, which they compute in much more detail. We will evaluate whether this behaviour is reproduced in Sec. 6.2.2. In line with what would be expected based on conservation of angular momentum, most of the semi-major axis

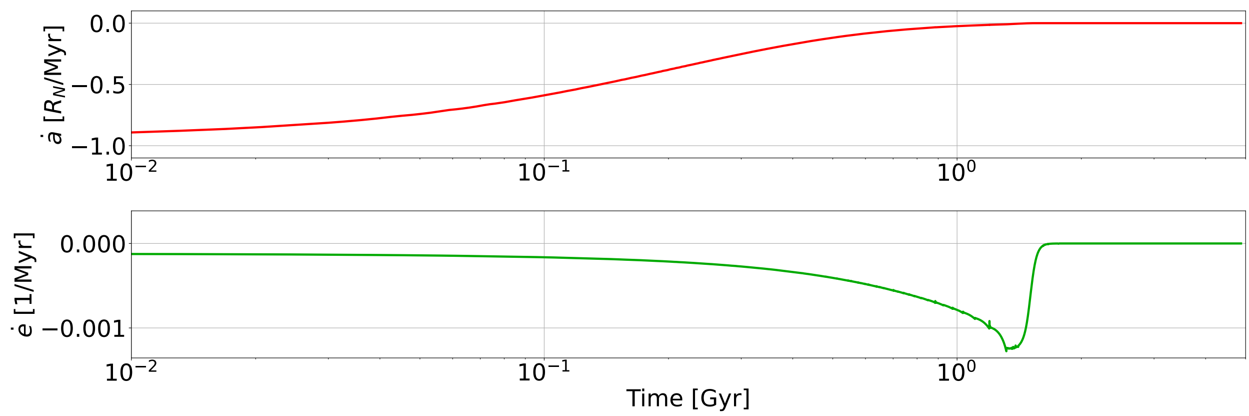

Figure 5.2: Rates of change of the semimajor axis (top) and eccentricity (bottom) over time in the nominal case. The spikes in the eccentricity rate are real, not integration or interpolation artefacts, and coincide with decay between spin-orbit resonances.

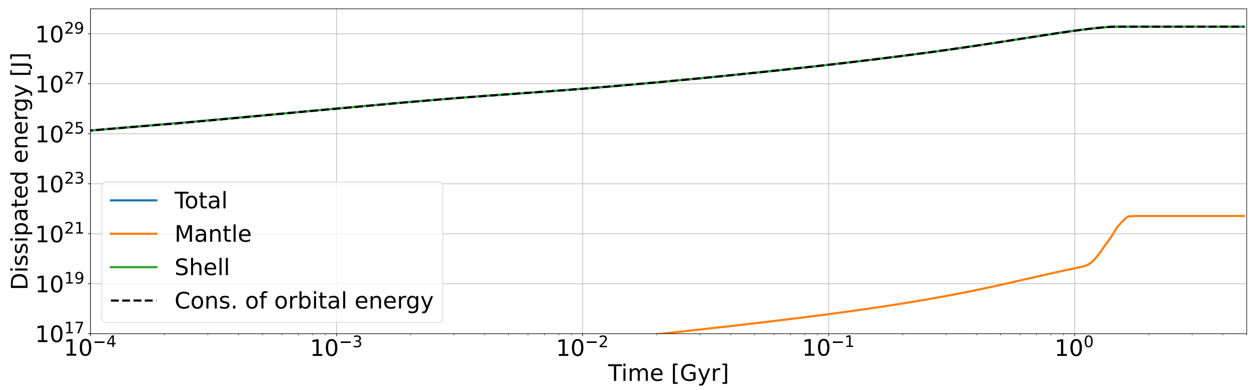

Figure 5.3: Dissipated energy in Triton's shell and mantle, as well as the amount of dissipated energy predicted by conservation of energy. The shell contribution dominates the dissipated energy, and so the total and shell dissipation values overplot.

evolution happens at high eccentricity, with the eccentricity only damping out at the very end. The dissipation rate (shown in Fig. 5.6; we will discuss the relevant heat flows in more detail in Sec. 5.1.2) is briefly very intense initially, as a result of the initial non-equilibrium rotation rate and the shell not yet being at its equilibrium thickness, but then settles into a lower-dissipation state. This dissipation rate slowly comes to a peak after ~ 1 Gyr, but overall the dissipation rate is spread out with dissipation rates of $\sim 2 - 6 \cdot 10^3$ GW over the full epoch of circularisation: this places it well above estimates of ~25-40 GW for the present-day heat loss of Enceladus (Nimmo et al., 2023), but severely in deficit of the $\sim 10^{11}$ GW for that of Io (Lainey et al., 2009).

5.1.2. Interior evolution

Aside from Triton's dynamics, its interior of course also evolves. An important contribution here is made by tidal dissipation, which proves to be an important heat flow in the coupled evolution of Triton's interior and orbit. We start with an overview of Triton's interior evolution: Fig. 5.4 shows the evolution of Triton's interior over time. In comparison to the tideless scenario (Fig. 4.1), it is clear that the shell experiences a significant disruption. The ocean and shell thicknesses over time are shown in Fig. 5.5, and corroborate this story: during the epoch of intense dynamical activity shown in Sec. 5.1.1, Triton's shell thins significantly. Afterwards, Triton's interior, broadly speaking, appears to retain little thermal memory of this dynamically active state.

Fig. 5.6 shows the heat fluxes through Triton over time. In contrast to the tideless case, we see that there is a significant variation in power radiated away at Triton's surface, with the power dissipated in the shell contributing a large component upwards of 10^3 GW at its peak. Correspondingly, as can be seen in the bottom panel of Fig. 5.7, the surface temperature reaches temperatures in excess of 50 K, significantly in excess of its equilibrium temperature. Dissipation in the mantle is negligible compared to all other heat flows, however, never exceeding 10^{-3} GW, and the mantle outflow is therefore not appreciably different from the tideless case. Indeed, the conditions in the mantle are altogether not any different than the tideless case, reflected in the temperature evolution shown for the mantle in the top panel of Fig. 5.7 being identical to the tideless case shown in Ch. 4. While this result meshes with those of Hammond & Collins (2024), it does not agree with the

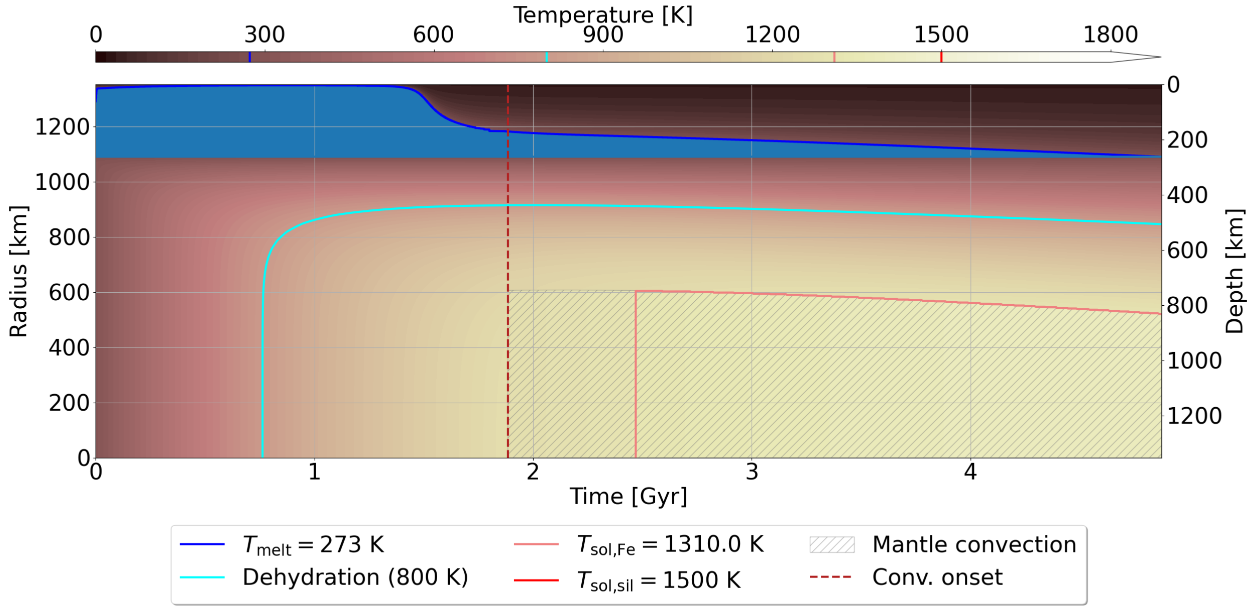

Figure 5.4: Evolution of the thermal profile throughout Triton through time in the nominal case including tides. The stair-step pattern at the ocean-ice interface is a plotting artefact, and the true evolution of the ocean thickness is continuous and smooth (see Fig. 5.5). Also indicated are the convective region, the melting temperature of pure water, as well as approximate values for the temperature of dehydration onset in silicate (Perrillat et al., 2005), the solidus temperature of silicates (Hammond & Collins, 2024) and the 20% melt-fraction temperature of iron (Taylor, 1992; Neumann et al., 2012).

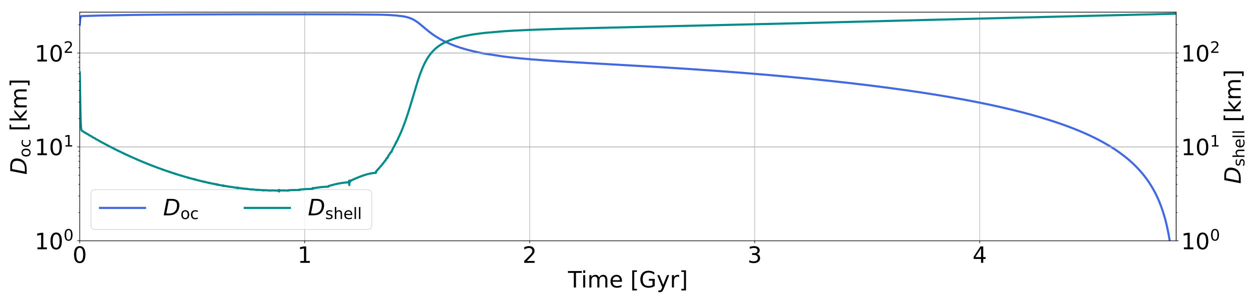

Figure 5.5: Evolution of the ocean and shell thickness over time for the tidally evolving, nominal scenario.

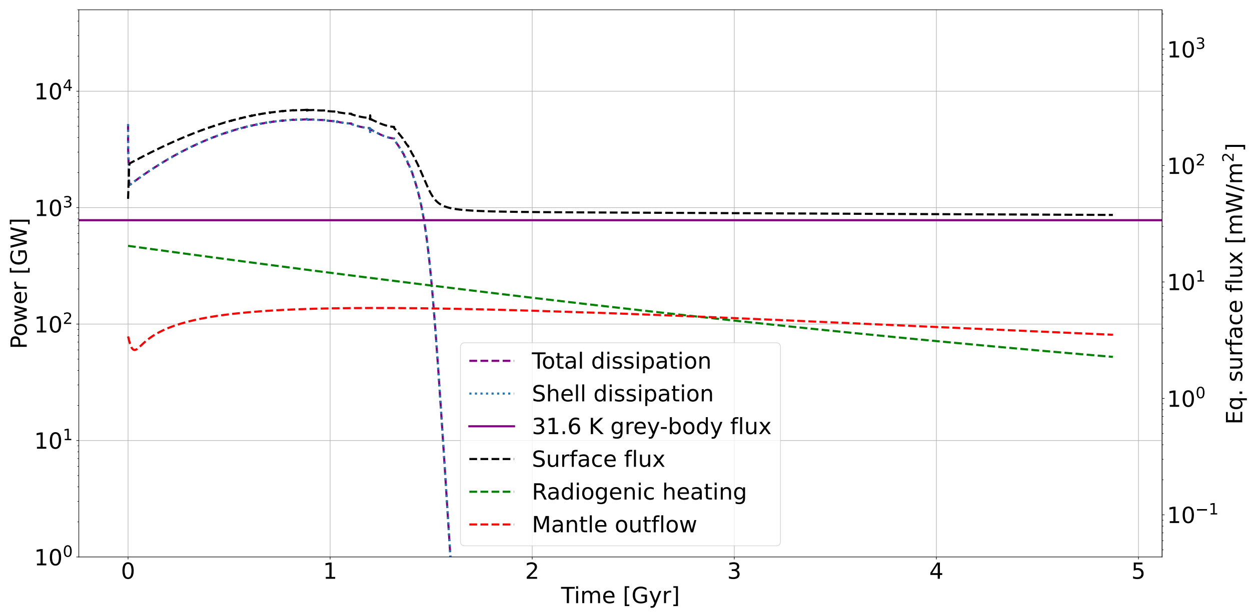

Figure 5.6: Relevant heat flows over time for the nominal, coupled dynamical-interior evolution of Triton. Shown are the total power and the equivalent surface flux i.e. the power normalised to the surface area of Triton (and so the mantle outflow is *not* scaled to the mantle area, and should therefore be scaled by $(R_m/R)^2$ to yield the true mantle heat flux). For comparison, the surface heat flux expected for a body of Triton's size and emissivity emitting grey-body radiation at the equilibrium temperature at Neptune are shown. Mantle dissipation amounts to less than 10^{-3} GW at all times, and is therefore not shown. For this same reason the shell and total dissipation lines overplot, though we show either for completeness.

description of McKinnon et al. (1995); we will investigate this discrepancy in further detail in Ch. 6.

5.1.3. Triton's spin-orbit evolution

The rotational rate of Triton over time, expressed as a ratio of its mean motion, is given in the bottom panel of Fig. 5.1. Over a large part of the circularisation process, Triton is not in synchronous rotation as e.g. Hammond & Collins (2024) assume; it takes about 1.3 Gyr for Triton to settle into the 1:1 spin-orbit resonance. When it does so, it does so without passing through pseudo-synchronous rotation, in line with the expectations of Makarov & Efroimsky (2013) for moons whose tidal response is not well-described by the CTL model. However, it takes only ~ 0.2 Myr for Triton to achieve a state of rotational equilibrium, and afterwards the equilibriation timescale is always on the order of ~ 0.1 Myr or smaller. Hence, while synchronous rotation is not a good approximation, the assumption of equilibrium rotation does appear to be valid.

The equilibrium rotation rate value is determined by a combination of factors, but most importantly by (1) the eccentricity and obliquity of the body and (2) its interior structure and rheology (e.g. Renaud et al., 2021). As we keep the obliquity fixed at zero, we expect that the driving factors should be the eccentricity and interior of the body. We will vary the interior properties of Triton and evaluate whether that has any effects on the evolution of the equilibrium rotation rate in Ch. 6, and so we will restrict the discussion in this chapter to the evolution with eccentricity. Though in the context of a rocky exoplanet rather than an icy moon like Triton, Renaud et al. (2021) evaluate rotational evolution as a function of eccentricity, and note that viscous bodies will maintain an equilibrium (resonant) rotation rate until the eccentricity is lowered enough, when the previous equilibrium rate abruptly becomes unstable, and the equilibrium rotation rate drops to the next half-integer resonance (see e.g. their Figs. 6-8). Fig. 5.8 shows the evolution of the rotational rate as a function of the accompanying eccentricity, and it can be seen that Triton's evolution clearly follows this pattern. As the accompanying spikes in tidal dissipation are relatively minute, we should not expect (though we cannot rule out the possibility) that this spin-orbit resonance progression will have left any observational consequences at present, however: the primary consequence of this rotational state will be in affecting the forcing frequencies that are excited in Triton.

5.2. Comparison against simplified dynamical models

A large number of simplified models are frequently used to approximate tidally-driven dynamical evolution in a computationally affordable or conceptually simple manner. Hence, we compare the coupled evolution of our model to the predictions made by several simpler models.

While the CTL model often finds use, Van Woerkom (2024) showed that its use is not justified in cases like

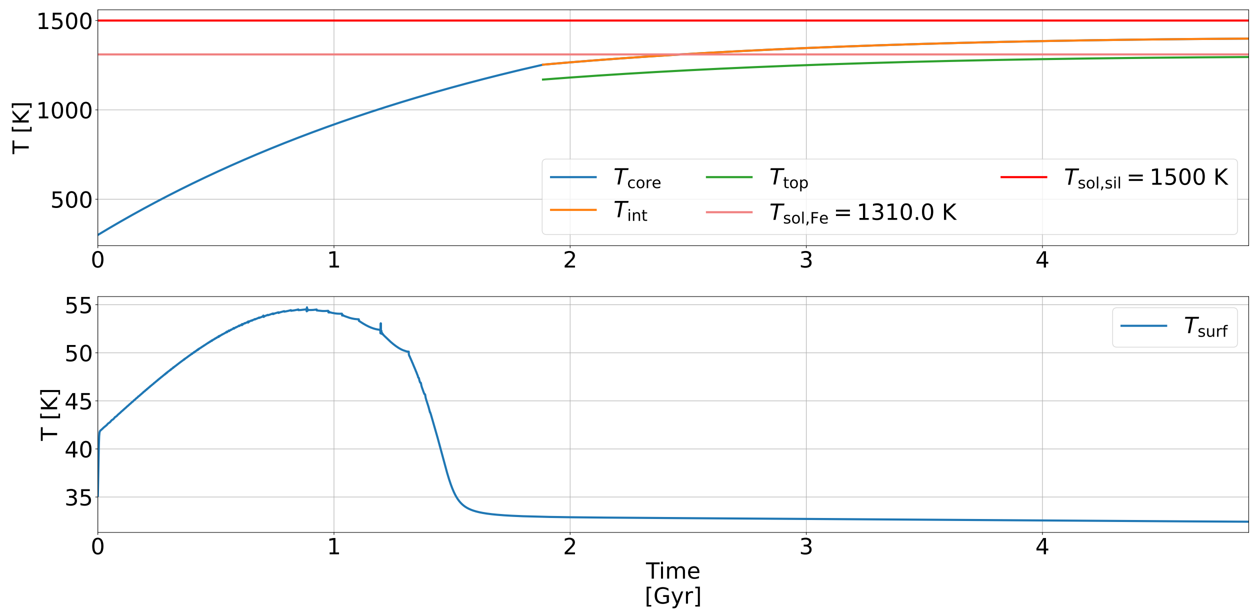

Figure 5.7: The time-dependent evolution of key mantle temperatures (top) and the surface temperature (bottom) for a nominal, tidally evolving Triton.

that of Triton, at high eccentricity, as the additionally excited tidal Fourier modes at such eccentricities do not follow the linear relation with frequency that is assumed (implicitly or explicitly) when using the CTL model, grossly misestimating both tidal dissipation as well as failing to correctly predict possibly important phenomena such as spin-orbit resonances. Hence, we will consider only the CPL model of MacDonald (1964)[1], as used by Hammond & Collins (2024), and a version of the CPL model that simply takes the equations of motion (Eqs. 3.1-3.4), with the Darwin-Kaula expansion (Eq. 3.8) truncated to include only the terms for which the tidal quality function is evaluated at the orbital rate or its negative[2], which in this case corresponds to terms with $|q| \leq 1$; this expression is roughly equivalent to the CPL expressions that are commonly derived for low eccentricities. To investigate whether an approximation of only the first couple of terms can perhaps suffice, we also test a run in which we include only the terms with $|q| \leq 10$. We also perform a run using a decoupled model: in this instance, we use an evolving interior model (with the correspondingly evolving tidal quality function), but without incorporating tidal heating in the interior evolution.

The resulting predictions for the dynamical evolution are shown in Fig. 5.9. A first observation is the fact that the decoupled model underestimates the tidal evolution timescale by a factor of ~ 3, lending credence to the proposal of Hammond & Collins (2024) that tidally-induced thinning of Triton's shell extends its circularisation timescale; that is, to accurately describe Triton's orbital evolution, one needs to account for the resulting interior evolution. A second result pertaining to the decoupled model (though not shown) is the fact that it alone does not get locked into any spin-orbit resonances, whereas the other models do.

Additionally, we note that the two approximations including only the lower terms $|q| \leq 1$ and $|q| \leq 10$ fail to circularise in the age of the Solar System: their use is thus clearly not warranted. Broadly speaking, this is in line with the results of Van Woerkom (2024), who used a companion series of the Darwin-Kaula expansion to bound the number of terms one needs to expand it to. This indicates that the tidal Fourier modes responsible for the greatest amount of dissipated energy correspond to a tidal Fourier mode with $|q| > 10$: Van Woerkom (2024) finds that one needs ≥ 1000 terms to correctly truncate the Darwin-Kaula expansion at such high eccentricities. In a similar setting (the high-eccentricity evolution of the exoplanet TRAPPIST-1e), Renaud et al. (2021) showed that lower-order truncations of the Darwin-Kaula expansion underestimate tidal heating by several orders of magnitude: Fig. 5.10 shows the dissipated power over time, and it is clear that the truncated versions all significantly underestimate the true tidal heating; for the $|q| \leq 1$-approximation, we are off by five orders of magnitude, and even the $|q| \leq 10$-approximation is off by three orders of magnitude.

It is surprising, then, that the constant phase-lag expression derived by MacDonald (1964), despite its inherent limitations, does so well: simplified tidal models tend to underestimate dissipation (Renaud et al., 2021), so it is not a given that the model of MacDonald (1964) gives an estimate of tidal evolution that is close to the prediction

[1] Note that this model implicitly assumes synchronous rotation, too.
[2] The tidal quality function is in general an odd function, such that $K_l(-\omega) = -K_l(\omega)$.

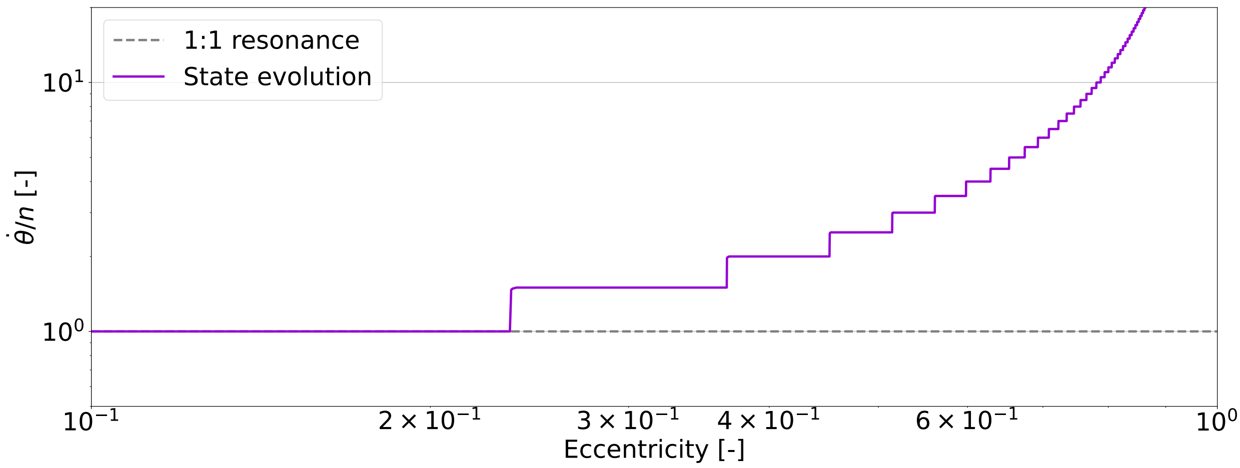

Figure 5.8: The migration of the state of Triton through the phase space of eccentricity and spin rate over time for the nominal scenario: the values of the eccentricity over time are plotted against the corresponding value of the spin rate normalised to the mean motion. The discrete, step-like behaviour is real, and not an interpolation or integration artefact.

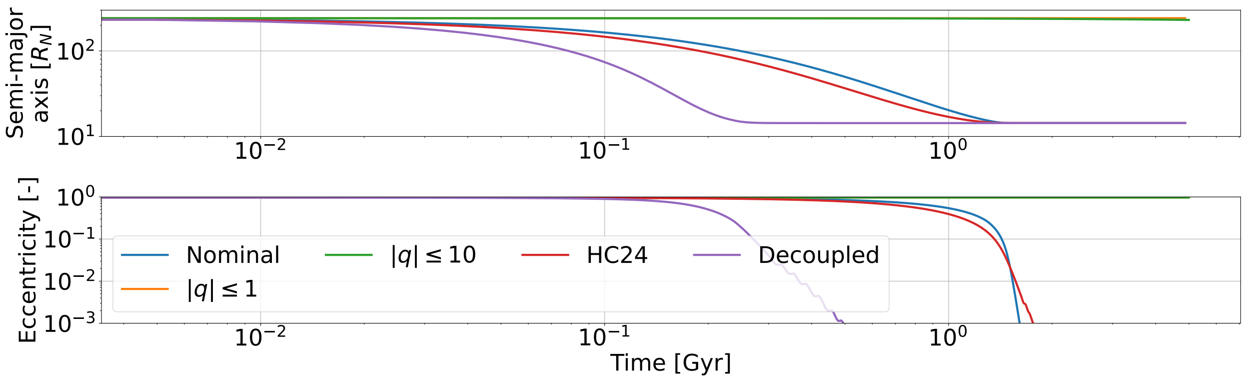

Figure 5.9: Evolution of the semi-major axis and eccentricity over time for the nominal scenario using our nominal model, versions of the Darwin-Kaula expansion truncated to the terms $|q| \leq 1$ and $|q| \leq 10$, the model of MacDonald (1964) used by Hammond & Collins (2024), denoted as "HC24," and a decoupled model, with the tidal quality function evolving according to the interior evolution of the tideless scenario.

accounting for the frequency-variation of the tidal response. The root cause for this result, we expect, is the fact that the active tidal modes of Triton all occur in the rigid-mantle regime of the tidal quality function, as the tidal quality function (and correspondingly, the phase lag) is close to constant here. In contrast to the truncated versions of the Darwin-Kaula expansion, the constant phase-lag model of MacDonald (1964) is therefore not off by orders of magnitude, but only by some factor determined by the (small) variation of the tidal quality function that *does* occur with frequency in the rigid-mantle domain.

5.3. The coupled evolution of Triton's tidal response

We test this hypothesis by analysing the frequency-dependence of Triton's tidal response over time, and investigating at which frequencies the majority of Triton's tidal response is sampled. To do so, we will first study the evolution of the tidal quality function (due to evolution of the interior) of Triton over time in Sec. 5.3.1. We will also examine the frequency-dependence of the partitioning of dissipation between the shell and mantle and its evolution over time in Sec. 5.3.2. To finally explain the results we see, we can then combine the analysis of Sec. 5.3.1 and Sec. 5.3.2 with an analysis of the evolution of the excited tidal forcing frequencies over time: we will present this in Sec. 5.3.3.

5.3.1. Evolution of the tidal quality function

Fig. 5.11 shows the evolution of the tidal quality function for a broad range of frequencies over time: we will elaborate upon the $n/2$-line momentarily. From the panel above, showing the co-evolution of the maximum mantle temperature and the shell thickness over time, we infer that the evolution of the shell thickness is responsible for the changes at frequencies $> 10^{-14}$ rad/s, while the mantle temperature only appears to affect

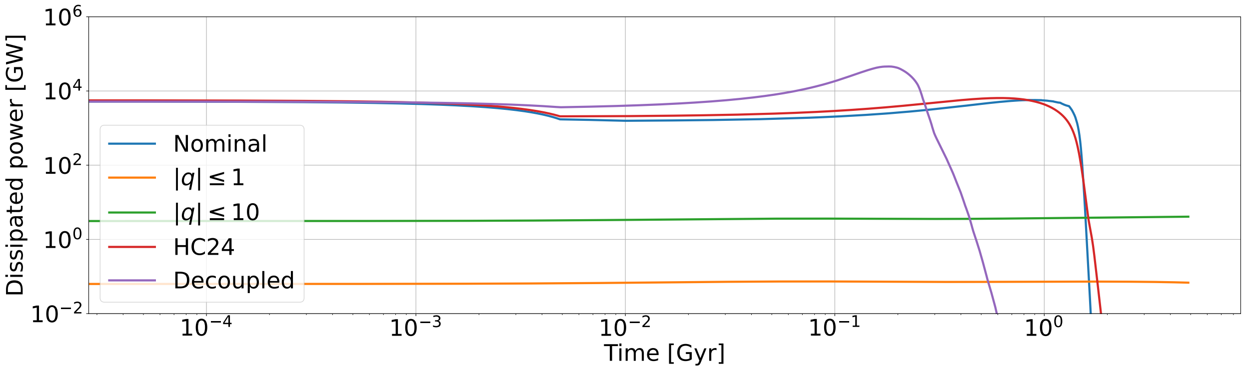

Figure 5.10: Evolution of the dissipated tidal power over time for the nominal scenario using our nominal model, versions of the Darwin-Kaula expansion truncated to the terms $|q| \leq 1$ and $|q| \leq 10$, the model of MacDonald (1964) used by Hammond & Collins (2024), denoted as "HC24'," and a decoupled model, with the tidal quality function evolving according to the interior evolution of the tideless scenario. The spiked structure around ~ 1.5 Gyr for the nominal scenario is real, and a result of Triton passing through spin-orbit resonances.

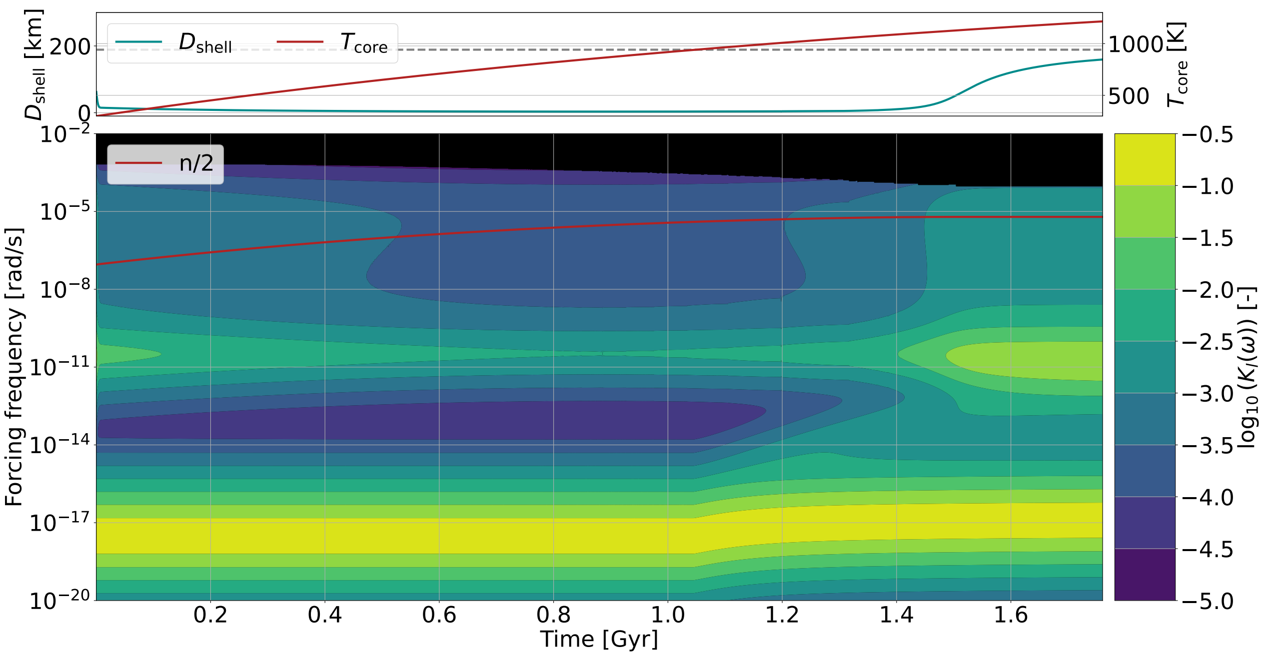

Figure 5.11: Time-evolution of the degree-2 tidal quality function $K_2(\omega)$ as a function of forcing frequency ω in the nominal scenario. For reference, we also plot the shell thickness and maximum mantle temperature (which control the tidal response) over time in the top panel; the dashed line indicates the temperature below which the mantle viscosity is set to the maximum value of 10^{26} Pa s, explaining the lack of change in the low-frequency regime at earlier times. Black regions are upper bounds above which frequency space is not sampled by the Darwin-Kaula expansion at the corresponding time, and therefore we do not compute the tidal response in those regions. The half-mean motion ($n/2$) line indicates the bound below which sampling by the Darwin-Kaula expansion should theoretically be sparse (see Fig. 5.13).

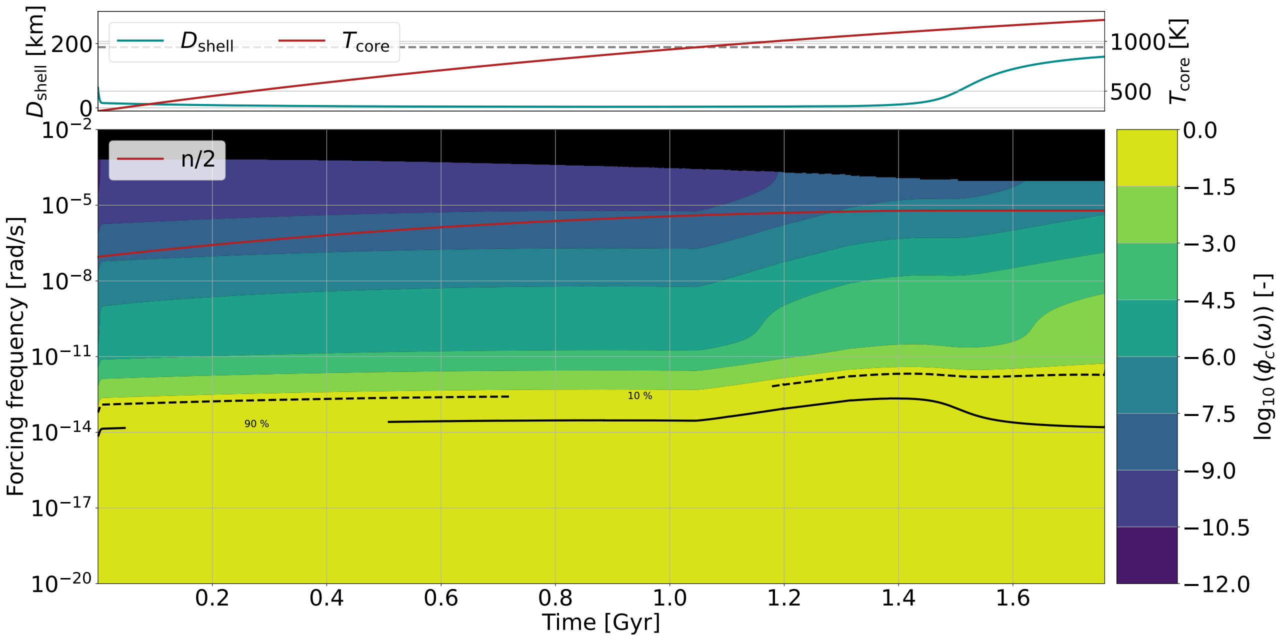

Figure 5.12: Evolution of the mantle-shell partitioning of dissipated power at various frequencies over time. For reference, we also plot the shell thickness and maximum mantle temperature (which control the tidal response) over time in the top panel; the dashed line indicates the temperature below which the mantle viscosity is set to the maximum value of 10^{26} Pa s, explaining the lack of change in the low-frequency regime at earlier times. Black regions are upper bounds above which frequency space is not sampled by the Darwin-Kaula expansion at the corresponding time, and therefore we do not compute the tidal response in those regions; the dashed and solid black lines show the 10% and 90% mantle dissipation fraction contours, respectively. The half-mean motion ($n/2$) line indicates the bound below which sampling by the Darwin-Kaula expansion should theoretically be sparse (see Fig. 5.13).

the evolution of the (very) low-frequency tidal response.

In principle, this aligns with our understanding of the thin-shell tidal response: the fluid-crust tidal response (which dominates at low frequencies) is largely governed by the properties of the mantle, while the rigid-mantle response (dominant at high frequencies) is controlled by the shell (see Sec. C.3.2 for an elaboration on terminology and a numerical exploration of the thin-shell tidal response). The burning question that remains, then, is at which frequencies the tidal response is sampled in the dynamical evolution of Triton. Before answering this question (which we will defer to Sec. 5.3.3), we will first give this suspicion more weight: beyond this heuristic explanation, it is in fact possible to show that the low-frequency tidal response preferentially dissipates in the mantle, while the dissipation due to the tidal response forced at higher frequencies is instead located overwhelmingly in the shell: we will briefly examine this relationship in Sec. 5.3.2.

5.3.2. Evolution of the mantle-shell partitioning of tidal dissipation

The thin-shell expressions of Beuthe (2019) allow one to derive an expression for the partitioning of dissipated tidal power between the mantle and shell that depends only on forcing frequency, $\phi_c(\omega)$ (Eq. 3.36); that is, in the tidal dissipation-expression given in Eq. 3.8, a fraction $\phi_c(\omega_{lmpq})$ of the term corresponding to the indices $(lmpq)$ will go into the mantle, and the remaining part $(1 - \phi_c(\omega_{lmpq}))$ is dissipated in the shell. We can therefore also compute and study the evolution and frequency-dependence of this mantle-dissipation fraction over time, separate from the particular values of the excited tidal Fourier frequencies ω_{lmpq} at each point in time.

We do precisely this, and the result is shown in Fig. 5.12. As with the tidal quality function, the mantle-shell partitioning factor ϕ_c shows significant differences at different forcing frequencies. While the mantle dissipation fraction quickly goes to unity at frequencies below $\sim 10^{-13}$ rad/s, the amount of mantle dissipation is generally negligible for forcing frequencies above $\sim 10^{-11}$ rad/s. A natural explanation for the lack of dissipation we observed in the mantle in Sec. 5.1 is then for the forcing frequencies excited in the tidal evolution of Triton to be located primarily in the higher-frequency region, where the mantle does not dissipate significantly. Let us therefore examine the excited tidal forcing frequencies.

5.3.3. Evolution of the tidal forcing frequencies

From the form of the tidal Fourier frequencies that appear in the Darwin-Kaula expansion for the tidal response of Triton (Eq. 3.9):

$$\omega_{T,lmpq} = (l - 2p + q)n - m\dot{\theta}_T \tag{5.1}$$

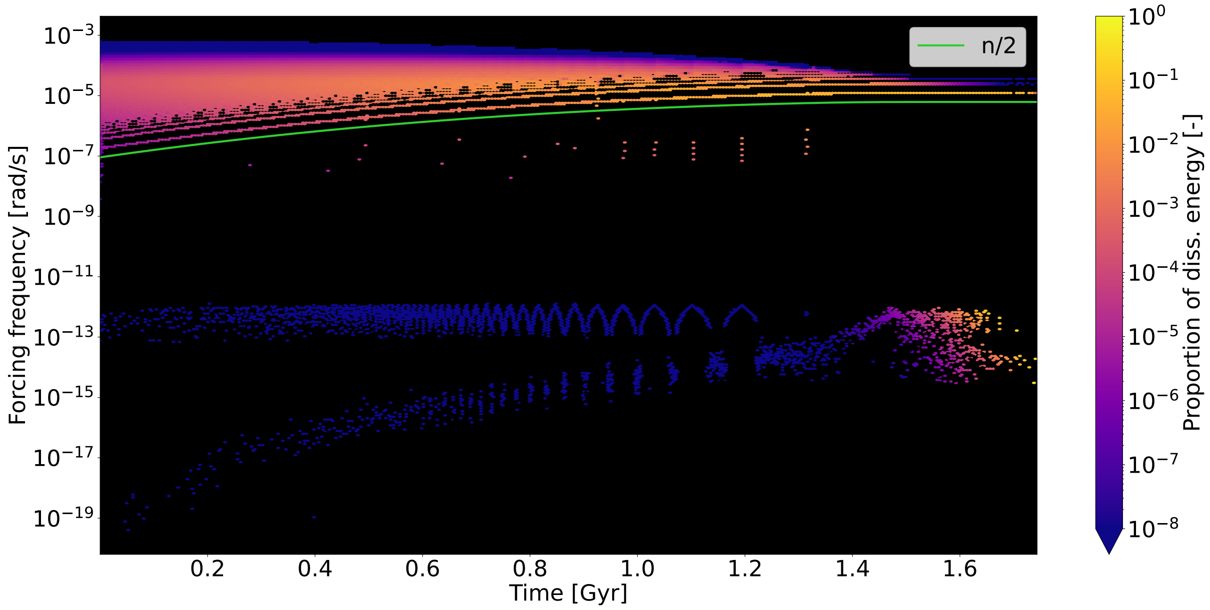

Figure 5.13: Two-dimensional histogram of the forcing frequencies sampled by the Darwin-Kaula expansion over time, weighted by the fraction of the total dissipated energy at that time dissipated at the given frequency; black regions are not sampled. The half-mean motion ($n/2$) line indicates the bound below which sampling by the Darwin-Kaula expansion should theoretically be sparse. The horizontal structures (excepting those resulting from the histogram resolution) seen are physical, and a consequence of the discrete nature of the Darwin-Kaula expansion; the vertical delineations are a result of our sampling in time.

we find that, in resonance (i.e. when $\dot{\theta}_T = rn/2$ for some integer r), there exists one or more tidal Fourier mode with indices $(l'm'p'q')$ such that

$$\omega_{T,l'm'p'q'} = (l' - 2p' + q')n - m'\dot{\theta}_T = \left(l' - 2p' + q' - \frac{m'r}{2}\right) n \approx 0 \tag{5.2}$$

whence it can be shown that the smallest-magnitude non-zero tidal Fourier mode has absolute value $|\omega_{T,lmpq}| \gtrsim n/2$. Hence, we predict that the frequency-values sampled by the Darwin-Kaula expansion will generally be situated above the $n/2$-line; only close-to-resonant frequencies can sample at lower frequencies.

Fig. 5.13 shows a histogram of the tidal frequencies at which the tidal response is sampled at each time in the computation of the dynamical evolution of Triton, weighted by the (fractional) amount of energy dissipated at that frequency. The $n/2$-prediction appears to be largely borne out: only a small number of frequencies (those corresponding to the resonances in which Triton is found at that point in time) sample the tidal response at the low frequencies dictated by the mantle, while the majority of all sampled tidal frequencies are found above the $n/2$-line, where the effect of the shell dominates.

The lack of mantle dissipation observed in Sec. 5.1 and the agreement with the constant phase lag model of Hammond & Collins (2024) found in Sec. 5.2 then share a common explanation: the tidal Fourier frequencies excited in the evolution of Triton are in general on the order of (half) the orbital rate or greater. In this regime, (1) the tidal response is dominated by the rigid-mantle contribution (which varies slowly with frequency), and it is therefore well-approximated (to roughly within an order of magnitude) by the tidal response at the orbital rate, and (2) the mantle dissipates a negligible amount of energy.

5.4. Conclusions

We have investigated the coupled thermal-orbital evolution of Triton, propagating the interior evolution consistently with its dynamical evolution. In doing so we find that, in our reference scenario:

- Triton takes ~ 1.7 Gyr to circularise, for the first ~ 1.3 of which it is in an equilibrium but non-synchronous rotational state, remaining in a higher-order spin-orbit resonance until its eccentricity damps to ~ 0.2.
- Mantle dissipation is negligible, and practically all of Triton's orbital energy dissipates in its shell.
- Correspondingly, during circularisation, Triton's shell becomes $\lesssim 10$ km thick, while its mantle evolves identically to the tideless case.
- After circularising, Triton's interior rapidly goes back to its unperturbed state, with conditions practically identical to the tideless scenario of Ch. 4.

We assessed how our model differs from several often-used approximations, as well as the recent model of Hammond & Collins (2024) and a decoupled thermal-orbital model. In this context, we can conclude:

- Lower-order truncations of the Darwin-Kaula expansion severely underestimate the dissipation rate at higher eccentricities.
- The orbital evolution of Triton cannot be modelled accurately without accounting for interior-orbital feedback.
- The constant phase-lag model of MacDonald (1964), used by Hammond & Collins (2024), agrees remarkably well (though not exactly) with our model.

Finally, we investigated the forcing frequencies at which Triton's tidal response is excited during its dynamical evolution. From this analysis, we conclude that both (1) the lack of mantle dissipation and (2) the surprisingly good agreement with the constant phase-lag model of MacDonald (1964) can be explained by the slowly-varying behaviour of the tidal response for our assumed interior model at the frequencies at which it is excited during Triton's post-capture evolution. The small variation that the tidal response *does* experience over the range of sampled frequencies is sufficient to cause the dynamical model of MacDonald (1964) to slightly overestimate dissipation at high eccentricities, while underestimating them at lower eccentricities: when corrected for this effect, the evolution of Triton or the timescales involved are not qualitatively different from the predictions of Hammond & Collins (2024), though. Of course, the tidal response does hinge on the assumptions we have made on Triton's interior: hence, we will assess the sensitivity of these results to our assumptions in Ch. 6.

6 Sensitivity of Triton's coupled evolution

Before being ready to accept the conclusions that follow from the results presented in Ch. 5, we must also assess their sensitivity to the assumptions we have made. Of particular interest is the discrepancy in mantle dissipation we find with respect to earlier results, already identified by Hammond & Collins (2024); though we have explained this phenomenon in Ch. 5, it remains to see whether this explanation hinges implicitly any assumptions on the mantle. Hence, we perform a sensitivity analysis with respect to mantle conditions in Sec. 6.1. We perform a sensitivity analysis with respect to the remaining uncertain parameters in Sec. 6.2, and finally apply nuance to some of the conclusions drawn in Ch. 5, concluding in Sec. 6.3.

6.1. The susceptibility of Triton's mantle to tidal heating

In the nominal scenario, tidal dissipation in Triton's mantle appears to be of negligible influence: the amount of tidal energy dissipated in Triton's deep interior is far below that provided by radiogenic heating (as we saw in Figs. 5.3 and 5.6), and the temperatures attained in the interior are in general not any different than those for a tideless Triton (cf. Figs. 4.4, 5.7). We have explained this behaviour in Sec. 5.3, and it is in line with e.g. the results found by Hammond & Collins (2024): however, it is at odds with the predictions of e.g. McKinnon (1988, 1992), McKinnon & Benner (1990) and McKinnon et al. (1995). Instead, they predict that Triton's shell melts in full, leaving the core to dissipate the brunt of the remaining orbital energy. While these two scenarios may seem at total odds, McKinnon et al. (1995) predict that this melting behaves like a runaway process, as a warmer mantle will have a lower viscosity, thus being more susceptible to tides: in this interpretation, the scenario that Hammond & Collins (2024) and we find and that of McKinnon et al. (1995) are possibly very similar, with a sudden transition between the two if Triton reaches a certain critical mantle viscosity before circularising. In the context of our explanation in Ch. 5, this is equivalent to the region of mantle dissipation sensitivity in Fig. 5.12 moving up (to roughly orbital frequencies), such that the mantle dissipation fraction at the tidal Fourier frequencies excited during circularisation are no longer negligible.

A notable difference between the version of a tidally circularised Triton described by McKinnon et al. (1995) and e.g. the gas drag model preferred by Benner & McKinnon (1995) and McKinnon & Leith (1995) had been the fact that orbital energy dissipated through gas drag would rapidly re-radiate into space, leaving little thermal evidence of capture, while an interior molten by tides would leave marks possibly still detectable today. If tidal dissipation in Triton instead occurs primarily in the shell, as the results of Hammond & Collins (2024) and ourselves suggest, this implies that a tidally circularised Triton suffers the same fate, therefore limiting the measurements by which Triton's past can be constrained in-situ.

Finding out whether the discrepancy in the results of McKinnon et al. (1995) compared to those found by Hammond & Collins (2024) and ourselves is therefore of fundamental importance: if the difference arises from a difference in assumed parameter values, a (null) detection of a (formerly) largely molten interior at Triton can be used to constrain Triton's mantle parameters. Otherwise, the discrepancy comes down to a model difference, and such a (null) detection will allow us to decide on which model is more appropriate, but it will not enable us to infer anything on the interior properties of Triton's mantle.

We will thus evaluate whether our conclusions are sensitive to changes in (1) the mantle temperature (Sec. 6.1.1) or (2) to changes in the mantle density (Sec. 6.2.1). Finally, we tested a scenario in which all parameters are tuned to make Triton's mantle as susceptible to tides as possible, and present its results in Sec. 6.1.3.

6.1.1. Changes in mantle temperature

In general, a warmer mantle will be more susceptible to tides (owing to lower viscosities): hence, we will vary the temperatures of early Triton over a range of reasonable values to see what the consequences are. In Sec. 4.2, we showed that there are two primary factors controlling mantle temperature over time: (1) the assumed value of the radiogenic heating rate and (2) the initial mantle temperature. The primary effect of an increased radiogenic heating rate on the mantle is to alter the attained mantle temperatures in a very similar way to variations in the initial temperature, though with a small time lag; as altering the initial temperature of the mantle has a qualitatively similar but more easily interpretable effect, we will prefer to vary the initial temperature to assess the consequences of a warmer mantle.

We find that there is a small but not insignificant change in dynamical evolution between the scenarios. Hence, the dynamical evolution over time compared to the nominal case (an initial temperature of 300 K) is shown in Fig. 6.1: counter-intuitively, increased mantle temperatures (which should make Triton's mantle more susceptible

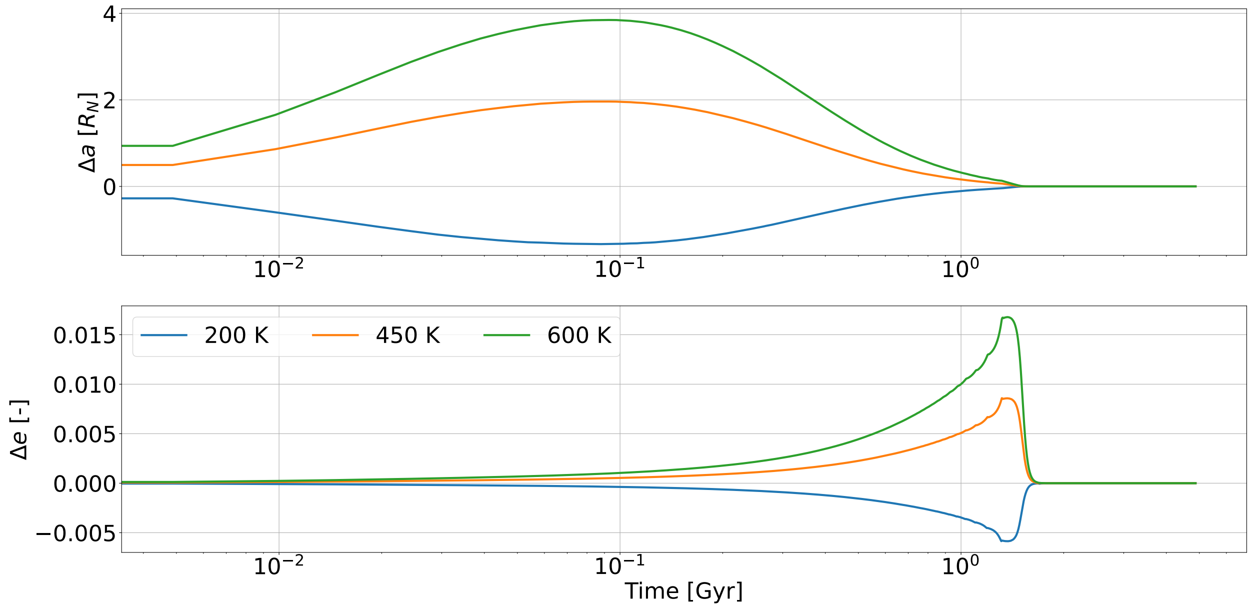

Figure 6.1: Change in semi-major axis (top) and eccentricity (bottom) over time as a function of initial mantle temperature, compared to the nominal evolution scenario (with an initial temperature of 300 K).

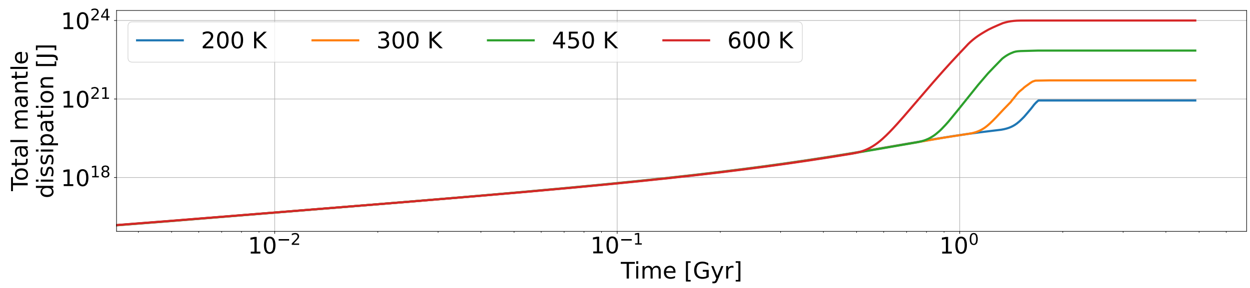

Figure 6.2: Cumulative (i.e. time-integrated) energy dissipated in the mantle over time for various initial temperatures.

to tides) lead to slower circularisation! This is not an error; rather, this is a consequence of the shell thinning more for an initially hotter mantle (Fig. 4.9), and consequently experiencing less tidal dissipation, at least until the contribution of tidal dissipation starts to dominate the shell thickness. The increased tidal dissipation in the mantle enabled by higher temperatures loses out to this secondary effect, and hotter mantles circularise (marginally) slower. This raises two pathways by which the mantle viscosity might be lowered, such that it could potentially dissipate more energy: (1) a higher initial temperature, and (2) a higher temperature during the high-dissipation phases of circularisation, as those happen (marginally) later for hotter mantles.

Let us see whether these effects have any significant thermal consequences: to isolate the effect of increased tidal effects on the mantle from the change in temperature that we change between runs (as the effect of that change on the temperature profile turns out to be far more severe than that of increased/decreased dissipation), we compare the cumulative amount of energy dissipated in the mantle over time, shown in Fig. 6.2. While there is a significant (up to $\sim$ 1000-fold) increase in the total energy going into the mantle for various initial temperatures, going from $\sim 10^{21}$ J for an initial temperature of 200 K to $\sim 10^{24}$ J for an initial temperature of 600 K, this amount of energy is still negligible compared to that dissipated in the shell (on the order of $\sim 10^{29}$ J), and only enough to raise the mantle temperature uniformly by an increment on the order of $\sim$ 0.1 K. While the increased susceptibility of the mantle to tidal heating appears to cause a relatively significant increase in the tidal heating, in absolute terms this does not amount to any significant change in mantle conditions.

6.1.2. Mantle viscosity

There are two more methods by which the tidal behaviour of the mantle might change: (1) through the mass-radius constraint, the mantle density controls the total mass of the mantle, which controls its thermal inertia as well as the rock-to-ice ratio of Triton, and (2) the reference viscosity of the mantle controls the scaling of the Arrhenius relation (Eq. 3.30). The first is not a true physical dependency, but rather a methodological

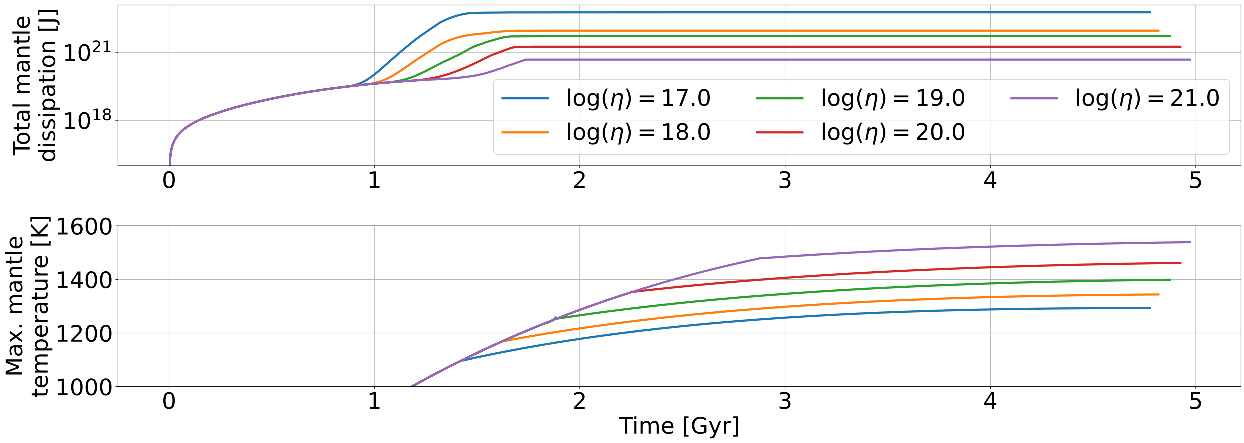

Figure 6.3: Cumulative amount of energy dissipated in the mantle (top) and the maximum attained mantle temperature (bottom) over time for various mantle reference viscosities (given in Pa s).

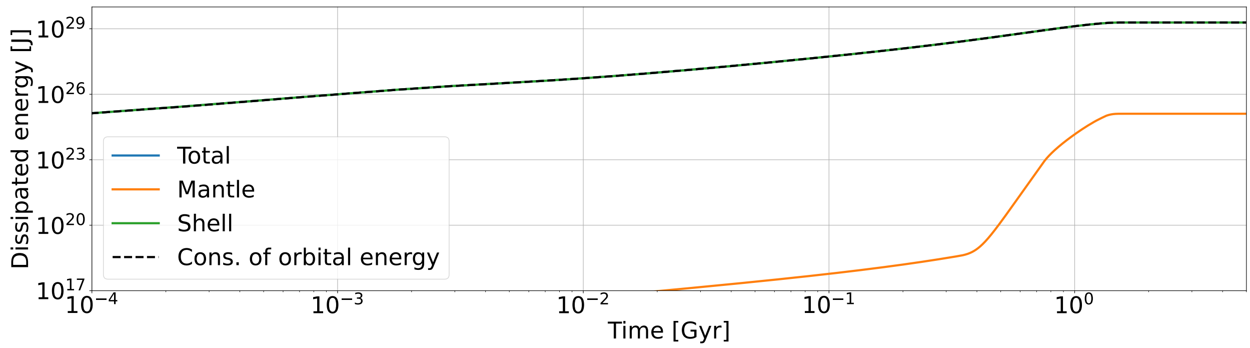

Figure 6.4: Dissipation for a hot-start (600 K), low-viscosity ($\eta_0 = 10^{17}$ Pa s) mantle. Shell dissipation dominates over mantle dissipation, and so the lines of total and shell dissipation coincide.

one because of our incorporation of the mass-radius constraints through a dependency on mantle density (see Sec. 3.5). Hence, we will discuss dependencies on the assumed mantle density in Sec. 6.2.1. The second one, however, is fundamentally what controls the amount of tidal dissipation going on in the mantle, and so we would like to assess the vulnerability of the balance of tidal heating between mantle and shell to our poor knowledge of the mantle viscosity (see Sec. 3.5).

Fig. 6.3 shows the dependency of the total amount of mantle dissipation on the assumed reference viscosity, as well as the resulting change in maximum attained mantle temperature. The resulting change in mantle dissipation is, as with the change in temperature, severe: however, not severe enough to overcome the orders of magnitude separating mantle and shell dissipation. Even for a reference viscosity of 10^{17} Pa s, the total amount of energy does not surpass 10^{23} J, such that the thermal influence of this change is negligible: the maximum attained mantle temperature, shown in the bottom panel of Fig. 6.3, confirms this suspicion. The five scenarios coincide until convection sets on, which happens well after the brunt of the tidal heating in all cases. Afterward, the maximum mantle temperature is governed by convection, showing identical results to those found for the tideless case in Ch. 4.

6.1.3. Pushing to extremes; hot formation of a low-viscosity mantle

From Sec. 6.1.1 and Sec. 6.1.2, it is clear that neither an increase in temperature nor a decrease in reference viscosity can make the mantle susceptible to tides to the degree necessary to produce the energy required for the wide-spread melting of the interior predicted by McKinnon et al. (1995). A natural extension to this question is, of course, to ask whether perhaps the combined effects of a particularly hot Triton at a particularly low reference viscosity are capable of matching their predictions, and so we perform an experiment setting the mantle viscosity to the low extreme of 10^{17} Pa s, and the initial mantle temperature to a hot 600 K.

The resulting (cumulative) dissipation is shown in Fig. 6.4, and we see that mantle dissipation now reaches quantities on the order of $\sim 10^{25}$ J. This corresponds to an effective temperature change of the mantle on the order of ~ 1 K: hence, we expect that the temperatures in the interior are hardly effected, and this prediction is

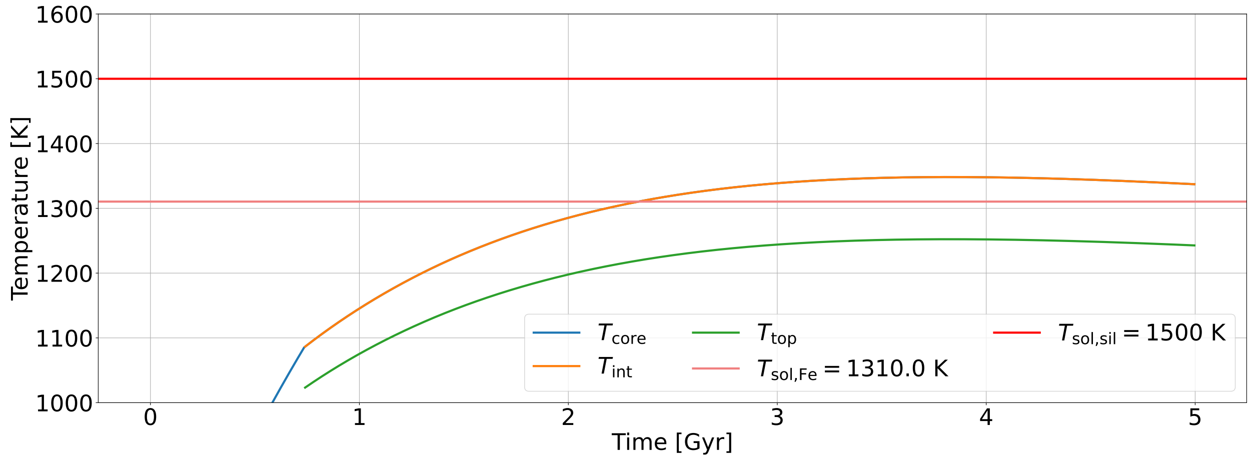

Figure 6.5: The time-dependent evolution of key mantle temperatures compared to the 20% melt fraction temperature of iron (Neumann et al., 2012) and the solidus of silicate (Hammond & Collins, 2024) for the hot-start (T_0 = 600 K) and low-viscosity ($\eta_0 = 10^{17}$ Pa s) model.

borne out by the temperature values computed by our model, shown in Fig. 6.5. The effect of mantle dissipation is clearly still not enough to affect any significant change in the temperatures reached by the mantle, and indeed nowhere near the kind of run-away interaction between viscosity and dissipation necessary to produce the results of McKinnon et al. (1995) from our model. In fact, the primary effect of the lower viscosity is to promote convection at lower temperatures already, such that the mantle is cooler than it is in the nominal scenario. While the total amount of energy dissipated in the mantle is, in this case, thus significantly greater than in the nominal case (by ~ 3 orders of magnitude), this far from sufficient to set on any kind of runaway melting; such a scenario would require viscosities even lower than 10^{17} Pa s, which require significant melt fractions to occur (Bierson & Nimmo, 2016, and references therein). A possible mechanism by which this might still occur is if dissipation by the shell is somehow suppressed sufficiently that circularisation is extended to beyond the time at which Triton's interior reaches the temperatures necessary to start iron-rock differentiation under its own power: we will discuss such a mechanism in more detail in Sec. 7.2.3.

6.2. Sensitivity to bulk parameters

Having analysed the sensitivity of the results and conclusions of Ch. 5 to the properties governing the susceptibility of Triton's mantle to tidal heating, two more parameters remain to vary. We also vary the mantle density (Sec. 6.2.1) and shell viscosity (Sec. 6.2.2), and evaluate the consequent differences.

6.2.1. Mantle density

As already alluded to in Sec. 6.1.2, our assumed value of the mantle density controls the mantle radius and mass as well as the rock-to-ice ratio through the mass-radius constraint (see Sec. 3.5), and it might therefore be expected that the assumed mantle density can significantly impact our results. Hence, we also perform coupled interior-orbital simulations using different values of the mantle density of Triton, corresponding to low- and high-density end-members of 2800 and 3400 kg/m^3, respectively. The corresponding mantle radius that satisfies the mass-radius constraints varies between ~ 1150 km for a low density, to ~ 1050 km for a high density (see Fig. 3.4) as a result, such that the hydrosphere can vary in thickness from ~ 200 – 300 km. Additionally, lower densities correspond to a higher rock-to-ice ratio resulting in a larger mass of radiogenic material in the body, with a higher-density mantle of course experiencing the opposite effect. The assumed mantle density therefore varies a number of high-level parameters that are fed into both the interior and dynamical evolution: in the case of interior-only evolution, we showed in Sec. 4.2.2 that the effect of the change in hydrosphere thickness dominates, while the other variations that result do not carry consequences that are as severe.

In the coupled case, we see a similar behaviour to that of the tideless case, with one small caveat. While the shell thickness was different between densities in the isolated, tideless case, the shell thickness (Fig. 6.7) is now close to identical during the epoch of intense tidal heating (which is expected for a shell thickness dominated by the dissipation rate), and only diverges afterward (returning to their tidally unperturbed evolution). The major difference after this time is in the time at which the various scenarios freeze over, with the low-density end-member freezing over after only ~ 3.5 Gyr (at a shell thickness of ~ 200 km), while the other two hold out until ~ 4.9 Gyr (at a shell thickness of ~ 260 and ~ 270 km), identical to what we found in Sec. 4.2.2. This difference can thus be entirely explained by the difference in hydrosphere thickness. As expected, then, the evolution of the dynamics, shown in Fig. 6.6, is hardly affected by this change in conditions. Differences

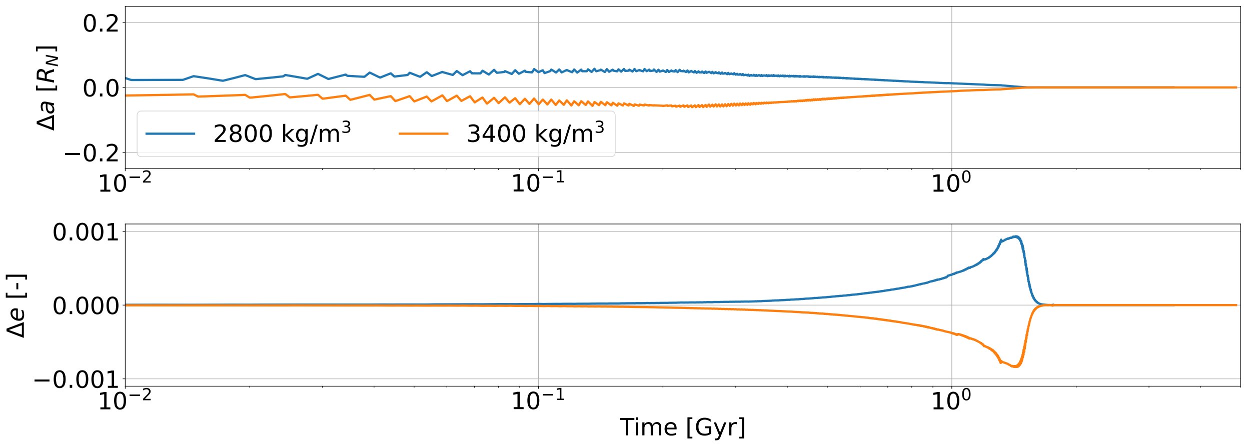

Figure 6.6: Change in semi-major axis (top) and eccentricity (bottom) over time for the two end-members for mantle density, compared to the nominal evolution scenario (with a density of 3100 kg/m^3. The jagged pattern is a result of rapid decay between spin-orbit resonances at different times for the different runs.

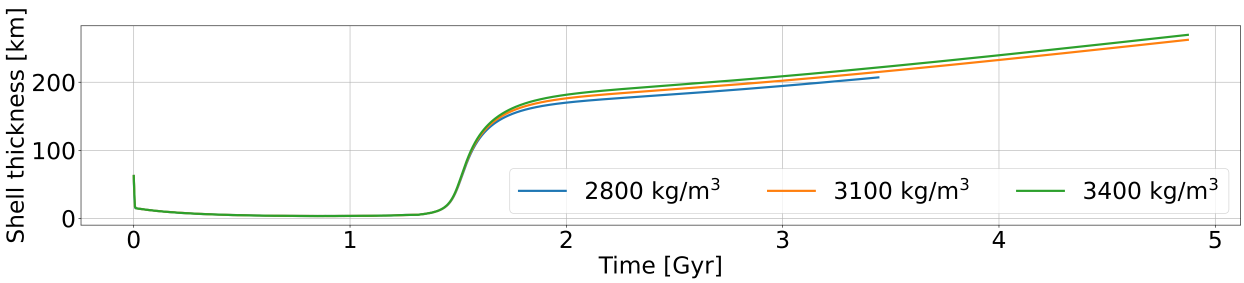

Figure 6.7: Evolution of the shell thickness over time for the nominal mantle density and two end-member densities.

in semi-major axis occur very early, but are small and a result of differences in timing of the decay between spin-orbit resonances, not of any true difference in dynamical evolution; in eccentricity, a difference appears that seems to be more systematic, but even that is only of marginal influence. The mantle density is therefore generally not of major influence, except in determining the allowed thicknesses of the hydrosphere.

6.2.2. Shell viscosity

In Sec. 6.1, we showed that, for reasonable values of the mantle temperature and viscosity, the mantle does not appear to be susceptible to tides, as already shown for our reference scenario in Ch. 5. Consequently, the tidal evolution of Triton appears to be, in all cases, largely dominated by the tidal response of its ice shell: as the shell thickness rapidly self-corrects to accommodate the amount of heat flowing through it such that the initial thickness is largely irrelevant, and the (equilibrium) temperature profile is fixed by the shell thickness, the most important variable parameter controlling the tidal evolution is the reference viscosity of Triton's shell.

Hence, we vary the reference shell viscosity over a range of reasonable values to evaluate the sensitivity of the coupled evolution to this parameter. The dynamical evolution for various reference shell viscosities is shown in Fig. 6.8; it is clear that, in contrast to the insensitivity of the dynamical evolution to the mantle viscosity, the shell viscosity *does* significantly affect the dynamical evolution of Triton. In going from $5 \cdot 10^{11}$ to $5 \cdot 10^{15}$ Pa s, the circularisation timescale varies from $\sim 1 - 3$ Gyr; for higher viscosities, Triton fails to circularise in the age of the Solar System altogether, with the eccentricity only damping to a value of ~ 0.85 after 5 Gyr. A notable feature is the fact that the sensitivity of dynamical evolution to a changing reference value at low viscosities ($5 \cdot 10^{13}$ Pa s and below) is only marginal, while the change is more severe when reaching high viscosities.

This change in dynamical evolution through changes in shell viscosity also affects the evolution of the shell itself; Fig. 6.9 shows the evolution of the shell for the tested values of the reference viscosity. In general, the shell recedes to thicknesses on the order of ~ 10 km during tidal evolution regardless of the shell viscosity, and remains that thin until the semi-major axis has damped to roughly its present-day value. Afterward, the shell thickness rapidly returns to its unperturbed value.

An interesting variation that appears for the shell viscosity, but not for the other parameters that we varied, is the fact that the passage of Triton through the phase space of eccentricity and rotation rate (shown in Fig. 6.10)

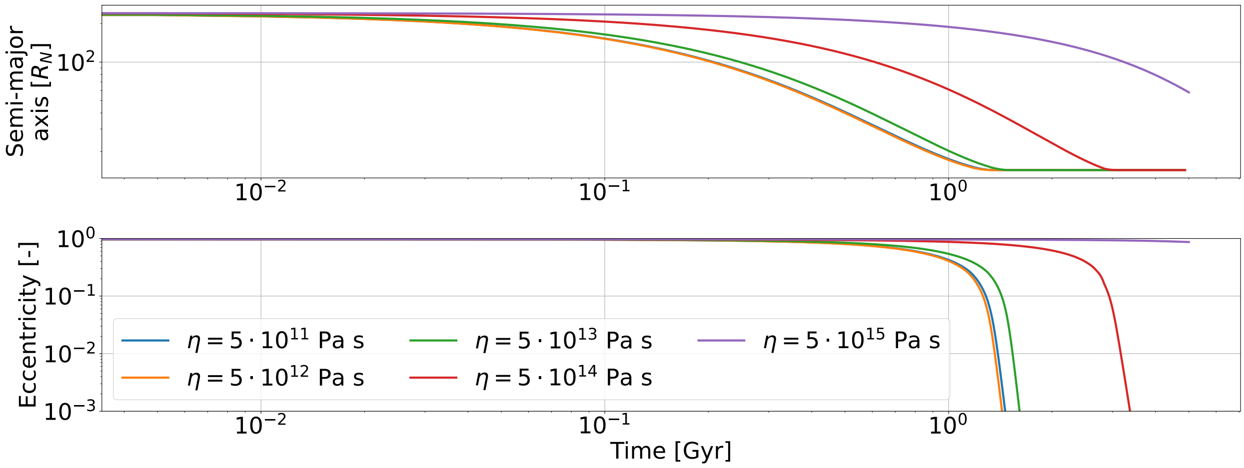

Figure 6.8: Sensitivity of the dynamical evolution to assumed reference values for the shell viscosity.

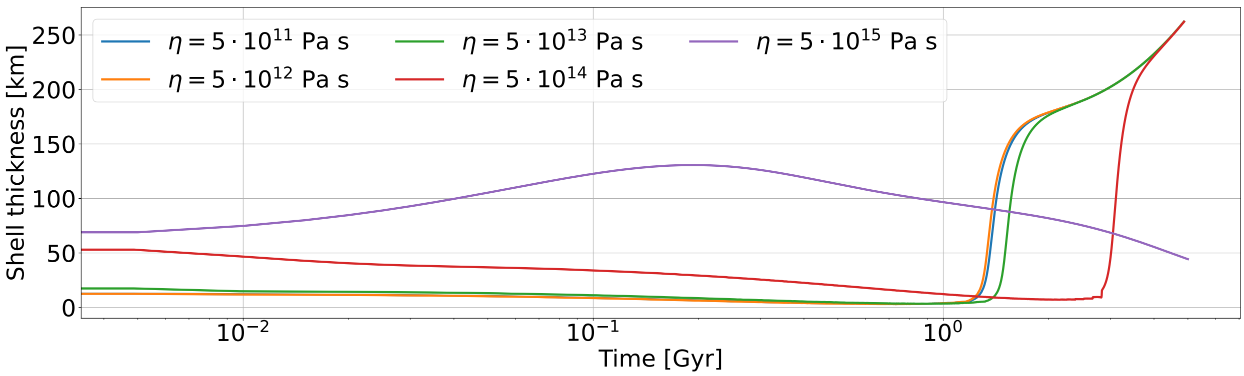

Figure 6.9: Sensitivity of the evolution of the shell thickness to changes in the assumed reference value for the shell viscosity.

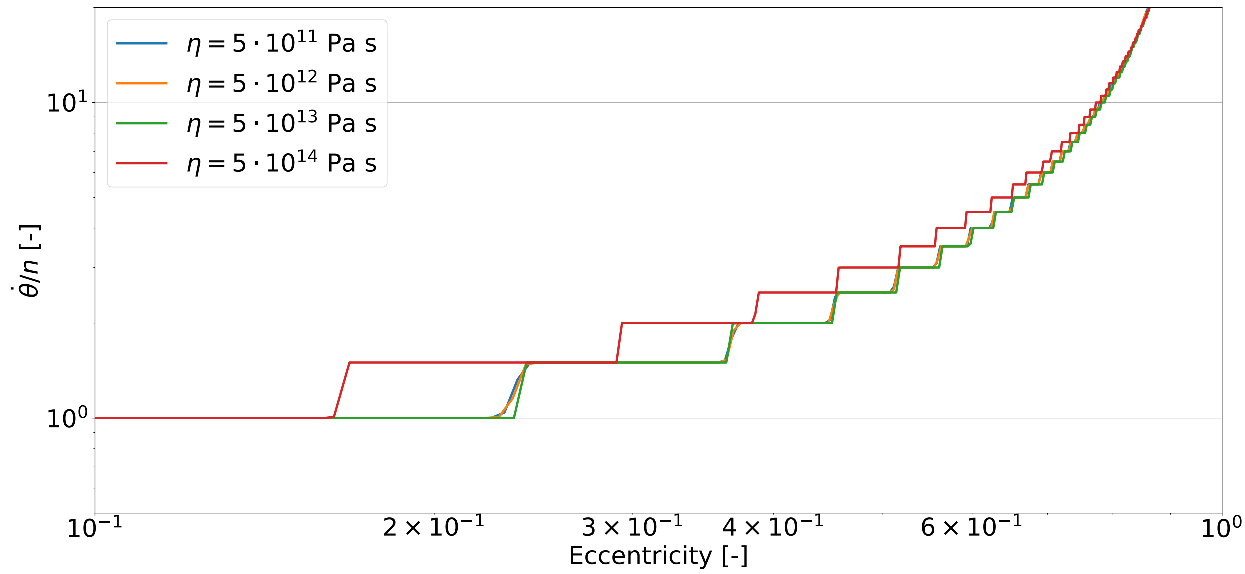

Figure 6.10: The migration of the state of Triton through the phase space of eccentricity and spin rate over time for the tested shell viscosities: the values of the eccentricity over time are plotted against the corresponding value of the spin rate normalised to the mean motion. The discrete, step-like behaviour is real, and not an interpolation or integration artefact. $\eta = 5 \cdot 10^{15}$ Pa s is not shown, as it does not reach the pictured region of phase space within the age of the Solar System.

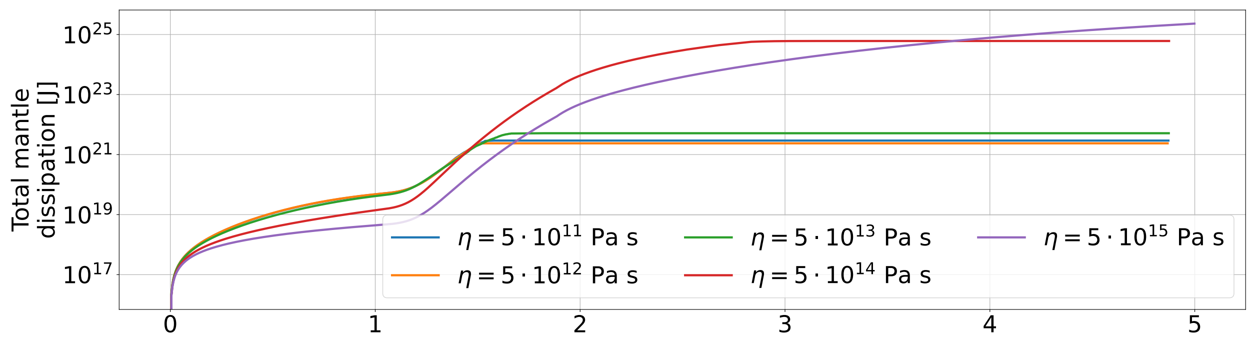

Figure 6.11: The total (cumulative) energy dissipated in the mantle over time for various reference shell viscosities.

appears to be controlled by the shell viscosity. While Renaud et al. (2021) and Van Woerkom (2024) predict that this step-like behaviour should be smooth for lower viscosities, this does not appear to be the case: we find step-like behaviour (i.e. passage through resonances) even for viscosities as low as $5 \cdot 10^{11}$ Pa s. It is likely that this is a property of multi-layered bodies possessing a highly viscous layer, as both Renaud et al. (2021) and Van Woerkom (2024) draw this conclusion on the basis of models using homogeneous Maxwell bodies.

Another surprising consequence of changing the shell viscosity is shown in Fig. 6.11, which illustrates the time-evolution of the cumulative energy dissipated in the mantle for various shell viscosities. A knock-on effect of the extended period of circularisation appears to be an eventually greater amount of total mantle dissipation. While still never reaching the types of energies required to significantly affect the evolution and present-day state of the mantle, this opens a possible pathway by which Triton *could* have experienced significant mantle dissipation, which we will discuss in more detail in Sec. 7.2.1.

6.3. Conclusions

Having evaluated the sensitivity of our results to variations in the major interior parameters we have assumed, we can now apply some nuance to the results of Ch. 5, and conclude:

- The true circularisation time of Triton depends heavily on the assumed (reference) viscosity of the ice shell, but for plausible shell viscosities generally lasts at least ~ 1 Gyr or more.
- Excepting the viscosity of its shell, the process of circularisation is largely impervious to changes in the assumed interior parameters for Triton.

- For all plausible parameters and even in scenarios tailored to promote mantle dissipation, our model predicts that tidal dissipation in Triton's mantle is never vigorous enough to have any significant consequences for its interior evolution, which is therefore identical to its unperturbed evolution.
- Consequently, practically all of Triton's orbital energy is dissipated in its shell, which thins to the order of ~ 10 km in scenarios that circularise within the age of the Solar System.
- After circularisation, Triton's shell rapidly returns to its unperturbed thickness, at present leaving no direct evidence of the process of capture.

Consequently, we conclude that, at least on a qualitative level, the results found in Ch. 5 are robust to reasonable variations in the values we assume for our model. The largest uncertainty of all lay in the timescale of circularisation, which varies from ~ 1 Gyr to the age of the Solar System, depending on the assumed shell viscosity. Additionally, our sensitivity analysis suggests that the disagreement between our results and those described McKinnon et al. (1995) is unlikely to be a result of a difference in assumed mantle conditions.

7 Discussion and recommendations

Before moving on to the conclusions of this work, we will take some time to reflect on the importance of these results in the context of broader literature. We will discuss how our results compare against previous work in Sec. 7.1, and give an overview of the shortcomings of the thermal model (Sec. 7.2), deformation model (Sec. 7.3) and dynamical model (Sec. 7.4) that we recommend be accounted for in future work. Finally, we will discuss the implications our results on the habitability of Triton (Sec. 7.5) and on our understanding of the formation history of the Neptunian system (Sec. 7.6).

7.1. Comparison against previous work

As already discussed in Ch. 6, our results, while in line with those of Hammond & Collins (2024), are very different from those predicted by a large number of older pieces of literature, such as the work of McKinnon (1988, 1992), McKinnon & Benner (1990), and McKinnon et al. (1995). As shown in Ch. 6, we cannot reproduce the results of McKinnon (1988, 1992) by changing our assumed parameters, and so we assume the difference lay in our modelling approach; unfortunately, McKinnon never published a detailed article on these models.

Based on the descriptions given by McKinnon (1988, 1992) as well as that of McKinnon et al. (1995), however, we infer that he used a constant phase-lag model with an assumed value for the phase lag of the shell and mantle based on the expressions used in the Europa model of Ojakangas & Stevenson (1989), which assumes a thin shell: it is therefore likely that McKinnon (1988, 1992) studied whether the tidal dissipation in a Triton comprised of two thin, dissipating shells with inviscid fluids in and between the shells would be sufficiently dissipative so as to be self-sustaining: as dissipation in the rocky interior does not have the same strong self-damping effect that dissipation in the ice shell does, this process will lead to a much larger amount of tidal heat being dissipated in the silicate interior than in our simulations.

The reconciliation suggested by the work of Hammond & Collins (2024) and ourselves is then that that may well be – but that Triton's mantle was never sufficiently dissipative to arrive in such a state to begin with. In that case, the work of McKinnon (1988, 1992) does suggest that one avenue still remains by which Triton's mantle could be largely molten by tidal heating: if Triton's shell is sufficiently resistant to tidal dissipation that its circularisation lasts long enough for core formation to start, the reduction in effective viscosity caused by a liquid core might greatly boost the susceptibility of Triton's interior to tides. Doing so would require that one properly accounts for the behaviour of the viscoelastic-gravitational equations for a mantle atop a liquid core, however, which our model is at present not capable of doing.

A second note concerns the validity of approximations made in previous work: Gaeman et al. (2012) and Ross & Schubert (1990) both assumed that the heat flux out of Triton's interior is in equilibrium with its radiogenic heat production. We find, in agreement with Hammond & Collins (2024) and Nimmo & Spencer (2015), that this is not a valid assumption, with radiogenic heating never equilibriating with mantle outflow in our simulations. To add to this, Hammond & Collins (2024) and Nimmo & Spencer (2015) assumed a fully conductive mantle: in all of our simulations, however, Triton's mantle eventually starts convecting, and continues doing so into the present.

7.2. Shortcomings of the thermal model

Though we have tested the resilience of our results to variations in assumptions on Triton's interior structure and composition, there are also some shortcomings present in the methodology of our thermal model itself, or in parameters for which we did not perform a sensitivity analysis. We will briefly discuss where these shortcomings may be found.

7.2.1. Core formation and its consequences

In practically all of our simulations, and in all scenarios we deem most plausible, Triton reaches the temperatures necessary to start forming iron melt. Even more intriguingly, in most scenarios temperatures then further rise (even without the influence of tides) to temperatures at which we expect a 20% melt fraction of iron ($\sim$ 1310 K: Neumann et al., 2012), which is sufficient to start forming a core by percolation (Ghanbarzadeh et al., 2017; Berg et al., 2018), a process which could potentially be aided by the deformation experienced by early Triton (Berg et al., 2017). Hammond & Collins (2024) only conclude that melt formation happens for temperatures over 1500 K, which they find are only reached in enhanced-dissipation scenarios (in contrast, we never find any significant mantle dissipation). This temperature corresponds roughly to the silicate solidus, not the 20% melt-fraction of iron that we use to evaluate whether core formation occurs. This therefore explains their apparent disagreement on this result.

It therefore appears that, while not by tides, Triton is capable of initiating core formation under its own power. This is interesting, as core formation can power a magnetic field like that of Ganymede (e.g. Hauck et al., 2006; Bland et al., 2008), which might potentially be detectable by future missions to the moon. While previous work has assumed that such a core would form as a consequence of tidal action (e.g. McKinnon et al., 1995), we therefore deem it likely that this need not be the case: conversely, we argue that evidence of a core at Triton need not be taken as evidence of past intense tidal activity in Triton's deep interior.

Core formation also carries with it some caveats relating to interior evolution that we have at present not accounted for. To start with, core formation is an exothermic process, and the formation of an inner solid iron core that follows (as Triton does not reach the liquidus of iron: Bland et al., 2008, 2009) will release even more energy. Consequently, Triton's interior will heat up, or at the very least be more vigorously convective, leading to a thicker ocean at present. A second caveat is the fact that a liquid core imposes different boundary conditions on the viscoelastic-gravitational equations than a solid one: see e.g. Sabadini et al. (2016). Our model does not account for the accompanying changes in tidal Love number, which would in general lead to an effectively less viscous and therefore more dissipative interior.

7.2.2. Mantle conditions

Our mantle model also admits some shortcomings: one large issue is the fact that the convection model of Hussmann & Spohn (2004) uses a fixed critical Rayleigh number, whereas this is not necessarily a good approximation (Solomatov, 1995). That being said, preliminary tests show that while changing this critical Rayleigh number over the range $10^2 - 10^4$ has some impact on the time at which convection sets on, it does not change the fact that convection eventually does happen.

A second note concerns our particular implementation of the convection model used by Hussmann & Spohn (2004): as we only reach Rayleigh numbers some 10-100 times above critical, the boundary layer thickness (i.e. the transition length between the convective and conductive layers) will not be negligible, as we assume it to be. We do not expect that this will change our results much, but it might have some impact if we move on to a higher-fidelity description of the deformation of the mantle.

Finally, we have not accounted for the latent heat of dehydration of silicate: this value is on the order of several ~ 100 kJ/kg (e.g. Trinh et al., 2023, and references therein), enough to significantly affect the evolution of the interior. Additionally, the hydration state can have an impact of up to a factor ~ 140 on the viscosity of the mantle (Hirth & Kohlstedt, 1996). We therefore recommend that future work account for the (de)hydration state of Triton.

7.2.3. Thermal properties of the shell and ocean

We have described Triton's shell under the assumption of an equilibrium conduction profile in the shell. While we have shown that this is apparently a valid assumption in App. C, this does possibly neglect some pathways by which the shell might interact with the dynamical evolution of Triton. In particular, thermal inertia of the shell (which we have thus neglected) might induce oscillations in the tidal heating rate, as the tidal heating rate is directly controlled by the shell thickness.

A second note concerns our assumption on the composition of the shell: while we have assumed the shell and ocean to be comprised of pure water, the presence of clathrates might suppress its conductivity or increase its viscosity (e.g. Carnahan et al., 2022), while the presence of ammonia or other antifreezes might suppress its melting point to as low as 176 K (Leliwa-Kopystyński et al., 2002; Choukroun & Grasset, 2010), and Nimmo & Spencer (2015) infer that the ocean temperature must indeed currently be roughly 240 K rather than the 273 K we assume. Similarly, porosity might suppress conductive heat transfer in the shell as discussed by Bierson & Nimmo (2022) for the Uranian moons Titania and Oberon. In general, each of these properties will serve to lengthen the lifetime of subsurface oceans, and so we expect that our predictions on the lifetimes of Triton's ocean are highly conservative, especially as we do not account for obliquity tides at present. A second, less immediate consequence of these properties, is to increase the effective viscosity of the shell, either by increasing the melting point viscosity (in the case of clathrates) or, by lowering the melting point, increasing the average viscosity of the shell. Consequently, as we found that the circularisation timescale is very sensitivity to higher viscosities, this might significantly lengthen the duration of tidal activity on Triton.

Finally, we remark that we have assumed that the ice shell is always purely conductive: however, Nimmo & Spencer (2015) predict that Triton's ice shell is, at least at present, convecting, so as to explain its young surface. Hammond & Collins (2024), however, find that convection only occurs during the first couple Myr, and afterwards ceases entirely, as Triton's shell becomes too thin to accommodate convection. Both appear to use the

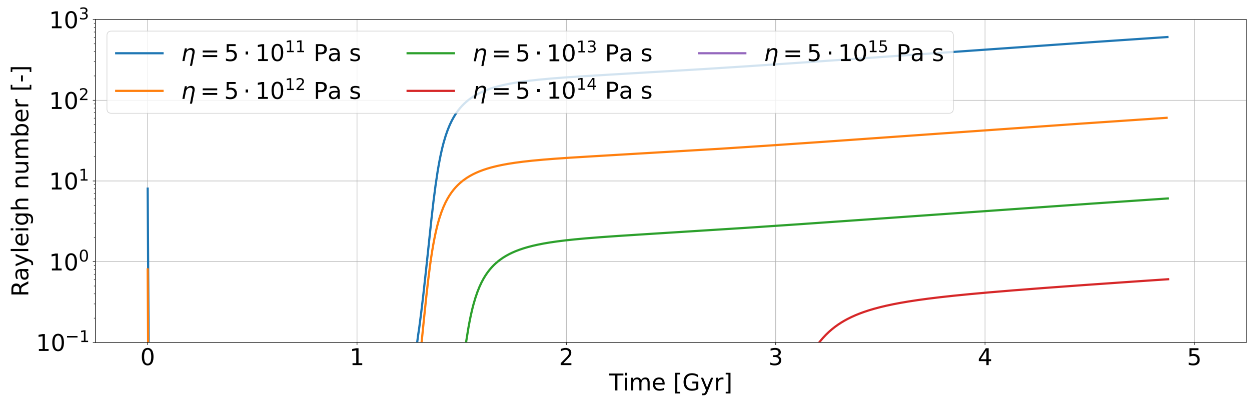

Figure 7.1: Upper bounds on the Rayleigh number of the conductive shell for the various tested values of the reference shell viscosity.

same scheme by which to compute the critical Rayleigh number, so it is not clear where their difference lay: we compute conservative approximations to the Rayleigh number throughout the shell for our simulations using Eq. 3.26 but with the relevant quantities for ice, and taking for the temperature difference $\Delta T = T_{\text{melt}} - T_{\text{surf}}$ and for the convective layer thickness taking the shell thickness D_s: the resulting value over time for the various shell reference viscosities is shown in Fig. 7.1. These results seem to indicate that we should side with Hammond & Collins (2024), even when using the critical Rayleigh number of Nimmo & Spencer (2015), and so we expect that a conductive shell is largely a reasonable approximation.

7.2.4. Surface conditions on early Triton

In our thermal model, we have assumed that the ice shell radiates as a grey body into free space with an equilibrium temperature of 31.6 K, corresponding to conditions at present-day Triton. In doing so, we do neglect the effects of a potential atmosphere as may have been raised on early Triton: in fact, however, even on present-day Triton the atmosphere is of appreciable thermal influence, homogenising surface conditions across the body and enabling it to keep a constant temperature globally (Lellouch, 2018). If temperatures rise significantly, this could potentially even raise an atmosphere that not just homogenises, but actively contributes to the surface temperature: given Triton's past, it is no surprise that this scenario was already considered by Nolan & Lunine (1988), who further worked it out in the aftermath of the *Voyager 2* visit to Triton (Lunine & Nolan, 1992). By their metric, however, establishing a runaway vapour-equilibrium atmosphere (i.e. one that self-stabilises) requires surface fluxes on the order of ~ 0.7 W/m^2, of which Triton in general just falls shy in our simulations. A vapour-equilibrium atmosphere is therefore unlikely.

We do, however, note that Triton's shell thins to even sub-Enceladan thicknesses of less than 10 km: it is therefore not unthinkable that plume activity like that seen on Enceladus might have arisen on Triton too. Though no scaling relationships of this type appear in literature, it seems plausible that the $\sim 10 - 100$-fold or more increase above Enceladan total dissipation levels might translate to a comparable increase in outgassed plume material. This matter certainly deserves attention in future work.

7.3. Shortcomings of the deformation model

Aside from the thermal model, our deformation model also knows several shortcomings. We will highlight in particular (1) our use of a Maxwell rheology, and (2) our use of a thin-shell deformation model.

7.3.1. Higher-fidelity rheological models

As we had acknowledged in Ch. 3, our use of Maxwell rheology is not necessarily without issue. Particularly in the context of Io, Maxwell rheology is known to significantly underestimate tidal heating at realistic viscosities, requiring viscosities of order $10^{13} - 10^{16}$ Pa s to match observed heat output on Io (Bierson & Nimmo, 2016). While a common technique used to compensate for this difference, also used by Hammond & Collins (2024), is to resort to such unrealistically low viscosities for silicate to "simulate" the Andrade model, we note that this is ad-hoc solution does not do much to solve the problem in the frequency-varying tidal quality function that one has to account for at higher eccentricities. The corrections one can apply to Maxwell to "recover" the values of Andrade rheology only work at a particular frequency, especially as we are working with a mixed tidal response determined partially by silicate, and partially by ice. It is therefore advisable that future work make the change to Andrade rheology.

If doing so, Renaud & Henning (2018) showed that tidal dissipation predicted by the Andrade and Sundberg-

Cooper rheologies produces $\sim 10\times$ the tidal heating for a warm, Io-like satellite predicted by a Maxwell rheology. While such an increase alone would still not be enough to allow the mantle to heat up significantly as a result of tides, in combination with other factors evaluated in our sensitivity study (e.g. a reduction in shell viscosity, or an increase in mantle temperature) it might be sufficient to promote a greater deal of mantle dissipation to the degree that would significantly affect the interior.

7.3.2. Deformation formalism shortcomings

As we propose in Sec. 7.1 that the predictions of McKinnon (1988, 1992) turn out to be flawed as a consequence of his thin-shell assumption, it is only honest that we reflect on our own use of such a model (though only for the shell), too. We have used the thin-shell expressions of Beuthe (2019) to evaluate the frequency-dependent tidal response of Triton's shell, and must thus concede that we admit some error whenever Triton's shell is not thin: at present, we have not quantified this error, though our agreement with the results of Hammond & Collins (2024), who do not use the thin-shell assumption but *do* neglect the coupling of mantle and shell, suggests that this error is acceptable.

More troubling is the method by which we compute the tidal response of the mantle, however: while our averaging of the rigidity over the mantle is physically motivated by the viscoelastic-gravitational equations from which analytical expressions for the tidal Love number arise (Beuthe, 2015b), a better approach would be to properly account for the variation of rigidity with radius. An implementation of the matrix-propagator expressions of Sabadini et al. (2016) would be able to resolve this at a computationally affordable cost while simultaneously circumventing the need for thin-shell equations.

A final point of possible contention is our use of a maximum viscosity in both the shell and mantle. While the tidal response is only sampled sparsely at frequencies where this matters, the low-frequency tidal response does potentially matter as it (1) controls the locking of Triton into spin-orbit resonances and (2) low-frequency tides will preferentially dissipate heat in the mantle. This first point is precisely what causes short-period behaviour that trips up the adaptive step size of our integrator if the viscosity is not capped, but it would thus be preferable if future work could resolve this issue without needing to cap the viscosity in this way.

7.4. Relaxing dynamical assumptions

Having discussed our perceived shortcomings of the thermal and deformation models we use, we will finally discuss the shortcomings of our third model component, being the dynamical model. Here, we will recognise in particular several additions that can be made to the dynamical model so as to relax the assumptions we have to make on the dynamical mechanisms at play.

In particular, a major assumption that we have made is for Triton's obliquity to always be equal to zero: while this is a reasonable assumption if Triton were to be perfectly spherical, this is not expected for a rotating body in hydrostatic equilibrium. Though the shape data on Triton is not sufficient to prove consistency with the hydrostatic assumption, it is at least not inconsistent with this assumption (Thomas, 2000). For a moment of inertia factor of 0.33, Chen et al. (2014) obtain an stable obliquity of $\sim 0.3°$ for a fully solid Triton, which they find might be exaggerated by a factor 2 by the fact that Triton possesses an ocean. At this obliquity, Nimmo & Spencer (2015) predict that present-day Triton is still dissipating $10 - 100$ GW in obliquity tides. Hence, while eccentricity tides are certainly dominant for the first $\sim$ Gyr or longer, depending on the length of circularisation, obliquity tides could potentially be a major source of tidal dissipation, and therefore potentially also of orbital evolution continuing into the present day. Accounting for this would therefore be worthwhile.

A second assumption that we might want to relax (if at least to assess its impact) is that of equilibrium rotation: as decay between spin-orbit resonances will see at least one resonance moving through the region of frequency space in which the mantle is prone to dissipation, it would be interesting to see whether this would result in increased mantle dissipation over those epochs, or whether the rapidity with which such transitions happens compensates for this.

Finally, we have not accounted for the tides that Triton raises in Neptune: while those were almost certainly not important in Triton's initial, high-eccentricity evolution (e.g. Van Woerkom, 2024), they may well allow us to put more useful constraints on Triton's initial orbit (see Sec. 7.6), by allowing us to eliminate orbits that fall into Neptune before present as a result of tides Triton raises in Neptune.

7.5. Habitability on past and present Triton

As we introduced Triton in Ch. 1, we spoke of its potential as a unique habitable moon, especially given its captured past. How (if at all) has this changed in light of our results? We have shown that Triton underwent at least ~ 1 Gyr (and possibly longer) of evolution with a thick ocean: however, it seems that this tidal evolution will not, under the conditions we have explored, be sufficient to melt Triton's shell in full. It is therefore unlikely that Triton ever harboured truly Earth-like conditions.

Additionally, we have shown that even with a convective interior more effective at removing heat than the conductive interior used by Hammond & Collins (2024), it seems that Triton cannot be stopped from reaching the temperatures required for large-scale dehydration and even potentially late-onset core formation: in a lot of ways, this reflects an evolution that is very similar to that of Europa described by Trinh et al. (2023). While the jury is still out on whether such conditions are favourable for life or would in fact work adversely (Trinh et al., 2023, and references therein), this does at least place Triton in a different class of object in terms of habitability than the smaller KBOs that do not reach such temperatures. Additionally, large-scale dehydration could lead to large extension of Triton's shell, potentially promoting ice-ocean exchange processes which are thought to be beneficial in promoting habitable conditions (Soderlund et al., 2020). On the flip side of this, the mantle dissipation-less Triton we envision will not, at least through tidal dissipation, lead to any (additional) formation of hydrothermal systems like envisioned by Shock & McKinnon (1993) and Mandt et al. (2023). This would indicate that, contrary to the conclusions of Mandt et al. (2023), the differences in volatile composition between Triton and Pluto should be purely due to a difference in their size, rather than a consequence of Triton's tidally heated past. Consequently, this would also mean that enhancement of hydrothermal or volcanic systems is not a mechanism by which tidal heating could promote habitability of captured moons.

7.6. Formation histories for the Neptunian system

Our results indicate that Triton likely took in excess of ~ 1 Gyr to circularise to its present orbit: unless Triton's silicate mantle is somehow substantially more receptive to tides than both we and Hammond & Collins (2024) calculate (e.g. by our assumption of Maxwell rheology), this result is fairly robust to variations in assumptions. While Ćuk & Gladman (2005) and Rufu & Canup (2017) propose that such circularisation times are unrealistic as those would not have preserved Nereid on its present orbit, we subscribe to the view of Nogueira et al. (2011) and Hammond & Collins (2024): it is more plausible that Nereid simply migrated onto its present orbit later. Rufu & Canup (2017) did show that, assuming a Uranian-like primordial satellite system for Neptune, it is likely that Triton experienced at least one (non-disruptive) impact during the process of disrupting that same primordial satellite system, and so that might be an interesting scenario for future research.

An unfortunate side-effect of the broad range of allowed circularisation times that we find for the range of plausible interior properties that we have is that, at present, we cannot put any constraints on Triton's initial orbit following capture. Regardless of the eccentricity at which we start Triton, there is always some combination of plausible range of interior properties that will see it circularise within the age of the Solar System. Resolving this would require that we put constraints on the viscosity of Triton's shell.

8 Conclusions

With the results behind us, we have now set up a framework by which we can answer the questions we initially set out to answer:

- We have set up the scientific (Ch. 2) scaffolding necessary to understand the evolution of Triton.
- Following this, we introduced our methodology in Ch. 3.
- We evaluated the tideless evolution of an isolated Triton in Ch. 4, as well as its sensitivity to assumed model parameters, which allows us to describe the evolution Triton would have gone through had it not been captured by Neptune;
- Consequently, we considered the combined dynamical and interior evolution of Triton in Ch. 5, allowing us to conclude the features of Triton that can be attributed to this dynamical evolution;
- Finally, we assessed the robustness of these results to changes in our assumed model values in Ch. 6, allowing us to isolate those that stand strong from those that are still uncertain.

Hence, we are now well-situated to answer the questions we put forth in Ch. 2, and assess which of those answers are more or less robust. Before moving on to answering the primary question we posed, we will first go through each of the sub-questions so as to be able to adequately support our concluding answer to the primary question: we will discuss our findings on the effectiveness of various modelling approaches for Triton's tidal response in Sec. 8.1, following up with a description of the effect of capture on Triton's thermal-interior state in Sec. 8.2. We will describe the our version of the history and process of Triton's capture in Sec. 8.3, and consequently discuss the constraints that we conclude are (or are not) available by which to constrain Triton's history in Sec. 8.4. Finally, we assimilate these answers into an answer to our primary question in Sec. 8.5.

8.1. What are the consequences of different modelling approaches to Triton's orbital-interior evolution?

Our model tidal evolution model is built on the Darwin-Kaula expansion for the perturbing tidal potential, primarily developed by Kaula (1961, 1964). Over the years, various simplified expressions have been derived from this formalism, and so we have assessed their suitability for use in describing high-eccentricity evolution. Additionally, a number of these assume a constant value for the tidal quality function, regardless of frequency: we are therefore interested in knowing the frequencies at which the tidal response of Triton is excited.

8.1.1. Are simplified expressions acceptable for computation of its high-eccentricity evolution?

Aside from the constant time-lag (CTL) model already shown to be inadmissibly erroneous on epistemological grounds by Makarov & Efroimsky (2013) and on practical grounds by Van Woerkom (2024), we have shown that lower-order truncations of the Darwin-Kaula expansion, amongst which one version of the constant phase lag (CPL) model (e.g. Boué & Efroimsky, 2019), are not suitable to describe the coupled interior-orbital evolution of Triton, in agreement with similar results obtained by Renaud et al. (2021) in a different context. Surprisingly, the version of the CPL model derived by MacDonald (1964), despite the objections levied by Efroimsky & Makarov (2013) and its inherent limitation in requiring the assumption of synchronous rotation, does remarkably well. While not a good approximation in the mathematical sense, its predictions agree qualitatively with ours, lending credence to the results of Hammond & Collins (2024) despite their use of a simplified dynamical model; we attribute this mostly to the relative stiffness of the tidal response of Triton over the range of forcing frequencies excited during its tidal evolution.

8.1.2. What forcing frequency ranges shape the tidal evolution of circularising Triton?

The forcing frequencies excited during Triton's circularisation are largely limited to those exceeding half the orbital rate. As this value is comfortably in the regime where our tidal deformation model predicts the rigid-mantle contribution to the tidal response (owing to the deformation of the shell over an ocean) dominates, the tidal response of Triton is well-described by the *hard-shell* deformation regime described by Beuthe (2018), which in this case has only a relatively mild dependency on frequency as the thermal profile in the (conductive) ice shell does not give significantly more weight to the contribution at any particular temperature (i.e. viscosity). The variation with frequency over this range does include a peak, however, such that the CTL model is a poor approximation even disregarding its mis-judgement of the rotational rate of Triton, which was the ground on which Van Woerkom (2024) dismissed the CTL model.

8.1.3. Conclusions

We can thus conclude that, in comparison to our frequency-depenedent, full-fidelity tidal model, of the tested simplified modelling approaches that of MacDonald (1964) appears to work best, because of the behaviour of the tidal response of Triton over the particular range of frequencies excited during its circularisation. Other simplified models grossly misestimate the dissipation rate for early Triton, with prematurely-truncated versions of the Darwin-Kaula expansion severely underestimating and models not accounting for the tidal-interior feedback severely overestimating the tidal dissipation rate. Despite the good approximation afforded by the dynamical model of MacDonald (1964), there is one prediction that is uniquely made by our model, however, concerning the rotational rate: we will highlight this in Sec. 8.3.

8.2. How did capture affect Triton's thermal-interior state?

We have evaluated the evolution of Triton's interior throughout capture for various plausible structures and compositional scenarios, both for the mantle and shell. By comparison of the tideless interior evolution scenario presented in Ch. 4 and that including the dynamical-interior coupling presented in Ch. 5, we can thus assess the influence of capture on Triton's thermal-interior state; in particular, we can conclude on (1) the effect capture on the development of a Tritonian core, (2) the repercussions of capture on surface conditions, and (3) the consequences of capture on Triton's subsurface ocean.

8.2.1. Did capture set on the development of a core?

In general, we find that, unless accepted radiogenic heating estimates are grossly in excess of the true value, Triton always reaches the temperatures necessary to start large-scale subsolidus mantle convection, eventually followed by that convective region rising to the temperatures at which sufficient formation of iron-melt takes place that Triton should start forming a core. In contrast with the predictions made by McKinnon et al. (1995), however, Triton does so under its own power, unaided by tidal dissipation in the mantle. In fact, none of our tested scenarios predict that tidal dissipation in the mantle is sufficient for tides to make any appreciable contribution to the energy budget going into core formation. This is further exacerbated by the fact that the conditions for core formation, excepting scenarios of excessive radiogenic heating, generally arise only after ~ 2 Gyr, while tidal evolution ceases before that time in most of our simulations. Capture alone is therefore is never directly responsible for the development of an iron core on Triton.

We envision one scenario, however, in which core formation is not set on but at least aided by tidal dissipation: large-scale melt formation in the convective interior of Triton will see the viscosity of that region drop drastically, possibly enhancing the tidal susceptibility of that region significantly. If (1) the timeline of capture is extended to last ~ 2 Gyr or longer (e.g. for a shell more viscous than $5 \cdot 10^{14}$ Pa s) and (2) the production of melt decreases the (effective) viscosity of the mantle sufficiently, it is a distinct possibility that the resulting feedback might see tidal dissipation making a significant contribution to core formation at Triton. This therefore carries important consequences for the generalisation of this result to larger captured (exo)moons; if the body is sufficiently large to form with a core, it might see this development vastly exacerbated by capture.

8.2.2. Could early Triton have possessed a substantial atmosphere?

By the criteria of Lunine & Nolan (1992), Triton raises a runaway atmosphere (that is, with the insulating effect of the atmosphere further reinforcing the formation thereof) in vapour-pressure equilibrium for surface fluxes above ~ 0.7 W/m^2; only in the fastest-circularising scenario (corresponding to a particularly low shell viscosity of $5 \cdot 10^{11}$ Pa s) do we attain such fluxes, and even then only momentarily. The self-damping effect of pure ice-shell dissipation therefore seems to limit dissipation rates to levels below those which would raise an atmosphere in vapour-pressure equilibrium.

In all scenarios, however, we see the ice shell thinning to sizes on the order of ~ 10 km, below even those found at present on much smaller Enceladus (Thomas et al., 2016). If this thin shell is accompanied by an extreme version of the large-scale ejection of water vapour observed on Enceladus' south pole (Porco et al., 2006; Hansen et al., 2011), it is plausible that a substantial (secondary) water atmosphere may have been supplied in that manner instead. Investigating whether this would be sufficient to raise and sustain an atmosphere requires in-depth modelling of the processes involved, however, which we have not undertaken.

8.2.3. How far did Triton's primordial ocean extend?

Assuming a conservative melting temperature of 273 K, we find that Triton's shell recedes to thicknesses of ~ 10 km, with the exception of scenarios with large shell viscosities ($\gtrsim 5 \cdot 10^{14}$ Pa s); in those cases, Triton fails to circularise within the age of the Solar System, and so we do not take those scenarios to be plausible. The thickness of the ocean then depends on the thickness of the full hydrosphere of Triton, which is at present not constrained by e.g. determination of Triton's moment of inertia; for plausible ranges of densities for the mantle, we find that this varies between $\sim 200 - 300$ km, with the estimate for the ocean thickness varying accordingly. We thus envision no scenario in which Triton did not spend its first ~ 1 Gyr or more with a thick, global ocean.

8.2.4. Conclusions

We conclude that the effects of capture on Triton's thermal-interior state are largely limited to its effects felt in the hydrosphere, where the shell thins to sub-Enceladan thicknesses of ~ 10 km or less; while Triton does likely form a core, it does not do so as a result of tidal heating. Additionally, the self-damping effect of tides in the ice shell cause surface heat fluxes to remain below the levels required to raise a vapour-equilibrium atmosphere.

8.3. What does the process of Triton's capture look like?

Having concluded what the thermal-interior effects of Triton's capture are, we turn our gaze to the dynamical process of capture itself. Before moving on to a phenomenological description of the dynamical process, we will briefly discuss the spin-orbit resonances experienced by Triton during its capture, as well as the prospects of observing this process in extrasolar systems.

8.3.1. Will partially-molten Triton undergo spin-orbit resonances?

Contrary to the predictions on a low-viscosity Maxwell body made by Van Woerkom (2024) or the dynamical evolution model of Correia (2009), we always find that Triton passes through higher-order spin-orbit resonances during capture, even at low shell viscosities and with a thin shell. Moreover, this spin-orbit resonance progression is always exact, and Triton is captured into this resonance within ~Myr-timescales of the initialisation of capture.

8.3.2. Would capture of exo-Tritons be observable in exoplanetary systems?

In general, our simulations never reach the temperatures required to be directly detectable in nearby exoplanetary systems by the criteria of van Woerkom & Kleisioti (2024); however, if a thin shell causes expulsion of significant amounts of material from the ocean into orbit around the host planet, we envision that detection might be possible analogous to the claimed detection of an exo-Io plasma torus by Oza et al. (2019). The energy dissipated in Triton at any given time is proportional to the mass of its host as M_N^2 (see Eq. 3.8), so while a more massive exo-Triton will not be subject to more vigorous tides (rather, it will have a larger reservoir of orbital energy to draw from), preliminary results indicate that a Triton-like dwarf planet captured around a (super-)Jovian planet will indeed suffer significantly more severe tidal heating, possibly sufficient to melt the shell entirely and/or be observable in exoplanetary systems by brightness temperature alone.

8.3.3. Conclusions

Throughout Triton's capture, it is stuck in a spin-orbit resonance; the process of capture is, in none of our scenarios, vigorous enough to cause Triton's surface temperature to rise to the point of detectability in exoplanetary systems. Aside from this, Triton's capture proceeds largely as envisioned already by Ross & Schubert (1990), initially damping out its semi-major axis before circularising; our timescales differ slightly, though, with thinning of the ice shell extending out the circularisation of Triton to at least ~ 1 Gyr, possibly extending out to recent times for particularly viscous shells. The timescales of equilibriation for Triton's ice shell are always fast enough that it reaches a shell thickness in equilibrium with its dissipation rate, such that no oscillations analogous to e.g. the limit cycles that occur for dissipation by libration occur (e.g. Goldreich et al., 2025). Consequently, the circularisation of Triton is a smooth and continuous process.

8.4. Do any constraints on Triton's capture and history remain into the present?

An important question for any mission hoping to return to Triton is whether it could possibly detect any evidence for or constraints on Triton's extraordinary history. Hence, we will briefly evaluate what evidence may still be available (1) in Triton's geology or chemical makeup, and (2) whether Triton's present ocean thickness might be affected by its past evolution.

8.4.1. Could geological or geochemical evidence of Triton's capture remain?

In all of the scenarios we consider, Triton has spent the time since finishing circularisation freezing over. This timespan varies depending on the viscosity of Triton's shell, though a plausible upper limit is ~ 3 Gyr; this is similar to the length of freeze-over consistent with extensional faults observed on Pluto, hypothesised to be a result of a hot start followed by freeze-over on that body (Bierson et al., 2020). Though we note that no such features have been observed on Triton (Schenk et al., 2021), the full northern hemisphere of Triton remains unmapped, and so it is possible that similar geological evidence of Triton's history may remain there. The lack of feedback between tidal heating and evolution of the deep interior we find means that geological clues as to Triton's evolution are, unfortunately, largely limited to its hydrosphere.

The longer-lasting presence of a large ocean on Triton as a result of tidal heating has in the past been used to explain differences in geochemical makeup of Triton compared to Pluto (Mandt et al., 2023), and our results lend credit to this idea. While we have not done any modelling of hydrothermal processes, we do caveat this with the fact that our results indicate that Triton's larger (rock) mass allows it to reach the temperatures required for widespread dehydration much more readily than Pluto, yielding a possible explanation for this difference without requiring the influence of tides.

8.4.2. Does the evolution of Triton affect its current ocean thickness?

In all scenarios we test (except those not circularising within the age of the Solar System), we find that Triton's ocean returns to (a value close to) its unperturbed thickness within a couple ~ 100 Myrs after tidal activity ceases at most. Unless conditions are fine-tuned such that Triton circularised only recently in Solar System history, it is therefore not likely that Triton's ocean is at present still thick as a result of capture. It is possible, however, that chemical processes promoted by the additional heat provided by capture might have altered the ocean composition, and consequently, its melting point, altering Triton's present-day ocean thickness indirectly. Evaluating the influence of such a feedback point is therefore a useful way in which future modelling studies might produce testable constraints on Triton's ocean thickness conditioned on its dynamical history, but that would require development of a coupled geochemical model.

8.4.3. Conclusions

In conclusion, if any evidence remains of Triton's capture, it will be geochemical or geological in nature. While the process of an ocean largely freezing over over the timescales we predict would be capable of producing tectonic features that could be detectable today, those have not been observed on the hemisphere of Triton that was mapped by *Voyager 2*. We expect that the best hope of constraining Triton's history by further observation is therefore going to be found in coupling geochemical models to its dynamical-interior evolution, which would require a more advanced model than ours.

8.5. Concluding the primary research question

Having answered all of the partial questions we described, we can finally answer the primary question we set out to answer:

> **What are the thermal-interior and dynamical consequences of the process of capture and high-eccentricity tidal circularisation on an icy moon like Triton?**

Concluding, we can give the following answers to this question:

- Triton's capture cannot alone be responsible for the formation of a core; a sensitivity study suggests this is a general feature of captured Triton-like moons, with core formation being promoted but never initialised by capture.
- Consequently, the majority of captured Triton's orbital energy is lost by dissipation in its shell. Self-damping of this process prevents it from raising a vapour-equilibrium atmosphere in the case of Triton, but allows the shell to thin to ~ 10 km in thickness or less.
- Synchronous rotation is only expected to occur after Triton's eccentricity has damped to ~ 0.2, the moon being in an equilibrium but non-synchronous series of spin-orbit resonances before that time.
- After circularisation ceases, the thermal-interior evolution of Triton is largely identical to its unperturbed evolution, and so any possible remnants of this epoch of circularisation are limited to (1) extensional faults in Triton's unmapped northern hemisphere and (2) geochemical evidence.

That is, for a body like Triton that does not form with a deep interior susceptible to tides, the consequences of capture are largely dynamical and possibly geochemical in nature, aligning with the results obtained by Hammond & Collins (2024) using a simpler dynamical model. Only for a body already possessing a partially-molten interior will the consequences possibly extend to a full-scale melting of the interior as was once envisioned for Triton.

Bibliography

Agnor, C. B., & Hamilton, D. P. 2006, Nature, 441, 192, doi: 10.1038/nature04792

Alden, H. L. 1940, The Astronomical Journal, 49, 71

Allen, C. W. 1973, Astrophysical Quantities, 3rd edn. (London: The Athlone Press)

Andersson, O., & Suga, H. 1994, Physical Review B, 50, 6583

Bagheri, A., Khan, A., Deschamps, F., et al. 2022a, Icarus, 376, doi: 10.1016/j.icarus.2021.114871

Bagheri, A., Efroimsky, M., Castillo-Rogez, J., et al. 2022b, Advances in Geophysics, 63, 231, doi: 10.1016/bs.agph.2022.07.004

Baland, R. M., Van Hoolst, T., Yseboodt, M., & Karatekin, Ö. 2011, Astronomy and Astrophysics, 530, doi: 10.1051/0004-6361/201116578

Barr, A. C. 2016, Astronomical Review, 12, 24, doi: 10.1080/21672857.2017.1279469

Barr, A. C., & Schwamb, M. E. 2016, Monthly Notices of the Royal Astronomical Society, 460, 1542, doi: 10.1093/mnras/stw1052

Běhounková, M., Tobie, G., Choblet, G., et al. 2021, Geophysical Research Letters, 48, doi: 10.1029/2020GL090077

Benedetti-Rossi, G., Sicardy, B., Buie, M. W., et al. 2016, The Astronomical Journal, 152, 156, doi: 10.3847/0004-6256/152/6/156

Benisty, M., Bae, J., Facchini, S., et al. 2021, The Astrophysical Journal Letters, 916, L2, doi: 10.3847/2041-8213/ac0f83

Benner, L. A., & McKinnon, W. B. 1995, Icarus, 114, 1

Berg, M. T., Bromiley, G. D., Le Godec, Y., et al. 2018, Frontiers in Earth Science, 6, doi: 10.3389/feart.2018.00077

Berg, M. T., Bromiley, G. D., Butler, I. B., et al. 2017, Physics of the Earth and Planetary Interiors, 263, 38, doi: 10.1016/j.pepi.2017.01.004

Bertrand, T., Lellouch, E., Holler, B. J., et al. 2022, Icarus, 373, doi: 10.1016/j.icarus.2021.114764

Beuthe, M. 2015a, Icarus, 248, 109, doi: 10.1016/j.icarus.2014.10.027

—. 2015b, Icarus, 258, 239, doi: 10.1016/j.icarus.2015.06.008

—. 2016, Icarus, 280, 278, doi: 10.1016/j.icarus.2016.08.009

—. 2018, Icarus, 302, 145, doi: 10.1016/j.icarus.2017.11.009

—. 2019, Icarus, 332, 66, doi: 10.1016/j.icarus.2019.05.035

Bierson, C. J. 2024, Icarus, 116026, doi: 10.5281/zenodo.1

Bierson, C. J., & Nimmo, F. 2016, Journal of Geophysical Research: Planets, 121, 2211, doi: 10.1002/2016JE005005

—. 2019, Icarus, 326, 10, doi: 10.1016/j.icarus.2019.01.027

—. 2020, The Astrophysical Journal, 897, L43, doi: 10.3847/2041-8213/aba11a

—. 2022, Icarus, 373, doi: 10.1016/j.icarus.2021.114776

Bierson, C. J., Nimmo, F., & Stern, S. A. 2020, Nature Geoscience, 13, 468, doi: 10.1038/s41561-020-0595-0

Bills, B. G., & Nimmo, F. 2011, Icarus, 214, 351, doi: 10.1016/j.icarus.2011.04.028

Bland, M. T., Showman, A. P., & Tobie, G. 2008, Icarus, 198, 384, doi: 10.1016/j.icarus.2008.07.011

—. 2009, Icarus, 200, 207, doi: 10.1016/j.icarus.2008.11.016

Bonneau, D., & Foy, R. 1986, Astronomy and Astrophysics, 161, L12

Boué, G., & Efroimsky, M. 2019, Celestial Mechanics and Dynamical Astronomy, 131, doi: 10.1007/s10569-019-9908-2

Boyce, J. M. 1993, in Abstracts of the 24th Lunar and Planetary Science Conference, 165–166

Breuer, D., Spohn, T., Van Hoolst, T., et al. 2022, Surveys in Geophysics, 43, 177, doi: 10.1007/s10712-021-09677-x

Brown, M. E. 2013, Astrophysical Journal Letters, 778, doi: 10.1088/2041-8205/778/2/L34

Brown, M. E., & Butler, B. J. 2017, The Astronomical Journal, 154, 19, doi: 10.3847/1538-3881/aa6346

—. 2023, Planetary Science Journal, 4, doi: 10.3847/PSJ/ace52a

Brown, R. H., Johnson, T. V., Goguen, J. D., Schubert, G., & Ross, M. N. 1991, Science, 251, 1465. https://www.science.org

Brown, R. H., & Kirk, R. L. 1994, Journal of Geophysical Research, 99, 1965, doi: 10.1029/93JE02618

Brown, R. H., Kirk, R. L., Johnson, T. V., & Soderblom, L. A. 1990, Science, 250, 431

Buratti, B. J., & Thomas, P. C. 2014, in Encyclopedia of the Solar System (Elsevier), 759–777, doi: 10.1016/b978-0-12-415845-0.00034-7

Cabrera, J., Csizmadia, S., Lehmann, H., et al. 2014, Astrophysical Journal, 781, doi: 10.1088/0004-637X/781/1/18

Canup, R. M., & Ward, W. R. 2002, The Astronomical Journal, 124, 3404

—. 2006, Nature, 441, doi: 10.1038/nature04860

Carnahan, E., Vance, S. D., Hesse, M. A., Journaux, B., & Sotin, C. 2022, Geophysical Research Letters, 49, doi: 10.1029/2021GL097602

Carslaw, H. S., & Jaeger, J. C. 1959, Conduction of heat in solids, 2nd edn. (London: Oxford University Press)

Cassen, P., Reynolds, R. T., & Peale, S. J. 1979, Geophysical Research Letters, 6, 731, doi: 10.1029/GL006i009p00731

Castillo-Rogez, J. C., Efroimsky, M., & Lainey, V. 2011, The tidal history of Iapetus: Spin dynamics in the light of a refined dissipation model, doi: 10.1029/2010JE003664

Castillo-Rogez, J. C., & Lunine, J. I. 2010, Geophysical Research Letters, 37, doi: 10.1029/2010GL044398

Chen, E., Nimmo, F., & Glatmaier, G. 2014, Icarus, 229, 11, doi: 10.1029/2009GL038300

Cherniack, J. R. 1972, SAO Special Report, 346

Choukroun, M., & Grasset, O. 2007, Journal of Chemical Physics, 127, doi: 10.1063/1.2768957

—. 2010, Journal of Chemical Physics, 133, doi: 10.1063/1.3487520

Chyba, C. F., Jankowski, D. G., & Nicholson, P. D. 1989, Astronomy & Astrophysics, 219, 23

Cilibrasi, M., Szulágyi, J., Mayer, L., et al. 2018, Monthly Notices of the Royal Astronomical Society, 480, 4355, doi: 10.1093/mnras/sty2163

Cioria, C., & Mitri, G. 2022, Icarus, 388, doi: 10.1016/j.icarus.2022.115234

Connolly, J. A. D. 1990, American Journal of Science, 290, 666

Correia, A. C. 2009, Astrophysical Journal, 704, L1, doi: 10.1088/0004-637X/704/1/L1

Correia, A. C. M., & Valente, E. F. S. 2022, Celestial Mechanics and Dynamical Astronomy, 134, 24, doi: 10.1007/s10569-022-10079-3

Cottaar, S., Heister, T., Rose, I., & Unterborn, C. 2014, Geochemistry, Geophysics, Geosystems, 15, 1164, doi: 10.1002/2013GC005122

Croft, S. K. 1990, in Abstracts of the Lunar and Planetary Science Conference, Vol. 21, 246–247

Croft, S. K. 1993, in Abstracts of the 24th Lunar and Planetary Science Conference, 349–350

Cruikshank, D. P., Stockton, A., Dyck, H. M., Becklin, E. E., & Macy, W. 1979, ICARUS, 40, 104

Ćuk, M., & Gladman, B. J. 2005, The Astrophysical Journal, 626, 113

Curtis, H. D. 2013, Orbital Mechanics for Engineering Students (Butterworth-Heinemann)

Cynar, S. J. 1987, ACM Signum Newsletter, 22, 12

Darwin, G. H. 1879, Philosophical Transactions of the Royal Society of London, 170, 447

—. 1880, Philosophical Transactions of the Royal Society of London, 171, 713

Davaille, A., & Jaupart, C. 1993, Journal of Fluid Mechanics, 253, 141

Denton, C. A., Johnson, B. C., Wakita, S., et al. 2021, Geophysical Research Letters, 48, doi: 10.1029/2020GL091596

Desch, S. J., Kalyaan, A., & Alexander, C. M. O. 2018, The Astrophysical Journal Supplement Series, 238, 11, doi: 10.3847/1538-4365/aad95f

Deschamps, F. 2021, Geophysical Journal International, 224, 1870, doi: 10.1093/gji/ggaa540

Deschamps, F., & Vilella, K. 2021, Journal of Geophysical Research: Planets, 126, doi: 10.1029/2021JE006963

Dobos, V., Haris, A., Kamp, I. E. E., & van der Tak, F. F. S. 2022, Monthly Notices of the Royal Astronomical Society, 513, 5290, doi: 10.1093/mnras/stac1180

Dobos, V., & Turner, E. L. 2015, Astrophysical Journal, 804, doi: 10.1088/0004-637X/804/1/41

Efroimsky, M., & Makarov, V. V. 2013, Astrophysical Journal, 764, doi: 10.1088/0004-637X/764/1/26

Elliot, J. L., Hammel, H. B., Wasserman, L. H., et al. 1998, Letters to Nature, 393, 765

Ellsworth, K., & Schubert, G. 1983, ICARUS, 54, 490

Farinella, P., Milani, A., & Nobili, A. M. 1980, Icarus, 44, 810

Farinella, P., Milani, A., Nobili, A. M., & Valsecchi, G. B. 1979, The Moon and the Planets, 20, 415

Fayolle, M., Dirkx, D., Lainey, V., Gurvits, L. I., & Visser, P. N. 2022, Planetary and Space Science, 219, doi: 10.1016/j.pss.2022.105531

Fayolle, M., Magnanini, A., Lainey, V., et al. 2023, Astronomy and Astrophysics, 677, doi: 10.1051/0004-6361/202347065

Ferguson, S. N., Rhoden, A. R., & Kirchoff, M. R. 2024, Earth and Planetary Science Letters, 642, doi: 10.1016/j.epsl.2024.118859

Forgan, D., & Dobos, V. 2016, MNRAS, 457, 1233, doi: 10.1093/mnras/stw024

Forgan, D., & Kipping, D. 2013, MNRAS, 432, 2994, doi: 10.1093/mnras/stt662

Fornasier, S., Lellouch, E., Müller, T., et al. 2013, TNOs are Cool: A survey of the trans-Neptunian region: VIII. Combined Herschel PACS and SPIRE observations of nine bright targets at 70-500, doi: 10.1051/0004-6361/201321329

Fornberg, B. 1988, Mathematics of Computation, 51, 699

Fortes, A. D. 2012, Planetary and Space Science, 60, 10, doi: 10.1016/j.pss.2011.04.010

Fox, C., & Wiegert, P. 2021, Monthly Notices of the Royal Astronomical Society, 501, 2378, doi: 10.1093/mnras/staa3743

Fraser, W. C., Bannister, M. T., Pike, R. E., et al. 2017, Nature Astronomy, 1, doi: 10.1038/s41550-017-0088

Gaeman, J., Hier-Majumder, S., & Roberts, J. H. 2012, Icarus, 220, 339, doi: 10.1016/j.icarus.2012.05.006

Gerald, C. F., & Wheatley, P. O. 2004, Applied numerical analysis, 7th edn. (Pearson/Addison-Wesley), 609

Ghanbarzadeh, S., Hesse, M. A., Prodanović, M., & Schubert, G. 2017, Proceedings of the National Academy of Sciences of the United States of America, 114, 13406, doi: 10.1073/pnas.1707580114

Goldreich, P., Lithwick, Y., & Luan, J. 2025. http://arxiv.org/abs/2503.01967

Goldreich, P., Murray, N., Longaretri, P. Y., & Banfield, D. 1989, Science, 245, 500. https://www.science.org

Goldreich, P., Soter, S., & Cameron, A. G. W. 1966, ICARUS, 5, 375

Gomes, R., & Morbidelli, A. 2024, Icarus, 420, doi: 10.1016/j.icarus.2024.116142

Gooding, R. H., & Wagner, C. A. 2008, Celestial Mechanics and Dynamical Astronomy, 101, 247, doi: 10.1007/s10569-008-9145-6

Goossens, S., Van Noort, B., Mateo, A., Mazarico, E., & Van Der Wal, W. 2024, Nature Astronomy, 8, 846

Grasset, O., & Parmentier, E. M. 1998, Journal of Geophysical Research: Solid Earth, 103, 18171, doi: 10.1029/98jb01492

Grundy, W. M., Noll, K. S., Buie, M. W., et al. 2019a, Icarus, 334, 30, doi: 10.1016/j.icarus.2018.12.037

Grundy, W. M., Young, L. A., Stansberry, J. A., et al. 2010, Icarus, 205, 594, doi: 10.1016/j.icarus.2009.08.005

Grundy, W. M., Noll, K. S., Roe, H. G., et al. 2019b, Icarus, 334, 62, doi: 10.1016/j.icarus.2019.03.035

Hairer, E., Nørsett, S. P., & Wanner, G. 2008, Solving Ordinary Differential Equations, 2nd edn., Vol. I (Springer)

Hammond, N. P., & Collins, G. C. 2024, Planetary Science Journal, 5, doi: 10.3847/PSJ/ad6744

Hammond, N. P., Parmenteir, E. M., & Barr, A. C. 2018, Journal of Geophysical Research: Planets, 123, 3105, doi: 10.1029/2018JE005781

Hansen, C. J., Shemansky, D. E., Esposito, L. W., et al. 2011, Geophysical Research Letters, 38, doi: 10.1029/2011GL047415

Hansen, P. A. 1855, Abhandlungen Der Malhematisch Physischen Classer Der Koniglich Sachsischen Gesellschaft Der Wissenschaften, 4, 181

Harrington, R. S., & Van Flandern, T. C. 1979, Icarus, 39, 131

Hauck, S. A., Aurnou, J. M., & Dombard, A. J. 2006, Journal of Geophysical Research: Planets, 111, doi: 10.1029/2005JE002557

Heller, R., & Hippke, M. 2024, Nature Astronomy, 8, 193, doi: 10.1038/s41550-023-02148-w

Heller, R., Rodenbeck, K., & Bruno, G. 2019, Astronomy and Astrophysics, 624, doi: 10.1051/0004-6361/201834913

Hind, J. R. 1854, Monthly Notices of the Royal Astronomical Society, 15, 46

Hippke, M. 2015, Astrophysical Journal, 806, doi: 10.1088/0004-637X/806/1/51

Hirth, G., & Kohlstedt, D. L. 1996, Earth and Planetary Science Letters, 144, 93

Hofgartner, J. D., Birch, S. P., Castillo, J., et al. 2022, Icarus, 375, doi: 10.1016/j.icarus.2021.114835

Holler, B. J., Young, L. A., Grundy, W. M., & Olkin, C. B. 2016, Icarus, 267, 255, doi: 10.1016/j.icarus.2015.12.027

Hsu, H. W., Postberg, F., Sekine, Y., et al. 2015, Nature, 519, 207, doi: 10.1038/nature14262

Hu, R., Ehlmann, B. L., & Seager, S. 2012, Astrophysical Journal, 752, doi: 10.1088/0004-637X/752/1/7

Hu, X., Stark, A., Dirkx, D., et al. 2023, Celestial Mechanics and Dynamical Astronomy, 135, doi: 10.1007/s10569-023-10131-w

Huang, P., Steffen, R., Steffen, H., et al. 2023, Geophysical Journal International, 235, 2231, doi: 10.1093/gji/ggad354

Hughes, S. 1981, Celestial Mechanics, 29, 101

Hussmann, H., Choblet, G., Lainey, V., et al. 2010, Space Science Reviews, 153, 317, doi: 10.1007/s11214-010-9636-0

Hussmann, H., Sohl, F., & Spohn, T. 2006, Icarus, 185, 258, doi: 10.1016/j.icarus.2006.06.005

Hussmann, H., & Spohn, T. 2004, Icarus, 171, 391, doi: 10.1016/j.icarus.2004.05.020

Hussmann, H., Spohn, T., & Wieczerkowski, K. 2002, Icarus, 156, 143, doi: 10.1006/icar.2001.6776

Hut, P. 1981, Astronomy & Astrophysics, 99, 126

Iess, L., Jacobson, R. A., Ducci, M., et al. 2012, Science, 337, 457, doi: 10.1039/c2sm25813g

Ingersoll, A. P., & Tryka, K. A. 1990, Science, 250, 435

Izsak, I. G., Gerard, J. M., Efimba, R., & Barnett, M. P. 1964, SAO Special Report, 140

Jacobson, R. A. 2009, Astronomical Journal, 137, 4322, doi: 10.1088/0004-6256/137/5/4322

Jankowski, D. G., Chyba, C. F., & Nicholson, P. D. 1989, Icarus, 80, 211

Jara-Orué, H. M., & Vermeersen, B. L. 2011, Icarus, 215, 417, doi: 10.1016/j.icarus.2011.05.034

Journaux, B., Brown, J. M., Pakhomova, A., et al. 2020, Journal of Geophysical Research: Planets, 125, doi: 10.1029/2019JE006176

Karato, S.-i. 2010, Gondwana Research, 18, 17, doi: 10.1016/j.gr.2010.03.004

Kaula, W. M. 1961, Geophysical Journal of the Royal Astronomical Society, 5, 104, doi: 10.1111/j.1365-246X.1961.tb00417.x

—. 1964, Reviews of Geophysics, 2, 661, doi: 10.1029/RG002i004p00661

Kenworthy, M. A., & Mamajek, E. E. 2015, Astrophysical Journal, 800, doi: 10.1088/0004-637X/800/2/126

Khurana, K. K., Kivelson, M. G., Stevenson, D. J., et al. 1998, Nature, 395, 777

Kipping, D. 2020, The Astrophysical Journal, 900, L44, doi: 10.3847/2041-8213/abafa9

Kipping, D., Bryson, S., Burke, C., et al. 2022, Nature Astronomy, 6, 367, doi: 10.1038/s41550-021-01539-1

Kipping, D. M., Huang, X., Nesvorný, D., et al. 2015, Astrophysical Journal Letters, 799, doi: 10.1088/2041-8205/799/1/L14

Kiss, C., Marton, G., Parker, A. H., et al. 2019, Icarus, 334, 3, doi: 10.1016/j.icarus.2019.03.013

Kivelson, M. G., Khurana, K. K., Russell, C. T., et al. 2000, Science, 289, 1340. https://www.science.org

Kivelson, M. G., Khurana, K. K., & Volwerk, M. 2002, Icarus, 157, 507, doi: 10.1006/icar.2002.6834

Kleisioti, E., Dirkx, D., Rovira-Navarro, M., & Kenworthy, M. A. 2023, Astronomy & Astrophysics. http://arxiv.org/abs/2305.03410

Kreidberg, L., Luger, R., & Bedell, M. 2019, The Astrophysical Journal, 877, L15, doi: 10.3847/2041-8213/ab20c8

Kruzynska, D., Pospieszynski, R., Kruzynski, M., Golebiewska, J., & Wnuk, E. 2013, in Proceedings of the 6th European Conference on Space Debris

Lainey, V., Arlot, J. E., Karatekin, Ö., & Van Hoolst, T. 2009, Nature, 459, 957, doi: 10.1038/nature08108

LeBlanc, F. 2010, An Introduction to Stellar Astrophysics (Wiley)

Leliwa-Kopystyński, J., Maruyama, M., & Nakajima, T. 2002, Icarus, 159, 518, doi: 10.1006/icar.2002.6932

Lellouch, E. 2018, in Handbook of Exoplanets (Springer International Publishing), 215–233, doi: 10.1007/978-3-319-55333-7{_}47

Lewis, J. S. 1971, Science, 172, 11271128, doi: 10.1126/science.172.3988.1127

—. 1973, Space Science Reviews, 14, 401

Li, D., & Christou, A. A. 2020, The Astronomical Journal, 159, 184, doi: 10.3847/1538-3881/ab7cd5

Li, D., Johansen, A., Mustill, A. J., Davies, M. B., & Christou, A. A. 2020, Astronomy and Astrophysics, 638, doi: 10.1051/0004-6361/201936672

Limbach, M. A., & Turner, E. L. 2013, Astrophysical Journal, 769, doi: 10.1088/0004-637X/769/2/98

Lissauer, J. J., & De Pater, I. 2019, Fundamental Planetary Science: Physics, Chemistry and Habitability, updated edition edn. (Cambridge University Press)

Lodders, K., & Fegley, B. 1998, The Planetary Scientist's Companion (Oxford: Oxford University Press)

Luna, S. H., Navone, H. D., & Melita, M. D. 2020, Astronomy and Astrophysics, 641, doi: 10.1051/0004-6361/201936551

Lunine, J. I., & Nolan, M. C. 1992, Icarus, 100, 221

Lyttleton, R. A. 1936, Monthly Notices of the Royal Astronomical Society, 97, 108

MacDonald, G. J. 1964, Reviews of Geophysics, 2, 467, doi: 10.1029/RG002i003p00467

Makarov, V. V., & Efroimsky, M. 2013, Astrophysical Journal, 764, doi: 10.1088/0004-637X/764/1/27

Malamud, U., & Prialnik, D. 2015, Icarus, 246, 21, doi: 10.1016/j.icarus.2014.02.027

Mandt, K., Luspay-Kuti, A., Mousis, O., & Anderson, S. E. 2023, The Astrophysical Journal, 959, 57, doi: 10.3847/1538-4357/ad09b5

Marchi, S., Barbieri, C., & Lazzarin, M. 2004, Planetary and Space Science, 52, 671, doi: 10.1016/j.pss.2004.02.002

Martin-Herrero, A., Romeo, I., & Ruiz, J. 2018, Planetary and Space Science, 160, 19, doi: 10.1016/j.pss.2018.03.010

McCord, T. B. 1966, The Astronomical Journal, 71, 585

McKay, C. P., & Davis, W. L. 2014, in Encyclopedia of the Solar System (Elsevier), 209–231, doi: 10.1016/B978-0-12-415845-0.00010-4

McKinnon, W. 1984, Nature, 311, 355

McKinnon, W. B. 1988, Eos: Transactions of the American Geophysical Union, 69, S1297

—. 1992, Eos: Transactions of the American Geophysical Union, 73, 190

McKinnon, W. B., & Benner, L. A. M. 1990, in Abstracts of the Lunar and Planetary Science Conference, Vol. 21, 777–778

McKinnon, W. B., & Kirk, R. L. 2014, in Encyclopedia of the Solar System (Elsevier), 861–881, doi: 10.1016/b978-0-12-415845-0.00040-2

McKinnon, W. B., & Leith, A. C. 1995, Icarus, 118, 392

McKinnon, W. B., Lunine, J. I., & Banfield, D. 1995, in Neptune and Triton, ed. D. P. Cruikshank (University of Arizona Press), 807–877

McKinnon, W. B., & Mueller, S. 1989, Geophysical Research Letters, 16, 591, doi: 10.1029/GL016i006p00591

McKinnon, W. B., Singer, K. N., Robbins, S. J., et al. 2024, Icarus, 422, doi: 10.1016/j.icarus.2024.116230

Merlin, F., Lellouch, E., Quirico, E., & Schmitt, B. 2018, Icarus, 314, 274, doi: 10.1016/j.icarus.2018.06.003

Message, P. J. 1972, Physics of the Earth and Planetary Interiors, 6, 17

Meurer, A., Smith, C. P., Paprocki, M., et al. 2017, PeerJ Computer Science, 3, e103, doi: 10.7717/peerj-cs.103

Mignard, F. 1979, The Moon and the Planets, 20, 301

—. 1980, The Moon and the Planets, 23, 185

Miguel, Y., & Ida, S. 2016, Icarus, 266, 1, doi: 10.1016/j.icarus.2015.10.030

Moore, J. M., & McKinnon, W. B. 2021, The Annual Review of Earth and Planetary Sciences, 49, 173, doi: 10.1146/annurev-earth-071720

Moraes, R., Borderes-Motta, G., Winter, O. C., & Mourão, D. C. 2023, Monthly Notices of the Royal Astronomical Society, 520, 2163

Moraes, R. A., Kley, W., & Vieira Neto, E. 2018, Monthly Notices of the Royal Astronomical Society, 475, 1347, doi: 10.1093/mnras/stx3268

Morbidelli, A., & Nesvorný, D. 2020, in The Trans-Neptunian Solar System (Elsevier), 25–59, doi: 10.1016/B978-0-12-816490-7.00002-3

Morgado, B. E., Sicardy, B., Braga-Ribas, F., et al. 2023, Nature, 614, 239, doi: 10.1038/s41586-022-05629-6

Mousis, O., Schneeberger, A., Lunine, J. I., et al. 2023, The Astrophysical Journal Letters, 944, L37, doi: 10.3847/2041-8213/acb5a4

Multhaup, K., & Spohn, T. 2007, Icarus, 186, 420, doi: 10.1016/j.icarus.2006.09.001

Murray, C. D., & Dermott, S. F. 1999, Solar System Dynamics (Cambridge University Press)

Nakajima, M., Genda, H., Asphaug, E., & Ida, S. 2022, Nature Communications, 13, doi: 10.1038/s41467-022-28063-8

Nelson, R. M., Buratti, B. J., Wallis, B. D., et al. 1990, Geophysical Research Letters, 17, 1761, doi: 10.1029/GL017i010p01761

Néri, A., Guyot, F., Reynard, B., & Sotin, C. 2020, Earth and Planetary Science Letters, 530, doi: 10.1016/j.epsl.2019.115920

Néron De Surgy, O., & Laskar, J. 1997, ASTRONOMY AND ASTROPHYSICS, 318, 975

Nesvorný, D. 2011, Astrophysical Journal Letters, 742, doi: 10.1088/2041-8205/742/2/L22

—. 2015, Astronomical Journal, 150, doi: 10.1088/0004-6256/150/3/73

Nesvorný, D., & Vokrouhlický, D. 2016, The Astrophysical Journal, 825, 94, doi: 10.3847/0004-637x/825/2/94

Nesvorný, D., Youdin, A. N., & Richardson, D. C. 2010, Astronomical Journal, 140, 785, doi: 10.1088/0004-6256/140/3/785

Neumann, W., Breuer, D., & Spohn, T. 2012, Astronomy and Astrophysics, 543, doi: 10.1051/0004-6361/201219157

Nicholson, S. , Van Maanen, A., & Willis, H. C. 1931, Publications of the Astronomical Society of the Pacific, 43, 261

Nimmo, F., & McKinnon, W. B. 2021, in The Pluto system after New Horizons, ed. S. A. Stern, J. M. Moore, W. M. Grundy, L. A. Young, & R. P. Binzel (Tucson: University of Arizona), 89–103

Nimmo, F., Neveu, M., & Howett, C. 2023, Origin and Evolution of Enceladus's Tidal Dissipation, Springer Science and Business Media B.V., doi: 10.1007/s11214-023-01007-4

Nimmo, F., & Spencer, J. R. 2015, Icarus, 246, 2, doi: 10.1016/j.icarus.2014.01.044

Nogueira, E., Brasser, R., & Gomes, R. 2011, Icarus, 214, 113, doi: 10.1016/j.icarus.2011.05.003

Nolan, M. C., & Lunine, J. I. 1988, Geophysical Research Letters, 15, 1315, doi: 10.1029/GL015i011p01315

Noyelles, B., Frouard, J., Makarov, V. V., & Efroimsky, M. 2014, Icarus, 241, 26, doi: 10.1016/j.icarus.2014.05.045

Ojakangas, G. W., & Stevenson, D. J. 1989, Icarus, 81, 220

O'Neill, C., Jellinek, A. M., & Lenardic, A. 2007, Earth and Planetary Science Letters, 261, 20, doi: 10.1016/j.epsl.2007.05.038

Ortiz, J. L., Santos-Sanz, P., Sicardy, B., et al. 2017, Nature, 550, 219, doi: 10.1038/nature24051

Oza, A. V., Johnson, R. E., Lellouch, E., et al. 2019, The Astrophysical Journal, 885, 168, doi: 10.3847/1538-4357/ab40cc

Peltier, W. R. 1974, Reviews of Geophysics, 12, 649, doi: 10.1029/RG012i004p00649

Perna, D., Dotto, E., Barucci, M. A., et al. 2009, Astronomy and Astrophysics, 508, 451, doi: 10.1051/0004-6361/200911970

Perrillat, J. P., Daniel, I., Koga, K. T., et al. 2005, Earth and Planetary Science Letters, 236, 899, doi: 10.1016/j.epsl.2005.06.006

Piralla, M., Villeneuve, J., Schnuriger, N., Bekaert, D. V., & Marrocchi, Y. 2023, Icarus, 394, doi: 10.1016/j.icarus.2023.115427

Pollack, J. B., Burns, J. A., & Tauber, M. E. 1979, Icarus, 37, 587

Porco, C. C., Helfenstein, P., Thomas, P. C., et al. 2006, Science, 311, 1393. https://www.science.org

Prinn, R. G., & Fegley, B. 1981, The Astrophysical Journal, 249, 308

Prockter, L. M., Mitchell, K. L., Howett, J. A., et al. 2019, in EPSC-DPS Joint Meeting 2019, Geneva

Proulx, R. J., & McClain, W. D. 1988, Journal of Guidance, Control and Dynamics, 11, 313

Ragozzine, D., & Brown, M. E. 2009, Astronomical Journal, 137, 4766, doi: 10.1088/0004-6256/137/6/4766

Reese, C. C., Solomatov, V. S., Baumgardner, J. R., & Yang, W.-S. 1999, Physics of the Earth and Planetary Interiors, 116, 1. www.elsevier.comrlocaterpepi

Renaud, J. P., & Henning, W. G. 2018, The Astrophysical Journal, 857, 98, doi: 10.3847/1538-4357/aab784

Renaud, J. P., Henning, W. G., Saxena, P., et al. 2021, Planetary Science Journal, 2, doi: 10.3847/PSJ/abc0f3

Reynolds, R. T., McKay, C. P., & Kasting, J. F. 1987, Advances in Space Research, 7, 125

Reynolds, R. T., Squyres, S. W., Colburn, D. S., & McKay, C. P. 1983, ICARUS, 56, 246

Roberts, J. H., & Nimmo, F. 2008a, Geophysical Research Letters, 35, doi: 10.1029/2008GL033725

—. 2008b, Icarus, 194, 675, doi: 10.1016/j.icarus.2007.11.010

Roig, F., & Nesvorný, D. 2015, Astronomical Journal, 150, doi: 10.1088/0004-6256/150/6/186

Ross, M. N., & Schubert, G. 1990, Geophysical Research Letters, 17, 1749, doi: 10.1029/GL017i010p01749

Rovira-Navarro, M., Gerkema, T., Maas, L. R., et al. 2020, Icarus, 343, doi: 10.1016/j.icarus.2020.113711

Rovira-Navarro, M., Matsuyama, I., & Berne, A. 2023. http://arxiv.org/abs/2311.15710

Rovira-Navarro, M., Van Der Wal, W., Steinke, T., & Dirkx, D. 2021, The Planetary Science Journal, 2, 119, doi: 10.3847/PSJ/abf6cb

Rufu, R., & Canup, R. M. 2017, The Astronomical Journal, 154, 208, doi: 10.3847/1538-3881/aa9184

—. 2022, The Astrophysical Journal, 928, 123, doi: 10.3847/1538-4357/ac525a

Ruiz, J. 2003, Icarus, 166, 436, doi: 10.1016/j.icarus.2003.09.009

Russell, C. T., Raymond, C. A., Coradini, A., et al. 2012, Science, 336, 684, doi: 10.1126/science.1219381

Rymer, A. M., Runyon, K. D., Clyde, B., et al. 2021, Planetary Science Journal, 2, doi: 10.3847/PSJ/abf654

Sabadini, R., Vermeersen, B., & Cambiotti, G. 2016, Global Dynamics of the Earth, 2nd edn. (Dordrecht: Springer Nature)

Sabadini, R., Yuen, D. A., & Boschi, E. 1982, Journal of Geophysical Research, 87, 2885, doi: 10.1029/JB087iB04p02885

Sagan, C. 1969, Icarus, 11, 268

Saillenfest, M., Sulis, S., Charpentier, P., & Santerne, A. 2023, Astronomy & Astrophysics, 675, A174. http://arxiv.org/abs/2306.07348

Schenk, P. 1992, in Abstracts of the Lunar and Planetary Science Conference, Vol. 23, 1215–1216

Schenk, P., & Jackson, M. P. A. 1993, Geology, 21, 299. http://pubs.geoscienceworld.org/gsa/geology/article-pdf/21/4/299/3514289/i0091-7613-21-4-299.pdf

Schenk, P. M., & Zahnle, K. 2007, Icarus, 192, 135, doi: 10.1016/j.icarus.2007.07.004

Schenk, P. M., Beddingfield, C. B., Bertrand, T., et al. 2021, Remote Sensing, 13, doi: 10.3390/rs13173476

Scott, H. P., Williams, Q., & Ryerson, F. J. 2002, Earth and Planetary Science Letters, 203, 399. www.elsevier.com/locate/epsl

Shock, E. L., & McKinnon, W. B. 1993, Icarus, 106, 464

Slack, G. A. 1980, Physical Review B, 22, 3065

Smith, B. A., Soderblom, L. A., Banfield, D., et al. 1989, Science, 246, 1422. https://www.science.org

Soderblom, L. A., Kieffer, S. W., Becker, T. L., et al. 1990, Science, 250, 410. https://www.science.org

Soderlund, K. M., Kalousová, K., Buffo, J. J., et al. 2020, Space Science Reviews, 216, doi: 10.1007/s11214-020-00706-6

Sohl, F., Spohn, T., Breuer, D., & Nagel, K. 2002, Icarus, 157, 104, doi: 10.1006/icar.2002.6828

Solomatov, V. S. 1995, Physics of Fluids, 7, 266, doi: 10.1063/1.868624

Souami, D., Braga-Ribas, F., Sicardy, B., et al. 2020, Astronomy and Astrophysics, 643, doi: 10.1051/0004-6361/202038526

Spencer, J. R., & Nimmo, F. 2013, Annual Review of Earth and Planetary Sciences, 41, 693, doi: 10.1146/annurev-earth-050212-124025

Spohn, T., & Schubert, G. 2003, Icarus, 161, 456, doi: 10.1016/S0019-1035(02)00048-9

Squyres, S. W., Reynolds, R. T., Cassen, P. M., & Peale, S. J. 1983, Nature, 301, 225

Stern, S. A. 2014, in Encyclopedia of the Solar System (Elsevier), 909–924, doi: 10.1016/B978-0-12-415845-0.00042-6

Stern, S. A., Grundy, W. M., Mckinnon, W. B., Weaver, H. A., & Young, L. A. 2018, Annual Review of Astronomy and Astrophysics, 56, 357, doi: 10.1146/annurev-astro-081817

Stern, S. A., & McKinnon, W. B. 2000, THE ASTRONOMICAL JOURNAL, 119, 945

Stevenson, D. J. 2003, Comptes Rendus - Geoscience, 335, 99, doi: 10.1016/S1631-0713(03)00009-9

Stevenson, D. J., & Gandhi, A. S. 1990, in Abstracts of the Lunar and Planetary Science Conference, Vol. 21, 1202–1203

Strom, C., Nordheim, T. A., Patthoff, D. A., & Fieber-Beyer, S. K. 2024, Planetary Science Journal, 5, doi: 10.3847/PSJ/ad77d7

Strom, R. G., Croft, S. K., & Boyce, J. M. 1990, Science, 250, 437. https://www.science.org

Sulcanese, D., Cioria, C., Kokin, O., et al. 2023, Icarus, 392, doi: 10.1016/j.icarus.2022.115368

Szulágyi, J., Cilibrasi, M., & Mayer, L. 2018, The Astrophysical Journal, 868, L13, doi: 10.3847/2041-8213/aaeed6

Takeuchi, H., & Saito, M. 1972, in Methods in computational physics, ed. B. Bolt, B. Alder, S. Fernbach, & M. Rotenberg, Vol. 11 (New York: Academic Press), 217–295

Taylor, G. J. 1992, Journal of Geophysical Research, 97, doi: 10.1029/92je01501

Teachey, A., Kipping, D., Burke, C. J., Angus, R., & Howard, A. W. 2020, The Astronomical Journal, 159, 142, doi: 10.3847/1538-3881/ab7001

Teachey, A., & Kipping, D. M. 2018, Science Advances, 4, eaav1784. https://www.science.org

Teachey, A., Kipping, D. M., & Schmitt, A. R. 2018, The Astronomical Journal, 155, 36, doi: 10.3847/1538-3881/aa93f2

Thirouin, A., Noll, K. S., Ortiz, J. L., & Morales, N. 2014, Astronomy and Astrophysics, 569, doi: 10.1051/0004-6361/201423567

Thomas, P. C. 2000, Icarus, 148, 587, doi: 10.1006/icar.2000.6511

Thomas, P. C., Tajeddine, R., Tiscareno, M. S., et al. 2016, Icarus, 264, 37, doi: 10.1016/j.icarus.2015.08.037

Tiesinga, E., Mohr, P. J., Newell, D. B., et al. 2024, The 2022 CODATA Recommended Values of the Fundamental Physical Constants (Web Version 9.0), Tech. rep., National Institute of Standards and Technology, Gaithersburg. https://physics.nist.gov/constants

Tisserand, F. 1889, Traité de Mécanique Céleste (Paris: Gauthier-Villars et fils)

Tobie, G., Lunine, J. I., Monteux, J., Mousis, O., & Nimmo, F. 2014, in Titan: Interior, Surface, Atmosphere and Space Environment (Cambridge University Press), 29–62

Tobie, G., Mocquet, A., & Sotin, C. 2005, Icarus, 177, 534, doi: 10.1016/j.icarus.2005.04.006

Tokadjian, A., & Piro, A. L. 2022, The Astrophysical Journal Letters, 929, L2, doi: 10.3847/2041-8213/ac61e8

Trinh, K. T., Bierson, C. J., & O'Rourke, J. G. 2023, Science Advances, 9, eadf3955. https://www.science.org

Tyler, G. L., Sweetnam, D. N., Anderson, J. D., et al. 1989, Science, 246, 1466

Van Woerkom, Q. B. 2024, The trans- and post-capture orbital evolution of Triton, Leiden: Leiden Observatory

van Woerkom, Q. B., & Kleisioti, E. 2024, Astronomy and Astrophysics, 684, doi: 10.1051/0004-6361/202348604

Van Zelst, I., Crameri, F., Pusok, A. E., et al. 2022, Solid Earth, 13, 583, doi: 10.5194/se-13-583-2022

Vernazza, P., Ferrais, M., Jorda, L., et al. 2021, Astronomy and Astrophysics, 654, doi: 10.1051/0004-6361/202141781

Virtanen, P., Gommers, R., Oliphant, T. E., et al. 2020, Nature Methods, 17, 261, doi: 10.1038/s41592-019-0686-2

Vokrouhlickỳ, D., Nesvornỳ, D., & Levison, H. F. 2008, Astronomical Journal, 136, 1463, doi: 10.1088/0004-6256/136/4/1463

Von Zeipel, H. 1912, Arkiv för Matmematik, Astronomy och Fysik, 8, 1

Wada, K., Kokubo, E., & Makino, J. 2006, The Astrophysical Journal, 638, 1180

Wahr, J., Selvans, Z. A., Mullen, M. E., et al. 2009, Icarus, 200, 188, doi: 10.1016/j.icarus.2008.11.002

Walterová, M., & Běhounková, M. 2020, The Astrophysical Journal, 900, 24, doi: 10.3847/1538-4357/aba8a5

Williams, D. M., Kasting, J. F., & Wade, R. A. 1997, Nature, 385, 234

Wisdom, J. 2008, Icarus, 193, 637, doi: 10.1016/j.icarus.2007.09.002

Wnuk, E. 1997, Advances in Space Research, 19, 1735

Wu, L., & Zhang, M. 2024, Hansen Coefficients in Satellite Orbital Dynamics (Singapore: Springer Nature Singapore)

Wu, P., & Peltier, W. R. 1982, Geophysical Journal of the Royal Astronomical Society, 70, 435, doi: 10.1111/j.1365-246X.1982.tb04976.x

Zahnle, K. 2001, Nature, 412, 209. www.nature.com

Zimmer, C., Khurana, K. K., & Kivelson, M. G. 2000, Icarus, 147, 329, doi: 10.1006/icar.2000.6456

Zolotov, M. Y. 2009, Icarus, 204, 183, doi: 10.1016/j.icarus.2009.06.011

A Numerical implementation

A.1. Finite difference schemes

In a conductive mantle or shell, solving the heat equation (Eq. 3.16) in the general, non-analytical case requires a numerical implementation. We opt to discretise body along the radius, and approximate Eq. 3.16 at each grid point using 6th-order finite difference schemes: we will find that we require an implementation both for the first and second derivative. Additionally, we identify two scenarios: in the case of a fully solid conductive layer, we only need a discretisation scheme that accounts for static grid points, for which expressions are provided in Sec. A.1.1. Once a liquid layer starts to form, however, the discretisation scheme must account for a moving boundary condition (that of the advancing or receding melting front), which requires an adapted treatment. We provide a suitable 6th-order scheme for this purpose in Sec. A.1.2.

A.1.1. Static finite difference schemes

In the static-grid case, the coefficients of the finite difference scheme are constant and rational: for the usual central, forward and backward difference schemes, the finite difference coefficients tabulated by Fornberg (1988) can be used, or in the central case they can be computed e.g. by the method of Cynar (1987). To properly account for boundary conditions at the grid edges, however, we need more general asymmetric schemes, which we therefore derive using a generalisation of the methods of Gerald & Wheatley (2004, Ch. 5.1). Let us denote the N-step finite difference scheme by which to approximate the m-th derivative of a function f at a point x_0 as follows:

$$f^{(m)}(x_0) \approx \frac{1}{h^m} \sum_{i=1}^{N} \alpha_i f(x_0 + s_i h) \tag{A.1}$$

where h is the grid step size and the s_i denote the stencil-points in units of the step size. By Taylor expansion, the optimal-order (i.e. with highest order of the error term: for asymmetric schemes, this is in general $o = N - m$, while for a central scheme this is $o = N - m + 1$) approximation to $f^{(m)}(x_0)$ on a stencil s_i can be shown to satisfy (Gerald & Wheatley, 2004)

$$\begin{pmatrix} 1 & \dots & 1 \\ s_1 & \dots & s_N \\ s_1^2 & \dots & s_N^2 \\ \vdots & \ddots & \vdots \\ s_1^{N-1} & \dots & s_N^{N-1} \end{pmatrix} \begin{pmatrix} \alpha_1 \\ \vdots \\ \alpha_N \end{pmatrix} = m! \begin{pmatrix} \delta_{0m} \\ \vdots \\ \delta_{(N-1)m} \end{pmatrix} \tag{A.2}$$

where δ_{ij} is the Kronecker delta. As the s_i are known a priori for a static grid, the numerical values of the α_i can be pre-computed. For a uniform grid the coefficients are rational numbers, which we compute using the computer algebra software SymPy (Meurer et al., 2017): the coefficients for a 6th-order scheme are given in Tab. A.1. We only give the forward versions of the discretisations: the backward versions (with stencil points $s_i \to -s_i$) follow by multiplying the coefficients by -1 for odd order derivatives, while they remain identical for even order derivatives. That is, the stencil $[-4, -3, -2, -1, 0, 1]$ has coefficients $[1/60, -2/15, 1/2, -4/3, 7/12, 2/5, -1/30]$ for the first derivative, while the stencil $[-5, -4, -3, -2, -1, 0, 1, 2]$ has coefficients $[-1/90, 4/45, -3/10, 17/36, 13/18, -21/10, 107/90, -11/180]$ for the second derivative.

Table A.1: 6th-order finite difference coefficients α_i for an approximation to the m-th derivative using stencil points on a static grid.

	s_i										
m	-3	-2	-1	0	1	2	3	4	5	6	7
1	-1/60	3/20	-3/4	0	3/4	-3/20	1/60				
		1/30	-2/5	-7/12	4/3	-1/2	2/15	-1/60			
			-1/6	-77/60	5/2	-5/3	5/6	-1/4	1/30		
				-49/20	6	-15/2	20/3	-15/4	6/5	-1/6	
2	1/90	-3/20	3/2	-49/18	3/2	-3/20	1/90				
		-11/180	107/90	-21/10	13/18	17/36	-3/10	4/45	-1/90		
			7/10	-7/18	-27/10	19/4	-67/18	9/5	-1/2	11/180	
				469/90	-223/10	879/20	-949/18	41	-201/10	1019/180	-7/10

Table A.2: Parameters summarising the variable-boundary finite difference coefficients α_i for an approximation to the first derivative for different stencils. a_i, b_i, c_i, d_i are as in Eq. A.3.

s_i	$-\delta$	0	1	2	3	4	5
a_i	-	-137	5	-5	10	-5	1
b_i	-120	60	0	0	0	0	0
c_i	-	60	1	1	3	4	5
d_i	-	0	1	2	9	16	25
s_i	$-\delta-1$	-1	0	1	2	3	4
a_i	-	-1	-13	2	-1	1	-1
b_i	24	-1	-1	2	-1	1	-1
c_i	-	5	12	1	1	3	20
d_i	-	0	12	2	3	12	100
s_i	$-\delta-2$	-2	-1	0	1	2	3
a_i	-	1	-1	-1	1	-1	1
b_i	-12	2	-2	1	2	-2	2
c_i	-	20	2	3	1	4	30
d_i	-	0	2	6	3	16	150

A.1.2. Dynamic-boundary finite difference schemes

When, as is the case for a conductive Triton with a growing core and ocean, boundary conditions are given by an advancing/receding melting front, a static finite difference scheme is no longer an appropriate discretisation of the heat equation. In this case, the finite difference approximation Eq. A.1 still has the optimal-order solution given by Eq. A.2, but one of the stencil points s_i is no longer uniformly spaced. In our case, this will always be the stencil point at the left-most boundary[1], s_1: we will denote the distance from the next grid-point in units of the step size h by δ. In approximating the heat equation, we will need asymmetric estimates for the first and second derivative incorporating this moving boundary for the three grid points closest to the melting front: beyond that, the static difference schemes given in Tab. A.1 will suffice again. In this case, the system Eq. A.2 can be solved analytically: we again find expressions using SymPy (Meurer et al., 2017). At each of the three points closest points to the boundary, the optimal-order finite difference scheme coefficients, which are now a function of δ, can be written in the form

$$\alpha_i(\delta) = \begin{cases} \frac{b_i}{\delta^6+15\delta^5+85\delta^4+225\delta^3+274\delta^2+120\delta} & \text{for } i=0 \\ \frac{a_i\delta+b_i}{c_i\delta+d_i} & \text{for } i>0 \end{cases} \tag{A.3}$$

for the first derivative, and

$$\alpha_i(\delta) = \begin{cases} \frac{b_i}{\delta^7+21\delta^6+175\delta^5+735\delta^4+1624\delta^3+1764\delta^2+720\delta} & \text{for } i=0 \\ \frac{a_i\delta+b_i}{c_i\delta+d_i} & \text{for } i>0 \end{cases} \tag{A.4}$$

for the second derivative. The values a_i, b_i, c_i and d_i for each stencil are tabulated in Tab. A.2 for the first derivative and Tab. A.3 for the second derivative. It can be verified that they reduce to the values in Tab. A.1 for $\delta = 1$.

Additionally, to compute the energy balance across the melting front, we will require an estimate for the first derivative at the melting front, which allows us to evaluate the total heat conducted away from the boundary. The corresponding finite difference scheme is more complicated than those evaluated away from the boundary (as a result of the stencil being dependent on the value of δ at each point), and is better given directly:

$$\alpha_i(\delta) = \begin{cases} -\frac{6\delta^5+75\delta^4+340\delta^3+675\delta^2+548\delta+120}{\delta^6+15\delta^5+85\delta^4+225\delta^3+274\delta^2+120\delta} & \text{for } i=1 \\ \frac{\delta^5+15\delta^4+85\delta^3+225\delta^2+274\delta+120}{120\delta} & \text{for } i=2 \\ -\frac{\delta^5+14\delta^4+71\delta^3+154\delta^2+120\delta}{24\delta+24} & \text{for } i=3 \\ \frac{\delta^5+13\delta^4+59\delta^3+107\delta^2+60\delta}{12\delta+24} & \text{for } i=4 \\ -\frac{\delta^5+12\delta^4+49\delta^3+78\delta^2+40\delta}{12\delta+36} & \text{for } i=5 \\ \frac{\delta^5+11\delta^4+41\delta^3+61\delta^2+30\delta}{24\delta+96} & \text{for } i=6 \\ -\frac{\delta^5+10\delta^4+35\delta^3+50\delta^2+24\delta}{120\delta+600} & \text{for } i=7 \end{cases} \tag{A.5}$$

for the stencil $[0, \delta, \delta+1, \delta+2, \delta+3, \delta+4, \delta+5]$.

[1]Though the expression for a right-most boundary can be derived easily by the odd (even) property of odd (even) order derivatives.

Table A.3: Parameters summarising the variable-boundary finite difference coefficients α_i for an approximation to the second derivative for different stencils. a_i, b_i, c_i, d_i are as in Eq. A.4.

s_i	$-\delta$	0	1	2	3	4	5	6
a_i	-	406	-87	117	-254	33	-27	137
b_i	3528	-441	60	-60	120	-15	12	-60
c_i	-	90	5	4	9	2	5	180
d_i	-	0	5	8	27	8	25	1080
s_i	$-\delta - 1$	-1	0	1	2	3	4	5
a_i	-	137	-49	-17	47	-19	31	-13
b_i	-308	77	-203	43	-13	1	1	-1
c_i	-	180	60	12	18	12	60	180
d_i	-	0	60	24	54	48	300	1080
s_i	$-\delta - 2$	-2	-1	0	1	2	3	4
a_i	-	-13	19	-14	10	1	-1	1
b_i	56	-14	26	-35	44	-10	2	-1
c_i	-	180	15	6	9	12	15	90
d_i	-	0	15	12	27	48	75	540

A.2. Dynamic gridding

The size of Triton's ice shell and conductive mantle varies wildly between over time. To avoid having to maintain an unnecessarily fine grid, we therefore adapt the grid to follow the evolution of the ocean or convective region. This additionally allows us to circumvent the problems that arise from the singularity in the variable-boundary finite difference stencil at the moving boundary (Eq. A.5), by adapting the grid before the moving boundary reaches one of the grid points (i.e. before $\delta = 0$).

A.2.1. Defining the adaptive grid

To effectuate this, we define some boundaries at which to "re-grid" the sampling grid. We recursively define a series of grids, beginning with the starting grid g_0 that simply uniformly samples radial positions between the inner and outer radii of the full layer, R_i and R_o: let us assume some number N of interior grid points (left unspecified, but kept constant), and a starting grid spacing of $h_0 = \frac{R_o - R_i}{N+1}$. There is some moving boundary $r_d(t)$ that bounds from below the region over which the gridding is relevant (i.e. the ocean boundary for the conductive ice shell, or the convective region boundary for the mantle), and at which the temperature is known. For this initial definition, we will assume that $r_d(0) = R_i$, but the extension to other cases is natural (see Sec. A.2.2). The node closest to R_i shall be dubbed r_0, and we wish to adapt our grid once the moving boundary r_d reaches r_0 to within some margin, expressed as a fraction δ_m of the step size h_0: this "critical" radius we will call $\tilde{r}_0 = r_0 - \delta_m h_0$.

Once $r_d(t) \geq \tilde{r}_0$, we wish to re-define our grid, and generate a new grid g_1. We choose to set the new lowest node in the grid to be the second node in the old grid: $r_1 = r_0 + h_0$, so as to avoid exciting numerical oscillations from interpolation onto the new grid. The new grid g_1 is then evenly sampled between r_1 and R_o such that we once again have N interior points in total, and the old temperature profile is interpolated onto the new grid using *scipy*'s *PchipInterpolator* routine. The new grid spacing, h_1 is then given by $h_1 = h_0 \frac{N-1}{N}$, and the new critical radius is $\tilde{r}_1 = r_1 - \delta_m h_1$. If $r_d(t) \geq \tilde{r}_1$, this process repeats to generate r_2, h_2, g_2, and $\tilde{r}_2$; if at some point instead $r_d(t)$ falls below $\tilde{r}_0$ again, we go back to the old grid g_0.

Generalising this process, we find that the grid g_j for $j \geq 0$ is defined by the following quantities:

$$h_j = h_0 \left(\frac{N-1}{N} \right)^j \tag{A.6}$$

$$r_j = r_0 + \sum_{i=0}^{j-1} h_i = R_o - h_0 N \left(\frac{N-1}{N} \right)^j \tag{A.7}$$

$$\tilde{r}_j = r_j - \delta_m h_j = R_o - h_0 \left(N + \delta_m \right) \left(\frac{N-1}{N} \right)^j . \tag{A.8}$$

While using the grid g_j, we will "downgrid" to g_{j-1} if $r_d(t) \leq \tilde{r}_{j-1}$, and "upgrid" to g_{j+1} if $r_d(t) \geq \tilde{r}_j$. Consequently, the grid g_j can be used for dynamic boundary values $r_d(t)$ over the interval $[\tilde{r}_{j-1}, \tilde{r}_j]$, with exception of g_0, which is appropriate for values over the interval $[R_i, \tilde{r}_0]$. As $h_j \to 0$ for $j \to \infty$, the adaptive grid can handle all values for the dynamic boundary over the semi-open interval $[R_i, R_o)$. The only problem that arises is then if the region to be gridded disappears entirely ($r_d(t) = R_o$): this can happen in the case of a fully molten ice shell, which would require separate treatment.

A.2.2. Non-zero starting states for the dynamic boundary

It is also possible for the dynamic boundary to be initialised at a value other than R_i: in this case, we simply have to select the appropriate grid g_j at which to initialise the adaptive grid. As g_j is used for dynamic boundary radii $r_d \in [\tilde{r}_{j-1}, \tilde{r}_j)$[2], we have for $j \geq 1$:

$$\tilde{r}_{j-1} \leq r_d < \tilde{r}_j \tag{A.9}$$

from which we can derive using Eqs. A.6-A.8 that

$$j(r_d) = \left\lfloor 1 + \frac{\ln\left(\frac{R_o - \tilde{r}_0}{R_o - r_d}\right)}{\ln\left(1 + \frac{1}{N-1}\right)} \right\rfloor \tag{A.10}$$

where $\lfloor \cdot \rfloor$ is the floor function, which returns the integral part of a real number. For $R_i \leq r_d < \tilde{r}_0$ (i.e. $j = 0$), this expression can also be shown to hold.

A.3. Thermal evolution for a non-equilibrium ice shell

To test that our assumption of an equilibrium ice shell is valid, we wrote a code to simulate the non-equilibrium thermal evolution of the shell. The boundary conditions going into that code are provided here for completeness.

A.3.1. The radiative boundary condition for the surface of a discretised ice shell

The thermal evolution of the upper part of the ice shell will in general be described by conduction. The surface layer is going to be radiating away whatever heat is conducted to the surface, however, and so we must incorporate the accompanying boundary condition in our algorithm. Doing so requires us to determine, at each timestep, the surface temperature that satisfies conservation of energy across the surface. That is, we write:

$$-\frac{C_k}{T(R)}\frac{\partial T(R)}{\partial r} = \varepsilon\sigma_{SB}\left(T^4(R) - T_{eq}^4\right), \tag{A.11}$$

where T_{eq} is the equilibrium temperature of the surface. We note that we must estimate the radial derivative of the temperature numerically. To do this, we use an N-th order implicit (i.e. including $T(R)$) finite difference scheme (while we will in general use a 6th-order scheme, we do not specify this here for generality) of the general form A.1:

$$\frac{\partial T(R)}{\partial r} \approx -\frac{1}{h}\sum_{i=1}^{N} \alpha_i T(R - s_i h) \tag{A.12}$$

where we have transformed the derivative to use the coefficients of the forward finite difference scheme, even though we use a backward stencil. While an explicit scheme would allow for computation of a trivial expression for the surface temperature, an implicit expression is less sensitive to error in the numerical derivative and so is to be preferred.

This expression allows us to rewrite Eq. A.11 as a quintic polynomial of the following form:

$$T^5(R) - AT(R) - B = 0 \tag{A.13}$$

where

$$A = T_{eq}^4 + \frac{C_k \alpha_0}{\varepsilon\sigma_{SB} h} \tag{A.14}$$

$$B = \frac{C_k}{\varepsilon\sigma_{SB} h}\sum_{i=2}^{N} \alpha_i T(R - s_i h). \tag{A.15}$$

for physical temperature gradients (increasing with depth), we can show that $B \geq 0$; as α_0 is in general negative, the sign of A depends on the dynamic shell grid spacing, and can possibly become negative. We can apply the transformation $T(R) = |A|^{1/4}x$ to find the following expression to solve:

$$x^5 - \mathrm{sgn}(A)x - C = 0 \tag{A.16}$$

[2] g_j can in principle be used for $r_d \in [\tilde{r}_{j-1}, \tilde{r}_j]$, but using a semi-open interval makes each $r_d \in [R_i, R_o)$ unambiguously part of one interval.

where

$$C = \frac{B}{|A|^{5/4}}. \tag{A.17}$$

We solve Eq. A.16 using *SciPy*'s *optimize.brentq* function (Virtanen et al., 2020), and note without proof the following bounds that hold for the relevant root of Eq. A.16 (and which are therefore useful in initialising the root-finder):

$$(1 + C)^{1/5} \leq x \leq \left(1 + \frac{256}{2869}\right)^{1/5} (1 + C)^{1/5} \text{ for } A > 0 \tag{A.18}$$

$$\left(C - C^{1/5}\right)^{1/5} \leq x \leq \left(C - \left(C - C^{1/5}\right)^{1/5}\right)^{1/5} \text{ for } A < 0. \tag{A.19}$$

The bounds for $A > 0$ become exact respectively for $C = 0$ and $C = \frac{1845}{1024}$, and are otherwise strict; the bounds for $A < 0$ become exact only for $C = 0$.

A.3.2. Thermal evolution of a conductive ice shell in contact with the mantle

For a conductive shell in direct contact with the conductive part of the mantle, we impose conservation of energy by conduction through this interface (which we find at radius R_m):

$$-k_m(t, r, T)\frac{\partial T_m(R_m)}{\partial r} = -k_s(t, r, T)\frac{\partial T_s(R_m)}{\partial r} \tag{A.20}$$

where the subscript m denotes "of the mantle" and s denotes quantities belonging to the shell. For our discretised heat equation (approximating the radial derivative by a finite difference scheme), this boundary condition then amounts to selecting the mantle-shell interface temperature such that Eq. A.20 is satisfied.

B Simplified tidal expressions

While the propagator-matrix formalism (e.g. Sabadini et al., 2016) allows one, in theory, to derive analytical expressions for the Love numbers of an arbitrary layered, incompressible body, the resulting expressions will in practice become unwieldy and poorly interpretable for anything more than two layers for a fully solid body, and already for the two-layer case if those two layers encase an interior fluid layer. Nonetheless, on the basis of the assumption of an ice shell that is thin with respect to the total radius of the body, Beuthe (2015a,b, 2016, 2018, 2019) developed a formalism that allows for a relatively simple computation of the Love numbers and division of dissipated power between the shell and mantle in an icy body satisfying the thin-shell assumption, the process of which we will sketch in Sec. B.1.

B.1. Thin-shell tidal theory

Under the assumption of a thin shell, we have implemented the radial and gravitational Love number expressions given by Beuthe (2019), which we provide in Sec. B.1.1; Beuthe (2019) also gives an expression for the partitioning of dissipated energy between the shell and mantle (core in his terminology) of a thin-shell body, which we will discuss in Sec. B.1.2.

B.1.1. Love numbers for a thin-shell Triton

We will recount here the Love number expressions given by Beuthe (2019), adapted to our notation. To start with, the gravitational and radial Love numbers $\bar{k}_l(\omega)$ and $\bar{h}_l(\omega)$ are given:

$$\bar{k}_l(\omega) = (1 + \Lambda_l)\bar{h}_l(\omega) - 1 \tag{B.1}$$

$$\bar{h}_l(\omega) = \frac{\bar{h}_l^\circ}{1 + (1 + \xi_l \bar{h}_l^\circ)\Lambda_l} \tag{B.2}$$

where $\bar{h}_l^\circ$ is the fluid-crust radial Love number[1], Λ_l is the thin-shell spring constant, and ξ_l is the degree-l density ratio:

$$\xi_l = \frac{3}{2l + 1}\frac{\rho_s}{\rho_b} \tag{B.3}$$

with ρ_s, ρ_b being the shell and bulk density, respectively. The expressions for $\bar{h}_l^\circ$ and Λ_l are slightly more involved, and we will simply copy them and the relations involved in their computation here from Beuthe (2019) without further elaboration upon terminology (for which we refer the reader to Beuthe 2019):

$$\Lambda_l = \frac{\chi}{\psi}\Lambda_l^M + \chi\psi\Lambda_l^B \tag{B.4}$$

$$\bar{h}_l^\circ = \bar{k}_l^\circ + 1 = \frac{A_l + (2l + 1)y^4\hat{\mu}_c}{B_l + (2l + 1 - 3\xi_1)y^4\hat{\mu}_c} \tag{B.5}$$

[1] The fluid-crust Love numbers, following Beuthe (2019), are the Love numbers for a body equivalent to the thin-shell body under evaluation, but assuming that the ocean extends to the surface, rather than ending at the shell. In this manner, the elegance in the approach formulated by Beuthe (2015b) lay in extending the use of existing analytical formulae for a model Earth comprising of a rocky core covered by a water ocean to models covered by a thin icy shell.

where

$$\Lambda_l^M = \frac{\delta_l}{\delta_l - 1 - \nu} \frac{1}{\rho_s g R^2 \alpha_{\text{inv}}} \tag{B.6}$$

$$\Lambda_l^B = \delta_l(\delta_l - 1 + \nu) \frac{D_{\text{inv}}}{\rho_s g R^4} \tag{B.7}$$

$$\delta_l = -(l-1)(l+2) \tag{B.8}$$

$$\chi = \frac{\mu_0 + \mu_1 \varepsilon}{\mu_0 + 2\varepsilon\mu_1 + \varepsilon^2 \mu_2} \tag{B.9}$$

$$\psi = \frac{\mu_0}{\mu_0 + \varepsilon \mu_1} \tag{B.10}$$

$$\varepsilon = \frac{d}{R} \tag{B.11}$$

$$\alpha_{\text{inv}} = \frac{1}{2(1+\nu)\mu_0 d} \tag{B.12}$$

$$D_{\text{inv}} = \frac{2\mu_{\text{inv}} d^3}{1-\nu} \tag{B.13}$$

$$\mu_{\text{inv}} = \mu_2 - \frac{\mu_1^2}{\mu_0} \tag{B.14}$$

$$\mu_p(\omega) = d^{-p-1} \int_{R-d}^{R} \mu(\omega, r)(r-R)^p \, \mathrm{d}r \tag{B.15}$$

$$\hat{\mu}_c = \frac{\mu_{\text{mantle}}}{\rho_b g R} \tag{B.16}$$

$$y = \frac{R_{\text{core}}}{R} \tag{B.17}$$

$$A_l(y, \xi_1) = f_l(1-\xi_1)(2l+1)p_A \tag{B.18}$$

$$B_l(y, \xi_1) = f_l(1-\xi_1)p_B \tag{B.19}$$

$$f_l = \frac{l}{2(l-1)(3+4l+2l^2)} \tag{B.20}$$

$$p_A = (2(l-1) + 3y^{2l+1})(1-\xi_1) + (2l+1)y^3\xi_1 \tag{B.21}$$

$$p_B = (2l+1-3\xi_1)\left[2(l-1)(1-\xi_1) + (2l+1)y^3\xi_1\right] - 9(1-\xi_1)y^{2l+1}\xi_1 \tag{B.22}$$

with g the surface gravitational acceleration, R_{core}, μ_{mantle} the radius and rigidity of the core, d the thickness of the ice shell and ν being Poisson's ratio.

B.1.2. Core-shell partitioning of total tidal dissipation

Under these assumptions, Beuthe (2019) also derives an expression for the partitioning of the total dissipated energy between the rocky interior and the icy shell. This allows us to evaluate, at each forcing frequency ω, what part of the energy is dissipated in what part of the body. The total dissipated energy at a particular forcing frequency ω can be written in the following form (Beuthe, 2019, Eq. 48):

$$\dot{E}_{\text{tot}}(\omega) = -\frac{2l+1}{2} \frac{\omega R}{\mathcal{G}} \operatorname{Im}(\bar{k}_l) \left\langle \left|U_l^T\right|^2 \right\rangle \tag{B.23}$$

where $\left\langle \left|U_l^T\right|^2 \right\rangle$ is the component of the averaged squared tidal potential at frequency ω appearing in the Darwin-Kaula expansion (though this part is not made explicit by Beuthe). The energy dissipated in the rocky interior (or core, in the terminology used by Beuthe) is given instead by:

$$\dot{E}_{\text{core}} = -\frac{2l+1}{2} \frac{\omega R}{\mathcal{G}} \left| \frac{\bar{k}_l + 1}{\bar{h}_l^\circ} \right|^2 \operatorname{Im}(\bar{h}_l^\circ) \left\langle \left|U_l^T\right|^2 \right\rangle . \tag{B.24}$$

Hence, the fraction of the total power dissipated in the interior by the frequency ω-component, which we will denote $\varphi_c(\omega)$, is given by

$$\varphi_c(\omega) = \left| \frac{\bar{k}_l(\omega) + 1}{\bar{h}_l^\circ(\omega)} \right|^2 \frac{\operatorname{Im}(\bar{h}_l^\circ(\omega))}{\operatorname{Im}(\bar{k}_l(\omega))} \tag{B.25}$$

and therefore follows straightforwardly from the terms $\bar{k}_l(\omega)$ and $\bar{h}_l^\circ(\omega)$ already computed at each forcing frequency in the Love number-computations necessary to evaluate the total dissipated power in the first place. Noting that the tidal quality function $K_l(\omega) = -\operatorname{Im}(\bar{k}_l(\omega))$, we can then write explicitly the total dissipated power and the power dissipated in the interior using the Darwin-Kaula expansion:

$$\dot{E}_{\text{tot}} = -n^2 a^2 \beta \frac{M_N}{M_T} \sum_{l\geq 2} \left(\frac{R}{a}\right)^{2l+1} \sum_{m=0}^{l} \frac{(l-m)!}{(l+m)!}(2-\delta_{0m}) \sum_{p=0}^{l} F_{lmp}^2(i_T) \sum_{q=-\infty}^{\infty} G_{lpq}^2(e) \operatorname{Im}(\bar{k}_{l,T}(\omega_{T,lmpq}))\omega_{T,lmpq} \quad \text{(B.26)}$$

$$\dot{E}_{\text{core}} = -n^2 a^2 \beta \frac{M_N}{M_T} \sum_{l\geq 2} \left(\frac{R}{a}\right)^{2l+1} \sum_{m=0}^{l} \frac{(l-m)!}{(l+m)!}(2-\delta_{0m}) \sum_{p=0}^{l} F_{lmp}^2(i_T) \sum_{q=-\infty}^{\infty} G_{lpq}^2(e) \operatorname{Im}(\bar{k}_{l,T}(\omega_{T,lmpq}))\omega_{T,lmpq}\varphi_c(\omega_{T,lmpq}) \quad \text{(B.27)}$$

$$\dot{E}_{\text{shell}} = \dot{E}_{\text{tot}} - \dot{E}_{\text{core}} \quad \text{(B.28)}$$

where we include explicitly the dependency of ϕ_c on forcing frequency ω_{lmpq} to remind ourselves that each such term must be recomputed for every forcing frequency.

C Validation and verification

Before we present the results of our analysis of Triton, we show that our model works as intended, and validate assumptions made in our methodology. In Sec. C.1, we show that the dynamical model we use reproduces the results of the previously verified standalone dynamics code of Van Woerkom (2024), an altered version of which we have incorporated into our model; we also derive two restricted conservation laws that will be used to verify that the numerically integrated dynamical equations of motion satisfy the behaviour expected of them analytically. Sec. C.2 demonstrates that the interior-evolution component of the code works as intended and that the assumptions made there are valid. Finally, Sec. C.3 shows that the components coupling these two parts of the model also work as intended.

C.1. Dynamical evolution

The development of the dynamical part of the code was the subject of previous work (Van Woerkom, 2024), which has already been extensively validated. Nonetheless, we have made some changes in the adaptation to a combined interior-orbit evolution code, and we have changed the approach to the computation of the equilibrium rotational state. Hence, we will show (1) that the results of the code coincide with those produced by the previous code to the extent in which they might be expected to and (2) we introduce two conservation laws that the dynamical equations satisfy, which we use to check that the code behaves as intended and that our integrator tolerances are set appropriately.

C.1.1. Comparison against previous work

In Fig. C.1, a representative scenario for the mid-to-high eccentricity evolution of Triton is shown for a set of homogeneous Maxwell tidal models of Triton with various values of the viscosity η for an elastic rigidity $\mu = 4.8$ GPa (see Van Woerkom 2024 for the details of the computation; the value of the shear modulus is as in Bagheri et al. 2022a) that is representative of an icy body[1].

A notable difference between the two models is found in the rotation rate: for higher viscosities, the old and new models diverge for higher spin-orbit resonances. This is explained by the difference in approach to the determination of the equilibrium rotation rate: Van Woerkom (2024) used a root-finder to find the first (highest) stable spin-orbit resonance, whereas we propagate the rotational rate from the previous state, keeping all other dynamical values equal, until it reaches a stable spin state. At high viscosities, where the higher spin-orbit resonances are only marginally stable (see e.g. Van Woerkom, 2024; Renaud et al., 2021), such resonances are prone to being passed over by the latter algorithm. As perturbations are likely to kick Triton out of any such marginally stable spin-orbit resonances in practice, we will in fact prefer the latter model: in any case, the resulting differences in the evolution of the semimajor axis and eccentricity is negligible.

C.1.2. Conservation laws

Under the assumptions we have made, several more specific conservation laws can be derived that must hold for our propagated dynamical state. These allow us to check whether the numerically implemented equations of motion behave according to the properties that would analytically be expected of them: we check that these hold for each of the (both combined orbit-interior and isolated dynamical) runs presented in this work.

Conservation of angular momentum

The first conservation law for which a restricted version can be derived is conservation of angular momentum: the total angular momentum in Triton's rotation and orbit is given:

$$H_T = H_{\text{rotation}} + H_{\text{orbit}} = \tilde{C}_T \dot{\theta}_T + \sqrt{\mu a(1-e^2)} M_T \tag{C.1}$$

where $\mu = \mathcal{G} M_N$ is the gravitational parameter for Neptune. Taking the derivative with respect to time, inserting the derivatives given by Eqs. 3.1-3.4 and setting $U_N = 0$ (i.e. assuming no tides in Neptune) and $n = \sqrt{\mathcal{G} M_N / a^3}$ (assuming $M_N \gg M_T$, which is a good approximation), we find

$$\frac{\mathrm{d}H_T}{\mathrm{d}t} = \frac{\mathcal{G} M_N^2}{a} \left[\frac{\partial U_T}{\partial \varpi_T} - \frac{\partial U_T}{\partial \Omega_T} \right]. \tag{C.2}$$

[1]Though not shown here, the values for a rigidity of 60 GPa appropriate for rock were also verified to coincide: as the elastic rigidity does not affect the tidal response of a homogeneous body much, these comparisons are not shown in Fig. C.1.

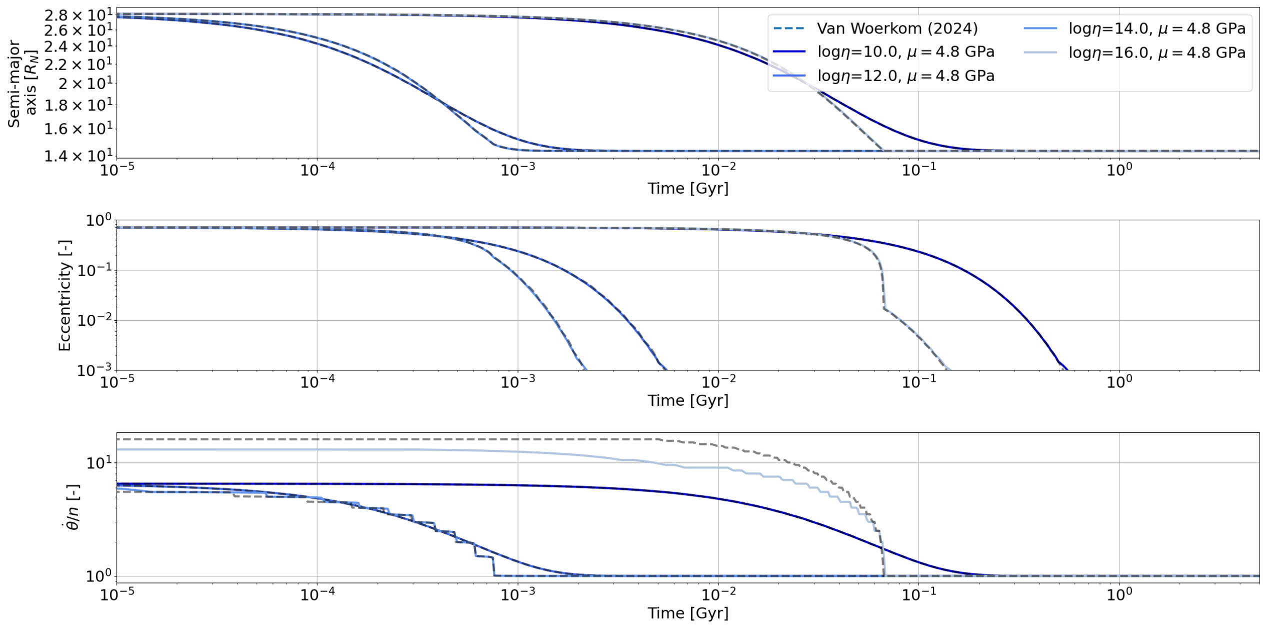

Figure C.1: A comparison between the predictions of the dynamical model presented and validated in Van Woerkom (2024) and the one used in this work for a rigidity of $\mu = 4.8$ GPa and a range of viscosities representative of the range of values that might be encountered in an icy body. From top to bottom: semi-major axis, eccentricity and rotation rate (expressed as fraction of the mean motion) over time.

For the assumed value of $i_T = 0$, $\frac{\partial U_T}{\partial \varpi_T} = \frac{\partial U_T}{\partial \Omega_T}$, and so $\frac{\mathrm{d}H_T}{\mathrm{d}t} = 0$. Hence, the combined angular momentum in Triton's orbit and rotation is conserved. When we assume rotational equilibrium, however, we no longer model the evolution of $\dot{\theta}$ by propagating Eq. 3.4, but find the rotation rate by enforcing $\frac{\partial U_T}{\partial \Omega_T} = 0$, with the implicit consequence that $\frac{\partial U_T}{\partial \varpi_T} = 0$. In that case, we see by the same construction that it is instead solely the orbital angular momentum that is conserved. Hence, our numerical implementation (if it accurately implements the equations of motion) should satisfy to at least the specified tolerances (1) conservation of total angular momentum of Triton during the non-equilibrium rotation epochs, and (2) conservation of orbital angular momentum during the equilibrium rotation epochs. This provides a first check for the correct implementation of the equations of motion: a second restricted conservation law can be shown to hold, however, and so that provides a second check.

Conservation of energy

Aside from conservation of angular momentum, we can also find a restriction to conservation of energy. In particular, the total energy in Triton is given by the sum of its orbital energy, which per the vis-viva equation can be expressed (e.g. Murray & Dermott, 1999; Curtis, 2013):

$$E_{\text{orbit}} = -\frac{\mu}{2a} \tag{C.3}$$

where μ is again the gravitational parameter of Neptune, and its rotational energy:

$$E_{\text{rot}} = \frac{1}{2}\tilde{C}_T\dot{\theta}_T^2 \tag{C.4}$$

such that

$$\dot{E}_{\text{tot}} = \dot{E}_{\text{rot}} + \dot{E}_{\text{orbit}} = \tilde{C}_T\dot{\theta}_T\frac{\mathrm{d}\theta_T}{\mathrm{d}t} + \frac{\mu}{2a^2}\frac{\mathrm{d}a}{\mathrm{d}t} = -\dot{\theta}_T\frac{\mathcal{G}M_N^2}{a}\frac{\partial U_T}{\partial \Omega_T} + \frac{n\mu}{a}\frac{M_N}{M_T}\frac{\partial U_T}{\partial \mathcal{M}} \tag{C.5}$$

where we have again assumed $U_N = 0$. By expanding $\omega_{lmpq} = (l-2p+q)n - n\dot{\theta}_T$, we can also rewrite the energy dissipated in Triton tidally $\dot{E}_T$ as given in Eq. 3.8 in the following way (using, as for conservation of angular momentum, $n = \sqrt{\mathcal{G}M_N/a^3}$ i.e. assuming $M_N \gg M_T$):

$$\dot{E}_T = \dot{\theta}_T\frac{\mathcal{G}M_N^2}{a}\frac{\partial U_T}{\partial \Omega_T} - \frac{n\mu}{a}\frac{M_N}{M_T}\frac{\partial U_T}{\partial \mathcal{M}} \tag{C.6}$$

from which it is clear that all energy dissipated in Triton comes out of Triton's rotational and orbital energy: $\dot{E}_T = -\dot{E}_{\text{tot}}$. In rotational equilibrium, we assume $\frac{\mathrm{d}\dot{\theta}}{\mathrm{d}t} = 0$ such that $\dot{E}_{\text{rot}} = 0$[2], and so all energy is taken out of

[2] Of course, we know this not to be true: if Triton decays into a lower spin-orbit resonance, that energy must go somewhere. The equations we use simply do not reflect that; see Van Woerkom (2024, Sec. A.5) for a discussion.

Triton's orbital energy instead. As Triton's orbital energy is much larger than its rotational energy, this does not affect the dynamical results in any appreciable way: as this energy is dissipated in a short timespan, it might well have important planetological consequences for the epochs of rapid spin-orbit evolution, however. For verification purposes it is important to keep this distinction in expected behaviour in mind.

C.2. Interior evolution

To verify that the interior-evolution code works as intended, we test its performance against analytical expressions. We also check that the assumption of an ice shell in equilibrium is valid for Triton.

C.2.1. Analytical expressions for the mantle evolution

Computing the evolution of the mantle in general (for arbitrary heating) requires numerical methods. However, if the volumetric heating rate is homogeneous and known a priori as a function of time, an analytical expression for the time-dependent thermal evolution of the mantle can be derived. Starting from the heat equation:

$$\rho_m C_m \frac{\partial T}{\partial t} = \frac{1}{r^2}\frac{\partial}{\partial r}\left(r^2 k_m \frac{\partial T}{\partial r}\right) + H_{rg}(t) \tag{C.7}$$

where $H_{rg}(t)$ is a (radially constant) volumetric heating rate (the subscript rg denotes the fact that, in physical situations, this term will correspond to the radiogenic heating rate), we can substitute $u = rT$ to arrive at the Cartesian heat equation:

$$\frac{\partial u}{\partial t} = \alpha \frac{\partial^2 u}{\partial r^2} + \frac{r H_{rg}(t)}{\rho_m C_m} \tag{C.8}$$

with $\alpha = k_m/(\rho_m C_m)$ constant, subject to $u(t, R_m) = R_m T_{\text{melt}}$ and $u(t, 0) = 0$. We can decompose this expression into a homogeneous and particular component $u = u_h + u_p$, setting $u_p = rT_{rg}(t)$ where $T_{rg}(t) = \int H_{rg}/(\rho_m C_m)(t)dt$ i.e. $T_{rg}(t)$ is an antiderivative of $H_{rg}(t)/(\rho_m C_m)$. Consequently, it remains to solve

$$\frac{\partial u_h}{\partial t} = \alpha \frac{\partial^2 u_h}{\partial r^2} \tag{C.9}$$

subject to the boundary and initial conditions

$$u_h(t, R_m) = R_m(T_{\text{me;t}} - T_{rg}(t)) \tag{C.10}$$

$$u_h(t, 0) = 0 \tag{C.11}$$

$$u_h(0, r) = r\left[T(0, r) + T_{rg}(0) - T_{\text{melt}}\right]. \tag{C.12}$$

This form is the usual heat equation in one coordinate with time-dependent boundary conditions, and its solution is well-known, constructed as a Fourier series with time-dependent coefficients (e.g. Carslaw & Jaeger, 1959, Ch. 3):

$$u_h(t, r) = \sum_{n\geq 1} [a_n + b_n(t)] \sin(\lambda_n r)\, e^{-\lambda_n^2 \alpha t} \tag{C.13}$$

$$a_n(t) = \frac{2}{R_m}\int_0^{R_m} r' \left[T(0, r') - T_{rg}(0)\right] \sin(\lambda_n r')\, \mathrm{d}r' \tag{C.14}$$

$$b_n(t) = 2\alpha\lambda_n(-1)^{n+1}\int_0^t e^{\lambda_n^2 \alpha t'}(T_{\text{melt}} - T_{rg}(t'))\, \mathrm{d}t' \tag{C.15}$$

$$\lambda_n = \frac{n\pi}{R_m} \tag{C.16}$$

such that

$$T(t, r) = u_h(t, r)/r + T_{rg}(t). \tag{C.17}$$

is the time-dependent solution to the heat equation in the mantle under the given assumptions. We compute the result of Eq. C.17 at various timesteps, and compare it against our numerical code for a reference mantle scenario starting at a uniform temperature of 250 K with 35 grid points in the mantle and absolute and relative tolerances on the temperature of 10^{-3} K and 10^{-6}, respectively: the results and corresponding error estimates are shown in Fig. C.2.

From Fig. C.2, it is clear that the error in the temperature profile our code estimates behaves desirably: the error shrinks rather than increases with time, and does not show any systematic behaviour with radius with the exception of the larger errors at the boundary conditions, which is to be expected given the different relations used there. To evaluate whether the performance of the code is sensitive to the magnitude of the heating rate, we also run a scenario with a radiogenic heating rate that is magnified by a factor of 10 (though this is of course not a physical heating rate): the result is shown in Fig. C.3, and shows a very similar behaviour.

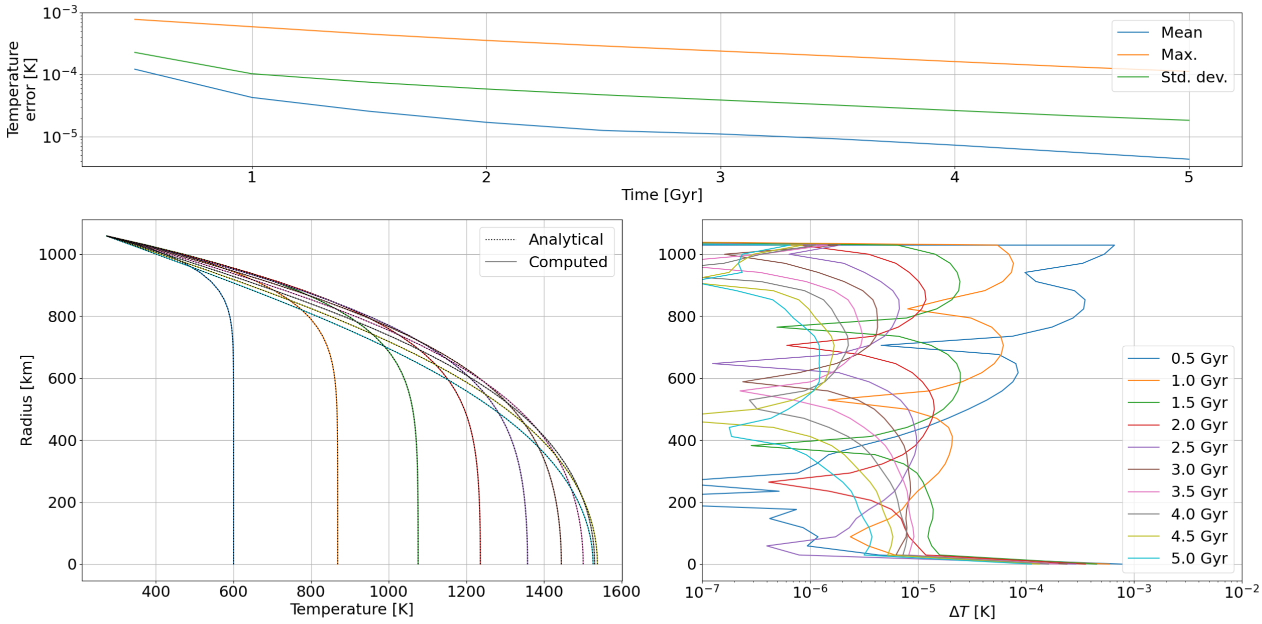

Figure C.2: Error analysis for the numerical implementation of the heat equation in the mantle for a representative mantle evolution scenario, showing the standard deviation as well as the mean and maximum absolute errors (top panel), the analytical and numerically computed temperature profiles at various times (bottom left) and the absolute error at these times as function of radius (bottom right).

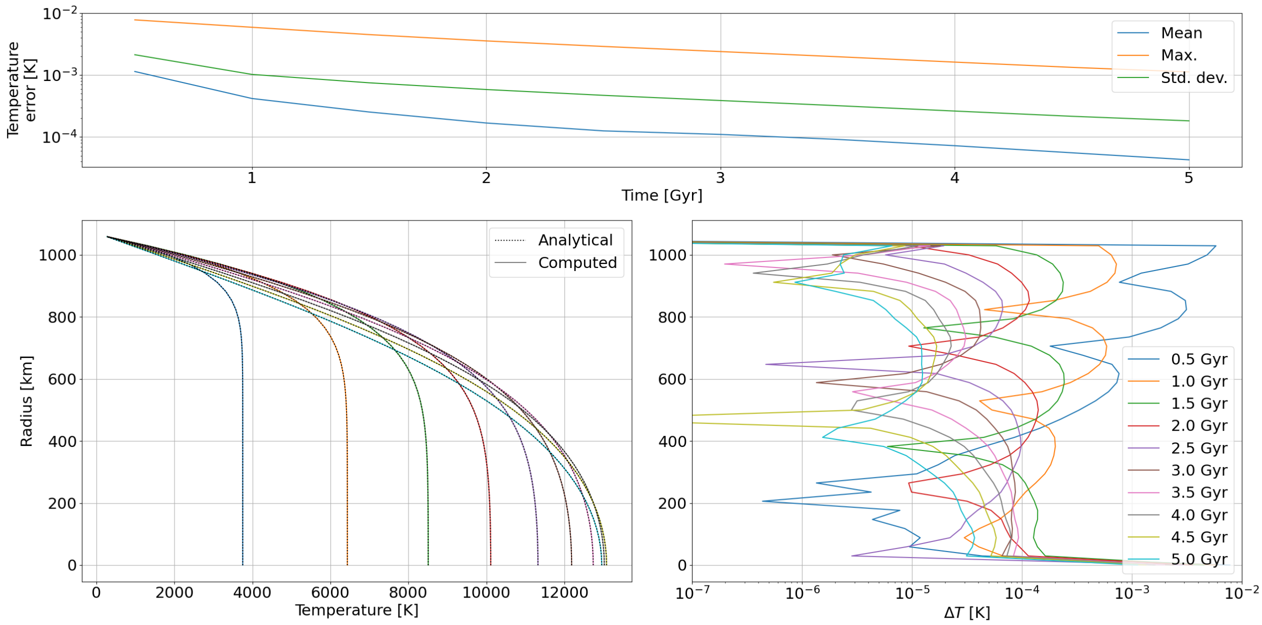

Figure C.3: Error analysis for the numerical implementation of the heat equation in the mantle for a mantle evolution scenario with a 10-times exaggerated radiogenic heating rate, showing the standard deviation as well as the mean and maximum absolute errors (top panel), the analytical and numerically computed temperature profiles at various times (bottom left) and the absolute error at these times as function of radius (bottom right).

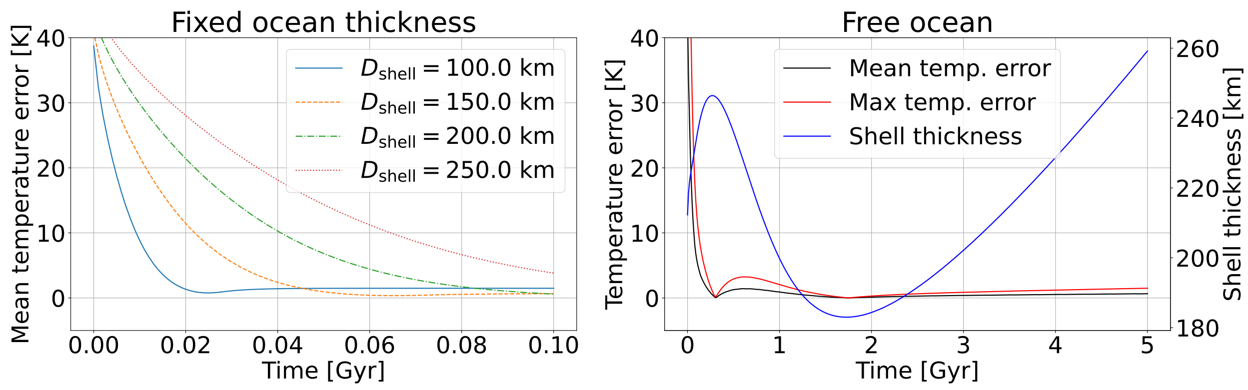

Figure C.4: Mean error incurred by the equilibrium shell profile over time for the fixed ocean thickness-scenario (left) and for an ocean varying according to the equations of motion from Ch. 3 (right; also shown is the ocean thickness over time); in either case, we do not account for tides. Note the difference in horizontal axis between the two scenarios. See text for a discussion on the lack of convergence.

C.2.2. Validity of the equilibrium-shell assumption

To validate our assumption of an equilibrium ice shell, we compare the temperature profile over time for a discretised shell (computed using the heat-equation implementation used for the mantle) coupled to our discretised mantle model against the prediction for an equilibrium shell (Eq. 3.21). We test two scenarios: a shell fixed at a given ocean radius (which allows us to evaluate the connection between shell thickness and equilibration time in a mathematical, even though the scenario is of course unphysical) and a tideless Triton with an ocean that varies in thickness according to Eq. 3.19, with an initial thickness of 50 km. In either scenario, the mantle is initially at 250 K, and the shell temperature is set to linearly decrease from 273 K to an initial surface temperature equal to the equilibrium temperature at Triton (31.6 K)

The results of this comparison are shown in Fig. C.4, expressed as the mean temperature error over all gridpoints in the shell incurred by the equilibrium shell profile. Note that neither case converges to the analytical equilibrium profile: we attribute this to the discretisation, as the mixed nature of the surface boundary condition means that finite difference error incurred at the bottom of the shell is propagated through the shell. This forms part of our decision to prefer the analytical profile over the numerical scheme in the shell: resolving this requires the use of a non-uniform grid or a suitable transformation of the governing equations into a form that does not suffer this problem. We leave this to future work.

From this analysis, it is clear that for tidally unperturbed Triton (the right panel of Fig. C.4) an equilibrium shell is a reasonable assumption beyond $\sim$ 100 Myr or so; based on the tendencies displayed in the left panel, we expect that this timescale is depressed even further for the thin shells (on the order of ~km thick) expected for early tidally heated Triton. This is congruent with what would be expected mathematically: in a similar manner to the expressions derived in Sec. C.2.1, one can show that the thermal damping timescale for a shell with thickness D, a constant conductivity k kept at constant temperatures at either end is $\tau_{\text{thermal}} \sim \frac{D^2 \rho C}{\pi^2 k}$. While the shell does of course not have a constant conductivity or specific heat (nor is the surface kept at a constant temperature), this gives us a reasonable estimate for the timescale of equilibriation: for the values of the specific heat corresponding to 32 and 273 K, we have that $\tau_{\text{thermal}} \sim 6(D/100\text{ km})^2$ Myr and $30(D/100\text{ km})^2$ Myr, respectively. Hence, for a shell thinner than 10 km (which is not unreasonable for early Triton), we expect that equilibriation happens on sub-Myr timescales.

C.3. Combined dynamical and interior evolution

To validate the combined dynamical and interior evolution to work properly, we check that, using their dynamics and our interior model set to roughly comparable settings as theirs, we reproduce the results of Hammond & Collins (2024): additionally, we check that the tidal quality function we use reproduces the behaviour that is expected of it on analytical grounds.

C.3.1. Reproducing Hammond & Collins (2024)

As our dynamical model can at present not go beyond $\sim 240 R_N$ for the initial semi-major axis due to eccentricity constraints, we reproduce the results of the left column of Fig. 3 by Hammond & Collins (2024): we do note that ocean obliquity tides, which we do not account for in our model, dominate in the results of Hammond & Collins (2024) after $\sim$ 1.2 Gyr (when Triton has nearly circularised), and so our results are no longer comparable to theirs by that point. This is a natural consequence of the expression used by Hammond & Collins (2024) for

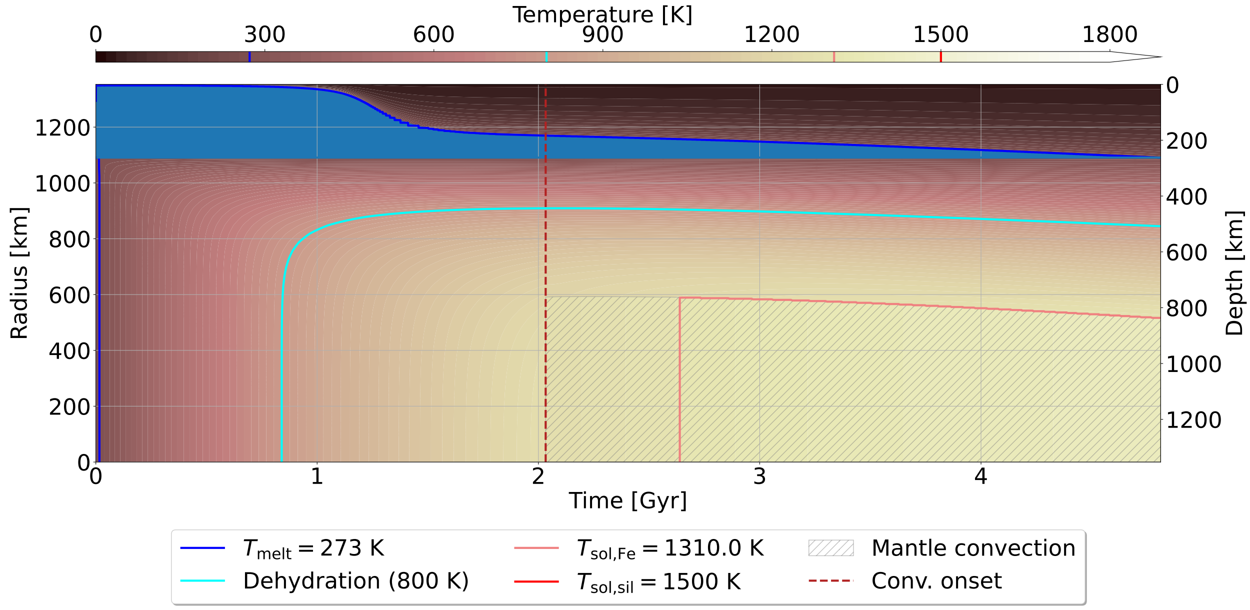

Figure C.5: A reproduction of the interior evolution showcased in Fig. 3 of Hammond & Collins (2024), reprinted as Fig. C.7.

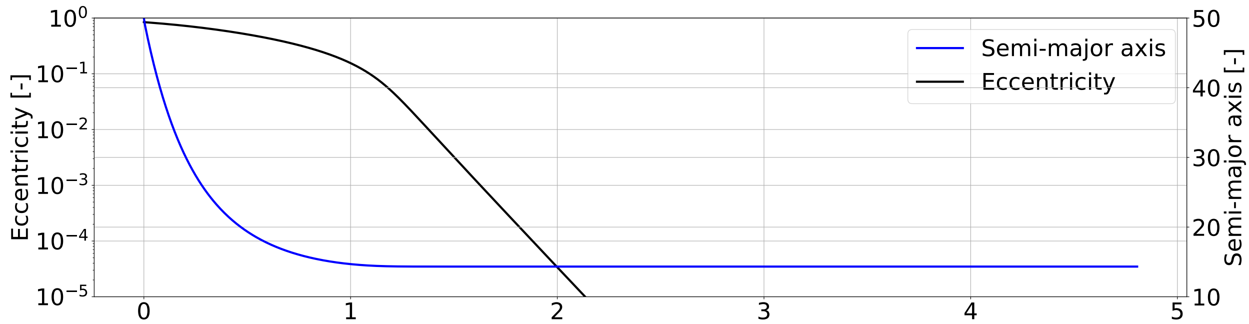

Figure C.6: A reproduction of the orbital evolution showcased in Fig. 3 of Hammond & Collins (2024), reprinted as Fig. C.7.

obliquity tides in the ocean, as this expression is strongly dependent on the orbital rate.

For completeness, we do show the full evolution of Triton's interior and orbit over that regime in Fig. C.5 and Fig. C.6, but keep in mind that the divergence at times when obliquity tides are important is not just explainable, but expected. As Hammond & Collins (2024) do not show the shell-viscosity evolution for this run, we assume a value of $2 \cdot 10^{14}$ Pa s similar the values obtained in the run they show in Fig. 1. Observe that the results found by Hammond & Collins (2024) and ours match until ~ 1.2 Gyr, and diverge afterward.

C.3.2. Tidal quality function for reference profiles

To check that the expressions we use to compute the tidal quality function were implemented as intended, we verify that the tidal quality function produces reasonable results for some reference profiles. For the shell, we will use the equilibrium thermal profile (Eq. 3.21); its use was validated in Sec. C.2.2. For the mantle, we will also use an equilibrium thermal profile, but with the integration constants parametrised in terms of the core and ocean temperature:

$$T(r) = (T_{\mathrm{melt}} - T_{\mathrm{core}})\frac{r^2}{R_m^2} + T_{\mathrm{core}}. \tag{C.18}$$

While we will later find that this is not an entirely reasonable assumption for Triton's mantle, we can at least check the qualitative behaviour of the tidal quality function as a rough function of the mantle temperature profile. The exact mantle profile used is not of importance.

Hard and soft shells

Before discussing the tidal response for various profiles, we briefly introduce some terminology: we will distinguish between *hard shells* and *soft shells*, following the discussion by Beuthe (2018, Sec. 4.3.2), noting that

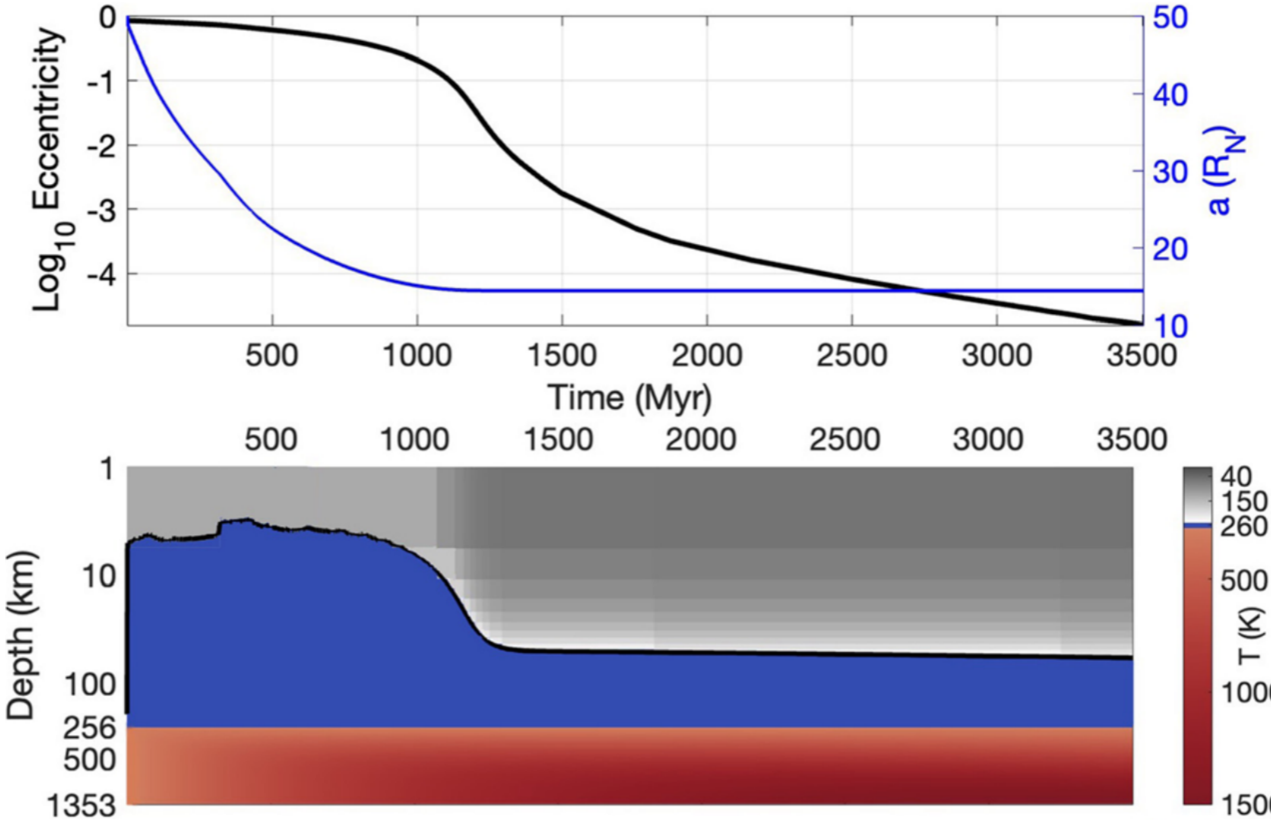

Figure C.7: Orbital and interior evolution starting at $a = 50R_N$ as computed by Hammond & Collins (2024). Reprinted from Hammond & Collins (2024).

the tidal response generally follows reasonably well in one of those two categories (Beuthe, 2015b). If the shear modulus of the shell is small, the shell readily deforms to follow the ocean, and the shell is called *soft*. In this case, the tidal response is close to that predicted by the fluid-crust shell (Beuthe, 2018):

$$K_l = -\operatorname{Im}\left(\bar{k}_l^\circ\right) = -\operatorname{Im}\left(\frac{A_l + (2l+1)y^4\hat{\mu}_c}{B_l + (2l+1-3\xi_1)y^4\hat{\mu}_c}\right) \tag{C.19}$$

where $y = R_\text{core}/R\text{m}$, $\xi_l = \frac{3}{2l+1}\frac{\rho_s}{\rho_b}$ is a function of the ratio between shell and bulk densities ρ_s and ρ_b, $\hat{\mu}_c = \frac{\mu_\text{core}}{\rho_b g R}$ is the dimensionless core rigidity, and A_l and B_l are dimensionless functions of y and ξ_1 defined in Sec. B.1.1. In this regime, the tidal response is largely modulated by the properties of the mantle, independent of the shell.

Whenever the shell is instead barely susceptible to tidal deformation, the shell is deemed *hard*, and deformation happens according to the rigid-mantle approximation (Beuthe, 2019, Eq. D.3):

$$K_l = -\operatorname{Im}\left(\bar{k}_l\right) \tag{C.20}$$

$$\bar{k}_l(\omega) = (1+\Lambda_l)\bar{h}_l(\omega) - 1 \tag{C.21}$$

$$\bar{h}_l(\omega) = \frac{\bar{h}_{l,r}^\circ}{1 + (1+\xi_l\bar{h}_{l,r}^\circ)\Lambda_l(\omega)} \tag{C.22}$$

where $\bar{h}_{l,r}^\circ$ is the rigid-mantle fluid-crust radial Love number (Beuthe, 2019):

$$\bar{h}_{l,r}^\circ = \frac{1}{1-\xi_l} \tag{C.23}$$

and Λ_l is the shell spring constant defined by Eq. B.4. In this case, we observe that the tidal response is determined primarily by the behaviour of the shell. Whenever more than one tidal Fourier mode is sampled by the Darwin-Kaula expansion (as is the case on highly eccentric orbits), it is important to acknowledge that the shell hardness of an icy satellite is a frequency-dependent phenomenon. Hence, we will speak of *hard-shell frequencies* and *soft-shell frequencies*: at hard-shell frequencies, the tidal response is governed by the properties of the icy shell, whereas at soft-shell frequencies the tidal response is close to the fluid-crust response, and its behaviour is determined by the properties of the mantle. A useful and often-made approximation is therefore

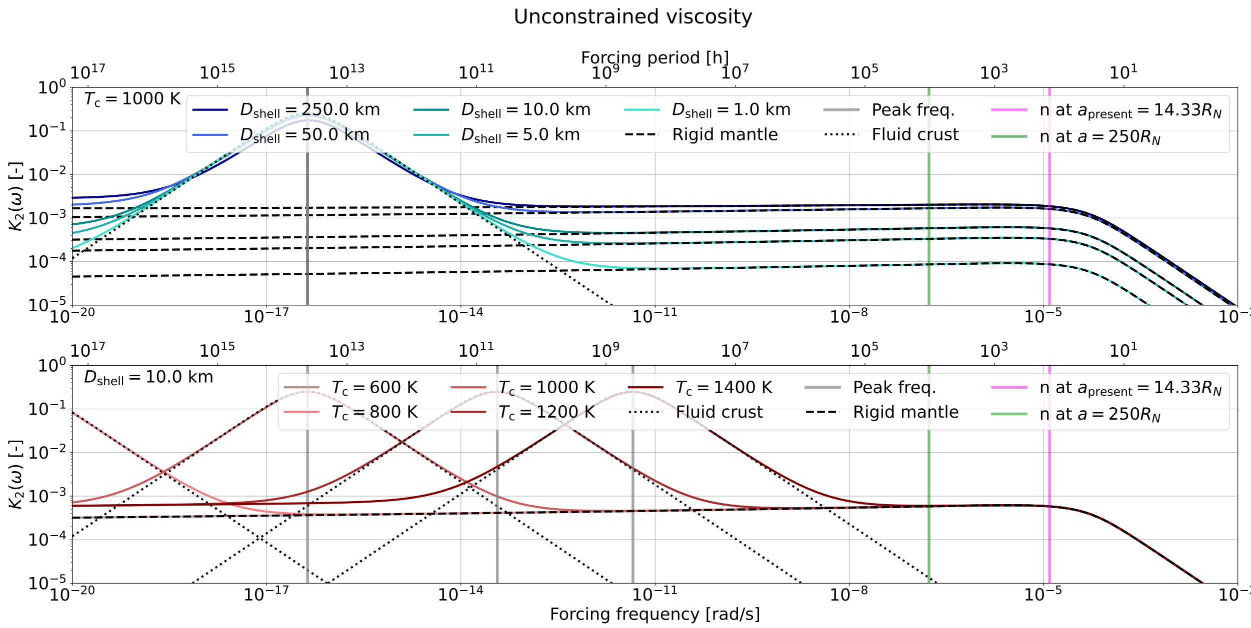

Figure C.8: Degree-2 tidal quality function (imaginary part of the gravitational tidal Love number) as a function of forcing frequency for a range of shell thicknesses (top) and core temperatures (bottom) for unconstrained viscosities. Also shown are the fluid-crust and rigid-mantle tidal response, and the peak fluid-crust frequencies predicted by Eq. C.24, and the mean motion at Triton's present-day semimajor axis and at a semimajor axis of $250R_N$ corresponding to a reasonably high eccentricity of $e \approx 0.97$.

to compute the tidal response by computing separately and then summing the rigid-mantle and fluid-crust components: Hammond & Collins (2024), for example, implicitly resort to this assumption by computing the tidal quality function of the silicate interior as though it were a separate body.

To determine the frequencies at which we expect soft-shell and hard-shell behaviour, we note that the fluid-crust tidal response (Eq. C.19) for a homogeneous Maxwell mantle with viscosity η and elastic rigidity μ_e can be shown analytically to have a maximum at a frequency of ω_{peak}

$$\frac{\omega_{\text{peak}}\eta}{\mu_e} = \frac{C - \sqrt{C^2 - 4C - 4}}{2(C+1)} \tag{C.24}$$

$$C = \frac{(2l + 1 - 3\xi_1)y^4\mu_e}{B_l \rho_b g R}. \tag{C.25}$$

For Triton, we find that $C \approx 161$ such that $\omega_{\text{peak}} \approx 6.26 \cdot 10^{-3} \frac{\eta}{\mu_e}$. Heuristically, we expect that the least viscous (i.e. hottest) part of the mantle dominates its tidal response, such that a mantle with radially-varying properties can be roughly approximated by a uniform mantle with a viscosity equal to the value at its core (where it is hottest).

Verifying the frequency-dependent behaviour of the tidal quality function

To verify that our implementation of the tidal quality function is correct, we check that the behaviour predicted at hard- and soft-shell frequencies is reproduced. Fig. C.8 shows the degree-2 tidal quality function as a function of frequency for a range of shell thicknesses and temperatures; also shown are the fluid-crust and rigid-mantle approximations. In this case, the viscosity is kept unconstrained. We see that the peak frequencies align excellently with the predicted fluid-crust dissipation peaks, and away from the soft-shell regime the rigid-mantle expression is an excellent approximation. At tidal (that is, orbital) frequencies (and, in fact, at higher frequencies), as remarked by Beuthe (2018, Sec. 4.3.2), the rigid-mantle expression provides a very good description even of the combined tidal response.

In practice, we choose to bound the viscosities to those corresponding to dissipation peaks at forcing periods smaller than astronomical timescales: this prevents the fluid-crust and rigid-mantle peaks from moving to arbitrarily low forcing frequencies, as this would introduce (apparent) discontinuities around spin-orbit resonances, which sample the tidal quality function at near-zero frequencies. We choose a maximum viscosity of 10^{23} Pa s for the shell and of 10^{26} Pa s for the mantle. The resulting tidal response is shown in Fig. C.9: it is clear that the tidal response is now well-behaved (going to zero) at forcing periods much larger than ~ 1 Gyr ($\sim 10^{13}$ h), while the response at orbital frequencies is unaffected by this approximation.

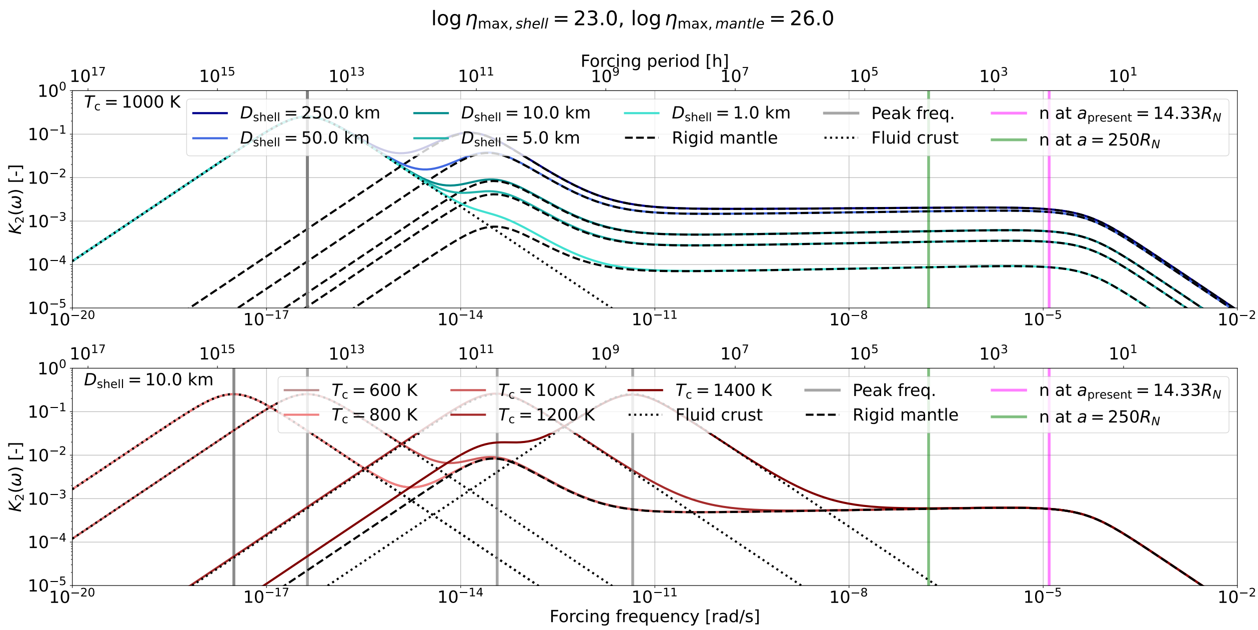

Figure C.9: Degree-2 tidal quality function (imaginary part of the gravitational tidal Love number) as a function of forcing frequency for a range of shell thicknesses (top) and core temperatures (bottom) for constrained viscosities of 10^{23} and 10^{26} Pa s for the shell and mantle, respectively. Also shown are the fluid-crust and rigid-mantle tidal response, and the peak fluid-crust frequencies predicted by Eq. C.24, and the mean motion at Triton's present-day semimajor axis and at a semimajor axis of $250R_N$ corresponding to a reasonably high eccentricity of $e \approx 0.97$.

D The Darwin-Kaula expansion

While we will, for brevity, generally refer to the infinite sum expressions for dissipated tidal energy and the partial derivatives of the perturbed potential as the Darwin-Kaula expansion, this terminology is not entirely correct: strictly speaking, the Darwin-Kaula expansion is the decomposition from which these quantities are derived. For completeness, we provide the corresponding expression in this section.

Following the notation used by Boué & Efroimsky (2019), we can write the perturbed tidal potential $\tilde{U}_j$ generated at a point $\mathbf{r}$ by the body j deformed by a perturbing body k located at a point $\mathbf{r}^*$ in the following form, derived by Kaula (1961, 1964):

$$\tilde{U}_j = -\frac{\mathcal{G}M_k}{a^*}\sum_{l=2}^{\infty}\left(\frac{R}{a*}\right)^l\sum_{m=0}^{l}\frac{(l-m)!}{(l+m)!}(2-\delta_{0m})\sum_{p=0}^{l}F_{lmp}(i^*)\sum_{q=-\infty}^{\infty}G_{lpq}(e^*)\sum_{h=0}^{l}F_{lmh}(i)\sum_{j=-\infty}^{\infty}G_{lhj}(e)k_l(\omega_{lmpq})\cos\psi_{lmpqhj} \tag{D.1}$$

where $k_l(\omega)$ is the dynamical Love number (the magnitude of the complex Love number),

$$\psi_{lmpqhj} = (v^*_{lmpq} - m\theta^*) - (v_{lmhj} - m\theta) - \epsilon_l(\omega_{lmpq}), \tag{D.2}$$

$$v^*_{lmpq} = (l-2p)\varpi^* + (l-2p+q)\mathcal{M}^* + m\Omega^*, \tag{D.3}$$

$$v_{lmhj} = (l-2h)\varpi + (l-2h+j)\mathcal{M} + m\Omega, \tag{D.4}$$

the orbital elements with and without asterisk are those corresponding to the locations $\mathbf{r}^*$ and $\mathbf{r}$, respectively, and all other quantities are as defined in Ch. 2 and Ch. 3. The expressions given in Eq. 3.8 can then be retrieved by taking the relevant partial derivatives[1], with one additional caveat: in the case of a system that can be treated gravitationally as a binary system, such as the Neptune-Triton system, the only terms that will arise in the equations of motion are those for which the perturbed potential is evaluated at the location of the perturbing body, such that $\mathbf{r}^* = \mathbf{r}$. Correspondingly, the orbital elements with and without the asterisk are equated. In that case, averaging over the fast angles, being the mean anomaly $\mathcal{M}$, the argument of pericentre ϖ and the longitude of the ascending node Ω, will eliminate all terms but those for which $h = p$ and $j = q$, finally yielding the expressions in Eq. 3.8.

[1]This must be done before equating $\mathbf{r}^*$ and $\mathbf{r}$: doing so in reverse order (equating the terms and taking the partial derivatives) will yield incorrect expressions.